PROGRAMA DE DOCTORADO EN FÍSICA

TESIS DOCTORAL:

Desarrollo y evaluación de técnicas radiométricas de observación de aerosoles y vapor de agua en la atmósfera desde plataformas terrestres

Presentada por Antonio Fernando Almansa Rodríguez para optar al grado de Doctor por la Universidad de Valladolid

Dirigida por:

Dr. Emilio Luis Cuevas Agulló
Dr. Benjamín Torres Rodríguez
Dr. Ángel Máximo de Frutos Baraja

La realización de esta tesis doctoral ha sido posible gracias a la colaboración entre el Centro de Investigación Atmosférica de Izaña (CIAI), perteneciente a la Agencia Estatal de Meteorología (AEMET), y el Grupo de Óptica Atmosférica (GOA) de la Universidad de Valladolid (UVA).

IV

A mi familia

«Este polvo cae en tal cantidad, que todo lo ensucia a bordo y ofende a los ojos; algunas veces hasta obscurece la atmósfera, tanto, que se han perdido buques y estrellado contra la costa. Con frecuencia cae sobre barcos que navegan a varios centenares de millas de la costa de Africa, hasta más de 1000 millas y en puntos distantes más de 1600 millas en dirección de norte y sur. Me ha sorprendido hallar en el polvo recogido a bordo de un barco, a 300 millas de tierra, partículas de piedra de más de una milésima de pulgada cuadrada mezcladas con materias más finas.»

Charles Darwin a bordo del Beagle navegando por las Islas de Cabo Verde.

Índice general

Agradecimientos

En primer lugar quisiera agradecer la dedicación mostrada a mis directores de tesis. Estoy especialemente agradecido a Emilio Cuevas por ser el promotor y director del proyecto ZEN, y por ser el director principal de esta tesis doctoral. Sin su determinación y buena dirección no hubiese culminado adecuadamente este trabajo. A Benjamín Torres por sus acertadas indicaciones y a Ángel de Frutos por ejercer de enlace con la Universidad de Valladolid.

A todos los coautores que han intervenido en los artículos, particularmente a Rosa García, Omaira García, Victoria Cachorro y Carmen Guirado.

A todo el equipo de Sieltec Canarias S.L., en especial a César López, Manuel Mallorquín, Priscila Ramos, Tomás Martín, Ramón Negrillo, Patricia Hernández y Jose Felipe, por su buen hacer en el desarrollo de los dispositivos ZEN-R.

A Carlos Torres y Alberto Redondas por ser mis tutores en los dos años que estuve como becario de formación de la AEMET, y a Bahaiddin Damiri por ser mi instructor en Cimel Electronique. Gracias a sus enseñanzas adquirí habilidades que me han sido muy útiles para la realización de la presente tesis doctoral.

Agradezco a todos mis compañeros del CIAI, a los que están y a los que ya no están, en particular a Ramón Ramos, Virgilio Carreño, Conchy Bayo, Cándida Hernández, Julián Pérez, Fernando de Ory, Rubén del Campo, Antonio Dorta, Marco Hernández, Saturnino Gutierrez, Juan Santos, Alejandro Dorta, Víctor Yanes, Javier García, Jose Martín, Antonia Chávez, Damián Expósito, Jose Hernández, Sandra Méndez, Antonio Hernández, Rocío López, Antonio Cruz, Néstor Castro, Sergio León, Juanjo Bustos, Carlos Marrero, Pedro Romero, Marcos Damas, Félix Santo Tomás, Alberto Berjón, Natalia Prats, Concha Sálamo, Tachy Fernández y Julieta Bethencourt, su implicación directa o indirecta en el proyecto, tanto en labores de mantenimiento como de logística.

A mi hija Aurora, por haber realizado la importante labor de dibujar con tanto amor y dedicación la preciosa cubierta de esta tesis. A mi pareja y compañera,

África, por haberme ayudado tanto y por haberme soportado aún más si cabe.

Y por último y con el mayor sentimiento de gratitud, a mis padres, porque sin ellos no hubiese podido llegar hasta aquí.

Resumen

La presente tesis doctoral pretende introducir herramientas que permitan aumentar
la capacidad observacional de los aerosoles y el vapor de agua en la atmósfera con el
fin de contribuir a la mejora de la representación espacio-temporal de estos compo-
nentes atmosféricos a nivel global/regional y la estimación de sus tendencias. Esta
labor será desarrollada haciendo uso de observaciones multi-plataforma capaces
de incrementar la cobertura y la disponibilidad de información relevante de los
aerosoles atmosféricos y vapor de agua desde el punto de vista científico. En este
trabajo se analiza, en primer lugar, la intercomparabilidad y consistencia de las
dos principales redes de observación de los aerosoles atmosféricos establecidas a
nivel global, GAW-PFR (Global Atmosphere Watch - Precision Filter Radiometer)
y NASA-AERONET (National Aeronautics and Space Administration - AErosol
RObotic NETwork). Estas dos redes se han implementado con el fin de obtener la
distribución espacio-temporal del espesor óptico de los aerosoles (AOD de las siglas
en inglés de "Aerosol Optical Depth") y una estimación de su tamaño mediante
el Exponente de Ångström (AE). La consistencia e intercomparabilidad de las dos
redes se llevó a cabo en el Observatorio Atmosférico de Izaña, que es un centro
de calibración absoluta de ambas redes y banco de pruebas de la Comisión de
Instrumentos y Métodos de Observación (CIMO) de la Organización Meteorológica
Mundial (WMO de las siglas en inglés de "World Meteorological Organization")
para instrumentos de teledetección de aerosoles y vapor de agua. En dicho análisis
se pudo comprobar que, a pesar de las marcadas diferencias técnicas entre ambas
redes, el AOD obtenido en las bandas espectrales de 440, 500 y 870 nm por me-
dio del fotómetro Cimel CE318, utilizado como referencia en la red AERONET,
cumplía con los requerimientos de trazabilidad establecidos por la WMO, que toma
como referencia la red GAW-PFR. A continuación, y como una segunda parte
de la presente tesis doctoral, se desarrollaron dos dispositivos instrumentales: los
radiómetros ZEN-R que miden la radiancia de cielo en dirección cenital (ZSR), y
que están caracterizados por su simplicidad y robustez al carecer de partes móviles.
El primero de estos desarrollos, el ZEN-R41, fue el primer prototipo destinado
sólo a la medida de aerosoles en la columna atmosférica, mientras que el segundo

desarrollo, el ZEN-R52, es una versión mejorada que permite además obtener el vapor de agua precipitable (PWV, de las siglas en inglés de "Precipitable Water Vapour") gracias a la inclusión de un canal óptico adicional en la banda espectral centrada en 940 nm. Para hacer posible este sistema de observación relativamente simple, hubo que desarrollar la metodología necesaria para la obtención del AOD (ZEN-AOD-LUT) y del PWV (ZEN-PWV-LUT), a partir de las medidas de ZSR. Este procedimiento está basado en tablas de consultas (LUT, de las siglas en inglés de "Look-up-table") y fue evaluado a priori a partir de medidas de ZSR del fotómetro Cimel CE318 en tres estaciones caracterizadas por la presencia de polvo mineral pero de características atmosféricas muy diferentes (Izaña, Tamanrasset y Santa Cruz de Tenerife), obteniéndose resultados muy satisfactorios. En un segundo paso, el sistema ZEN, compuesto por el radiómetro ZEN-R y la mencionada metodología LUT asociada, se evaluó en el Observatorio Atmosférico de Izaña, demostrando la viabilidad del mismo como herramienta de teledetección de aerosoles y vapor de agua suficientemente precisa para ser utilizado en redes desplegadas en zonas remotas y escasamente cubiertas por las actuales redes de teledetección terrestres. Esta última aplicación puede proporcionar información complementaria clave para entender los procesos de emisión de polvo desértico y para mejorar las redes actuales de alerta temprana, entre las que se encuentra el sistema de aviso y evaluación de tormentas de arena y polvo de la WMO (SDS-WAS, en sus siglas en inglés de "Sand and Dust Warning Advisory and Assessment System").

Abstract

The present doctoral thesis aims to introduce tools that allow us to increase the observational capacity of aerosols and water vapour in the atmosphere, in order to contribute to the improvement of the spatio-temporal representation of these atmospheric components at a global/regional level and the estimation of its tendencies. This work will be developed by making use of multi-platform observations capable of increasing the coverage and availability of relevant information on atmospheric aerosols and water vapour from a scientific point of view. This work analyzes, firstly, the intercomparison and consistency of the two main ground-based networks of observation of atmospheric aerosols established at a global level, GAW-PFR (Global Atmosphere Watch - Precision Filter Radiometer) and NASA-AERONET (National Aeronautics and Space Administration - AErosol RObotic NETwork). These two networks have been implemented in order to obtain the spatio-temporal distribution of the aerosol optical depth (AOD) and an estimate of its size using the Ångström Exponent (AE). The intercomparison and consistency was carried out at the Izaña Atmospheric Observatory, which is an absolute calibration centre for both networks and a test bed for the Commission for Instruments and Methods of Observation (CIMO) of the World Meteorological Organization (WMO) for aerosol and water vapour remote sensing instruments. In this analysis it was possible to verify that, despite the marked technical differences between both networks, the AOD, in the spectral bands of 440, 500 and 870 nm, retrieved with the Cimel CE318 photometer used by AERONET, met the traceability requirements with the GAW-PFR reference established by the WMO. Next, and as a second part of this doctoral thesis, two instrumental devices were developed: the ZEN-R radiometers that measure the zenith sky radiance (ZSR), which are characterized by their simplicity and robustness as they lack mobile parts. The first of these developments, the ZEN-R41, was the first prototype intended only for the measurement of atmospheric aerosols in the atmospheric column, while the second development, the ZEN-R52, is an improved version that also allows remote sensing of precipitable water vapour (PWV) thanks to the inclusion of an additional optical channel in the spectral band centred at 940 nm. In order to make this

relatively simple observation system possible, the necessary methodology had to be developed to obtain the AOD (ZEN-AOD-LUT) and the PWV (ZEN-PWV-LUT), from the ZSR measurements. This procedure based on look-up-table (LUT) was pre-evaluated from ZSR measurements of the Cimel CE318 photometer at three stations characterized by the presence of atmospheric dust, but with very different atmospheric characteristics (Izaña, Tamanrasset and Santa Cruz de Tenerife), obtaining very satisfactory results. In a second step, the ZEN system, made up of the ZEN-R radiometer and the aforementioned associated LUT methodology, was evaluated at the Izaña Atmospheric Observatory, showing its viability as a sufficiently precise aerosol and water vapour remote sensing tool to be used in networks deployed in remote areas and sparsely covered by current ground-based remote sensing networks. The latter application can provide key complementary information to understand desert dust emission processes, and to improve current early warning networks, in which we can find the SDS-WAS (Sand and Dust Warning Advisory and Assessment System) of the WMO.

Modalidad y estructura de la tesis

Esta tesis se realizará según la modalidad de "compendio de artículos". Todos los artículos han sido publicados en revistas científicas pertenecientes al primer y segundo cuartil . Las referencias de los artículos publicados son las siguientes:

1. ***Artículo 1***: Cuevas, E., Romero-Campos, P. M., Kouremeti, N., Kazadzis, S., Räisänen, P., García, R. D., Barreto, A., Guirado-Fuentes, C., Ramos, R., Toledano, C., Almansa, F., and Gröbner, J.: Aerosol optical depth comparison between GAW-PFR and AERONET-Cimel radiometers from long-term (2005–2015) 1 min synchronous measurements, Atmos. Meas. Tech., 12, 4309–4337, https://doi.org/10.5194/amt-12-4309-2019, 2019.

    - Índice de impacto (2019): 3,668.

    - Posición de revista: 27/93, Q2.

    - Base de indexación: JCR – Science Edition – Meteorology and Atmospheric Sciences.

2. ***Artículo 2***: Almansa, A. F., Cuevas, E., Torres, B., Barreto, Á., García, R. D., Cachorro, V. E., de Frutos, Á. M., López, C., and Ramos, R.: A new zenith-looking narrow-band radiometer-based system (ZEN) for dust aerosol optical depth monitoring, Atmos. Meas. Tech., 10, 565–579, https://doi.org/10.5194/amt-10-565-2017, 2017.

    - Índice de impacto (2017): 3,248.

    - Posición de revista: 19/86, Q1.

    - Base de indexación: JCR – Science Edition – Meteorology and Atmospheric Sciences.

3. ***Artículo 3***: Almansa, A. F., Cuevas, E., Barreto, Á., Torres, B., García, O. E., Delia García, R., Velasco-Merino, C., Cachorro, V. E., Berjón, A., Mallorquín, M., López, C., Ramos, R., Guirado-Fuentes, C., Negrillo, R. and de Frutos,

- Índice de impacto (2019): 4,509.

- Posición de revista: 9/30, Q2.

- Base de indexación: JCR – Science Edition – Remote Sensing.

La presente memoria se estructura de la siguiente manera:

En el capítulo 1 se realiza una introducción general sobre los aerosoles y el vapor de agua, se presenta las principales técnicas de medida, las principales redes radiométricas existentes, así como su cobertura en las regiones desérticas. Los capítulos 2 y 3 muestran la motivación y los objetivos respectivamente. En el capítulo 4 se realiza una descripción en términos de AOD (de las siglas en inglés de "Aerosol Optical Depth") y PWV (de las siglas en inglés de "Precipitable Water Vapour") de las localizaciones donde se llevó a cabo el estudio.

En el capítulo 5 se describe la instrumentación utilizada en este estudio: los radiómetros ZEN-R, que son los nuevos desarrollos a evaluar, el PFR como instrumento de referencia mundial de AOD, el Cimel CE318, como instrumento de referencia para las medidas de radiancia y AOD con el que se comparará los radiómetros ZEN, y por último el FTIR (espectrómetro de infrarrojos basado en transformada de Fourier) como instrumento de referencia para el PWV.

Los métodos empleados en el sistema ZEN se especifican en el capítulo 6. En él se describen brevemente el modelo de transferencia radiativa libradtran utilizado para la simulación de la ZSR, se muestra el proceso de calibración de los dispositivos en radiancia de los radiómetros, y por último se explican detalladamente los métodos de estimación de AOD y PWV, así como el algoritmo de control de calidad del sistema ZEN.

En el capítulo 7 se muestran cada uno de los artículos publicados acompañados de un resumen en español así como un resumen gráfico y las conclusiones generales de cada artículo. El orden en que son presentados no sigue un criterio cronológico sino en base a la coherencia de los resultados mostrados. Conforme a esto, se distinguen dos partes claramente diferenciadas: la primera parte representada por el artículo 1, que muestra una comparación exhaustiva del AOD entre las dos redes fotométricas más importantes, GAW-PFR y AERONET; y una segunda parte representada por los artículos 2 y 3, en la que se muestran los principales resultados de AOD y PWV obtenidos con el sistema ZEN en sus diferentes versiones.

Por último, en los capítulos 8 y 9 se indican las conclusiones finales de este trabajo

y las posibles líneas futuras respectivamente.

1. Introducción

1.1. Los aerosoles y el vapor de agua en la atmósfera

Los aerosoles son partículas materiales suspendidas en la atmósfera, una mezcla compleja de compuestos sólidos o líquidos, orgánicos o inorgánicos, con diferentes tamaños, formas (figura 1.1) y composición química (Boucher, 2015; Lenoble et al., 2013). Se tratan de entidades únicas en cuanto a su complejidad y su importante impacto radiativo (IPCC, 2013, y referencias en su interior), que también tienen un efecto en la salud (Schwartz et al., 1996; Davidson et al., 2005; Dominguez-Rodriguez et al., 2017), en el medio ambiente y los ecosistemas tanto terrestres como marinos (Koren et al., 2006; Ben-Ami et al., 2010; Abouchami et al., 2013; Ravelo-Pérez et al., 2016) y en la sociedad y economía a través de su impacto sobre factores como la visibilidad (White and Roberts, 1977; Xiao et al., 2014), la productividad primaria (Jickells et al., 2005; Lu et al., 2017), la precipitación (Twomey, 1977; Albrecht, 1989; Stevens and Feingold, 2009) o la producción energética (Neher et al., 2017).

Los aerosoles se encuentran en la atmósfera en concentraciones traza y con una alta variabilidad espacio-temporal en cuanto a concentraciones y naturaleza (Seinfeld and Pandis, 2016). Su compleja distribución geográfica depende de la compleja localización de sus fuentes (altamente variable), su ciclo de vida, y la dinámica atmosférica.

Pueden tener un origen natural, como el polvo mineral, el aerosol marino, el biológico (fragmentos de plantas, pólenes o esporas), y las partículas de origen volcánico, o antropogénico, como los productos de la quema de combustibles fósiles. Existen otros, como los sulfatos o el hollín, que pueden compartir ambos orígenes, natural y antropogénico. En la troposfera, una fracción significativa de los aerosoles es de tipo antropogénico. Este último tipo de aerosol es más pequeño y absorbente que el de origen natural, estimando su contribución al espesor óptico de aerosoles (AOD, de las siglas en inglés de "Aerosol Optical Depth") (Ångström, 1929, 1961, 1964;
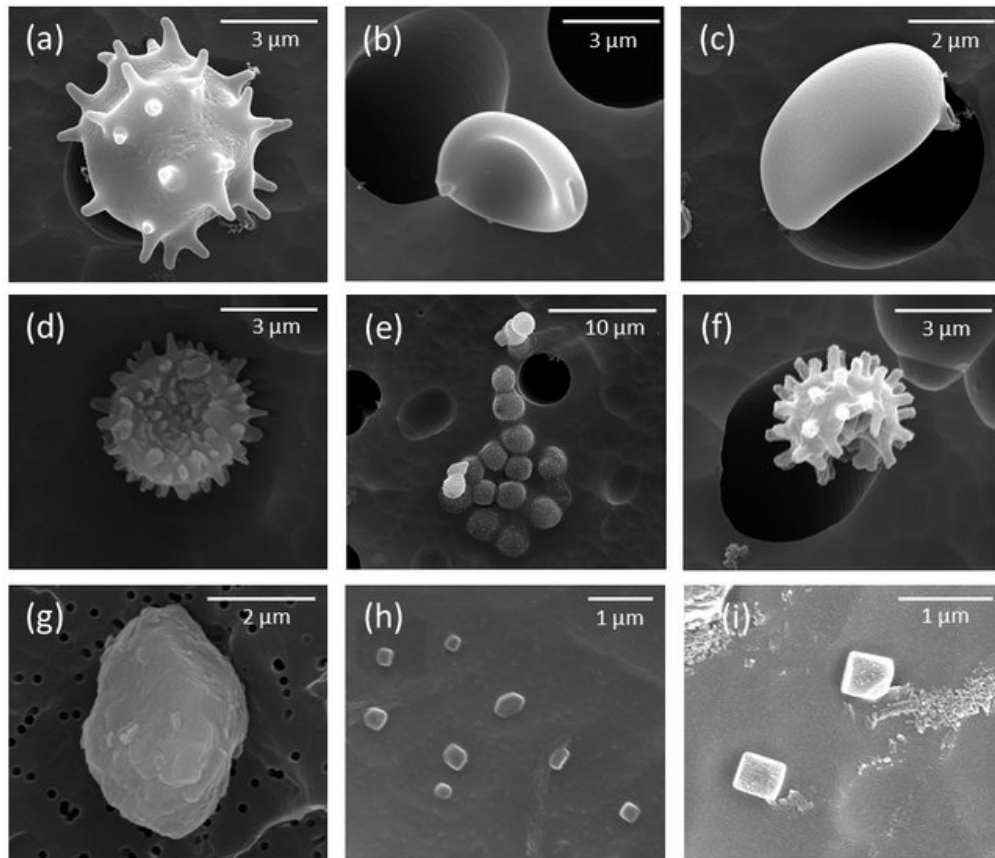
Figura 1.1: Imagen de diferentes aerosoles atmosféricos tomadas por medio de un microscopio electrónico de barrido (SEM) (extraído de Valsan et al., 2016). En ella se representan ejemplos de diferentes variedades de esporas (a-d), esporas con recubrimiento marino (e,f), polvo mineral (g) y aerosol marino (h,i).

WMO, 1986, 1994; Wehrli, 2000) medio global (en 550 nm) en un 20-40 % (IPCC, 2013).

Los aerosoles en la atmósfera sufren procesos de condensación, coagulación, reacciones químicas entre compuestos o activación en condiciones de sobresaturación que constituyen las gotas de niebla o lluvia. El ciclo de vida del aerosol en la atmósfera finaliza con el proceso de deposición. Esta deposición, entendida como la eliminación de los aerosoles en la atmósfera, se puede llevar a cabo por dos procesos, dependiendo de la ausencia o no de precipitación: deposición seca y húmeda (Boucher, 2015). La eficiencia de estos mecanismos depende fuertemente del tamaño, composición química y propiedades termodinámicas de las partículas. En particular, las partículas más gruesas suelen tener un tiempo de vida más breve, ya que el proceso de "caída del aerosol" viene fundamentalmente gobernado por la

ley de Stokes (Stokes, 1851), que establece que la velocidad de caída de la partícula aumenta con el radio de la misma.

La clasificación de los aerosoles en función de su origen no es la única posible. Otra clasificación puede realizarse en función de su tamaño. Los aerosoles se encuentran presentes en la atmósfera con un amplio rango de tamaños (desde conglomerados moleculares hasta partículas de decenas de micras de radio), aunque de manera general se puede decir que la mayor parte de ellos se encuentran contenidos dentro del intervalo de tamaños de $0,05 - 10$ micrómetros (o micras, μm) (Lenoble et al., 2013). Su distribución de tamaño surge a través de complejos procesos que marcan su dinámica de producción, transformación y lavado, en los que también interviene la interacción con las nubes y la precipitación. De acuerdo con Whitby (1978), se pueden identificar tres modos bien diferenciados en la distribución de tamaños de los aerosoles (Figura 1.2):

- Modo nucleación: formado por aerosoles pequeños, de pocos nanómetros de diámetro, hasta $0,1$ μm. Los aerosoles que dan lugar a este modo son principalmente el hollín, los sulfatos y los aerosoles orgánicos (primarios y secundarios).

- Modo acumulación: constituido por aerosoles de tamaños intermedios, con diámetros comprendidos entre $0,1$ y 1 μm. En este modo se encuentran los aerosoles orgánicos (primarios y secundarios), los sulfatos, la sal marina fina, el polvo mineral fino, los nitratos y el hollín.

- Modo grueso: con diámetros que oscilan entre 1 y 100 μm. Debido a su gran tamaño son eliminados fácilmente por sedimentación gravitacional. Son generados de manera mayoritaria por procesos mecánicos, siendo principalmente aerosoles primarios de origen natural, como el polvo mineral, la sal marina y los aerosoles biológicos.

En lo que se refiere a su efecto radiativo, el signo de la interacción aerosol-radiación, o efecto directo de los aerosoles en el sistema climático, depende de la naturaleza del aerosol. A pesar de la creciente sofisticación de las técnicas de medida de los aerosoles, aún existe una importante incertidumbre a la hora de cuantificar el importante papel que juegan los aerosoles atmosféricos dentro del sistema climático. Tanto es así, que el informe emitido en 2013 por el grupo intergubernamental de expertos sobre el cambio climático (IPCC) ha identificado el forzamiento radiativo de los aerosoles y las respuestas asociadas a ellos (muchas de ellas a través de complejos bucles de retroalimentación) como una de las mayores incertidumbres en nuestro conocimiento sobre el cambio climático. Este informe, realizado haciendo uso de modelos y de datos observacionales, estima en $-0,9$ Wm^{-2} el forzamiento radiativo efectivo global promedio como consecuencia del forzamiento conjunto
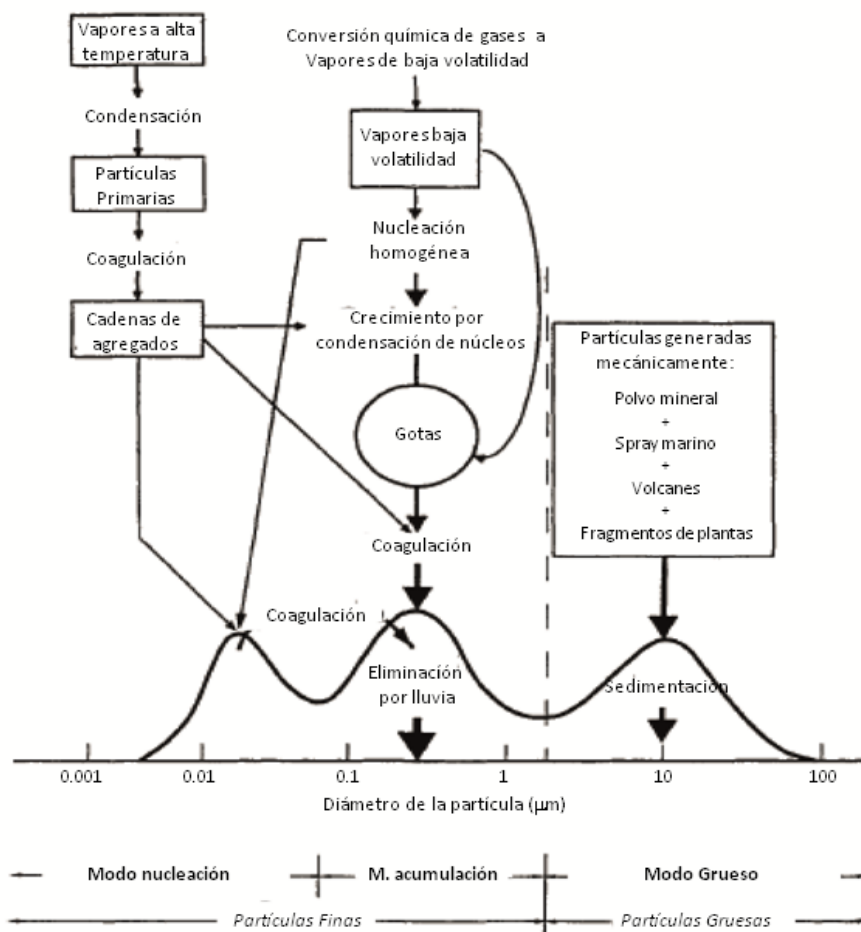
Figura 1.2: Esquema idealizado de la distribución de tamaños de los aerosoles incluyendo sus modos principales, fuentes y mecanismos de formación y eliminación (modificada de Seinfeld and Pandis, 2016).

aerosol-radiación y aerosol-nubes, con un amplio rango de variabilidad que oscila entre $-1,9\ Wm^{-2}$ y $-0,1\ Wm^{-2}$, lo cual explica la confianza media que se tiene sobre este resultado. Son varios los factores que explican estos resultados. En primer lugar, la alta variabilidad espacio-temporal en la concentración de los aerosoles y el tiempo de vida reducido de los mismos en la atmósfera que explican, en parte, esta alta incertidumbre. A este factor también se debe añadir que los mecanismos físicos/químicos/biológicos que producen los aerosoles primarios y secundarios y su relación con las nubes son aún más complejas de lo que se esperaba, y se pueden inducir respuestas a través de procesos de retroalimentación que pueden llevar a amplificar o a amortiguar el forzamiento radiativo de aerosoles y nubes.

A pesar de esta alta incertidumbre, el dato que debe ser destacado es el signo de dicha estimación, que indica que los aerosoles atmosféricos ejercen un efecto de enfriamiento sobre el clima. La reducción programada en las tasas de emisiones de aerosoles de origen antropogénico fruto de las políticas en curso de mejora de la calidad del aire a nivel global nos dejan sumidos en un nuevo escenario en el que se debe acoplar el cambio climático actual fruto de las concentraciones actuales (y crecientes) de gases de efecto invernadero con un menor contenido de aerosoles que pueda dar lugar a un nuevo escenario muy complejo y aún desconocido.

En lo que respecta al vapor de agua atmosférico, este es un componente atmosférico con un potente impacto de retroalimentación positiva (calentamiento) en el sistema climático (IPCC, 2013). Se trata del mayor contribuyente al efecto invernadero natural (Wagner et al., 2006; Chen and Liu, 2016), y posee un papel clave en la dinámica troposférica y el crecimiento de los aerosoles. La cantidad de este componente atmosférico está controlada principalmente por la temperatura del aire y no por emisiones, tal y como muestra Myhre et al. (2013). Su abundancia total en columna se estudia a través del PWV (de las siglas en inglés de "Precipitable Water Vapour"). Posee, al igual que los aerosoles, una gran variabilidad espacio-temporal, por lo que su observación supone también un reto para la comunidad científica, no sólo en relación a estudios de cambio climático (IPCC, 2007; Allan and Soden, 2008; Zhang et al., 2013), sino también en estudios de validación de productos obtenidos a bordo de plataformas espaciales (Mieruch et al., 2008, 2014, y referencias en su interior), en modelos numéricos de predicción del tiempo y en los procesos de asimilación de productos de vapor de agua en los mismos (Kunz et al., 2014; Jiang et al., 2015, y referencias en su interior). Por este motivo, resulta también una variable muy compleja para su implementación en modelos climáticos, lo cual afecta de manera importante en los procesos de representación de nubes y precipitación de estos modelos y sus predicciones.

1.2. Técnicas de monitorización de aerosoles y vapor de agua

La observación de los aerosoles puede dividirse en dos categorías: in-situ y teledetección (Lenoble et al., 2013).

Las técnicas de medida in-situ comprenden aquellas técnicas en las que el instrumento se encuentra en contacto directo con la partícula de aerosol en cuestión. Aunque se trata de técnicas extremadamente útiles para la observación de los aerosoles, tienen por contrapartida que alteran la naturaleza del aerosol durante los procesos de medida y recogida de la muestra.

Las técnicas de teledetección incluyen todas aquellas medidas realizadas de forma

remota, a una distancia determinada del aerosol a medir y sin interferencia alguna con él. En este caso, la descripción del aerosol se realiza a través del análisis de la radiación medida por el observador que previamente ha interaccionado con el aerosol. Se distinguen dos tipos de técnicas de teledetección en función del origen de la radiación. Así, si la radiación electromagnética es emitida de manera artificial por el observador, se dice que se trata de una técnica de teledetección activa, como la técnica lidar o radar. Si la observación se basa en el análisis de la radiación natural, como por ejemplo la radiación de emitida por el Sol, la técnica de teledetección se conoce como pasiva.

Los instrumentos utilizados en teledetección pueden estar ubicados en la superficie terrestre, o embarcados en satélites orbitando sobre nuestro planeta. Con independencia de la posición, a partir de las medidas de ambos se pueden inferir las propiedades de los aerosoles y del vapor de agua atmosférico. Además las medidas desde los satélites permiten describir las propiedades radiativas de la superficie terrestre. La caracterización realizada desde la superficie terrestre nos ofrece una información típicamente más detallada y con una frecuencia temporal mucho más amplia, especialmente si se compara con satélites polares, los cuales tienen una frecuencia temporal limitada por su órbita (una pasada diaria sobre un determinado lugar en el caso de satélites síncronos al sol). Por otro lado, los satélites poseen una mayor cobertura espacial proporcionando una visión global de la distribución de los aerosoles y del contenido de vapor de agua en columna. Además, los sensores embarcados en satélites han experimentado un enorme avance en las últimas décadas en cuanto a la tecnología utilizada, su resolución espacial y calidad de productos derivados. Aun así, continúan teniendo ciertas limitaciones que suponen una alta incertidumbre en sus productos. La más importante surge del acoplamiento de la reflectancia superficial y la señal que llega al sensor remoto con la contribución de los aerosoles. El uso de diferentes geometrías de visión, diferentes rangos espectrales o modelos de reflectancia superficial son posibles soluciones a este problema, pero llevan aparejados importantes incertidumbres sobre los productos finales, en especial sobre superficies brillantes en el rango visible del espectro electromagnético, como desiertos o superficies semiáridas (Li et al., 2009). Otras desventajas importantes de las técnicas de teledetección desde satélite son: la contaminación por nubes, los importantes problemas de calibración, la deriva que sufren los sensores o la baja resolución temporal (Li et al., 2009). Esta última representa una limitación fundamental a la hora de monitorizar procesos rápidos de aerosoles, como tormentas de polvo. Por este motivo, las técnicas de teledetección desde la superficie terrestre proporcionan información importante para la monitorización a lo largo del tiempo en un mismo lugar de aerosoles y vapor de agua, así como para la validación del producto de teledetección desde satélite, y en la asimilación y validación de modelos de aerosoles y vapor de agua en columna. La fotometría

solar/lunar aparece como una técnica útil y robusta para proporcionar información sobre la carga de aerosoles en la columna atmosférica (Holben et al., 1998; Wehrli, 2000; Takamura et al., 1994; Barreto et al., 2016; Giles et al., 2019).

El AOD es el parámetro que mejor representa la cantidad de aerosoles en columna, y es usado de forma generalizada para el estudio del efecto de los mismos en el cambio climático. Se trata de la variable más completa para evaluar dicha carga y representa el denominador común en relación a los productos procedentes de técnicas de teledetección tanto desde superficie como de satélite, y por parte de modelos climáticos, y de predicción de aerosoles. El AOD representa la extinción de la radiación solar en la columna atmosférica atribuida a los aerosoles, y es un parámetro típicamente medido en técnicas de teledetección pasiva, tanto desde superficie (basadas en la medida de la extinción de la radiación solar/lunar/estelar directa), como desde satélite (aplicando métodos más complejos sobre las medidas de la radiación solar reflejada). Otro parámetro importante para la caracterización de los aerosoles es el exponente de Ångström (AE) (Ångström, 1929, 1961, 1964), el cual representa la variación espectral del AOD y aporta información sobre el tamaño de las partículas, siendo más bajo cuanto mayor es la partícula. La curvatura espectral de este parámetro contiene además información importante sobre la distribución de tamaños de los aerosoles (O'Neill et al., 2001b,a, 2003; Schuster et al., 2006), propiedad relevante para conocer los efectos radiativos de estos constituyentes atmosféricos.

El PWV es una variable utilizada de manera generalizada para cuantificar el contenido de vapor de agua en observaciones operacionales y en estudios climáticos. Se define como el vapor de agua integrado en columna, contenido en una columna vertical de sección transversal unitaria, extendida entre dos niveles específicos (generalmente desde la superficie terrestre hasta el tope de la atmósfera). De las diferentes técnicas utilizadas para monitorizar esta variable, se consideran técnicas de referencia las siguientes metodologías, capaces de obtener el PWV con alta precisión: a) radiómetros de microondas (Cadeddu et al., 2013), b) radiosondas de referencia GCOS (Global Climate Observing System)-GRUAN (Reference Upper Air Network), a las que se le aplica un algoritmo específico de corrección (Dirksen et al., 2014) o c) por medio de espectrómetros infrarrojos basados en transformada de Fourier (FTIR) en superficie (Schneider et al., 2010a). Los radiómetros de microondas son los dispositivos más adecuados para la monitorización del PWV, al ser capaz de operar en muchas condiciones ambiente, y dar productos con alta precisión. Sus observaciones son ampliamente utilizadas en aplicaciones meteorológicas operacionales (Calpini et al., 2011) y sus datos están siendo asimilados de modo rutinario por los modelos numéricos de predicción del tiempo, mejorando así sus productos (Calpini et al., 2011). Sin embargo, su complejidad y coste hacen

que sea una técnica que difícilmente puede proporcionar el PWV con la suficiente resolución espacial global. Existen métodos menos precisos para la obtención de PWV, como las radiosondas (Miloshevich et al., 2009), los sistemas de satélite para la navegación global (GNSS, de las siglas en inglés de "Global Navigation Satellite System") (Bevis et al., 1992; Wang et al., 2007; Alexandrov et al., 2009), lidars Raman (Mattis et al., 2002; Whiteman et al., 2010, 2012), fotómetros solares, lunares o estelares (Halthore et al., 1997; Schmid et al., 2001; Torres et al., 2010; Barreto et al., 2016; Pérez-Ramírez et al., 2012, 2014) o espectrorradiómetros (Cachorro et al., 1998; Raptis et al., 2018). Con todos estos métodos de medida ha sido posible ampliar la cobertura de las medidas del PWV, aunque se estima que la precisión de éstas últimas oscila entre el 5 % y el 20 % (Schneider et al., 2010a; Raptis et al., 2018). La red de radiosondas puede ser considerada la técnica que proporciona una cobertura espacial más extendida, unas 1300 estaciones en todo el mundo (ver https://www.wmo.int/pages/prog/www/OSY/Gos-components.html#upper, último acceso: 19/11/2020) pero presenta como desventaja su baja resolución temporal (generalmente dos observaciones diarias, como máximo).

1.3. Redes radiométricas en superficie

La Organización Mundial de Meteorología (WMO, de las siglas en inglés de "World Meteorological Organization") recomienda establecer redes de medida a largo plazo con la suficiente calidad como para evaluar los efectos climáticos de los aerosoles atmosféricos y el vapor de agua (Myhre and Baltensperger, 2012; WMO, 2016). Hoy en día existen diversas redes globales con esta finalidad, basadas en protocolos de medidas programadas, con rigurosos programas para la verificación de su calidad (en términos instrumentales y de algoritmos), y con procedimientos de intercambio de datos estándar. Este tipo de técnicas están sujetas actualmente a procedimientos de control y verificación de calidad estandarizados, generalmente centralizados, y capaces de producir medidas trazables a una referencia primaria, garantizando de esta manera la alta calidad de las medidas. También tienen la ventaja de proporcionar medidas a largo plazo, en varias longitudes de onda y con una amplia cobertura geográfica. Actualmente las redes radiométricas más importantes son las siguientes:

- GAW-PFR (Global Atmosphere Watch - Precision Filter Radiometer): Esta red (Wehrli, 2000, 2005) surge como sucesora del programa BAPMON (Background Air Pollution Monitoring Network) que concluye en 1989. Está formada por 12 estaciones permanentes y 24 adicionales distribuidas por todo el globo (Figura 1.3). Garantiza una calibración centralizada por medio de una referencia calibrada (Wehrli, 2005), para lo cual la WMO estableció en

2006 el WORCC (World Optical Depth Research and Calibration Center) (WMO, 2007). Se trata de una red constituida por radiómetros PFR (Wehrli, 2000, 2005, 2008a,b), que fue establecida por la WMO para servir de referencia en las medidas de AOD. La incertidumbre en el AOD del PFR está establecida entre 0,002 y 0,01 dependeniedo de la longitud de onda (Wehrli, 2000; Kazadzis et al., 2018b). GAW-PFR no proporciona información sobre el PWV. Para más detalles sobre el radiómetro PFR véase la sección 5.1.

Figura 1.3: Mapa global de las localizaciones de las 24 estaciones GAW-PFR en el año 2020 (extraida de https://community.wmo.int/activity-areas/gaw/science/aerosol-research).

- AERONET (AErosol RObotic NETwork): Se trata de una red federada, compuesta por diferentes redes nacionales y regionales que surge en 1998 con el fin de validar productos de satélite y mejorar la caracterización que se tenía de los aerosoles proporcionando importante información sobre sus propiedades ópticas (Holben et al., 1998, https://aeronet.gsfc.nasa.gov). También proporciona información sobre el PWV. Entre las instituciones que colaboran para constituir esta red global destacan el programa NASA-EOS (National Aeronautics and Space Administration Earth Observing System) coordinado por el GSFC (Goddard Space Flight Center), PHOTONS-LOA (Photométrie pour le Traitement Opérationnel de Normalisation Satellitaire, Laboratoire d'Optique Atmosphérique), AEROCAN-CARTEL (Canadian Aeronet subnetwork, Centre d'Applications et de Recherches en Teledetec-

tion) o RIMA-GOA-UVA (Red Ibérica de Medida fotométrica de Aerosoles, Grupo de Óptica Atmosférica, Universidad de Valladolid). Engloban la medida de la extinción de la radiación directa en onda corta para diferentes fuentes naturales (sol y luna) y la distribución angular de la radiación difusa solar por medio del radiómetro Cimel CE318 (Holben et al., 1998; Barreto et al., 2016). Con más de 600 estaciones en la actualidad (Figura 1.4), es la red de fotómetros mundial más extensa, y la única en proporcionar datos en tiempo cuasi-real y de largo plazo. No realiza labores comparativas con la referencia WMO, aunque proporciona datos de alta calidad caracterizados por un procesado centralizado, distribución libre, y cobertura día/noche. Se estima la incertidumbre en el producto de AOD de AERONET en $0,01 - 0,02$ para instrumentos de campo, y $0,002 - 0,009$ para instrumentos de referencia (Eck et al., 1999). Posee diferentes niveles de calidad. El nivel 1.0 constituye los datos brutos sin control de calidad. El nivel 1.5 da cuenta de los datos filtrados de nubes aplicando la calibración no definitiva, mientras que el nivel 2.0 supone datos de calidad asegurada tras aplicarle un reprocesado con la calibración post-instalación así como la aplicación automática (en versión 3) o manual (en versión 2) de ciertos criterios de calidad. Respecto al PWV, proporciona un producto con una incertidumbre estimada del $10\,\%$ (Giles et al., 2019).
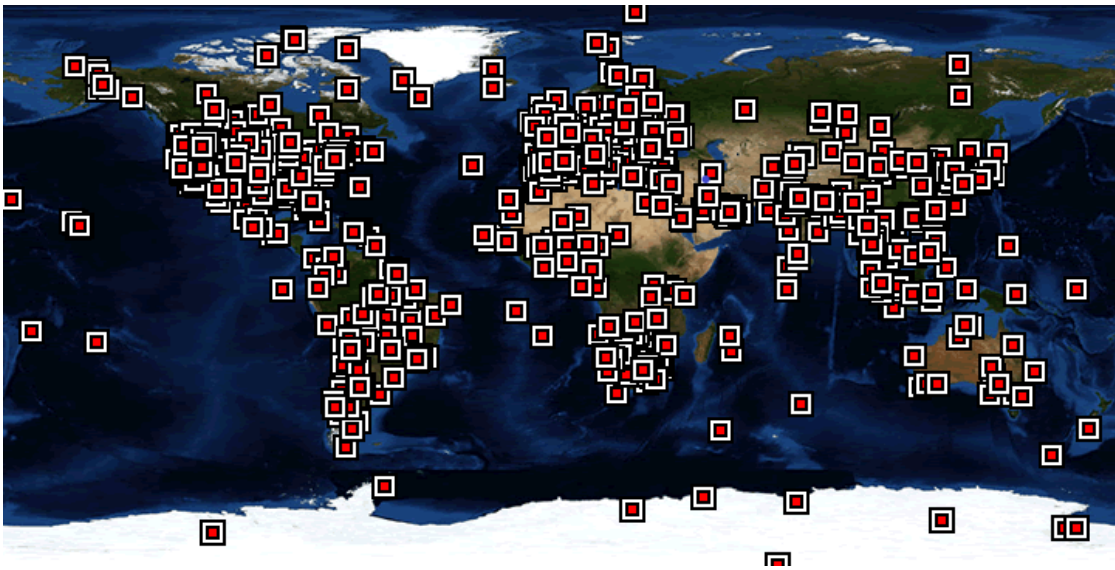

Figura 1.4: Mapa mundial de las estaciones permanentes y temporales de AERONET (extraída de https://aeronet.gsfc.nasa.gov).

En relación con la calibración de ambas redes, GAW-PFR y AERONET, utilizan medidas en estaciones de alta montaña (Mauna Loa e Izaña) con AOD muy estable

y bajo ($< 0{,}03$) en un amplio rango de masas ópticas relativas (aproximadamente entre 2 y 5) y en el menor tiempo posible, para calibrar instrumentos de referencia utilizando la técnica Langley (Ångström, 1970; Shaw et al., 1973; Forgan, 1988, 1994; Schmid and Wehrli, 1995; Schmid et al., 1998; Toledano et al., 2018).

En el caso de AERONET, las calibraciones de los instrumentos de referencia por medio de la citada técnica Langley se transfieren posteriormente a los instrumentos de campo de la red en otras estaciones a través de procedimientos regulares de intercomparación (Holben et al., 1998; Giles et al., 2019).

En el caso de GAW-PFR, el sistema de calibración es más complejo para garantizar la trazabilidad con la referencia mundial del WORCC. El mantenimiento de la referencia mundial por el WORCC se describe en Kazadzis et al. (2018b). Consiste en una tríada de instrumentos que miden continuamente en el PMOD/WRC (Phisikalisch-Meteorologisches Observatorium Davos/World Radiation Center) situado en Davos (Suiza), además de tres radiómetros de transferencia portátiles estándar adicionales ubicados en los observatorios de Mauna Loa (un instrumento) e Izaña (dos instrumentos). Cada 6 meses, uno de los radiómetros portátiles de transferencia estándar visita la tríada de referencia en el PMOD/WRC y compara las constantes de calibración obtenidas mediante las calibraciones Langley realizadas en las dos estaciones de alta montaña durante 6 meses (Tabla 1 de Kazadzis et al., 2018b) con el definido por la tríada. La comparación se basa en las señales (voltajes) y no en valores de AOD. Las diferencias entre los radiómetros de Izaña GAW-PFR y la tríada de referencia siempre han sido inferiores al $0{,}5\,\%$, estando dentro de la incertidumbre del método Langley, incluyendo las pequeñas degradaciones posibles del instrumento que se pueden detectar en un período de 6 a 12 meses. Hay que señalar que los radiómetros de transferencia GAW-PFR se calibran de forma rutinaria utilizando la técnica Langley para el doble control de aseguramiento de la calidad. Por lo tanto, estos radiómetros no pueden considerarse instrumentos de campo simples, sino radiómetros calibrados regularmente con trazabilidad asegurada con la referencia de la tríada del WORCC.

El Observatorio Atmosférico de Izaña es una de las dos estaciones de calibración Langley de ambas redes, lo que representa una ventaja al comparar los dos instrumentos, ya que elimina, en gran medida, los errores causados por la transferencia de calibración. Sin embargo, existen diferencias entre las metodologías de calibración utilizadas por ambas redes. AERONET obtiene la calibración mediante el promedio de unas pocas constantes extraterrestres (voltaje medido por el instrumento en ausencia de atmósfera, V_0) obtenidas de calibraciones Langleys y realizadas en un tiempo relativamente corto (el tiempo necesario para recopilar datos de al menos 10 calibraciones Langley). Sin embargo, en el caso de GAW-PFR, se realiza un ajuste lineal temporal que incluye un mayor número de V_0 obtenidas de calibraciones

Langley realizadas durante 6 meses (Wehrli, 2000; Kazadzis et al., 2018a). Los detalles de los requisitos para realizar calibraciones Langley de instrumentos de referencia por GAW-PFR y AERONET y sus incertidumbres se analizan en detalle en Toledano et al. (2018).

1.4. Cobertura de las técnicas de teledetección de aerosoles sobre regiones desérticas: impacto y características del polvo mineral

La WMO establece la necesidad de realizar medidas de aerosoles atmosféricos con cobertura global (Myhre and Baltensperger, 2012; WMO, 2016), y resalta el hecho de que existan actualmente pocas estaciones de medida en África (cerca de las principales zonas fuente de polvo mineral), Rusia, y gran parte de Asia, que impiden una correcta cobertura global en regiones clave para el estudio de los aerosoles atmosféricos (Wehrli, 2005; Myhre and Baltensperger, 2012). Cómo ya se indicó en la subsección 1.2, este problema de escasez de datos en las regiones fuente se ve amplificado por la alta reflectancia superficial característica de estas zonas, principalmente áridas, que afecta a las medidas de teledetección desde satélite que usan sensores pasivos en el visible (Li et al., 2009). También dificulta enormemente los estudios de asimilación y validación de modelos de aerosoles.

Las regiones áridas del Norte de África pueden ser consideradas como la fuente de polvo atmosférico más importante de la Tierra, emitiendo aproximadamente una cantidad de 800 Tg/año de polvo superficial a la atmósfera (Prospero and Mayol-Bracero, 2013). El polvo mineral es considerado un componente atmosférico clave (Knippertz and Stuut, 2016), que ejerce un importante papel en el clima (IPCC, 2013), la bioquímica (Jickells et al., 2005) y la calidad del aire (Rodríguez et al., 2011). La estimación del efecto climático de este componente atmosférico supone un reto para la comunidad científica debido a sus efectos radiativos directos o indirectos, la falta de conocimiento actual relativa a su forma y características absorbentes, además de la inhomogeneidad espacial de las plumas de polvo durante su transporte a diferentes escalas (Redemann et al., 2006), desde la escala local a la hemisférica. De hecho, se conoce que estos aerosoles tienen un importante efecto en el balance radiativo terrestre y en la microfísica de nubes. Un ejemplo importante de este efecto es su impacto en el Monzón de África Occidental (WAM) (N'Datchoh et al., 2018; Taylor et al., 2019). Por este motivo existen numerosas campañas de medida de aerosoles en estas regiones fuente, destacando entre todas ellas el Proyecto African Monsoon Multidisciplinary Analysis (AMMA) dedicado a mejorar el conocimiento que disponemos del WAM y su variabilidad a escala diaria e interanual (Redelsperger et al., 2006; Lebel et al., 2010, 2011; Galle et al., 2018). A pesar de estos importantes esfuerzos debe reconocerse que se trata de campañas

intensivas limitadas en el tiempo, que no ofrecen la necesaria cobertura temporal para el estudio completo de tales fenómenos.

La composición mineralógica del polvo mineral modula su eficiencia como núcleo de condensación nubosa o núcleo de hielo (Knippertz and Stuut, 2016) (relacionado con su contenido en feldespatos) (Atkinson et al., 2013), en el pH de la precipitación (relacionado con su contenido en calcita) (Loÿe-Pilot et al., 1986) o en la eficiencia de flujos de saltación en los procesos de emisión (relacionada con el contenido en arcillas) (Marticorena and Bergametti, 1995). No es un aerosol soluble, salvo en caso de interacción con ciertos ácidos orgánicos (recubrimiento de sulfatos o nitratos) o por la presencia de componentes orgánicos como los oxalatos (Erel et al., 1993; Pehkonen et al., 1993; Siefert et al., 1994). Este factor es clave para asegurar la biodisponibilidad de diversos nutrientes transportados en su seno.

Como otros aerosoles en la atmósfera, el polvo mineral tiene propiedades ópticas caracterizadas por una importante dependencia espectral, desde el ultravioleta (UV) al infrarrojo (IR). En este sentido, han aparecido diferentes técnicas y estudios en la literatura con el objetivo de caracterizar la depencia espectral del AOD en diferentes rangos espectrales, desde el UV al IR (Sokolik and Toon, 1996; Toledano et al., 2009; López-Solano et al., 2018; Barreto et al., 2020). Sin embargo, mientras que el efecto de la mayor parte de los aerosoles en el infrarrojo medio es considerado muy débil en comparación con el visible (VIS) e UV (Kim et al., 2008), el polvo mineral es capaz de interactuar tanto con la radiación solar como terrestre de muy larga longitud de onda (Clarisse et al., 2013). Se trata de aerosoles compuestos por partículas altamente absorbentes y dispersoras de la radiación solar, capaz de reemitir dicha radiación como radiación térmica. Por este motivo se puede entender la necesidad de conocer de manera precisa sus propiedades ópticas y radiativas, y su comportamiento espectral para la correcta modelización de su efecto radiativo en el clima. También es importante entender que tanto sus propiedades ópticas y radiativas como el comportamiento espectral de las mismas dependen fuertemente de la composición, forma y distribución de tamaño, que a su vez depende del proceso de envejecimiento del aerosol, ya que el modo grueso sufre un proceso de deposición más efectivo durante el transporte (Knippertz and Stuut, 2016). De manera general, podemos decir que se trata de un aerosol compuesto por partículas predominantemente grandes (radio superior a 0,6 μm, Dubovik et al., 2002), no esféricos, y una dependencia espectral del albedo de dispersión simple (SSA) en el rango UV-VIS muy característico, con valores inferiores en el UV, mostrando una mayor absorción en este rango espectral a consecuencia de la presencia de óxidos de hierro. También se caracteriza por valores de la parte real del índice de refracción (n) entre 1,48 y 1,56, así como una parte imaginaria del índice de refracción baja (k menor de 0,003), y una dependencia espectral marcada de este

parámetro para longitudes de onda cortas (Dubovik et al., 2002, y referencias en este artículo). Según Hess et al. (1998), el polvo mineral lleva asociado unos valores de AOD promedio de 0,286 (en 550 nm) y una visibilidad horizontal reducida a 19 km.

Pero no sólo preocupa el efecto radiativo del polvo mineral en el clima. Su impacto sobre la salud humana y las actividades socio-económicas está teniendo una gran relevancia en la actualidad. Se trata de partículas de tamaño respirable, que pueden transportar otros agentes biológicos patógenos o contaminación (Rodríguez et al., 2011), que pueden penetrar en el cuerpo humano principalmente por procesos de inhalación y que pueden ocasionar una serie de peligros para la salud humana que aún no son completamente conocidos (WHO, 2006; Baez-Ferrer et al., 2019; Dominguez-Rodriguez et al., 2020). La reducción de la visibilidad y sus consecuencias en el transporte (Al-Hemoud et al., 2017; ICAO, 2016; Weinzierl et al., 2012), producción de energía (Hussain et al., 2017) y producción primaria (Jickells et al., 2005; Lu et al., 2017) constituyen los principales efectos adversos desde el punto de vista socio-económico. Por este motivo han aparecido en las últimas décadas numerosas iniciativas para mitigar los efectos de tormentas de polvo y arena. En este sentido, el sistema de aviso y evaluación de tormentas de arena y polvo o SDS-WAS (siglas en inglés de "Sand and Dust Warning Advisory and Assessment System") de la WMO se creó en 2007 con la finalidad de mejorar las predicción de tales fenómenos y aumentar la información a la población en materia preventiva para minimizar sus impactos en la salud y socio-económicos (Cuevas, 2013; Terradellas et al., 2014; Nickovic et al., 2015; WMO, 2020). Este programa se nutre de una serie de observaciones multi-plataforma (satélite y medidas en superficie, como las realizadas dentro de las redes GAW y AERONET), muchas de ellas en tiempo cuasi-real, en combinación con modelos numéricos. Sin embargo, adolece de limitaciones en las parametrizaciones de los procesos de emisión y transporte, al tiempo que la escasez de instrumentación cerca de zonas fuentes impide mejorar nuestro conocimiento sobre estos procesos. Al tratarse de procesos esencialmente caóticos, resultan tremendamente sensibles a las condiciones meteorológicas iniciales, por lo que la asimilación de las diferentes observaciones de aerosoles resulta crucial para reducir los errores asociados en los modelos actuales.

La escasez de observaciones en el Norte de África y en Oriente Medio resulta evidente a la vista de la figura 1.5, que muestra la localización de los fotómetros integrantes de la red AERONET, la red de fotometría más amplia que existe. Las estaciones más importantes en cuanto a la disponibilidad de series largas de medidas son las estaciones de Tamanrasset (Argelia), Saada (Yemen), Ouazarzate y Oujda (Marruecos). Debido a su localización cercana a las fuentes de polvo mineral más importantes, así como a la disponibilidad de instrumentación avanzada y la

realización en la zona de diversas campañas de campo (e. g. Flamant et al., 2007; Bou Karam et al., 2008; Cuesta et al., 2008, 2009, 2010), Tamanrasset aparece como un emplazamiento clave en el Norte de África para la observación del polvo mineral atmosférico (Guirado-Fuentes et al., 2014).
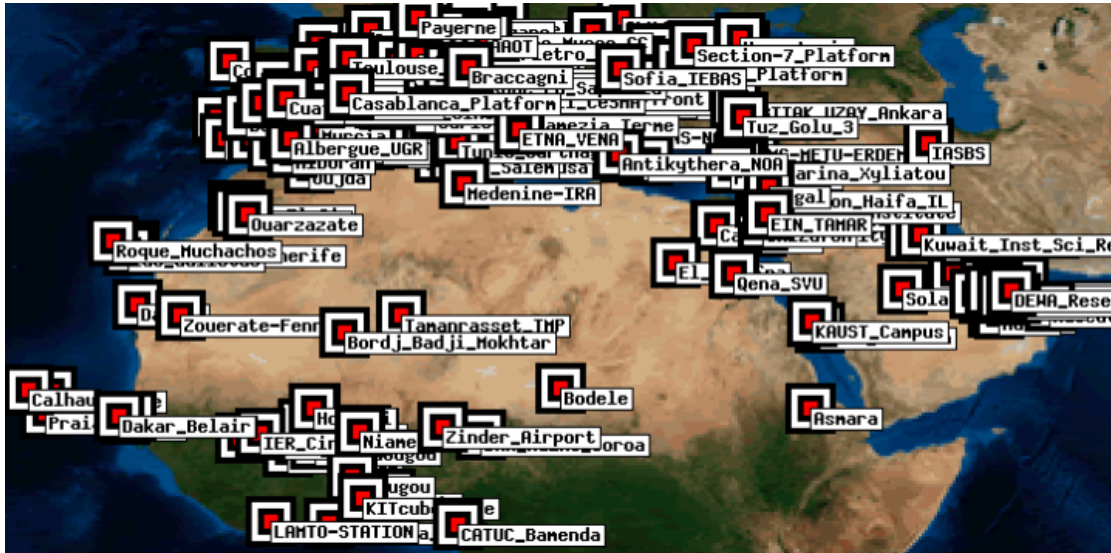

Figura 1.5: Localización de las estaciones de la red AERONET en el Norte de África, sur de Europa y Oriente Medio (extraída de https://aeronet.gsfc.nasa.gov).

2. Motivación

Como ya hemos detallado en el capítulo anterior, los aerosoles y el vapor de agua atmosféricos, así como sus interacciones, juegan un papel crucial dentro del sistema climático (Madonna et al., 2011). Por este motivo resulta esencial proporcionar una mejor representación de la distribución geográfica y la variabilidad temporal de los aerosoles en la atmósfera que permita mejorar la modelización o parametrizaciones que se usan en la actualidad para representar los procesos que gobiernan su ciclo de vida, además de realizar medidas de calidad que puedan ser utilizadas en procesos de asimilación y validación. Son tres los informes de organismos internacionales que abordan esta problemática y proporcionan soluciones "parciales" (Nickovic et al., 2015; WMO, 2016, 2017). Tal y como se recoge en el informe WMO (2017), es necesario establecer un programa de medidas que logre dar cuenta de la importante variabilidad interanual y la heterogeneidad regional de los aerosoles en la atmósfera con el fin de identificar, de la manera más precisa posible, las actuales tendencias en sus concentraciones. Por otro lado, la WMO y su grupo asesor científico sobre aerosoles recomiendan encarecidamente no sólo mantener sino también extender los esfuerzos de observación para cuantificar y detectar la perturbación actual en la atmósfera (WMO, 2016). La predicción de futuros cambios atmosféricos, así como su evolución requiere de información pasada y presente de composición atmosférica con técnicas avanzadas, realizadas a largo plazo, y que deben seguir estrictos criterios de calidad y estandarización. Este organismo destaca la importancia de realizar medidas en estaciones situadas en la troposfera libre, con el fin de garantizar la representatividad de las mismas en relación a la variabilidad a largo plazo en la baja troposfera en amplias zonas. Por último, y en relación al programa SDS-WAS y al ciclo de vida del polvo atmosférico, el informe de la WMO WWRP 2015-5 (Nickovic et al., 2015) hace mención de la escasez de observaciones del polvo atmosférico en las principales regiones fuentes y de cómo el desarrollo de nueva instrumentación robusta, automática y de bajo coste podría ayudar a paliar dicha falta de observaciones. Según este informe, esta nueva instrumentación mejoraría notablemente la asimilación y validación de modelos, incrementando notablemente la eficacia del sistema SDS-WAS.

Cabe destacar que en los últimos años está teniendo lugar una revolución en la aproximación y gestión/uso de las observaciones globales. Como es lógico, la información procedente de un único tipo de plataforma por sí sólo no será suficiente para satisfacer nuestras necesidades observacionales. El futuro y la evolución en nuestra comprensión de los complejos mecanismos de acoplamiento en los que aerosoles y nubes se encuentran involucrados, exigen la integración de las medidas multi-plataforma, y de aproximaciones que incorporen sinergias entre diferentes sensores y técnicas. Por esta razón se ha contemplado como objeto de estudio en esta tesis, la intercomparabilidad de los datos procedentes de las dos redes fotométricas más importantes en la actualidad, además de proponer la necesidad de complementar las redes clásicas actuales con nuevas estaciones equipadas con un nuevo radiómetro robusto que haga posible sus operaciones en zonas remotas.

3. Objetivos

El principal objetivo del presente trabajo es el de introducir herramientas para la mejora de la representación espacio-temporal de los aerosoles y vapor de agua en la atmósfera. Es necesario conocer con la mayor precisión posible las tendencias de los diferentes tipos de aerosoles atmosféricos y del vapor de agua a nivel global/regional en un contexto de cambio climático y un escenario de reducción programada en las tasas de emisiones de aerosoles de origen antropogénico fruto de las políticas para la mejora de la calidad del aire a nivel global. Para la determinación de estas tendencias se utilizan observaciones de aerosoles y vapor de agua, realizadas en diferentes plataformas de tal modo que dispongamos de la máxima cobertura y disponibilidad de información de calidad desde un punto de vista científico. En este trabajo contribuimos a este fin mediante los tres siguientes objetivos específicos:

1. Comprobar la comparabilidad y consistencia entre las redes radiométricas más importantes en la actualidad que proporcionan series largas de AOD de las que se pueden obtener tendencias.

2. Desarrollar una nueva técnica instrumental y las metodologías correspondientes que permitan favorecer la expansión de los sistemas observación terrestre de aerosoles y vapor de agua en la columna atmosférica a zonas remotas desérticas, aumentando así la cobertura espacio-temporal de las actuales redes de medida.

3. Validar los resultados de AOD y PWV obtenidos por medio de esta nueva técnica instrumental utilizando datos de alta calidad con instrumentos de referencia.

Las diferentes tareas desarrolladas en la presente tesis doctoral para la consecución de los objetivos anteriormente descritos son las siguientes:

- Análisis de la trazabilidad de las medidas AERONET a largo plazo con respecto a la referencia mundial GAW-PFR, lo que permitirá evaluar la intercomparabilidad y consistencia de las series largas de datos de AOD y

AE de AERONET a nivel global para estudios climáticos.

- Determinación del posible impacto que supone utilizar en estas redes de instrumentos con diferentes características técnicas, diferentes referencias, y diferentes metodologías de calibración y de cálculo del AOD y AE.

- Determinación de las posibles correcciones necesarias que garanticen la intercomparabilidad y consistencia entre los datos proporcionados por ambas redes.

- Desarrollo de un dispositivo instrumental relativamente simple y robusto, el radiómetro ZEN-R, para la medida de la radiancia de cielo en la dirección cenital o ZSR (por las siglas en inglés de "Zenith Sky Radiance") en diferentes bandas espectrales. Los criterios de robustez y sencillez garantizan su bajo mantenimiento y coste económico, lo cual facilitaría su implementación en redes de observación de países en vías de desarrollo. Las bandas espectrales se seleccionaran en base a la influencia que ejercen los aerosoles y el vapor de agua sobre la radiación solar en las mismas, y su similitud con las de otras redes.

- Evaluación de la ZSR medida por los radiómetros ZEN-R a partir de la comparación con la ZSR medida con los radiómetros Cimel CE318.

- Desarrollo de una metodología que permita estimar el AOD y el PWV a partir de la medida de la ZSR.

- Aplicación y verificación de la metodología anterior a un radiómetro Cimel-AERONET en diferentes localizaciones caracterizadas por la presencia de polvo mineral en su climatología de aerosoles, comparándolo con los productos estándar de AOD de AERONET.

- Validación de los resultados de AOD y PWV obtenidos por el sistema ZEN (dispositivo más metodología) mediante la comparación con los datos proporcionados por la red AERONET en el caso del AOD y del FTIR para el PWV.

4. Zona de estudio y caracterización preliminar de las estaciones utilizadas

Las regiones desérticas del Hemisferio Norte constituyen una de las fuentes más importantes de aerosoles emitidos a la atmósfera (Bakker et al., 2019), siendo además, una de las zonas con más déficit de observaciones de todo el planeta. En este sentido, el polvo mineral es el principal aerosol emitido en estas regiones y sus principales zonas fuente se localizan en el continente africano, especialmente el desierto del Sahara, la península arábiga y el este de Asia. Se estima que el aerosol mineral constituye el 75 % de la carga de aerosol global (Mona et al., 2012; Kinne et al., 2006), y que las regiones áridas del Norte de África contribuyen en aproximadamente un 70 % a las emisiones de polvo globales, valor seis veces superior al de la siguiente fuente de polvo en importancia, Asia (Prospero and Mayol-Bracero, 2013). Una gran cantidad del aerosol africano, una vez inyectado en la atmósfera, viaja transportado por el viento a través del Océano Atlántico, afectando a la costa atlántica del continente americano (Prospero and Carlson, 1972; Prospero, 1996; Prospero and Mayol-Bracero, 2013; Tsamalis et al., 2013). Este transporte a gran escala ocurre durante todo el año, pero posee un marcado ciclo estacional relacionado con la variabilidad en las regiones y procesos de emisión. Según Tsamalis et al. (2013), el transporte transoceánico de polvo mineral desde el Norte de África discurre a mayor altura (1-5 km) y desde fuentes situadas más al norte en verano. Es en esta época del año este transporte a gran escala ocurre en una capa en la troposfera libre, la denominada capa de aire sahariano o SAL (de las siglas en inglés de "Saharan Air Layer"), que discurre confinada entre dos inversiones de temperatura, lo cual explica la longevidad de estas masas de aire y el hecho de que sus características termodinámicas se mantengan relativamente constantes con la altura en su interior (Prospero and Carlson, 1972; Karyampudi et al., 1999; Reid et al., 2003). En invierno las intrusiones discurren a menor altura, entre aproximadamente 0 y 3 km (Prospero and Carlson, 1972; Tsamalis et al., 2013;

Cuevas et al., 2015). Existe también una fracción importante de este polvo mineral emitido a la atmósfera que sigue otro tipo de trayectorias, como el transporte hacia el Mediterráneo y Europa (Basart et al., 2009; Engelstaedter et al., 2006; Cuevas et al., 2017), hacia el este del Mediterráneo y Oriente Medio (Engelstaedter et al., 2006; Israelevich et al., 2003, 2012) e incluso existen evidencias de transporte transcontinental a más largo alcance, alcanzando zonas remotas de Asia (Tanaka et al., 2005; Engelstaedter et al., 2006) o zonas polares (Pacyna and Ottar, 1989; Goudie and Middleton, 2001; Barkan and Alpert, 2010; Ansmann et al., 2003).

En esta Tesis se utilizan los datos de tres estaciones situadas en áreas geográficas y condiciones medioambientales muy diferentes (Figura 4.1). Dos de ellas se encuentran en la Isla de Tenerife, situada en la región subtropical del Atlántico Norte. La estación situada en Santa Cruz de Tenerife se encuentra dentro de la capa de mezcla marina, caracterizada por la persistencia de los vientos Alisios del NE en superficie, mientras que Izaña se encuentra situada en la troposfera libre, caracterizada de manera predominante por un flujo catabático del NO-O. Ambas estaciones, debido a su proximidad al desierto del Sáhara (~ 350 km), se ven afectadas por intrusiones de polvo mineral aunque de forma muy diferente (Alonso-Pérez et al., 2007; Guirado-Fuentes, 2015), que además poseen un marcado ciclo estacional relacionado con la variabilidad en los mecanismos de emisión anteriormente descrita. Estas estaciones se encuentran en una región clave para el estudio del transporte y la deposición del polvo mineral desde las principales zonas fuente en el Norte de África sobre el Océano Atlántico subtropical oriental. La tercera estación, Tamanrasset (Argelia), se encuentra en el corazón del desierto del Sáhara, en una localización clave por su cercanía a las fuentes de polvo mineral más importantes localizadas en Mali, Níger, Argelia, Libia y Chad, con un impacto muy reducido de la actividad industrial (Guirado-Fuentes et al., 2014).

Siguiendo la misma línea de Guirado-Fuentes (2015), en este trabajo hemos analizado los promedios mensuales de AOD, AE y PWV de cada una de las tres estaciones utilizando series de más de diez años de datos (dependiendo de la estación analizada) proporcionados por AERONET nivel 2.0. Además, hemos analizado el AOD discriminando entre el modo fino y grueso gracias al algoritmo de deconvolución espectral de O'Neill et al. (2003) proporcionado también por AERONET. Las tres estaciones se analizan a continuación:

- Estación de Izaña (Tenerife, Islas Canarias, España; $28{,}3°$ N, $16{,}5°$ W; 2373 m s.n.m.): Esta estación perteneciente al Centro de Investigación Atmosférica de Izaña (CIAI) de la Agencia Estatal de Meteorología (AEMET), es una estación subtropical de alta montaña que representa de manera predominante condiciones atmosféricas de fondo de la baja troposfera subtropical como consecuencia de su ubicación sobre una fuerte y cuasi-permanente capa de

Figura 4.1: Imagen de Meteosat/TERRA mostrando una intrusión de polvo sahariano sobre la zona de estudio el 12 de enero de 2015. Las estaciones de Izaña, Santa Cruz y Tamanrasset se indican con estrellas amarillas (Figura extraída de Almansa et al. (2017)).

inversión térmica resultado de procesos de subsidencia general en la troposfera (rama descendente de la célula de Hadley) y la presencia de vientos alisios en niveles más bajos (Carrillo et al., 2016; Cuevas et al., 2019). Sin embargo, la proximidad al desierto del Sahara introduce una importante influencia del polvo mineral en su climatología de aerosoles (Rodríguez et al., 2011; Rodríguez et al., 2015; Basart et al., 2009; Guirado-Fuentes, 2015).

Tras analizar más de 15 años de datos (de 2004 a 2019), en este estudio se ha obtenido la siguiente climatología de AOD y PWV, con resultados similares a los obtenidos por Basart et al. (2009); Guirado-Fuentes (2015) (ver figuras 4.2a, 4.2d y 4.2g). El periodo de noviembre a febrero, con un AOD_{500} mensual promedio en torno 0,02 y un AE entorno 1,0, aparece como el periodo con condiciones más limpias. En los meses de verano la concentración de aerosoles aumenta obteniéndose un AOD_{500} promedio máximo de 0,14 en julio, dominado por el modo grueso con un AE promedio de 0,51, debido a la presencia de polvo mineral. Además, se observa un máximo secundario en el AOD_{500} en el mes de marzo, que se debe al transporte polvo mineral en la capa de mezcla marina que puede alcanzar los 3 km de altura (Cuevas et al., 2015; Guirado-Fuentes, 2015). Se trata de episodios cortos, esporádicos e intensos (Querol et al., 2004) causados tormentas de polvo desencadenadas por la actividad frontogenética desarrollada a consecuencia del fuerte gradiente térmico meridional de esta época del año capaz de activar masivamente

una o diversas zonas fuente (Escudero et al., 2005; Schepanski et al., 2009; Knippertz and Stuut, 2016). En cuanto al PWV, esta estación se caracteriza por condiciones secas, con un PWV promedio anual de 0,38 *cm*, como consecuencia de su altitud, con las condiciones más secas durante el invierno, con un PWV mínimo en febrero (0,21 *cm*), mientras que los meses más húmedos son los de verano (máximo en agosto de 0,62 *cm*), coincidiendo con una mayor frecuencia de intrusiones de polvo.

- Santa Cruz de Tenerife (Tenerife, Islas Canarias, España; 28,5° N, 16,2°; 52 m s.n.m.): Esta es una estación urbana del CIAI (AEMET) que se encuentra ubicada a nivel del mar, en la capa de mezcla marina. La climatología de aerosoles en esta estación está dominada por la combinación bien mezclada de fracción fina de aerosoles contaminantes (de industrias, barcos y vehículos) (Rodríguez et al., 2008; González et al., 2011; González and Rodríguez, 2013; Baldasano and Massagué, 2017) y partículas marinas de modo grueso (predominando $AOD_{675} > 0,15$) con influencia de polvo mineral de primavera a otoño (Basart et al., 2009), con valores de AOD_{675} altos y AE bajos.

En las figuras 4.2b, 4.2e y 4.2h se muestran los resultados de la caracterización del AOD_{500}, el AE y el PWV, con datos de AERONET nivel 2.0 de 2005 a 2018. La principal característica de los aerosoles de esta estación es el predominio del modo grueso sobre el fino como consecuencia de la presencia del aerosol marino (siempre presente) y del aerosol de polvo mineral (presente esporádicamente). En los meses de noviembre a febrero se tiene los valores de AOD más bajos, con el promedio mensual mínimo en febrero (AOD_{500} de 0,11 y AE de 0,57). Sin embargo, la alta desviación estándar en los datos de AOD de diciembre a febrero (de hasta 0,07) refleja la existencia de intrusiones de polvo localizadas a niveles bajos (por debajo de 3 km) que afectan esporádicamente a la estación durante el invierno, de acuerdo con el patrón de transporte de masas de aire propio de esta estación. En los meses de verano la concentración de aerosoles aumenta obteniéndose un AOD_{500} promedio máximo de 0,26 en agosto y un AE de 0,46. Además, al igual que ocurre en Izaña, también se observa un máximo secundario en el mes de marzo en el AOD_{500} más acusado en este caso, con un AOD_{500} promedio de 0,18 y un AE de 0,53. El valor mínimo en el PWV de 1,44 *cm* tiene lugar en febrero y el máximo de 2,45 *cm* en septiembre.

- Tamanrasset (Argelia; 22,8° N, 5,5° E; 1377 m s.n.m.): Esta estación es clave para el estudio del polvo mineral ya que se encuentra en pleno desierto del Sahara (figura 4.1) al sur de Argelia, cerca de las fuentes de polvo más importantes de Mali, Níger, Argelia, Libia y Chad, donde hay poco impacto de actividades antropogénicas. Por este motivo la climatología de aerosoles
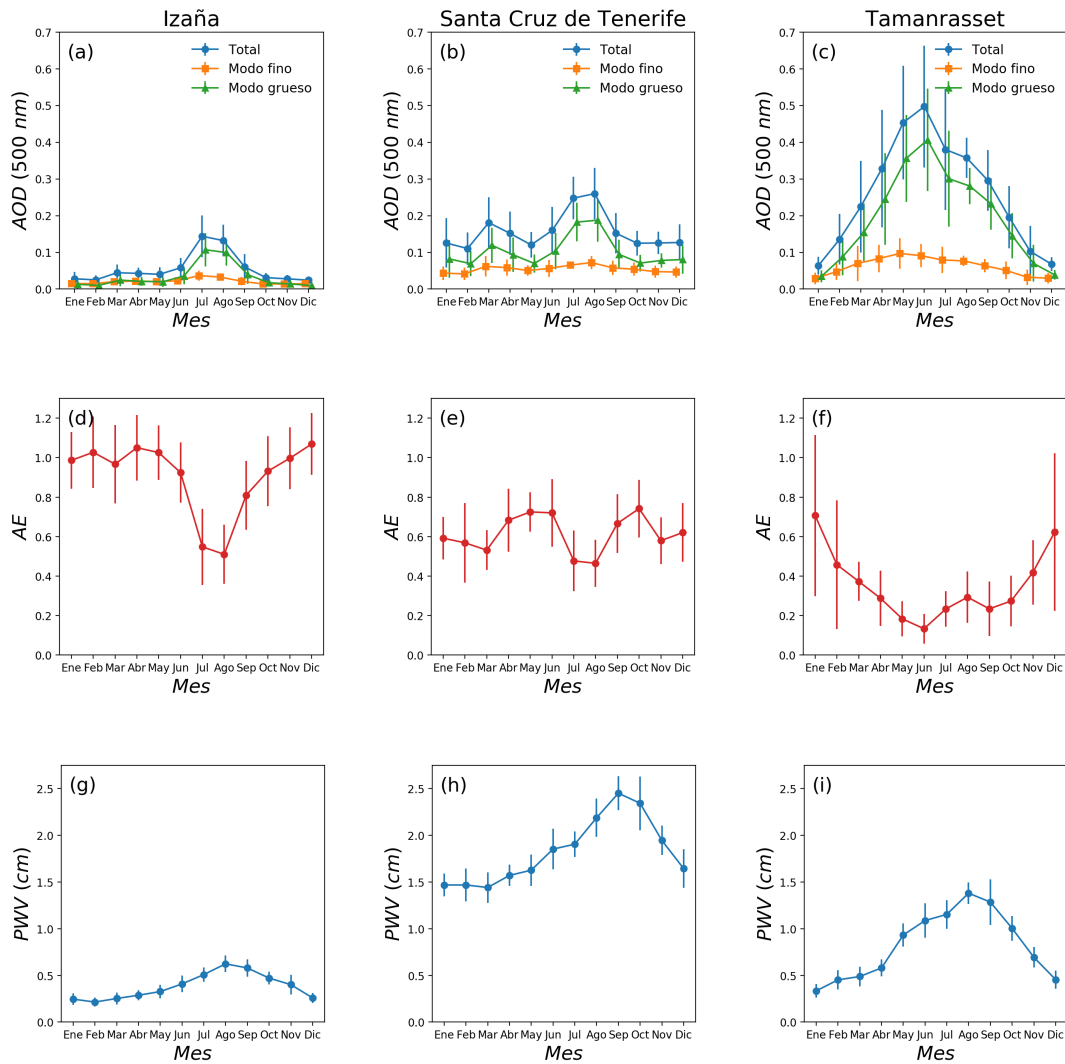
Figura 4.2: Promedios mensuales de AOD_{500}, total (círculos azules), modo fino (cuadrados naranjas) y modo grueso (triángulos verdes) y las correspondientes desviaciones estándar (barras de error) en las estación de Izaña, Santa Cruz de Tenerife y Tamanrasset (figuras a, b y c) obtenidos de la base de datos de AERONET. En las figuras d, e y f, se representan el promedio mensual y la desviación estándar del AE para cada estación, y en las figuras g, h e i, se muestra lo mismo para el PWV. Todos los resultados han sido calculados a partir de series de datos de más de 10 años proporcionados por AERONET nivel 2.0.

de esta estación está caracterizada principalmente por la presencia de polvo mineral (Guirado-Fuentes et al., 2011, 2014). Su clima está influenciado por

el monzón durante el verano y los vientos del oeste durante el resto del año (Cuesta et al., 2008). Guirado-Fuentes et al. (2014) realizaron un estudio exhaustivo para caracterizar los aerosoles en esta estación sahariana. En este estudio mostraron que el polvo mineral del desierto es el tipo de aerosol predominante en esta estación, donde la estación seca-fría (invierno) se caracteriza por condiciones predominantes de cielo limpio ($AOD_{440} \approx 0,09$ y $AE \approx 0,62$) y bajo PWV ($\approx 0,51\ cm$), mientras que en la temporada de húmeda-cálida (verano) son frecuentes los eventos de alta turbiedad con partículas de polvo gruesas asociadas a un valor AOD_{440} promedio de 0,39, un $AE \approx 0,28$ y un $PWV \approx 1,06\ cm$.

Por otro lado, del análisis realizado en la presente tesis de los promedios mensuales de más de 10 años (de 2006 a 2018) de datos proporcionados por AERONET nivel 2.0 (figuras 4.2c, 4.2f y 4.2i) observamos resultados similares a los mostrados por Guirado-Fuentes et al. (2014), con condiciones de mayor turbiedad en la estación húmeda-cálida, con un AOD_{500} promedio máximo de 0,50, con un dominio claro del modo grueso, un AE promedio de 0,13 en el mes de junio y un PWV promedio máximo en el mes de agosto de 1,38 cm. En la estación seca-fría, en cambio, se observan condiciones más limpias, con un AOD_{500} promedio de 0,06 y un AE promedio de 0,71, y secas, PWV promedio de 0,33 cm, para el mes de enero.

5. Instrumentación utilizada

5.1. Los fotómetros Cimel CE318 y PFR

En primer lugar deseamos aclarar el uso indistinto de los apelativos fotómetro y radiómetro para estos instrumentos, que aunque no signifiquen exactamente lo mismo, hemos mantenido por razones históricas, siendo más correcta en este caso la designación de radiómetro. En este estudio hemos utilizado dos fotómetros como instrumentos de referencia en la medida de AOD: el Cimel CE318 (Holben et al., 1998), que en sus diferentes versiones es el instrumento estándar de la red AERONET, y el PFR (Wehrli, 2005), el instrumento estándar de la red GAW-PFR. Las características principales de estos dos fotómetros se describen a continuación.

- El Cimel CE318 (Holben et al., 1994, 1998), manufacturado por la compañía Cimel Electronique, consta principalmente de una cabeza sensora montada en un seguidor de dos ejes (un eje acimutal y otro cenital), con una unidad de control (véase la figura 5.1). Este radiómetro realiza básicamente dos tipos de medidas: la radiación solar directa y la radiancia de cielo, con diferentes secuencias de medida. En la versión más reciente, la CE318-T (Barreto et al., 2016), el dispositivo también es capaz de realizar medidas de la radiación lunar directa. La cabeza sensora está equipada con uno o dos tipos de detectores, un fotodiodo de silicio, sensible desde el rango espectral ultravioleta hasta el infrarrojo cercano (de 300 a 1100 nm), que está presente en todas las versiones, y un detector InGaAs (Arseniuro de Indio y Galio) sensible entre 800 y 1900 nm, que está presente sólo en las versiones extendidas y T del Cimel CE318. La radiación medida por los detectores es previamente filtrada por un conjunto de filtros ópticos pasabanda montados en una rueda dentada accionada por un motor paso a paso. En total hay ocho filtros pasabanda con longitudes de onda nominales centradas en 340, 380, 440, 500, 675, 870, 940 y 1020 nm, con una anchura a media altura (FWHM) de 2 nm para 340 nm, 4 nm para 380 nm, y 10 nm para el resto de los canales. En las versiones extendidas y T, existe un filtro adicional con una longitud de onda

nominal centrada en 1640 nm, y con 25 nm de FWHM. El sistema óptico de la cabeza sensora queda completado con un conjunto de lentes colimadoras y diafragmas que hacen que el campo de visión (FOV de las siglas en ingles de "Field of View") del instrumento sea de aproximadamente 1,3° (Torres et al., 2013). Además, la cabeza sensora lleva acoplado un colimador desmontable específicamente diseñado para minimizar la luz parásita en las medidas de aureola solar (región circular con un radio de 6° alrededor de la posición del sol), capaz de reducirla hasta en un factor de 10^{-5} a una distancia angular 3° (Holben et al., 1998).

Figura 5.1: Radiómetro Cimel CE318-T.

El seguimiento solar se realiza usando efemérides basadas en el tiempo, la latitud y la longitud y se mejora utilizando un sensor de cuatro cuadrantes presente en la cabeza sensora, que guía al seguidor al punto donde la intensidad de la señal medida por la cabeza sensora es máxima. Según Torres et al. (2013), el error en el apuntamiento del Cimel CE318 es menor de 0,1°. En los intervalos de tiempo en que el radiómetro no está midiendo, el seguidor se coloca en posición de reposo mirando hacia abajo para limitar el posible deterioro de los filtros ópticos por los efectos de la radiación solar. El sistema, además, cuenta con un sensor de lluvia que hace que se mantenga en posición de reposo en el caso que esta tenga lugar.

Las medidas de la radiación solar directa para todos los filtros presentes se realizan en tripletes, es decir, en secuencias de tres medidas tomadas cada 30 segundos, con una duración total de un minuto por cada triplete. Los tripletes se efectúan cada 15 minutos entre las 9 y las 15, hora local, y con una frecuencia variable dependiendo de la masa de aire fuera de esas horas. Estas medidas se utilizan para obtener el AOD y PWV, con incertidumbres típicas de AOD de entre 0,002 y 0,009 para instrumentos de referencia, mayor para longitudes de onda más cortas, y entre 0,010 y 0,020 para instrumentos de campo, y mayor en la radiación UV en condiciones de cielos despejados (Eck et al., 1999; Barreto et al., 2016). El producto de PWV de AERONET tiene una precisión de aproximadamente de entre el $5-10\,\%$ (Torres et al., 2010; Ortiz de Galisteo Marín, 2011; Giles et al., 2019).

Históricamente, las medidas de radiancia de cielo se han realizado mediante dos secuencias distintas: la secuencia de almucantar y la secuencia de plano principal. En la secuencia de almucantar (figura 5.2a), el ángulo acimutal con el que apunta el fotómetro al cielo varía mientras el ángulo cenital se mantiene constante. Esta secuencia se ejecuta en dos alas: el almucantar derecho (ángulo azimutal desplazado hacia la derecha de la posición del sol) y el almucantar izquierdo (ángulo de acimut desplazado hacia la izquierda de la posición del sol). Por otro lado, en la secuencia de plano principal (figura 5.2b), el ángulo cenital del dispositivo varía mientras el ángulo acimutal se mantiene constante. Analizando la figura 5.2a, vemos como la secuencia de almucantar es perfectamente simétrica, y esta simetría se utiliza para realizar un filtrado que elimina datos afectados por nubes, lo cual no se puede hacer fácilmente con la secuencia del plano principal. Por otra parte, el plano principal permite medir siempre a ángulos de dispersión más grandes que con el almucantar para un mismo ángulo cenital solar. Este hecho es determinante en las horas centrales del día, donde el rango de dispersión medido por el almucantar es muy limitado (Torres et al., 2014) y el del plano principal siempre excede 90°. Conscientes de las ventajas y limitaciones de ambas medidas, se ha añadido recientemente en las versiones CE318-T la secuencia híbrida (figura 5.2c), donde se realiza una nueva medida mezcla entre un almucantar y plano principal. Esta nueva medida descrita por Sinyuk et al. (2020), permite por un lado alcanzar ángulos de dispersión altos (similares a los que se obtienen con el plano principal) y a la vez conservar la simetría del almucantar.

Con la información aportada por estas medidas de radiancia espectral junto con el AOD, AERONET utiliza el código desarrollado por Dubovik and King (2000), con algunas mejoras introducidas en Dubovik et al. (2002, 2006), para proporcionar información sobre los parámetros microfísicos y ópticos de los

aerosoles. En concreto, el código ofrece como salidas primarias una detallada distribución de tamaños, los índices de refracción espectral y el parámetro de esfericidad (Dubovik et al., 2006). A partir de estas salidas primarias se derivan otras propiedades del aerosol como el SSA o las funciones de fase.
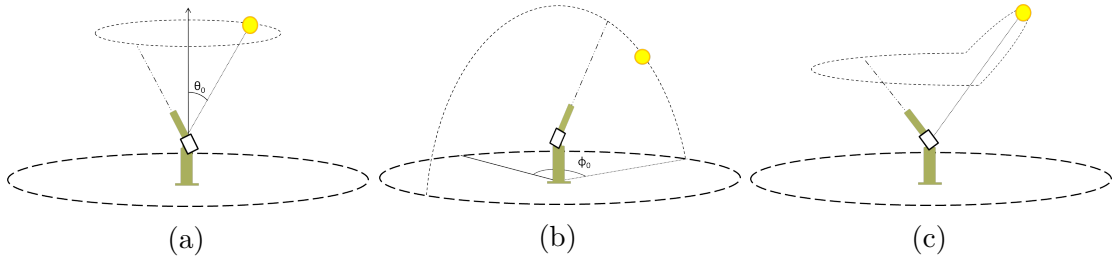

Figura 5.2: Descripción grafica de las secuencias de medida de plano principal (a), de almucantar (b) y de híbrido (c) ejecutadas por el radiómetro Cimel CE318.

- El PFR (Wehrli, 2000, 2005, 2008a,b) es un instrumento manufacturado por PMOD/WRC que consta de un cabeza sensora y una unidad de control. Al contrario que el Cimel CE318, esté no cuenta con un seguidor propio, por lo que se suelen montar en seguidores comerciales que siempre apuntan al sol (figura 5.3). La cabeza sensora tiene cuatro canales independientes con cuatro filtros ópticos pasabanda centrados en 368, 412, 500 y 862 nm, con un FWHM de 5 nm y cuatro fotodiodos de silicio inclinados 3° respecto al eje óptico para evitar reflexiones entre los filtros y los detectores. La geometría de visión está determinada por dos diafragmas de 3 y 7 mm de diámetro, separadas por 160 mm, que dan lugar a un FOV de 2,5°. El sistema está sellado herméticamente con una atmósfera interna ligeramente presurizada (2000 hPa) con nitrógeno seco y estabilizada en temperatura con un sistema de termostatización tipo Peltier que mantiene la temperatura de la cabeza sensora a 20,0° $\pm$ 0,5° C para un rango de temperatura ambiente de entre $-20,0°$ y 35,0° C . Este sistema hace innecesarias las posibles correcciones por temperatura a la señal de los sensores y también previene el envejecimiento acelerado de los filtros, asegurando la alta estabilidad del PFR. Los detectores sólo están expuestos por cortos períodos de tiempo, ya que un obturador automático se abre cada minuto durante 10 s para realizar medidas de radiación solar directa, minimizando la degradación relacionada con la exposición de los filtros. La incertidumbre esperada en el AOD depende de la incertidumbre en la calibración y de la masa de aire (Kazadzis et al., 2018b). El estudio realizado por Wehrli (2000) estimó la incertidumbre en la constante de calibración del PFR entre un 0,2 % (500 nm) y un 1 % (368 nm), lo que conduce a una incertidumbre en el AOD de entre 0,002 y 0,01 para una masa óptica relativa igual a 1.

Figura 5.3: Radiómetros PFR montados en un seguidor solar Owel en el Observatorio Atmosférico de Izaña.

5.2. Espectrómetro FTIR

En este estudio hemos utilizado el FTIR como instrumento de referencia para la medida de PWV.

El dispositivo FTIR tiene dos componentes principales: una óptica de entrada montada en un seguidor solar y un espectrómetro de alta resolución, cuyo elemento central es un interferómetro de Michelson. El FOV del instrumento es de sólo 0,07° (considerablemente más pequeño que el diámetro solar de 0,5°). Al tomar los espectros solares, el FOV del FTIR se centra automáticamente en el disco solar por medio del sistema Camtracker (Gisi et al., 2011).

En este trabajo, solo se utilizaron los espectros solares adquiridos con la configuración estándar de TCCON (Total Carbon Column Observing Network) (Wunch et al., 2011; Schneider et al., 2010b). Estas medidas se realizan entre 4000 y 9000 cm^{-1} (correspondientes a longitudes de onda entre 1111 y 2500 nm) a una resolución espectral de 0,02 cm^{-1}. Para aumentar la relación señal-ruido de las medidas, un espectro resulta del promedio de 3 barridos individuales, por lo que la frecuencia

de muestreo es de aproximadamente 2 minutos.

Las medidas con el FTIR comenzaron en el Observatorio Atmosférico de Izaña en 1999 como resultado de una colaboración entre el CIAI (AEMET) y el IMK-ASF (Institut für Meteorologie und Klimaforschung - Atmosphärische Spurengase und Fernerkundung), perteneciente al KIT (Karlsruher Institut für Technologie). Desde entonces, dos espectrómetros FTIR han operado en el observatorio (un IFS 120M entre 1999 y 2005, y un IFS 120 / 5HR a partir de 2005) en el marco de la red internacional de redes de composición atmosférica para la detección de cambios en la composición atmosférica (NDACC, (De Mazière et al., 2018)) desde 1999, y TCCON (Wunch et al., 2011) desde 2007.
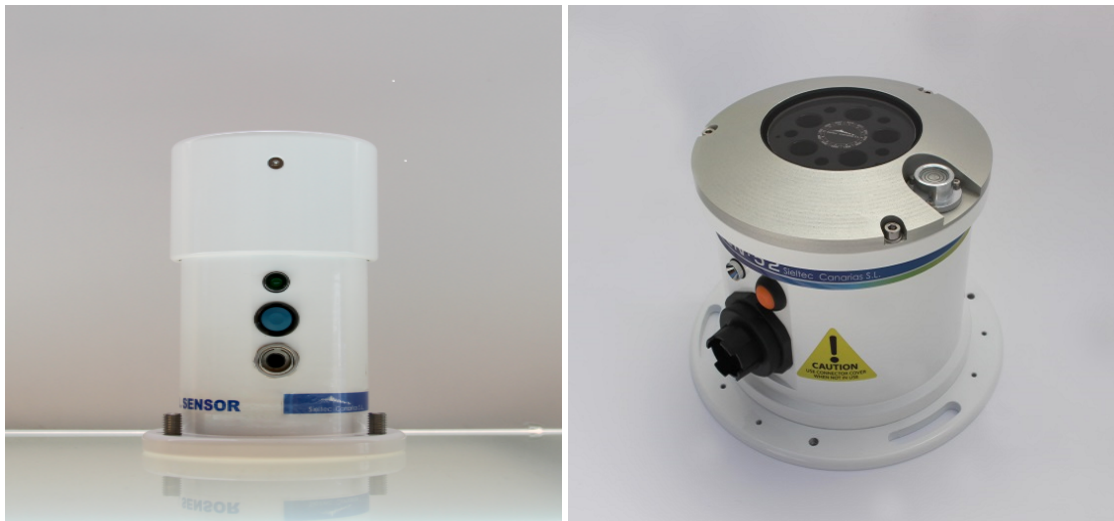
5.3. Radiómetros ZEN-R

En esta sección se presenta las características más importantes de las dos versiones del radiómetro ZEN-R. El análisis de dicho instrumento junto con la metodología ZEN asociada (que permite caracterizar el vapor de agua y el AOD a partir de los datos de radiancia cenital) son el objetivo principal del presente estudio. El ZEN-R41 (Figura 5.4a) es un radiómetro desarrollado conjuntamente por Sieltec Canarias S.L. y el CIAI, concebido para observar el AOD a partir de medidas de la ZSR y en diferentes bandas espectrales. Este dispositivo consta básicamente de cuatro canales ópticos con un FOV de 3°, equipados con cuatro fotodiodos de silicio (350–1100 nm), y cuatro filtros ópticos de 10 nm FWHM con longitudes de onda nominales centradas en 440, 500, 675 y 870 nm. Las medidas de ZSR se realizan simultáneamente en todos los canales, con una frecuencia de 1 minuto (promedio de 30 muestras). Además no necesita seguidor solar y carece de otras partes móviles, por lo que su diseño es muy compacto y robusto.

La electrónica interna comprende un registrador de datos de 16 bits y una memoria de 4 MB con comunicaciones Ethernet para la adquisición, visualización, descarga, configuración y diagnóstico del instrumento. El dispositivo es capaz de procesar los datos internamente gracias a un microcontrolador, con 16 MIPS (Microprocessor without Interlocked Pipeline Stages) de velocidad de CPU (Central Processing Unit) y 96 KB de memoria RAM (Random Access Memory). La alimentación y las comunicaciones se realizan a la vez a través de un puerto PoE (Power over Ethernet).

El ZEN-R52 (Figura 5.4b) es una versión más moderna cuyo hardware y software se han mejorado y optimizado significativamente. En cuanto a las principales diferencias del hardware, son notables tanto la inclusión de un nuevo canal centrado en 940 nm para la estimación del PWV así como un ordenador interno más potente.

Estas mejoras requieren de una carcasa más grande con aletas de enfriamiento. Gracias a unas lentes con mejor recubrimiento y un tratamiento especial para las paredes internas, la luz parásita ha sido reducida. En este caso el FOV es de 2°.

Con respecto a las mejoras de software, vale la pena destacar la nueva interfaz gráfica, que permite una visualización interactiva de los datos, búsquedas en su base de datos interna, configuración del envío de datos a través de FTP (File Transfer Protocol) o HTTP (Hypertext Transfer Protocol), sincronización del tiempo a través de servidores NTP (Network Time Protocol) y configuración del tiempo manual interno. Además el usuario tiene la opción de cambiar los archivos de las tablas de consulta o LUT precalculadas o cambiar los parámetros de calibración radiométrica. También es posible acceder a la configuración del disco y a las actualizaciones remotas de software.

(a)   (b)

Figura 5.4: Radiómetros ZEN-R41 (a) y ZEN-R52 (b).

6. Metodologías aplicadas en el sistema ZEN

6.1. Modelo de transferencia radiativa libRadtran

Para generar las tablas de consulta de las radiancias necesarias como entradas de los métodos ZEN-AOD-LUT y ZEN-PWV-LUT (secciones 6.3 y 6.4) se utilizó el paquete de software de transferencia radiativa libRadtran (Mayer and Kylling, 2005; Emde et al., 2016). Este paquete de software consta de un conjunto de herramientas para el cálculo de transferencia radiativa en la atmósfera terrestre. La principal es el programa uvspec (Mayer et al., 1997), desarrollado originalmente para calcular la irradiancia espectral UV. Con el tiempo, la herramienta se ha desarrollado incrementando el número de aplicaciones disponibles, permitiendo actualmente calcular radiancias, irradiancias y flujos actínicos en el rango visible e infrarrojo del espectro. LibRadtran está disponible gratuitamente bajo Licencia Pública General en la dirección www.libradtran.org (último acceso: 21/11/2020).

LibRadtran es un software de transferencia radiativa flexible y fácil de usar gracias a que sus archivos de entrada permiten definir múltiples parámetros de forma sencilla. LibRadtran estructura la atmósfera en múltiples capas, considerando los perfiles verticales de temperatura, presión y componentes atmosféricos, como gases y aerosoles. Además ofrece la posibilidad de insertar perfiles definidos por el usuario, por ejemplo, a partir de radiosondeos, y dispone de opciones para escalar los perfiles para que coincidan con una cantidad integrada en la columna, como la columna de vapor de agua o la columna de ozono. También incluye varias bibliotecas que ayudan a describir la atmósfera y la contribución de la superficie en el campo de radiación simulado. Por otro lado, el usuario tiene la posibilidad de elegir diferentes métodos para resolver la ecuación de transferencia radiativa y diferentes parametrizaciones para definir la absorción de los gases atmosféricos.

6.2. Calibración en radiancia de los radiómetros ZEN-R

La señal de salida del instrumento viene dada en cuentas digitales (DN por las siglas en inglés de "digital numbers") y está relacionada con el voltaje de salida del detector a través de la ganancia electrónica del instrumento. Debido a que los algoritmos de obtención del AOD y el PWV se basan en la comparación de la radiancia simulada con los valores medidos, la señal del instrumento debe transformarse a unidades de radiancia ($Wm^{-2}sr^{-1}nm^{-1}$) mediante una calibración frente a una fuente de radiación cuya radiancia espectral sea conocida. En este estudio se utilizó una esfera integrante calibrada espectralmente en radiancia, modelo Labsphere's HELIOS 4-lamps de $20''$, como fuente de calibración. La radiancia de la esfera ponderada con el ancho de banda de un determinado canal del instrumento L_{w,λ_n} con longitud de onda nominal, λ_n, vendría dada por:

$$L_{w,\lambda_n} = \frac{\int_{\lambda_1}^{\lambda_2} T(\lambda) L_s(\lambda)\, d\lambda}{\int_{\lambda_1}^{\lambda_2} T(\lambda)\, d\lambda} \tag{6.1}$$

donde $T(\lambda)$ es la función de la transmisividad del filtro óptico y $L_s(\lambda)$ es la radiancia espectral de la esfera. Suponiendo que existe una relación lineal entre la señal de salida del instrumento y la radiancia, tenemos que (Li et al., 2008; Tao et al., 2014)

$$V_{\lambda_n} = c_{\lambda_n} L_{w,\lambda_n}, \tag{6.2}$$

donde V_{λ_n} es la señal de salida del instrumento corregida de corriente de oscuridad, y c_{λ_n} es el coeficiente de calibración que depende de la respuesta espectral del sensor, de la ganancia electrónica y de la transmisividad de la óptica de entrada, entre otros factores.

Por lo general, es suficiente suponer el coeficiente de calibración como una constante, pero existen ciertos factores que hacen que esto no sea del todo cierto. Un ejemplo de ello es la temperatura, que tiene un impacto apreciable en los detectores de silicio. En nuestro caso dicha influencia ha sido caracterizada para cada una de las bandas espectrales siguiendo el procedimiento descrito por Giles et al. (2019) y González et al. (2020).

La incertidumbre involucrada en este procedimiento de calibración ha sido estimada en un 5 % por Walker et al. (1991), por lo que hemos asumido esta estimación como el valor límite inferior para la incertidumbre de la ZSR mediada por los instrumentos ZEN-R.

6.3. Método ZEN-AOD-LUT

Para estimar el AOD a partir de medidas de ZSR en condiciones libres de nubes, utilizamos el método ZEN-AOD-LUT. En el artículo 2 este método se denomina como ZEN-LUT, puesto que en ese momento sólo se calculaba el AOD. Desde que se empezó a calcular el PWV en el artículo 3 este se renombró como ZEN-AOD-LUT. Este método tipo LUT se basa en la comparación de las ZSR medidas, corregidos de la distancia tierra-sol, con una LUT de ZSR simuladas en cada una de las bandas espectrales de los radiómetros ZEN-R con una baja absorción por gases atmosféricos (440, 500, 675 y 870 nm). Las LUT se determinaron utilizando el software de transferencia radiativa libRadtran, descrito en la subsección 6.1. La descripción completa del método se explica paso a paso a continuación:

1. En primer lugar, se definen los parámetros de entrada al modelo de transferencia radiativa. Estos se distinguen entre los parámetros fijos, comunes a todas las simulaciones para un mismo lugar, y los parámetros variables. A continuación citamos los parámetros fijos más relevantes:

   - Irradiancia solar extraterrestre. Se seleccionó el espectro proporcionado por Kurucz (1992) con una resolución espectral de 1 nm.

   - Perfil vertical de la atmósfera. Se utilizó el modelo estándar "midlatitude summer" (Anderson et al., 1986) para definir el perfil vertical de temperatura, presión y las concentraciones de gases.

   - Absorción molecular. En el artículo 2 se utilizó la parametrización LOWTRAN (Pierluissi and Peng, 1985), y en el tercero se utilizó la parametrización REPTRAN (Gasteiger et al., 2014). Esta última parametrización es más precisa que LOWTRAN pero no estaba disponible en libradtran en el momento de la publicación del artículo 2.

   - Definición de las bandas espectrales de los instrumentos. Se utilizó una función filtro común para las bandas espectrales centradas en 440, 500, 675 y 870 nm con un FWHM de 10 nm cada una.

   - Reflectancia superficial. Hemos considerado las definiciones de albedo dadas en la biblioteca IGBP (International Geosphere-Biosphere Programme), que se origina en el Proyecto de Propiedades de Superficie de la NASA CERES / SARB (Clouds and the Earth's Radiant Energy System / Surface and Atmosphere Radiation Budget) (Loveland and Belward, 1997).

   - Método de resolución de la ecuación de transferencia radiativa. Se utilizó el código CDISORT (Buras et al., 2011), que es una versión en código C

del programa DISORT (Discrete Ordinate Radiative Transfer) desarrollado por Stamnes et al. (1988), que se basa en el método de ordenadas discretas introducido por Chandrasekhar (1960).

En cuanto a los parámetros variables tenemos la posición solar y los aerosoles. A continuación se detalla cada uno de ellos:

- Posición solar. Sólo se proporciona el ángulo cenital solar o SZA (de las siglas en inglés de "Solar Zenith Angle"), ya que la ZSR para un cielo sin nubes es invariable con el ángulo acimutal solar. La corrección de la distancia tierra-sol se aplica directamente en la ZSR medida, por lo que las ZSR simuladas sólo se calculan para la distancia media tierra-sol.

- Aerosoles. Para establecer la contribución de los aerosoles, se define un conjunto de perfiles verticales, caracterizados por una determinada concentración de aerosoles. Cada concentración es, en realidad, una mezcla de concentraciones de componentes de aerosoles de la librería OPAC (Optical Properties of Aerosols and Clouds) (Hess et al., 1998) incluida en libradtran. Los aerosoles en OPAC se pueden definir mediante 10 componentes básicos. Estos componentes son: insolubles en agua (INSO), solubles en agua (WASO), hollín (SOOT), dos componentes de sal marina (modo de acumulación o SSAM y modo grueso o SSCM), cuatro componentes de polvo mineral (modo nucleación, MINM, modo de acumulación, MIAM, modo grueso, MICM y mineral transportado, MITR) y el componente sulfato (SUSO). Además, libRadtran incluye cuatro componentes esferoides (esferoides MINM, MIAM, MITR y MICM) para definir los aerosoles de polvo mineral. Los efectos de la humedad relativa se tienen en cuenta para aquellos componentes que se vean afectados. Cada componente se define por sus propiedades microfísicas, es decir, el índice de refracción, tomado principalmente de D'Almeida et al. (1991) y una distribución de tamaño log-normal (Deepak and Gerber, 1983). Luego, a través del cálculo de dispersión de Mie (Mie, 1908; Wiscombe, 1980; Bohren and Huffman, 2008), o el método T-Matrix (Mishchenko and Travis, 1998), en el caso de los esferoides, las propiedades ópticas se calculan para cada componente y se normalizan a 1 partícula cm^{-3}.

  La altura de todas las capas y la mezcla de componentes de aerosol presentes en cada capa, excepto la capa límite, se establecieron siguiendo las indicaciones dadas en Hess et al. (1998). En el caso de la capa límite, decidimos establecer una combinación de componentes variable según las indicaciones dadas en el informe GADS (Global Aerosol Data Set) (Koepke et al., 1997) para las regiones desérticas. En este informe se

propone una mezcla de cuatro componentes diferentes, tres componentes de polvo mineral (MINM, MIAM y MICM), más una cantidad fija de componente soluble en agua (WASO). La proporción de los tres componentes de polvo mineral presentes en la mezcla es variable, y depende de la concentración total de partículas de polvo mineral ($N_{mineral}$). Los tres componentes del polvo mineral están relacionados con $N_{mineral}$ a través de las siguientes expresiones:

$$\ln N_{MINM} \approx 0{,}104 + 0{,}963 \ln N_{mineral} \tag{6.3}$$

$$\ln N_{MIAM} \approx -3{,}94 + 1{,}29 \ln N_{mineral} \tag{6.4}$$

$$\ln N_{MICM} \approx -13{,}7 + 2{,}06 \ln N_{mineral} \tag{6.5}$$

donde N_{MINM}, N_{MIAM} y N_{MICM} representan la concentración de los componentes MINM, MIAM y MICM, respectivamente. Por tanto, tendremos un perfil vertical por cada valor de $N_{mineral}$. El conjunto de valores $N_{mineral}$ conforma una tupla que denominaremos como $N_{mineral}^{lut}$.

Las relaciones empíricas 6.3, 6.4 y 6.5, fueron derivadas para condiciones promedio en áreas desérticas, por lo que resultan adecuadas para describir los aerosoles en una estación como la de Tamanrasset, ubicada en medio del desierto del Sahara, pero no para las estaciones de Izaña y Santa Cruz de Tenerife, situadas en el océano Atlántico Norte alejadas cientos de kilómetros de las fuentes de polvo mineral. En estas dos estaciones, la presencia de grandes partículas de polvo mineral se reduce considerablemente debido a una rápida deposición de estos componentes durante su transporte desde las regiones de origen. Debido a que no existe una definición concreta de los aerosoles en términos de componentes OPAC para estos casos, se ha realizado una modificación en la mezcla de componentes propuesta por Koepke et al. (1997). Esta modificación implica el reemplazo del componente MIAM por MITR, manteniendo la misma relación con $N_{mineral}$ que MIAM, se descarta el aporte de MICM y se mantiene la misma relación de WASO y MINM.

2. Con todos los parámetros de entrada definidos, libRadtran calcula las propiedades ópticas de los componentes atmosféricos, es decir los perfiles de extinción, el SSA, la función de fase, etc. Uno de los productos obtenidos en este paso es el AOD asociado a cada uno de los perfiles verticales de los aerosoles establecidos. De aquí se deriva que la tabla de AOD, AOD_λ^{lut}, consta de un número de elementos definido por el producto del número de elementos de la tupla $N_{mineral}^{lut}$ y el número de bandas espectrales.

3. Las propiedades ópticas obtenidas en el paso anterior son utilizadas por el modelo para calcular la LUT de ZSR computadas, ZSR_λ^{lut}, a partir de la resolución de la ecuación de transferencia radiativa en cada banda espectral. Cada elemento de esta LUT estará asociado con una pareja de componentes dados por las tuplas SZA^{lut} y $N_{mineral}^{lut}$ para cada longitud de onda.

4. Las ZSR_λ^{lut} se comparan con las ZSR medidas, ZSR_λ^m, buscando el conjunto de valores más próximos. Para ello se minimiza la raíz de las diferencias cuadráticas medias normalizadas (NRMSD o ϵ_k) , es decir:

$$\epsilon_k = \sqrt{\frac{1}{N_\lambda} \sum_{\lambda=1}^{N_\lambda} \left(\frac{ZSR_\lambda^m(\theta_v = 0, \theta_s) - ZSR_{\lambda,k}^{lut}(\theta_v = 0, \theta_s, N_{mineral,k}^{lut})}{ZSR_\lambda^m(\theta_v = 0, \theta_s)} \right)^2} \quad (6.6)$$

donde N_λ es el número total de bandas espectrales, θ_v es el ángulo cenital de visión que es igual a cero, θ_s es el ángulo cenital solar y k es el índice que indica un elemento determinado de la tupla $N_{mineral}^{lut}$. El valor del índice k que hace mínimo el parámetro ϵ_k, indica el valor estimado del AOD para cada banda espectral a partir de la tabla AOD_λ^{lut}.

6.4. Método ZEN-PWV-LUT

La técnica ZEN-PWV-LUT, es una extensión del método ZEN-AOD-LUT para la estimación del PWV. En este caso, además de los parámetros fijos y variables descritos en la sección anterior, se ha añadido un conjunto de valores de PWV como parámetros de entrada variables al modelo de transferencia radiativa. Esta extensión sólo se realiza para el canal centrado en 940 nm (FWHM $\approx$ 10 nm), ya que esta es la única región espectral medible por el instrumento donde el vapor de agua absorbe la radiación de manera apreciable.

El espectro de absorción del vapor de agua en la banda centrada en 940 nm ($\sim$ 100 nm) tiene una estructura muy compleja con un alto número de líneas de absorción estrechas (del orden de miles). Modelar las ZSR para un número tan alto de longitudes de onda requiere de un alto tiempo de computación. Para reducir el elevado tiempo de cálculo requerido, en este estudio se ha optado por utilizar la parametrización REPTRAN (Gasteiger et al., 2014) incluida en libRadtran con una resolución de 15 cm^{-1} (REPTRAN COARSE). Con esta parametrización sólo se requieren unas pocas longitudes de onda representativas para resolver toda la banda espectral, reduciendo así el coste computacional. Además, esta parametrización incluye el modelo MT_CKD (MlawerTobinCloughKneizysDavies) (Clough et al.,

2005) para la absorción del continuo del vapor de agua. La ZSR simulada para toda la banda espectral se obtiene convolucionando las ZSR calculadas en las longitudes de onda representativas con la función de transmisividad del filtro. Por tanto, el conocimiento preciso de la función de transmisividad del filtro es un factor importante en la determinación precisa del PWV. La contribución de los aerosoles se estima en un paso anterior a partir del método ZEN-AOD-LUT. En este caso, los componentes de la LUT resultante, ZSR_{940}^{lut}, dependerán de los tríos de elementos dados por las tuplas SZA^{lut}, $N_{mineral}^{lut}$ y PWV^{lut}. Una vez que se ha estimado la concentración de aerosoles, el PWV se calcula minimizando la NRMSD entre la ZSR medida (ZSR_{940}^m) y la ZSR calculada (ZSR_{940}^{lut}), es decir:

$$
\epsilon_{k,l} = \sqrt{\left(\frac{ZSR_{940}^m(\theta_v = 0, \theta_s) - ZSR_{940,k,l}^{lut}(\theta_v = 0, \theta_s, N_{mineral,k}^{lut}, PWV_l^{lut})}{ZSR_{940}^m(\theta_v = 0, \theta_s)} \right)^2}.
$$
(6.7)

En este caso el índice l es el índice que indica un elemento determinado de la tupla PWV^{lut} y análogamente que para el método ZEN-AOD-LUT el valor del índice l que minimice el parámetro $\epsilon_{k,l}$, indica el valor estimado del PWV.

6.5. Algoritmo de control de calidad de los datos del ZEN-R (ZEN-QC)

El algoritmo ZEN-QC se desarrolló con el fin de detectar y eliminar las posibles anomalías instrumentales presentes en los datos de los radiómetros ZEN-R y los datos afectados por nubes. Este algoritmo, esquematizado en la figura 6.1, consta de los siguientes pasos:

1. Control de calidad de la señal: los dispositivos ZEN-R realizan 30 medidas en un minuto, pero sólo se almacenan los valores promedio y las correspondientes desviaciones estándar (σ_v) de los diferentes canales. El ruido de alta frecuencia se elimina analizando la señal, considerando un umbral del 5 % en σ_v, que fue determinado tras analizar empíricamente los datos bajo condiciones tanto limpias como de alta turbiedad. También se eliminan las medidas cuya señal exceda el valor de saturación menos un 1 % en al menos uno de los canales.

2. Verificación de la radiancia: se analizó la NRMSD entre las radiancias medidas y estimadas utilizadas en el proceso de cálculo del AOD con el método ZEN-AOD-LUT (sección 6.3). Se determinó un umbral del 10 % para el valor de ϵ_k, dado en la ecuación 6.6, eliminando los datos por encima de este umbral.

3. Control del AOD: en este caso hemos adaptado parte del algoritmo de control de calidad de AERONET (Giles et al., 2019; Smirnov et al., 2000) al sistema ZEN. Este consta de los siguientes pasos :

   - Criterio de suavidad del AOD. Se considera como datos afectados por nubes a aquellos cuyo ritmo de cambio en el AOD_{500} sea superior a $0,01/minuto$.

   - Criterio de estabilidad del AOD. Todos los datos cuya desviación estándar en el AOD_{500} diario sea menor de 0,015 pasan el control de calidad de AOD. En caso contrario los datos se someten al siguiente control.

   - Los datos que no superan el control anterior se someten al control 3σ en el AOD_{500} diario, es decir se desecharon los datos fuera de los límites comprendidos por el promedio diario ±3 veces la desviación estándar en el AOD_{500}.

4. Por último, si los datos restantes de un día determinado son inferiores a tres, o al 10 % del total (el que sea mayor), se eliminan los datos de este día.
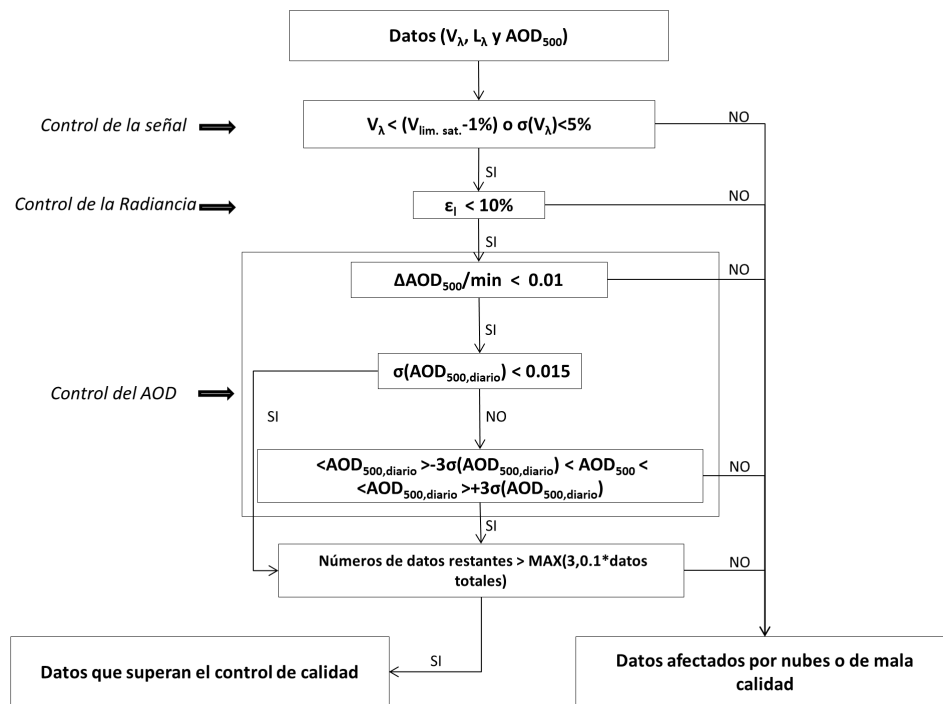
Figura 6.1: Diagrama del algoritmo de control de calidad ZEN-QC.

7. Resultados

En esta sección se resumen cada una de las tres publicaciones que forman parte de esta memoria de tesis, ordenándolas en base a la coherencia de contenido. En base a la naturaleza de su contenido, podemos distinguir dos partes: la constituida por el artículo 1 y la constituida por los artículos 2 y 3. En el artículo 1, el principal objetivo fue realizar una comparación de AOD entre la red GAW-PFR que incluye la referencia mundial de AOD, y AERONET, la más extendida espacialmente, con un gran número de estaciones, y la más utilizada en informes técnicos y artículos científicos. Este estudio se realizó en el Observatorio Atmosférico de Izaña utilizando exclusivamente equipos de referencia ("Masters") de cada una de las dos redes. En dicho artículo el doctorando contribuyó activamente en la descripción de detalles no publicados del fotómetro Cimel-AERONET, en la identificación de las diferencias técnicas entre el Cimel-AERONET y el PFR, así como en tratar de cuantificar las diferencias ocasionadas por el uso de diferentes algoritmos de procesamiento de datos por cada una de las redes. Los resultados de este artículo, que muestran una excelente trazabilidad en el AOD del Cimel-AERONET con la referencia mundial, dan validez al empleo del Cimel-AERONET como instrumento de referencia del AOD. En los artículos 2 y 3 se evalúan las dos versiones del radiómetro ZEN-R así como las diferentes metodologías desarrolladas para el cálculo del AOD y del PWV, comparándolos con datos de instrumentos de referencia de AERONET. En ambas publicaciones el doctorando lideró el proceso de composición y redacción de los artículos, desarrollo de las metodologías y cálculo de los resultados, asesorado por los directores de tesis. La utilización de la red AERONET como referencia en los artículos 2 y 3, en lugar de la referencia mundial GAW, vino impuesta por el hecho de que las calibraciones de los equipos de referencia de la primera están accesibles mucho antes que las de la referencia mundial, y porque las comparaciones directas en otras estaciones utilizadas en este estudio (Santa Cruz de Tenerife, y Tamanrasset) son sólo posibles con la red AERONET. Los excelentes resultados en la trazabilidad del AOD de Cimel-AERONET con la referencia mundial mostrados en el artículo 1, justifica la idoneidad del uso de los datos AERONET como referencia de AOD en las diversas comparaciones de los radiómetros ZEN realizadas en los artículos 2

y 3. A continuación se exponen cada uno de ellos siguiendo el orden establecido.
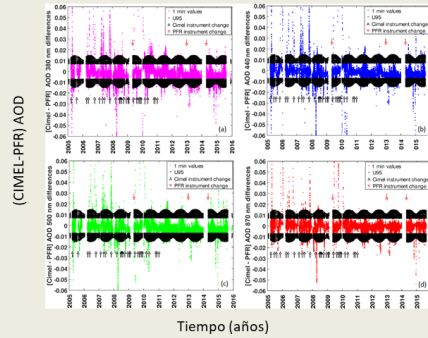
7.1. Artículo 1: Comparación a largo plazo (2005–2015) del espesor óptico de aerosoles de los fotómetros GAW-PFR y AERONET-Cimel a partir de medidas síncronas de 1 min.
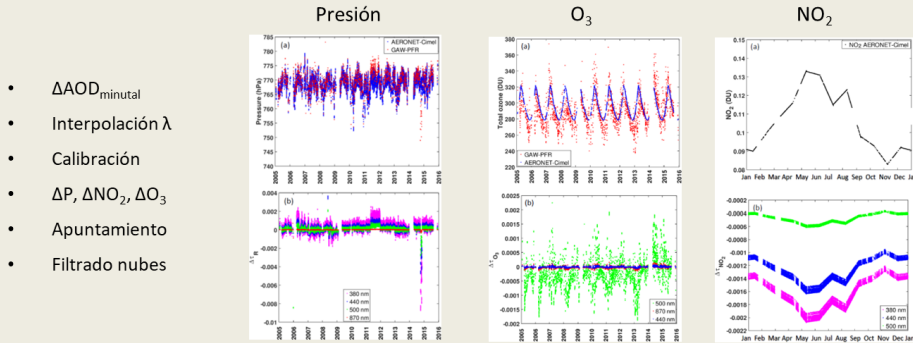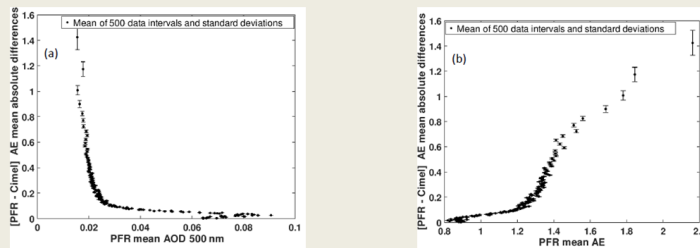
7.1.1. Resumen gráfico
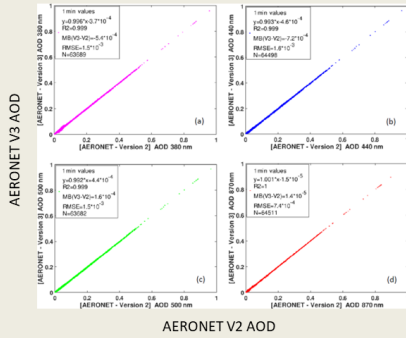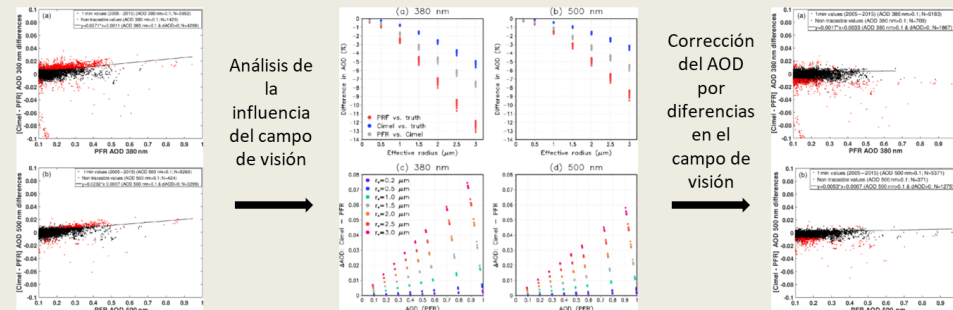
Figura 7.1: Esquema gráfico del artículo 1.

7.1.2. Resumen

En este artículo presentamos una comparación exhaustiva de las medidas de AOD proporcionadas por el radiómetro PFR de la red GAW-PFR de la WMO, que es la referencia internacional del AOD establecida por la WMO, y el radiómetro Cimel CE318 utilizado por AERONET, que es la red de medida de AOD más extensa a nivel mundial y la más utilizada para la caracterización de aerosoles y para la evaluación de modelos y observaciones satelitales. El objetivo de este estudio es evaluar si, a pesar de las marcadas diferencias técnicas entre ambos y el número de instrumentos utilizados en su comparación de 11 años, los datos de AOD de Cimel-AERONET son trazables a los de GAW-PFR.

La comparación se realizó sobre una serie de datos de AOD de AERONET de 11 años en el Observatorio Atmosférico de Izaña, perteneciente al CIAI (AEMET), utilizando un total de 15 radiómetros Cimel CE318 calibrados con la técnica Langley, 13 de ellos en el período 2005–2009, lo que significa que durante ese periodo de cuatro años un instrumento fue reemplazado por otro para ser calibrado aproximadamente cada 4,5 meses. Sus calibraciones se realizaron durante sus respectivos períodos de tiempo de medida en el Observatorio Atmosférico de Izaña. Por lo tanto, estas calibraciones no estaban vinculadas de ninguna manera con las de los instrumentos que las precedieron o reemplazaron o con la referencia GAW-PFR. Estos hechos nos llevaron a investigar la homogeneidad de la serie de datos de AOD de AERONET y su intercomparabilidad con la serie de datos AOD mucho más homogénea de GAW-PFR (tres instrumentos en 11 años). En total se analizaron más de 70000 pares de datos minutales síncronos GAW-PFR y AERONET en el período 2005-2015, para cuatro longitudes de onda comunes o"cercanas" (380, 440, 500 y 870 nm). Para tres de las bandas espectrales del GAW-PFR (368, 412 y 862 nm) el AOD se interpoló o extrapoló a los canales del Cimel CE318 correspondientes (380, 440 y 870 nm), utilizando la ley de Ångström (Ångström, 1929).

En primer lugar se realizó una comparación entre las versiones V2 y V3 de AERONET para los canales 380, 440, 500 y 870 nm para el período 2005-2015. Al realizar la comparación se obtuvo un excelente acuerdo entre V2 y V3 para los cuatro canales analizados con un coeficiente de determinación (R^2) > 0,999. Esto demuestra que los resultados de la comparación de AOD entre GAW-PFR y las dos versiones de AERONET son muy similares.

Seguidamente se realizó la comparación del conjunto de datos GAW-PFR con las dos versiones de AERONET (V2 y V3) en el período 2005-2015 en términos de trazabilidad. El concepto de trazabilidad de la WMO (WMO, 2005) aplicado en nuestro caso para el AOD, consiste en determinar si la diferencia de AOD de AERONET frente al proporcionado por la referencia PFR-GAW se encuentra

dentro de los límites U_{95}, es decir:

$$U_{95} = \pm \left(0{,}005 + \frac{0{,}010}{m} \right), \qquad (7.1)$$

donde m es la masa óptica relativa. La trazabilidad es aceptable cuando el 95 % de las diferencias de AOD se encuentran dentro de estos límites, en cuyo caso ambas poblaciones de datos se consideran equivalentes. Al efectuar dicho análisis se encontró una excelente trazabilidad con el AOD de AERONET (V2 y V3) para 440, 500 y 870 nm (entre el 95 y 98 % de los datos estaban dentro de los límites), así como buenos resultados, aunque ligeramente por debajo de los límites, para 380 nm, con el 92,7 % de los datos dentro de los límites U_{95}.

A continuación se realizó un análisis detallado de las causas que podrían explicar las diferencias encontradas en el AOD. Los factores analizados y los resultados obtenidos son los siguientes:

1. *Variabilidad del AOD a muy corto plazo (un minuto).*

   Analizando la variabilidad de AOD en un minuto se obtuvo que aproximadamente sólo el 0,8 % de los datos de AOD tienen una variabilidad mayor que 0,005 en todos los rangos espectrales. Esto significa que la variabilidad natural de AOD no es una causa que pueda explicar las diferencias de AOD registradas entre ambos instrumentos.

2. *Problema de apuntamiento solar.*

   El desalineamiento del seguidor solar constituye un problema grave y una causa importante de la no trazabilidad de los pares de datos de AOD, como así demuestran los datos de AOD fuera de los límites de U_{95} desde el período 2005-2009, como consecuencia de problemas puntuales con el seguidor solar del radiómetro GAW-PFR. Para el período 2010–2015, el porcentaje de pares de datos trazables mejora hasta el 93,5 % (380 nm), 97,4 % (440 nm), 97,2 % (500 nm) y 99,1 % (870 nm). Sin embargo, la mayoría de estos casos podrían identificarse y excluirse del análisis.

3. *Fallo en los algoritmos de detección de nubes de ambas redes.*

   Según nuestras observaciones, el fallo simultáneo en el cribado de nubes por parte de ambos algoritmos podría ocurrir sólo bajo la presencia de cirros grandes y estables. En estos casos, los radiómetros interpretan las nubes como capas de aerosol y pueden proporcionar valores muy diferentes del AOD real. Sin embargo, para la comparación realizada en el Observatorio Atmosférico de Izaña, este efecto es insignificante ya que los algoritmos de

detección de nubes GAW-PFR y AERONET proporcionan una identificación exitosa de sol directo despejado con cielos nublados (con fracciones de cielo despejado (FCS) $< 40\%$) para el $99,75\%$ de los casos.

4. *Errores en la medida de la presión atmosférica.*

   La precisión de los nuevos barómetros integrados en los nuevos radiómetros es de aproximadamente 3 hPa. Sólo los errores en la presión atmosférica > 30 hPa pueden producir un impacto en la dispersión de Rayleigh, y estos casos son fácilmente detectables, pudiendo descartar o corregir los valores de AOD correspondientes. Por tanto, la no trazabilidad del AOD debido a errores en la dispersión de Rayleigh es insignificante.

5. *Incertidumbre en el ozono total en columna.*

   La mayor influencia, en las bandas espectrales consideradas, en lo que respecta a la absorción de la radiación por parte del ozono, ocurre principalmente en 500 nm, por lo que la incertidumbre en el ozono total en columna considerado tendrá un efecto apreciable en la incertidumbre del AOD en esta banda. El ozono total debe determinarse con una incertidumbre de ± 30 unidades Dobson (UD) o el 10% de los valores típicos para garantizar una incertidumbre de absorción del ozono $\pm 0{,}001$ a 500 nm. En el caso de la comparación GAW-PFR-AERONET, a pesar de que ambas redes cuentan con métodos muy diferentes para la determinación de los valores O_3 necesarios para sus correspondientes correcciones, sólo se encontraron grandes diferencias en el ozono total en columna (> 40 UD) en el $2{,}4\%$ de los días, lo que resultó en una diferencia en el espesor óptico del ozono ligeramente superior a 0,001. Por tanto, la posible contribución a los valores de AOD no trazables entre las dos redes en la intercomparación a largo plazo llevada a cabo en el Observatorio Atmosférico de Izaña es insignificante. Sin embargo, en estaciones de latitud media o alta donde se pueden registrar variaciones rápidas de O_3 de varias decenas de UD, la corrección de las medidas de AOD minutal por absorción de ozono podría ser un problema a considerar en el canal de 500 nm.

6. *Incertidumbre en el NO_2 total en columna.*

   Las diferencias en el espesor óptico del NO_2, que tienen su origen en las diferencias en la cantidad de NO_2 total en columna considerado entre GAW-PFR y AERONET, es del orden de 10^{-3} para los canales de 380 y 440 nm, mientras que para el canal de 500 nm es aún menor, del orden de 10^{-4}. Por lo tanto, las diferencias en la absorción de NO_2 son insignificantes en la no trazabilidad del AOD minutal de nuestro estudio. Sin embargo, la absorción de NO_2 podría tener algún impacto en el AOD en regiones altamente con-

taminadas, como en las grandes ciudades industriales, donde los valores de NO_2 en columna son mucho mayores que los climatológicos.

Teniendo en cuenta las correcciones para la dispersión de Rayleigh y para las absorciones de O_3 y NO_2, hemos calculado el efecto combinado de todos ellos en la no trazabilidad de los valores de AOD minutales. El mayor impacto se produce en el canal de 380 nm, en el que el 25 % de los datos de AOD fuera de los límites U_{95} ($\approx 2\%$ del total de datos comparados) se deben a diferencias significativas en la presión y/o en la absorción de O_3 y NO_2. Los datos de AOD minutales fuera de los límites de U_{95} mediante estas correcciones son insignificantes en el canal de 870 nm.

7. *Impacto de la dispersión hacia adelante (forward scattering) del polvo en la incertidumbre de obtención del AOD debido a los diferentes FOV utilizados por cada instrumento.*

Dado que el PFR tiene un FOV de $\approx 2.5°$ (Wehrli, 2000), que es prácticamente el doble que el del Cimel CE318 ($\approx 1.3°$, Torres et al., 2013), y las medidas de irradiancia solar directa están afectadas por la radiación proveniente de la aureola solar, es razonable esperar que el PFR se vea más afectado por la irradiancia circunsolar que el radiómetro Cimel CE318 cuando el AOD es relativamente alto. Para evaluar el impacto de la irradiancia circunsolar en el PFR y el Cimel CE318, se aplicó un modelo de transferencia radiativa basado en Monte Carlo (Barker, 1992, 1996; Räisänen et al., 2003) actualizado para tener en cuenta el tamaño finito del disco solar y su oscurecimiento en los bordes (Räisänen and Lindfors, 2019). Al modelar la dispersión hacia adelante del polvo, hemos demostrado que un porcentaje no despreciable de los datos de AOD minutales no trazables para $AOD > 0.1$, que varía entre $\approx 0.3\%$ a 870 nm y $\approx 1.9\%$ a 380 nm, es causado por la diferencia de FOV. Debido a este efecto, GAW-PFR proporciona valores de AOD, que son $\approx 3\%$ más bajos a 380 nm y $\approx 2\%$ más bajos a 500 nm que los proporcionados por AERONET. Sin embargo, esta subestimación del AOD solo podría tener cierta relevancia en regiones con alta presencia de polvo atmosférico si se usan radiómetros con un FOV relativamente grande.

Finalmente, se realizó una comparación entre el AE proporcionado por GAW-PFR y AERONET utilizando 70716 pares de datos de AOD obtenidos de los cuatro canales comunes cercanos. Este es un cálculo de AE muy estricto, ya que es necesario que los cuatro canales midan con precisión el AOD simultáneamente. Las diferencias de AE son > 0.2 aumentando exponencialmente en condiciones extremadamente limpias ($AOD \leq 0.03$ y $AE \geq 1$), alcanzando diferencias de AE de hasta 1,6. Sin embargo, para estas condiciones, la carga de aerosol atmosférico es prácticamente

nula, por lo que la caracterización del AE no tiene ninguna importancia en la práctica. En condiciones no limpias, o con un alto contenido de polvo mineral (AOD asociado$> 0{,}03$ y $AE < 1$), las diferencias de AE permanecen $< 0{,}1$.

7.1.3. Artículo 1

Aerosol optical depth comparison between GAW-PFR and AERONET-Cimel radiometers from long-term (2005–2015) 1 min synchronous measurements

Emilio Cuevas[1], Pedro Miguel Romero-Campos[1], Natalia Kouremeti[2], Stelios Kazadzis[2], Petri Räisänen[3], Rosa Delia García[4,1], Africa Barreto[5,1,4], Carmen Guirado-Fuentes[4,1], Ramón Ramos[1], Carlos Toledano[4], Fernando Almansa[5,1,4], and Julian Gröbner[2]

[1]Izaña Atmospheric Research Center (IARC), State Meteorological Agency (AEMET), Santa Cruz de Tenerife, Spain

[2]Physikalisch-Meteorologisches Observatorium Davos, World Radiation Center (PMOD-WRC), Davos, Switzerland

[3]Finnish Meteorological Institute, Helsinki, Finland

[4]Atmospheric Optics Group, Valladolid University, Valladolid, Spain

[5]Cimel Electronique, Paris, France

Correspondence: Emilio Cuevas (ecuevasa@aemet.es)

Abstract. A comprehensive comparison of more than 70000 synchronous 1 min aerosol optical depth (AOD) data from three Global Atmosphere Watch precision-filter radiometers (GAW-PFR), traceable to the World AOD reference, and 15 Aerosol Robotic Network Cimel radiometers (AERONET-Cimel), calibrated individually with the Langley plot technique, was performed for four common or "near" wavelengths, 380, 440, 500 and 870 nm, in the period 2005–2015. The goal of this study is to assess whether, despite the marked technical differences between both networks (AERONET, GAW-PFR) and the number of instruments used, their long-term AOD data are comparable and consistent. The percentage of data meeting the World Meteorological Organization (WMO) traceability requirements (95% of the AOD differences of an instrument compared to the WMO standards lie within specific limits) is > 92% at 380 nm, > 95% at 440 nm and 500 nm, and 98% at 870 nm, with the results being quite similar for both AERONET version 2 (V2) and version 3 (V3). For the data outside these limits, the contribution

of calibration and differences in the calculation of the optical depth contribution due to Rayleigh scattering and O_3 and NO_2 absorption have a negligible impact. For AOD > 0.1, a small but non-negligible percentage ($\sim$ 1.9%) of the AOD data outside the WMO limits at 380 nm can be partly assigned to the impact of dust aerosol forward scattering on the AOD calculation due to the different field of view of the instruments. Due to this effect the GAW-PFR provides AOD values, which are $\sim$ 3% lower at 380 nm and $\sim$ 2% lower at 500 nm compared with AERONET-Cimel. The comparison of the Ångström exponent (AE) shows that under non-pristine conditions (AOD > 0.03 and AE < 1) the AE differences remain < 0.1. This long-term comparison shows an excellent traceability of AERONET-Cimel AOD with the World AOD reference at 440, 500 and 870 nm channels and a fairly good agreement at 380 nm, although AOD should be improved in the UV range.

1 Introduction

In recent decades there has been a growing interest in the role played by atmospheric aerosols in the radiation budget and the Earth's hydrological cycle, mainly through their physical and optical properties (IPCC, 2013). The most comprehensive and important parameter that accounts for the optical activity of aerosols in the atmospheric column is the aerosol optical depth (AOD) (WMO, 2003, 2005). This is also a key parameter used in atmospheric column aerosol modelling (e.g. Basart et al., 2012; Benedetti et al., 2018; Cuevas et al., 2015; Huneeus et al., 2016) and in satellite observations (e.g. Sayer et al., 2012, 2013; Kahn and Gaitley, 2015; Amiridis et al., 2015). The second aerosol optical parameter in importance is the Ångström exponent (AE; Ångström, 1929) that accounts for the spectral dependency of the AOD. Since the AE is inversely related to the average size of the aerosol particles, it is a qualitative indicator of the atmospheric aerosol particle size, and therefore a useful parameter to assess the aerosol type (WMO, 2003). At present, two global ground-based radiometer networks provide aerosol optical properties of the atmospheric column using centralized data processing procedures based on their respective standard criteria and also centralized protocols for calibration and quality control, linking all network instruments. These are GAW-PFR (Global Atmosphere Watch precision-filter radiometer; http://www.pmodwrc.ch/worcc/; last access: 5 September 2018) and AERONET-Cimel (AErosol RObotic NETwork Cimel Electronique radiometer; https://aeronet.gsfc.nasa.gov; last access: 1 September 2018) networks. AERONET is, in fact, a federation of ground-based remote-sensing aerosol networks established by NASA (National Aeronautics and Space Administration) and PHOTONS (PHOtométrie pour le Traitement Opérationnel de Normalisation

Satellitaire, University of Lille, Service d'Observation de l'INSU, France; Goloub et al., 2007), complemented by other sub-networks, such as AEROCAN (Canadian sun photometry network; Bokoye et al., 2001), AeroSibnet (Siberian system for Aerosol monitoring; Sakerin et al., 2005), AeroSpan (Aerosol characterisation via sun photometry: Australia Network; Mitchell et al., 2017), CARSNET (China Aerosol Remote Sensing NETwork; Che et al., 2015) and RIMA (The Iberian network for aerosol measurements; Toledano et al., 2011). There are other radiometer networks that in recent years have incorporated centralized protocols for data evaluation and databases and performed regular intercomparisons with GAW-PFR and AERONET-Cimel. These include, for example, SKYNET (SKYradiometer NETwork) and its seven associated subnetworks, which use the Prede-POM sky radiometer to investigate aerosol–cloud–solar radiation interactions (e.g. Campanelli et al., 2004; Nakajima et al., 2007; Takamura and Nakajima, 2004).

The World Optical Depth Research Calibration Center (WORCC) was established in 1996 at the Physikalisch Meteorologisches Observatorium Davos World Radiation Center (PMOD-WRC). The GAW-PFR network (Wehrli,2005) was initiated within PMOD-WRC for global and long-term atmospheric aerosol monitoring and accurate detection of trends. Aerosol data series measured at 12 core sites away from local and regional pollution sources that are representative of atmospheric background conditions in different climates and environments of the planet, in addition to another 20 associated stations, are included in this global network (Kazadzis et al., 2018a). For this reason, GAW-PFR uses the PFR, an accurate and reliable instrument regarding its absolute response stability over time that was designed for long-term AOD measurements (Wehrli, 2008a). The GAW-PFR was specifically designed by WORCC for this goal following the technical specifications defined by the World Meteorological Organization (WMO, 2003, 2016). In 2006, the Commission for Instruments and Methods of Observation (CIMO) of the WMO (WMO, 2007) recommended that the WORCC at the PMOD-WRC should be designated as the primary WMO Reference Centre for AOD measurements (WMO, 2005).

The AERONET-Cimel network (Holben et al., 1998) was, in principle, designed to validate satellite products and to characterize the spatio-temporal distribution of atmospheric aerosols based on their optical properties. It is the largest surface-based global aerosol network, with more than 84 sites with measurement series longer than 10 years and more than 242 sites having datasets > 5 years. Cimel radiometer data, part of AERONET, are processed centrally and freely delivered in near real time by the NASA Goddard Space Flight Center. Both networks, although designed to meet different objectives, are now global benchmarks for the study and characterization of aerosol optical properties worldwide and for the evaluation of aerosol observations made on board satellites and simulations made using models.

Multiple studies have proliferated in recent years to obtain aerosol climatology and to determine AOD trends in different parts of the world (e.g. Nyeki et al., 2012; Klingmüller et al., 2016; Chedin et al., 2018). However, these networks use radiometers with significant technical differences. Moreover, calibration methodologies, AOD calculation algorithms and data evaluation methods are also relatively different between the two networks. Consequently, the objective of this study is to assess whether, despite the marked differences between both networks, including the different day-to-day maintenance and operation procedures of the respective instruments during the study period, the long-term AOD data provided by the two networks are comparable and consistent.

The WMO has defined the GAW-PFR Triad (three Master PFR instruments) as the worldwide reference for AOD measurements (WMO, 2005). Based on this concept, an instrument provides traceable measurements of AOD to this WMO reference when this instrument can demonstrate an unbroken chain of calibrations between itself and the GAW-PFR Triad with AOD measurements within specified limits of the GAWPFR reference. This can either be achieved by a direct comparison to the GAW-PFR Triad (Kazadzis et al., 2018a) or by using a portable transfer standard radiometer as presented in this study. Several comparisons between AERONET-Cimel, GAW-PFR and other radiometers have been carried out in different places (Barreto et al., 2016; Kazadzis et al., 2014, 2018b; Kim et al., 2008; McArthur et al., 2003; Mitchell and Forgan, 2003; Nyeki et al., 2015; Schmid et al., 1999; Toledano et al., 2012). However, these comparisons have been performed during field intercomparison campaigns or during relatively short periods of time, thus they are not representative of a large variety of atmospheric conditions. In addition, the type of instrument maintenance and the number and qualifications of staff serving them during campaigns is generally of a higher quality compared to that of the instrument daily operation in unattended mode. This might cause an improvement in the instrument performance during intensive campaigns compared to the operational mode.

The growing interest in the analysis of long-term AOD and AE data series for climatological purposes requires an assessment of their quality assurance and long-term intercomparability. This is the first study to analyse the long-term traceability of AERONET-Cimel with respect to GAW-PFR and therefore to assess the validity of the long AOD and AE AERONET-Cimel data series for climatological and climate change studies under specific quality control requirements.

GAW-PFR has a comprehensive calibration system (Kazadzis et al., 2018a; Schmid and Wehrli, 1995) that is transferred by a worldwide suite of reference instruments. AERONET-Cimel does not have a WMO-CIMO linked reference and, as described by Holben et al. (1998), Eck et al. (1999) and Toledano et al. (2018), is based on

maintaining reference AERONET radiometers based on the Langley calibration technique at Izaña, Spain, and Mauna Loa, USA. Calibration of all other instruments is based on raw voltage ratio comparisons with reference instruments at dedicated sites (Carpentras, France; Washington D.C., USA; Valladolid, Spain). There are few places in the world where synchronous observations of these two networks are available for long time periods and variable AOD conditions. The Izaña Observatory (IZO; Tenerife, Canary Islands) is one of them. The GAW-PFR measurements started at Izaña Observatory in 2001 (Wehrli, 2005), while AERONET-Cimel started in 2003 (Goloub et al., 2007). Since 2005, synchronous measurements (1 min values) that have been evaluated following the calibration procedures of each of the networks are available.

In addition, the Izaña Observatory is one of the two places in the world (the other is Mauna Loa, Hawaii, USA) where sun calibrations are performed using the Langley plot technique for both AERONET-Cimel and GAW-PFR reference instruments (Toledano et al., 2018) because of stable and very low AOD conditions during many days each year. Consequently, the instruments compared at the Izaña Observatory have been calibrated under the same environmental conditions, and therefore AOD differences can be directly linked with calibration principles, AOD post-processing and other instrumental differences. In this work, we analyse and evaluate the comparison of 11 years (2005–2015) of 1 min synchronous observations of AOD with AERONET-Cimel and GAW-PFR in four common or "near" wavelengths, assessing the results and explaining the possible causes of these differences. Some preliminary technical details on the traceability between GAW-PFR and AERONET-Cimel were reported in a technical report by Romero-Campos et al. (2017).

In Sect. 2 the facility in which this long-term comparison has been carried out is described. The technical characteristics of the AERONET-Cimel and GAW-PFR instruments are shown in Sect. 3, with special emphasis on the technical and methodological differences of both networks. Section 4 describes the methodology followed in this intercomparison based on the concept of WMO-GAW traceability. Results are given in Sect. 5. A summary and conclusions are provided in Sect. 6. The Supplement contains case analyses of inaccurate calibration and cloud contamination, some additional results of the comparison between PFR and Cimel with AERONET version 3 (V3), complementary information of the very short natural AOD variability, and the simulations performed with the Monte Carlo model to evaluate the impact of dust forward-scattering radiation on AOD determination.

2 Site description

Izaña Observatory (28.3° N, 16.5° W; 2373 ma.s.l.) is located in Tenerife (Canary Islands, Spain) and is managed by the Izaña Atmospheric Research Center (IARC), which is part of the State Meteorological Agency of Spain (AEMET). It is a suitable place for long-term studies of aerosol optical properties under contrasting atmospheric and meteorological conditions. This is because IZO is located in the free troposphere (FT) above the temperature inversion caused by the trade wind regime in lower levels and general subsidence associated with the branch of the decay of Hadley's cell aloft (Carrillo et al., 2016). This meteorological feature favours, during most of the year, the presence of pristine skies and clean air, representative of atmospheric background conditions (Cuevas et al., 2013; Rodríguez et al., 2009). On the other hand, its proximity to the African continent makes it a privileged site for observing and characterizing the Saharan Air Layer (SAL), which normally presents a high burden of desert mineral dust, especially during the summer months (Basart et al., 2009; Cuevas et al., 2015; Rodríguez et al., 2011). At that time of the year, the SAL impacts the subtropical free troposphere over the North Atlantic with large interannual (Rodríguez et al., 2015) and sharp intraseasonal (Cuevas et al., 2017a) variability. The contrasting atmospheric conditions that occur at IZO allow the comparison of the two networks, which can be performed under a wide range of AOD values: mostly for pristine conditions (AOD$\leq$ 0.03) but also for relatively high turbidity (AOD$>$ 0.6) linked with dust-aerosol-related intrusions. In addition, the location offers the possibility of observing rapid changes in AOD, going from pristine conditions to dusty skies and vice versa in a matter of a few hours, especially in the summer period. The periodical presence of a dust-laden SAL allows us to evaluate the impact that the dust forward scattering into the field of view has on AOD retrieval. All this defines IZO as an excellent atmospheric aerosol natural laboratory to compare the performance of different radiometers measuring AOD. One of the first international AOD intercomparison campaigns was carried out at IZO in April 1984 (WMO, 1986), promoted and coordinated by PMOD-WRC.

The privileged conditions of pristine skies that characterize IZO during many days of the year have allowed this observatory to become a calibration site for the GAW-PFR and AERONET-Cimel networks since 2001 and 2003, respectively, where the extraterrestrial constants are determined with direct sun observations using the Langley plot technique (Toledano et al., 2018). Note that the extraterrestrial constant (calibration constant) is the signal the instrument would read outside the atmosphere at a normalized Earth–sun distance. In addition, since July 2014, IZO has also been designated by the WMO as a CIMO (WMO, 2014) test bed for aerosols and water vapour remote-sensing instruments. IZO is a station of

the Baseline Surface Radiation Network (BSRN) (Driemel et al., 2018; García et al., 2019). Details of IZO facilities, measurement programmes and main research activities can be found in Cuevas et al. (2017b).

3 GAW-PFR and AERONET-Cimel radiometers

The two types of radiometers intercompared in this study are Cimel CE318-N (Holben et al., 1998), hereinafter referred to as Cimel, the standard instrument of AERONET until the recent appearance of CE318-T (Barreto et al., 2016), and the PFR (Wehrli, 2005), the standard instrument of the GAW-PFR network. The main features of these two radiometers are described in Table 1. The Cimel (Holben et al., 1994, 1998) is a radiometer equipped with a two-axis robot that performs two types of basic radiation measurements: direct solar irradiance and sky (radiance) observations, thanks to an automatic pointing robot that executes the observation sequences that have been scheduled. The robot performs automatic pointing to the sun by stepping azimuth and zenith motors using ephemeris based on time, latitude and longitude. Additionally, a four-quadrant detector is used to improve the sun tracking before each scheduled measurement sequence. This sensor guides the robot to the point where the intensity of the signal channel is at a maximum. Diffuse-sky measurements are also performed by Cimel to infer aerosol optical and microphysical properties. Two different routines are executed: almucantar (varying the azimuth angle keeping constant the zenith angle) and principal plane (varying the zenith angle keeping constant the azimuth angle). The ability of Cimel to perform both direct and diffuse-sky measurements makes it necessary to use a specific robot rather than a simple sun tracker. The field-of-view angle (FOV) of the instrument is 1.29° (hereafter $\sim 1.3°$) (Torres et al., 2013). The wavelengths in which the measurements are sequentially made by a single detector depend on the interference filters that each version of the radiometer has installed in the filter wheel, which is located inside the sensor head and which is moved by a stepper motor. The Cimel versions used in this study have at least eight interference filters centred at 340, 380, 440, 500, 675, 870, 940, and 1020 nm and a 10 nm full-width-at-half-maximum (FWHM) bandwidth, except for 340 and 380 nm which have 2 and 4 nm FWHM, respectively. Solar irradiance is measured with a Silicon detector in these channels. The possible deterioration of the interference filters is reduced since they are only exposed to the sun during three consecutive 1 s direct sun measurements per channel, this cycle being scheduled every ~ 15 min. The rest of the time the Cimel is taking sky radiance measurements or at rest position looking downwards.

The PFR (Wehrli, 2000, 2005, 2008a, b) is designed for continuous and automated

Table 1: Main features of the GAW-PFR (PFR;Wehrli, 2000, 2005, 2008a, b) and AERONET-Cimel (Holben et al., 1994, 1998; Torres et al., 2013) radiometers used in this study.

	GAW-PFR	AERONET-Cimel
Type of instrument	Standard version	Standard version Reference instrument
Type of observation	Automatic continuous direct sun irradiance	Automatic sun-sky tracking
Available standard channels	368, 412, 500, 862 nm	340, 380, 440, 500, 675, 870, 1020, 1640 nm
FWHM	5 nm	2 nm (340 nm), 4 nm (380 nm), 10 nm (VIS-NIR), 25 nm (1640 nm)
AOD uncertainty	$\pm$ 0.01	0.002-0.009, spectrally dependent, with the higher errors in the UV (Reference instruments) (Eck et al., 1999)
FOV (FWHM)	2.5° (1.2° plateau, 0.7° slope)	1.3° (slope angle unknown)
Sun Tracker	Any sun tracker with a resolution of at least 0.08°	Robot specifically designed by CIMEL and controlled in conjunction with the radiometer
Temperature control and correction	Temperature controlled 20°C$\pm$0.5°C	Temperature correction to 1020 nm is applied in V2. Corrections from filter-specific temperature characterization in V3 for VIS and NIR spectral bands (Giles et al., 2019)
Power	Grid	Solar panels and grids
Data transmission	Local PC/FTP	Local PC/FTP Satellite transmission
Calibration	Comparison with reference triad. Additional in situ long-term Langleys	At least 10 good morning Langleys plots

operation under a broad range of weather conditions. It accurately measures direct solar radiation transmitted in four independent narrow wavelength channels centred at 368, 412, 500 and 862 nm, with a 5 nm FWHM bandwidth. The FOV of the instrument is 2.5° and the slope angle is 0.7°. Dielectric interference filters manufactured by the ion-assisted deposition technique are used to assure significantly

larger stability in comparison to the one manufactured by classic soft coatings. The PFR was designed for long-term stable measurements; therefore, the instrument is hermetically sealed with an internal atmosphere that is slightly pressurized (2000 hPa) with dry nitrogen and is stabilized in temperature with a Peltier-type thermostatic system maintaining the temperature of the detector head at 20°C±0.5°C. This system makes corrections of the sensitivity for temperature unnecessary and also prevents accelerated ageing of filters, ensuring the high stability of the PFR. The PFR is mounted on a sun tracker, which is always pointing at the sun without any active optimization. The detectors are only exposed for short time periods, since an automated shutter opens every minute for 10 s for sun measurements, minimizing degradation related to the filter exposure.

The expected uncertainty of AOD in the four channels of the PFR radiometer is from 0.004 (862 nm) up to 0.01 (368 nm) (Wehrli, 2000). For the Cimel radiometer, the expected uncertainty of the level 2 AOD product is between 0.002 and 0.009 for reference instruments, larger for shorter wavelengths, between 0.01 and 0.02 for field instruments, and larger in the UV under the conditions of clear skies (Eck et al., 1999; Barreto et al., 2016). It should be taken into account that, in general, in the UV range the AOD uncertainty is higher (Carlund et al., 2017).

In relation to the calibration of both networks, GAW and AERONET, they use measurements at high mountain stations with very stable and low AOD over 1 d in which consecutive measurements can be performed over a wide range of optical air mass (approximately between 2 and 5) in the shortest possible time, in order to calibrate reference instruments using the Langley plot technique. In the case of AERONET-Cimel these calibrations are subsequently transferred to the field instruments of the network in other sites through regular intercomparison campaigns. In the case of the GAW-PFR, the calibration system is more complex in order to ensure traceability with the WORCC world reference. The maintenance of the AOD standard by the WORCC laboratory is described in Kazadzis et al. (2018b). It consists of a triad of instruments that measure continuously and three additional standard portable transfer radiometers located at Mauna Loa (one instrument) and Izaña (two instruments) observatories. Every 6 months, one of the portable transfer standard radiometers visits the reference triad based at PMODWRC (Davos) and compares the calibration constants defined by the 6-month Langley calibrations in the two high mountain stations (Table 1 of Kazadzis et al., 2018b) with the one defined by the triad. The comparison is based on the signals (voltages) and not on AOD values. The differences between the Izaña GAW-PFR radiometers and the reference triad have been always lower than 0.5%, being within the uncertainty of the Langley method, plus the small possible instrument degradations that can be detected in a 6–12-month period. Such degradations are

quite small and are accounted for in the calibration analysis since extraterrestrial constants are linearly interpolated between two triad visits for every 6-month period. Additionally, the Izaña GAW-PFR "field" radiometers are calibrated on a routine basis using the Langley plot technique for double-checking quality assurance. Therefore, these radiometers cannot be considered simple field instruments but as regularly calibrated radiometers with assured traceability with the WORCC triad reference.

IZO is one of the two sites of Langley plot calibration of both networks, which represents an advantage when comparing the two instruments, eliminating, to a large extent, errors caused by the calibration transfer. However, there are differences between the calibration methodologies used by both networks. AERONET obtains the calibration by means of the average of a few extraterrestrial constants (V_0) obtained from Langleys and performed over a relatively short time (the time needed to collect data from at least 10 morning Langley plots). However, PFR-related Langleys are calculated by temporal linear fit to a larger number of extraterrestrial constants, V_0, obtained from Langley plots performed over 6 months (Wehrli, 2000; Kazadzis et al., 2018a). Details of requirements for performing Langley calibrations of reference instruments by GAW-PFR and AERONET and their uncertainties are analysed in detail by Toledano et al. (2018).

4 Data and methodology used in this study

The AOD at each wavelength is obtained from the Beer– Bouguer–Lambert law (Thomason et al., 1982; WMO, 2003) for radiometers collecting spectral direct sun measurements:

$$I(\lambda) = I_0(\lambda) \exp -\tau m, \tag{1}$$

where $I(\lambda)$ is the direct sun signal at ground level at wavelength λ, $I_0(\lambda)$ is the extraterrestrial signal of the instrument corrected by the Earth–sun distance and m is the optical air mass in the measurement path (Kasten and Young, 1989). A detailed description of how AOD is obtained and the determination of extraterrestrial constants by GAW-PFR and AERONET is provided by Holben et al. (1994), Holben et al. (1998), Holben et al. (2001), Toledano et al. (2018), Wehrli (2000) and Wehrli (2008b).

4.1 GAW-PFR and AERONET-Cimel data

GAW-PFR provides AOD values every 1 min as an average of 10 sequential measurements with a total duration of less than 1 s (20 ms for each channel), then

dark current is measured, going into sleep mode until the next minute. AERONET-Cimel takes a sequence of three separate measurements (1 s per filter) in 1 min interval (each one every 30 s). This sequence of measurements is called "triplet" and it is performed every ~ 15 min for air masses lower than 2 and with higher frequency for lower solar elevations. Therefore, AERONET-Cimel provides AOD values for each triplet at least every ~ 15 min. Note that AERONET-Cimel performs AOD measurements interspersed with sky radiance measurements, whose duration varies throughout the day, and therefore the AOD measurements are not necessarily provided at full minutes. We consider the 1 min data as synchronous when GAW-PFR and AERONET-Cimel AOD data were obtained with a difference of ~ 30 s.

GAW-PFR and AERONET-Cimel instruments use the same time reference. The synchronization between the PC and GAW-PFR data logger was performed every 12 h since 2005 and improved to 6 h after 2013 using network time protocol (NTP) servers via the internet. From 2005 to 2012 the time of the AERONET-Cimel reference instruments was checked manually once a day using a handheld GPS. From 2012 onwards, the time was adjusted automatically three times a day using the ASTWIN Cimel software. In turn, the PC time is adjusted through the AEMET internal time server every 15 min. The AOD comparison has been performed using 1 min synchronous data from the four closest channels of both instruments in the period 2005–2015 (more than 70000 data pairs in each channel). Thus, in the case of GAW-PFR, the four available channels of 368, 412, 500 and 862 nm were analysed, while in the case of AERONET-Cimel only the 380, 440, 500 and 870 nm channels were considered (Table 1). For the 500 nm channel, the nominal wavelengths of the two networks differ by a maximum of 1.8 nm. However, the nominal wavelengths in the rest of the compared channels present higher differences. Therefore, the AOD values of the original GAW-PFR 368, 412 and 862 nm channels have been interpolated or extrapolated to the corresponding AERONET-Cimel channels (380, 440 and 870 nm), using the Ångström power law and the GAW-PFR AE calculated from the four PFR AOD measurements.

Synchronous AE data provided by both instruments have also been compared (see Sect. 5.5). GAW-PFR determines AE using all four PFR wavelengths (Nyeki et al., 2015), while AERONET-Cimel uses different wavelength ranges (340–440, 380–500, 440–675, 440–870 and 500–870 nm) (Eck et al., 1999). As a consequence, we have calculated a new AE for the Cimel radiometer using the four channel equivalent to those of the PFR.

In this study we have used the two versions of the AERONET database. Version 2 (V2) has been used so far in many scientific publications in high-impact journals and version 3 (V3) has been released just recently (Giles et al., 2019). In Sect. 5.1, a

comparison of V2 and V3 is presented. A total of 3 GAW-PFR and 15 AERONET-Cimel instruments have been used in this intercomparison study covering the period 2005–2015. Their corresponding reference numbers are shown in Table 2.

Table 2: GAW-PFR and AERONET-Cimel instrument numbers used in this study in the period 2005–2015. Data from reference Cimel no. 398 were not upgraded to level 2 in V3 during the period 12 July–15 September 2008.

Instruments used in this study	Period 2005-2009	Period 2010-2015
GAW-PFR	2 instruments: no. 6, no. 25	2 instruments: no. 6, no. 21
AERONET-Cimel	13 instruments: no. 25, no. 44, no. 45, no. 79, no. 117, no. 140, no. 244, no. 245, no. 380, no. 382, no. 383, no. 398, no. 421	5 instruments: no. 244, no. 347, no. 380, no. 421, no. 548

4.2 Cloud filtering

The data matching in our comparison analysis was performed with synchronous 1 min AOD values of both networks labelled with quality control (QC) flags that guarantee proven quality data not affected by the presence of clouds. In the case of the AERONET-Cimel network, the selected AOD data are level 2 data from both V2 and V3 AERONET databases, which have been cloud filtered by the Smirnov algorithm (Smirnov et al., 2000), based on the triplet method with a second-order temporal derivative constraint (McArthur et al., 2003), and visually screened in V2. The cloud screening in AERONET V3 has been completely automated and notably improved, especially by refining the triplet variability and cirrus cloud detection and removal (Giles et al., 2019). These two cloud screening methods are able to detect rapid changes in the atmosphere and remove those measurements in which AOD variability within the triplet is higher than the following criteria:

- AOD triplet variability > MAX {0.02 or 0.03×AOD} at all wavelengths (V2)

- AOD triplet variability > MAX {0.01 or 0.015×AOD} at 675, 870 and 1020 nm simultaneously (V3)

The selection of these thresholds ensures the triplet average does not exceed 0.02 (V2) or 0.01 (V3) within 1 min in the case of low AOD conditions.

GAW-PFR cloud screening algorithms also use the Smirnov triplet measurement and the second-order derivative check but add a test for optically thick clouds with $AOD_{500\ nm} > 2$ (Kazadzis et al., 2018b). In the case of the GAW-PFR network

(Wehrli, 2008a) the flags take the value 0 for cloudless conditions, no wavelength crossings and sun pointing within certain limits. More details are provided in Kazadzis et al. (2018a) for all of the selected records.

4.3 WMO traceability criteria

The criterion for traceability used in this study follows the recommendation of the WMO (WMO, 2005), which states that 95% of the AOD measurements fall within the specified acceptance limits, taking the PFR as a reference:

$$U_{95} = \pm \left(0.005 + 0.010/m\right), \tag{2}$$

where m is the optical air mass. Note that the U_{95} range is larger for smaller optical air mass. The acceptance limits proposed by WMO take into account, on the one hand, the uncertainty inherent in the calculations of the AOD and, on the other hand, the uncertainty associated with the calibration of the instrument. The latter, for the case of instruments with finite field-of-view direct transmissions, such as the PFR and the Cimel, is dominated by the influence of the top-of-the-atmosphere signal determined by Langley plot measurements, divided by the optical air mass. The first term of Eq. (2) (0.005) represents the maximum tolerance for the uncertainty due to the atmospheric parameters used for the AOD calculation (additional atmospheric trace gas corrections and Rayleigh scattering). The second term describes the calibration-related relative uncertainties. The WMO recommends an upper limit for the calibration uncertainty of 1%.

4.4 Modelling the impact of near-forward scattering on the AOD measured by the PFR and Cimel radiometers

In order to study the impact of near-forward scattering on the irradiance measured by the PFR and Cimel instruments, a forward Monte Carlo model (Barker, 1992, 1996; Räisänen et al., 2003) was employed. For the present work, the model was updated to account for the finite width of the solar disk (Räisänen and Lindfors, 2019). The starting point of each photon was selected randomly within the solar disk, assuming a disk half-width of 0.267° and the impact of limb darkening on the intensity distribution was included following Böhm-Vitense (1989). Some diagnostics were also added to keep track of the distribution of downwelling photons at the surface with respect to the angular distance from the centre of the sun. Gaseous absorption was accounted for following Freidenreich and Ramaswamy (1999), while the Rayleigh scattering optical depth was computed using Bodhaine et al. (1999).

5 Results

5.1 Comparison of long-term AERONET V2 and V3 datasets at Izaña site

Since V3 has been released recently (Giles et al., 2019), we present a comparison between V2 and V3 for the Cimel channels 380, 440, 500 and 870 nm for the period 2005–2015. The results indicate that for the Izaña site the agreement and consistency between the two AERONET versions is very high for the four channels ($R^2 > 0.999$), in full agreement with the results of the V2–V3 comparison reported by Giles et al. (2019). It follows that the results of the AOD comparison between GAW-PFR and the two versions of AERONET are very similar, as shown throughout this work. A detailed description of AERONET V3 and its improvements with respect to V2 is given in Giles et al. (2019). As such, improvements depend on aerosol type, according to the changes introduced in V3, high mountain sites such as Izaña, characterized by low background AOD values or, alternatively, by the presence of dust (no pollution or biomass burning aerosols), show that the AOD differences between V2 and V3 are expected to be minimal, as is confirmed in this study (Fig. 1).

However, it should be noted that AERONET V3 does not restrict the calculation of AOD to optical air masses lower than 5.0 (Giles et al., 2019), as V2 does. This results in an increase in the number of solar measurements occurring in the early morning and the late evening. Consequently, the GAW-PFR comparisons with AERONET V3 consisted of ~ 9000 more data pairs than the GAW-PFR comparison with V2 (see Supplement S1).

5.2 AERONET-Cimel AOD comparison with GAW-PFR data

The comparison with GAW-PFR AOD shows that the AOD from AERONET-Cimel radiometers meet the WMO traceability criteria ("traceable AOD data" from now on) at the 440, 500 and 870 nm channels. The lowest agreement is found in the UV channel (380 nm), with 92.7% of the data, and the highest in the infrared channel (870 nm), with 98.0% for V2 (Fig. 2; Table 3), because this channel is less affected by trace gas absorption. Almost identical results are obtained for V3 (Supplement S1 and S2.1). However, in the first half of the comparison period (2005–2009) there were some mechanical problems in the solar tracker that the GAW-PFR was mounted on, which caused sporadic problems in sun pointing. This finding was confirmed with data from the four-quadrant silicon detector (Wehrli, 2008a) that showed diurnal variation in the PFR sensors position up to 0.3°. From
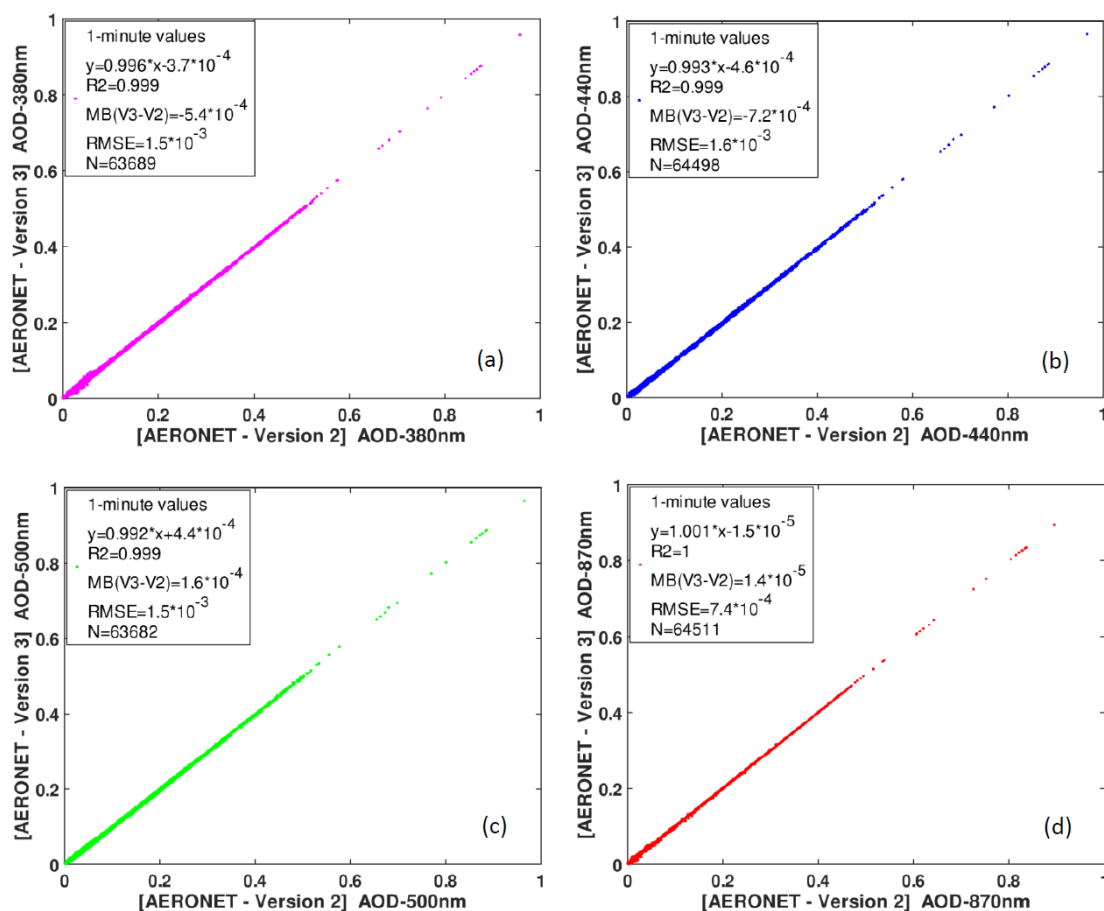
Figure 1: AERONET version 3 (V3) versus version 2 (V2) AOD 1 min data scatterplot at Izaña Observatory for the period 2005–2015: (a) 380 nm, (b) 440 nm, (c) 500 nm and (d) 870 nm. The corresponding equations of the linear fits, the coefficients of determination (R^2), mean bias (MB), root-mean-square error (RMSE) and the number of data pairs (N) used are included in each legend.

2010 onwards, the PFR was mounted on an upgraded solar tracker with higher performance and precision. This reduced problems in sun pointing, which were the main cause of most of the AOD discrepancies between PFR and Cimel, and therefore not attributable to the instruments themselves. In addition, since 2010, Cimel no. 244 has been in continuous operation (for most of the time) at the Izaña Observatory, greatly simplifying calibration procedures and the corresponding data evaluation and minimizing errors of calibration uncertainties introduced by the use of a high number of radiometers in the intercomparison. During the 2010–2015 period, the fraction of traceable AOD measurements of the total between the AERONET-Cimel radiometer and the GAW-PFR improves to 93.46% in the 380

nm channel and this percentage rises to 99.07% for the 870 nm channel. Despite the technical differences between both radiometers described above and the different calibration protocols, cloud screening, and data processing algorithms, the data series of both instruments can be considered equivalent, except for 380 nm, according to the WMO traceability criteria defined previously (Eq. 2). This explains the excellent agreement in the long-term AOD climatology shown for GAW-PFR and AERONET-Cimel in Toledano et al. (2018).
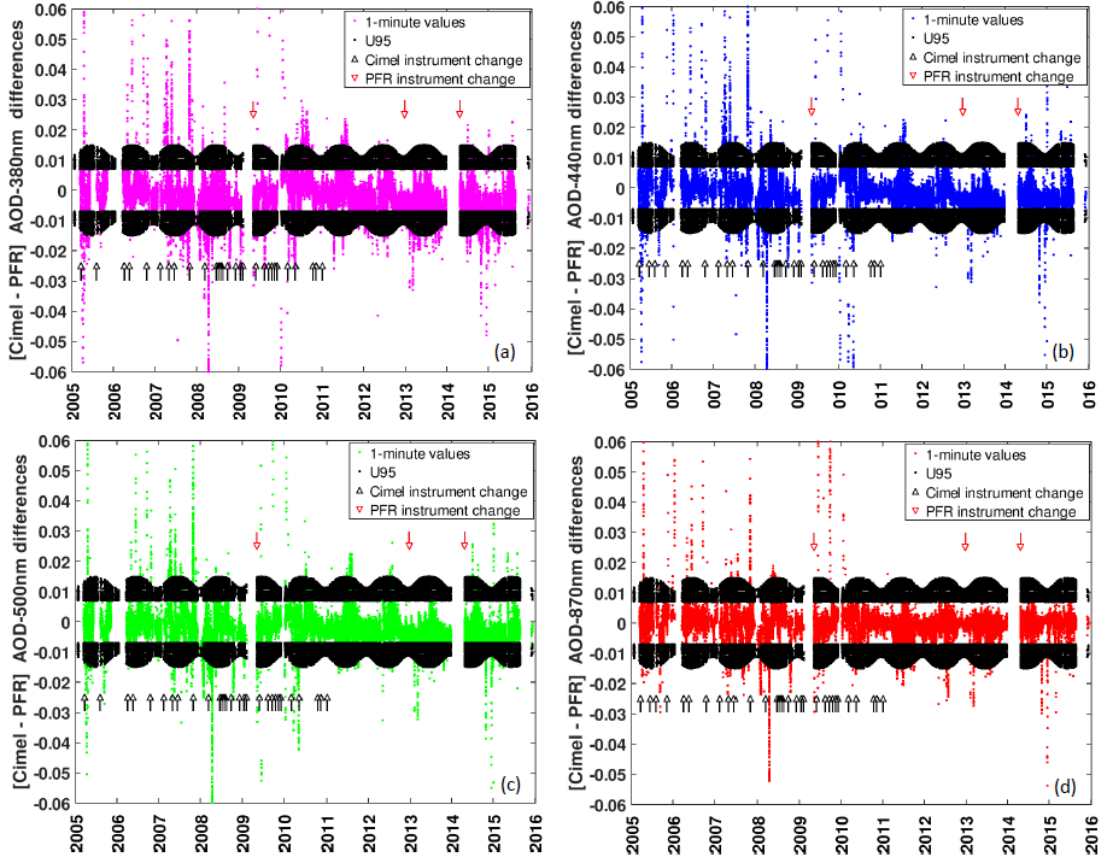
Figure 2: The 1 min AOD data differences between AERONET-Cimel (V2) and GAW-PFR for (a) 380 nm (70838 data pairs), (b) 440 nm (71645 data pairs), (c) 500 nm (70 833 data pairs) and (d) 870 nm (71660 data pairs) for the period 2005–2015. Black dots correspond to the U_{95} limits. A small number of outliers are out of the ~ 0.06 AOD difference range. Black arrows indicate a change of reference AERONET-Cimel radiometer and red arrows indicate a change of the GAW-PFR instrument.

We have compared the percentages of AERONET-Cimel AOD V2 data meeting the WMO criteria for the four interpolated GAW-PFR channels with those of AERONET V3 (Table 3). A more detailed statistical evaluation for different sce-

Table 3: Percentage of AERONET-Cimel (V2 and V3) 1 min AOD data meeting the WMO criteria for the four interpolated GAW-PFR channels for the period 2005–2015.

Channel (nm)	V2 (%)	V3 (%)
380	92.7	92.3
440	95.7	95.2
500	95.8	95.7
870	98.0	97.8

narios of aerosol loading (three ranges of AOD) and aerosol size (three ranges of AE) for each compared channel has been performed (see Table 4). We observe that the poorest agreement is obtained at the shorter wavelength channels (440 nm and especially 380 nm). Kazadzis et al. (2018b) also found a decrease in the percentage of AOD meeting the WMO criteria for 368 and 412 nm spectral bands during the Fourth WMO Filter Radiometer Comparison for aerosol optical depth measurements. As these authors pointed out, the shorter the wavelength, the poorer the agreement due to several reasons: AOD in the UV suffers from out-of-band leakage or at least different blocking of the filters, small differences in central wavelength or FWHM have a larger impact, the Rayleigh correction is more critical, and NO_2 absorptions are treated differently. Regarding the effect of the aerosol load and particle size on the AOD differences, our results confirm the decrease in agreement between the two instruments for very large particles is coincident with almost pure dust (AE $\leq$ 0.3) and high turbidity conditions (AOD$>$ 0.1). However, it should be noted that the percentage of data pairs in these situations is relatively low (e.g. 6% for AOD$>$ 0.1 and 3.2% for AE$<$ 0.25 at 380 nm) with respect to the total data (Table 4). A similar result was reported by Kim et al. (2008), who attributed these discrepancies to the possible spatial and temporal variability of aerosols under larger optical depths, in addition to the effect of the different FOV of both radiometers. In our case, and according to previous studies on AOD climatology at IZO (Barreto et al., 2014), the presence of high mineral dust burden when the station is within the SAL does not necessarily imply lower atmospheric stability conditions resulting in daily AOD means with greater standard deviation. For these reasons, we assumed that the different FOV of these instruments is the main cause of part of the AOD 1 min differences outside the U_{95} limits under high AOD conditions. This issue is specifically addressed in Sect. 5.3.

In general, the agreement obtained with the 1 min AOD data is slightly lower than that obtained during short campaigns, such as those reported by Barreto et al. (2016) at IZO (5566 data pairs), with agreement of $>$ 99% for $AOD_{870\,nm}$ and $AOD_{500\,nm}$. However, our results for $AOD_{500\,nm}$ ($>$ 95% of 70833 data pairs) are

Table 4: Percentage of AERONET-Cimel 1 min AOD data (V2) meeting the WMO criteria for the four compared channels and different AOD and AE scenarios for the period 2005–2015. The last row corresponds to the total percentages for the sub-period 2010–2015. AOD and AE traceability > 95% are marked in bold. The number of data pairs is in brackets.

Percentage of data within WMO limits	380 nm	440 nm	500 nm	870 nm
AOD≤0.05	94.4 (57008)	**96.8 (59130)**	**97.0 (58572)**	**98.5 (60191)**
0.05<AOD≤0.10	91.0 (4723)	93.1 (4850)	92.8 (4817)	94.2 (4908)
AOD>0.10	75.0 (3938)	86.5 (4615)	85.1 (4466)	**95.9 (5118)**
AE≤0.25	73.1 (2145)	82.3 (2417)	80.1 (2351)	**96.2 (2824)**
0.25<AE≤0.6	91.2 (5407)	**96.2 (5810)**	**96.0 (5691)**	**97.9 (5911)**
AE>0.6	94.6 (55114)	**96.9 (57089)**	**97.0 (56504)**	**98.7 (58146)**
Total 2005-2015	92.7 (65669)	**95.7 (68595)**	**95.8 (67855)**	**98.0 (70217)**
Total 2010-2015	93.5 (41977)	**97.4 (43745)**	**97.2 (43627)**	**99.1 (44498)**

significantly better than those observed by Kazadzis et al. (2014) (∼ 48% of 468 data pairs) covering a relatively narrow range of AOD. In addition, short-term campaigns usually cover a small range of AOD, and instruments are carefully and frequently supervised. On the contrary, during our intercomparison over a period of 11 years, the operation of the instruments can be considered the normal operation of such a system. An additional interesting aspect of this study is that it is not a simple intercomparison exercise between two instruments but a comparison of a number of instruments that acted as reference instruments for the AERONET Europe network.

In the first period (2005–2009), a total of 13 Cimel radiometers were used, while in the second period (2010–2015) 5 Cimel radiometers were used, and for much of this period Cimel no. 244 was operating as the permanent AERONET reference instrument at IZO. Once the most important causes of non-traceability in the first period, which were associated with a poor pointing of GAW-PFR due to problems in the sun tracker, were discounted, we can conclude that there are no significant differences in the percentages of traceable data between the two periods. This means that the continuous change of reference Cimel instruments used in the 2005–2009 period did not have a significant impact on AOD data comparison differences. This provides proof of the consistency and homogeneity of the long AERONET-Cimel AOD data series and their comparability with the GAW-PFR AOD data series,

regardless of the number of instruments used to generate these data series. In our study, with a number of comparison data pairs 1 or 2 orders of magnitude higher than those used in short campaigns, the results shown in Table 4 can be considered fairly good.

In addition to the traceability scores, we have introduced some basic skill scores corresponding to the AOD intercomparison between GAW-PFR and AERONET-Cimel for the period 2005–2015 (Table 5) to be in line with previous studies that have performed short-term comparisons between these two instruments. The definitions of the used skill scores can be found in Huijnen and Eskes (2012). The Pearson's correlation coefficient (r) values of the Cimel–PFR 1 min AOD data pairs are higher than 0.99 in all channels. Concerning mean bias (MB) and root-mean-square error (RMSE) associated with AOD differences, our results show quite similar skill scores to those found at Mauna Loa, USA, for $AOD_{500\ nm}$ (Kim et al., 2008), although the number of data pairs used at IZO ($\sim$ 71000) is much higher and the AOD range of our study is much larger than that of the comparison performed at Mauna Loa. Kim et al. (2008) summarize results of previous short-term intensive studies (McArthur et al., 2003; Mitchell and Forgan, 2003; Kim et al., 2005; Schmid et al., 1999) carried out at stations where the radiometers were calibrated by intercomparison with reference instruments. These results show MB values to be within 0.01 bias, 1 order of magnitude larger than at the Mauna Loa and Izaña Observatories, highlighting the importance of having well-calibrated instruments to carry out these type of comparisons. For the period 2010–2015 (not shown here), as expected, the RMSE and the Pearson's correlation improve slightly compared to the whole period 2005–2015.

Table 5: Basic skill scores from the AOD intercomparison between GAW-PFR and AERONET-Cimel V2 for the period 2005–2015. The skill score definitions are found in Huijnen and Eskes (2012).

Period	2005-2015			
Wavelengths (nm)	380	440	500	870
Mean bias (MB)	-0.0026	-0.0018	-0.0021	-0.0001
Modified normalized mean bias (MNMB)	-0.1301	-0.1046	-0.1474	0.0129
Fractional gross error (FGE)	0.1727	0.1546	0.1918	0.1837
Root-mean-square error (RMSE)	0.0081	0.0070	0.0064	0.0049
Pearson's correlation coefficient (r)	0.9910	0.9925	0.9939	0.9949
Number of data pairs	70838	71645	70833	71660

In relation to the comparison between GAW-PFR and AERONET-Cimel V3, we have calculated the percentage of AERONET-Cimel 1 min AOD data (V3) meeting the WMO criteria for optical air mass > 5.0 for the period 2005–2015 (Supplement

S2.2). The results are somewhat poorer than for optical air mass < 5.0, since the solar elevation is very low. Only for the 870 nm channel does 95% of the data meet with the WMO criteria, although the percentages of data in the 440 and 500 nm channels are close to this value. This would be the main reason to find slightly poorer traceability results with all V3 data compared to those found with V2 for which the AOD data are limited to optical air mass < 5.0.

5.3 Non-traceability assessment

As presented in Table 3, data outside the WMO traceability criteria vary from 2% for 870 nm up to 7.3% for 380 nm. In this section, the different possible causes of non-traceability in AOD are evaluated and, if possible, quantitatively estimated. In order to assess the relevance and quantitative impact of these causes and estimate errors derived from a nonperfect AOD data synchronization, we first made an analysis on the natural variability of AOD in a very short time period (1 min) shown below.

5.3.1 Short-term AOD variability

In order to determine the variability of AOD within 1 min, we have performed two independent analyses with AOD data from the PFR (at 368 and 501 nm) and Cimel (at 380 and 500 nm) channels during 1 year (2013). On the one hand, and taking into account that GAW-PFR provides AOD every minute, we have calculated all the AOD differences for each channel in the successive minutes. So we have the variation in AOD from 1 min to the next one during a whole year. On the other hand, for AERONET-Cimel, we have taken advantage of the triplets, since each triplet consists of three successive measurements made in 1 min. In this case, the strategy has been to calculate the standard deviation of the triplet AOD measurements during a whole year.

The results obtained of the AOD variability in 1 min from PFR data are very similar and consistent to those obtained with Cimel. Less than $\sim 0.8\%$ of the AOD data show variability higher than 0.005 in all wavelength ranges. It should be noted that the possible instrumental noise is included in this variability, so that the actual natural AOD variability would be, in any case, lower than that expressed in Table 6. The percentage of data with 1 min AOD variability for all four GAW-PFR channels is given in Supplement S3.1.

We have also determined the percentage of 1 min AOD data from the Cimel triplets (from 2013), whose diurnal range of variation is $\text{AOD}_{\text{max}} - \text{AOD}_{\text{min}} > 0.015$,

Table 6: Percentage of AOD data with variability within 1 min of less than 0.01 and 0.005, using AOD data from GAW-PFR (at 368 and 501 nm) and AERONET-Cimel (at 380 and 500 nm), respectively, for 2013. A total of $\sim$ 32000 data pairs per channel have been used from GAW-PFR and 20117 triplets (60351 individual AOD measurements) from Cimel no. 244 have been used to calculate the AOD variability.

GAW-PFR		
Percentage of data with 1 min AOD variability (%)		
	368 nm	501 nm
<0.01	99.8	99.91
<0.005	99.21	99.35
AERONET-Cimel		
Percentage of data with 1 min AOD variability (%)		
	380 nm	500 nm
<0.01	99.87	99.99
<0.005	99.82	99.42

for several AOD intervals. Note that this value is half of the WMO traceability interval when m = 1 (maximum possible interval) (see Eq. 2). The results shown in Supplement S3.2 indicate that the 1 min AOD variability is responsible for only 0.11% (0.01%) of 1 min Cimel AOD values outside the WMO limits in the [0–0.03] AOD range (pristine conditions) for 380 nm (500 nm). The AOD variability maximizes in the 0.1–1 AOD range causing 2.31% and 1.69% of the AOD data outside WMO limits for 380 and 500 nm, respectively. This last scenario corresponds, as expected, to changes of air masses, such as transitions from pristine to dusty conditions and vice versa, or to the sharp onset and disappearance of very sporadic biomass burning plumes. In any case, the AOD data with 1 min variability exceeding 0.02 (V2) or 0.01 (V3) are filtered by AERONET (see Sect. 4.2) and therefore are not included in the GAW-PFR and AERONET-Cimel comparison.

These results indicate that the natural AOD variability is very low, thus the non-ideal measurement synchronization cannot explain the percentages of non-traceable AOD cases shown in Tables 3 and 4.

5.3.2 Uncertainties of GAW-PFR channel interpolation to AERONET-Cimel channels

The interpolation of the CIMEL AODs to the PFR AOD wavelengths can be one of the sources of uncertainty in this comparison assessment. The greatest uncertainty arises in the extrapolation of the $AOD_{412\,nm}$ of the PFR to the Cimel wavelength

440 nm. Using the Ångström formula we have calculated that for an uncertainty of $\pm$ 0.5 in the AE the introduced uncertainty in the AOD extrapolation from 412 to 440 nm is $\sim$ 5% (i.e. 0.005 for $AOD_{412\ nm} = 0.1$). The introduced uncertainty in AOD extrapolation is reduced to $\sim$ 2% for an uncertainty of ±0.3 in AE. For all other AOD interpolations the errors are smaller.

5.3.3 Calibration-related errors

As described in Sect. 3, the calibration procedures of the AERONET-Cimel and GAW-PFR radiometers are different. While in the case of GAW-PFR frequent calibrations are established throughout the year and the calibration value is linearly interpolated in time, in AERONET-Cimel a constant calibration value is assumed in the intermediate period between two consecutive calibrations carried out on an annual basis. The typical calibration uncertainty for a single Langley plot is 0.7%-0.9% (at the 95% confidence level) and it is reduced to 0.4% in the case of IZO when averaging at least 10 Langley-derived extraterrestrial constants (which is the normal procedure) (Toledano et al., 2018). Regarding the GAW-PFR radiometers operated at IZO, a direct yearly comparison of the Langley-based V_0 with the reference triad at PMOD-WRC showed differences lower than 1% for all channels for the 2005–2015 period.

An insufficiently accurate determination of the calibration constant results in a fictitious AOD diurnal evolution presenting a concave or convex characteristic curve due to the calibration error dependence on solar air mass. The largest error occurs in the middle part of the day (lower air masses), mainly on clean days with very low aerosol load (< 0.02 in 500 nm), as reported by Romero and Cuevas (2002) and Cachorro et al. (2004) and can be derived from Eq. (2). According to Cachorro et al. (2004, 2008), fictitious differences of up to 0.06 between the minimum and the maximum AOD can be recorded in a day with constant AOD as a result of a non-accurate calibration or non-cleaned instruments. However, these fictitious differences in AOD depend on the related calibration magnitude errors.

We have represented the AOD differences between GAW-PFR and AERONET-Cimel versus optical air mass for the four channels for pristine conditions ($AOD_{500\ nm} \leq 0.03$) for both V2 and V3 (see Supplement S4). It should be noted that although the few outliers are evenly distributed throughout the whole air mass range, they are not equally distributed with respect to the zero of the AOD difference, but there is a bias with positive large outliers (higher Cimel AOD), already reported by Nyeki et al. (2013), and small negative outliers for optical air mass lower than 2.
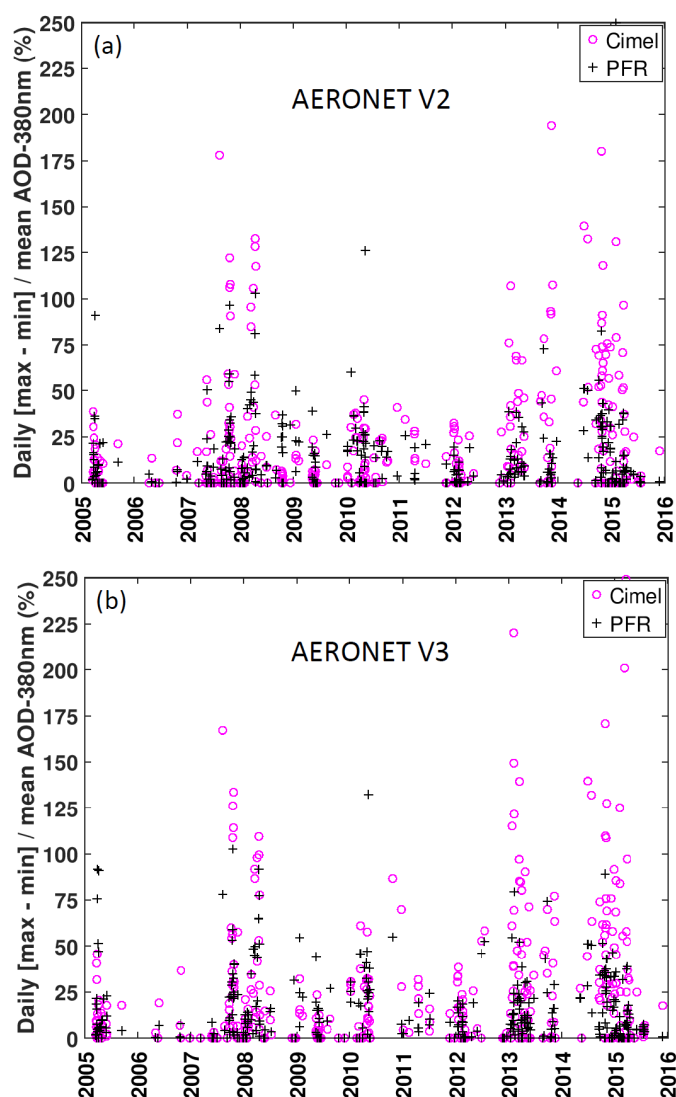
Figure 3: AOD diurnal range variation (maximum value minus minimum value of AOD in 1 d) at 380 nm corresponding to AOD outliers (non-traceable AOD) under pristine conditions (AODCimel-500 nm $\leq$ 0.03) in the period 2005–2015 for AERONET V2 **(a)** and V3 **(b)**.

The total percentage of AOD traceable data pairs under pristine conditions (AOD$_{500\ nm}$ $\leq$ 0.03) is very high for all wavelengths ($> 97.7\%$) falling within the U$_{95}$ limits (Table 7), except for 380 nm. There is no dependence on 1 min AOD differences with optical air mass for 440, 500 and 870 nm and a slight dependence for 380 nm (Table 7) with a higher percentage of AOD differences outside the U$_{95}$ limits at lower optical air masses. For the extended range of optical air mass > 5 in V3, the

AOD differences do not increase with optical air mass (Supplement S5). The lower traceability at 380 nm for low air masses is especially clear in V3, with 92.9% of traceable data (see Supplement S5). This result is consistent with the fact that the highest uncertainty in the determination of the calibration constants is observed in the UV range and the lowest uncertainty in the near-infrared channel (Eck et al., 1999; Jarosławski et al., 2003; Toledano et al., 2018). This is attributable to an imperfect calibration or to very small changes in the filters' transmittance, which can only be detectable in extreme conditions: UV range, very low optical air mass and pristine conditions. According to Toledano et al. (2018), the greatest variance in the extraterrestrial constant in the UV channel could be due to a number of factors: (1) higher AOD variability at the shorter wavelengths, (2) filter blocking issues or (3) temperature effects affecting AERONET-Cimel instruments that have not been accounted for in the UV range.

Table 7: Percentage of 1 min AOD data (V2) meeting the WMO criteria for each wavelength for different optical air mass intervals under pristine conditions (AOD$_{500\ nm}$ ≤ 0.03) in the period 2005–2015. See Supplement S5 for equivalent results with V3.

Percentage of AOD differences within the U$_{95}$ limits	Total	1 ≤ m < 2	2 ≤ m < 3	3 ≤ m < 4	4 ≤ m < 5
AOD$_{500\ nm}$ ≤ 0.03	(%)	(%)	(%)	(%)	(%)
380 nm	95.8	94.5	96.0	97.4	97.2
440 nm	97.9	97.9	97.7	98.2	97.7
500 nm	98.3	98.4	98.1	98.6	98.4
870 nm	99.2	99.4	99.3	99.2	98.6

The correct cause attribution of each outlier would require manual inspection and additional specific information on instrumental checking and maintenance information that is not always available. We have investigated in more detail the origin of the outliers and whether one of the two instruments predominantly caused them. Thus, we have calculated for the non-traceable AOD data the diurnal range of AOD variation (maximum value minus minimum value of AOD over 1d) at 380 nm for each instrument under pristine conditions (Fig. 3), using Cimel AOD$_{500\ nm}$ daily mean < 0.03 to select the pristine days. According to this approach, the instrument that shows the highest daytime AOD range is the one that is responsible for the outlier. As the wavelength increases, both the number of outliers and the magnitude thereof decreases significantly (Supplement S6). Then, we identified those outliers with a diurnal AOD range higher than 25% of the mean daily AOD value and investigated their possible causes. A total of 51 cases for GAW-PFR and 81 cases for AERONET Cimel V3 were obtained and analysed in detail, using auxiliary

information, such as 1 min in situ meteorological data, 5 min all-sky images, 1 min BSRN data and satellite imagery (not shown here). We obtained the percentage of AOD outliers of GAW-PFR and AERONET Cimel (V3) for which a certain cause has been identified, such as calibration uncertainties, cloud screening algorithm failures, mixture of the two previous causes, poor sun pointing or poorly defined causes (electronic problems, humidity inside the lenses, filter dirtiness, obstruction of the lenses collimators, insects on the optics outside, etc.) (see Supplement S7).

From the analysis of these cases, under the conditions described above, it should be noted that $\sim 44\%$ of the cases with fictitious AOD diurnal cycles were due to small uncertainties in the calibration of AERONET-Cimel (V3), while for this same cause $\sim 8\%$ of cases were identified in GAW-PFR. Some examples of AOD non-traceability for both AERONET-Cimel and GAW-PFR in the ~ 380 nm channel are shown in Supplement S8. The fictitious diurnal AOD cycle is mainly visible in the UV channels, as shown in the examples reported in Supplement S9, where the convex or concave diurnal AOD curvature symmetrical at noon provides a hint of calibration inaccuracies. Note that the fictitious diurnal AOD can be more easily identified under very low AOD conditions. We should emphasize that the rare finding of small calibration inaccuracies in a high mountain site with pristine skies and a stable atmosphere does not detract from the quality of any instrument as they often measure near or below the detection limit. Simply, these small inaccuracies are the result of limitations in the photometric measurement technique.

5.3.4 Differences in cloud screening and sun tracking

We have examined the effect that the presence of clouds might have on AOD differences and the percentage of cases outside the U_{95} limits. The impact of clouds on AOD differences only occurs when both GAW-PFR and AERONET-Cimel cloud screening algorithms fail to identify clouds in the direct sun path. In order to assess the impact that cloud conditions might cause on AOD traceability, we have used the concept of daily fractions of clear sky (FCS), which has been applied before to solar radiation data at IZO (García et al., 2014). FCS represents the percentage of observed sunshine hours in a day with respect to the maximum possible sunshine hours in that day. The higher the daily FCS, the higher the clear sky percentage we have on that day. The percentages of traceable and non-traceable AOD data versus FCS values grouped into five intervals are shown in Table 8.

It should be emphasized that the number of cases linked with FCS between 0% and 60% are less than 2% of the total cases. As the fraction of clear sky increases, the percentage of traceable AOD data significantly exceeds the number of non-traceable AOD data. The percentage of traceable data is especially large ($> 90\%$)

Table 8: Percentage of AOD data within the U_{95} limits for each channel and five daily fractions of clear sky (FCS) intervals. In brackets, the relative frequency of each FCS interval is given for AERONET V2 and V3, respectively. In bold are the percentages of V3 that are greater than those of V2.

	380 nm		440 nm		500 nm		870 nm	
	V2	V3	V2	V3	V2	V3	V2	V3
$0\% \leq$ FCS $< 20\%$ (0.03%) (0.04%)	47.6	44.4	43.5	44.4	47.6	44.4	87.0	**92.6**
$20\% \leq$ FCS $< 40\%$ (0.22%) (0.22%)	69.3	**76.6**	73.3	**82.2**	73.6	**80.8**	86.3	**94.1**
$40\% \leq$ FCS $< 60\%$ (1.08%) (1.09%)	79.1	77.5	87.8	84.8	88.8	87.2	91.9	**92.0**
$60\% \leq$ FCS $< 80\%$ (7.10%) (7.17%)	88.4	**89.6**	93.9	93.9	93.4	**94.4**	97.8	97.6
FCS $\geq 80\%$ (91.6%) (91.5%)	93.3	92.8	96.2	95.6	96.2	96.1	98.3	98.1

when FCS> 80% (almost clear skies).

This is the FCS range in which a significant percentage of days with cases presenting scattered clouds are recorded, which qualitatively confirms that V3 has introduced more efficient cloud screening than V2. However, the real impact of clouds on AOD traceability at IZO is very low due to its special characteristics as a high mountain station with very little cloudiness. Therefore, in practice, the possible impact of clouds on the non-traceability of AOD data pairs is insignificant at IZO. GAW-PFR and AERONET-Cimel cloud screening algorithms provide successful identification of clear direct sun conditions during cloudy skies (FCS< 40%) for 99.75% of the cases, excluding those with very thin clouds.

In the particular case of Izaña, there are two specific cloud scenarios in which cloud screening algorithms could fail, resulting in non-AOD traceability: (1) cirrus clouds (see Supplement S10) and (2) low clouds (stratocumulus), which sometimes exceed the observatory height level (see Supplement S11). As can be deduced from the analysis of these cloud cases, the impact of the different types of clouds on AOD retrieval is very complex and further specific investigations are required in order to understand the reasons behind failures in the GAW-PFR and AERONET-Cimel cloud screening algorithms.

5.3.5 Rayleigh scattering, absorption by O$_3$ and NO$_2$

In this section, we evaluate the possible impact on the 1 min AOD data outside the U$_{95}$ limits due to the different processing of each network regarding the correction by Rayleigh scattering and by the light absorption of column O$_3$ and NO$_2$. Although GAW-PFR and AERONET-Cimel use spectral channels with weak absorption by atmospheric gases, AOD can only be determined if optical depth contributions from those gases are well estimated and subtracted from the total optical depth (τ). GAW-PFR and AERONET-Cimel separate the contributions of the molecules (Rayleigh scattering, τ_R), aerosols (τ_a, in this study referred to as AOD) and absorbing gases, i.e. total column ozone (τ_{O_3}) and nitrogen dioxide (τ_{NO_2}), due to their different optical air masses at low solar elevation:

$$I(\lambda) = I_0(\lambda) \exp -(\tau_R m_R + \tau_a m_a + \tau_{O_3} m_{O_3} + \tau_{NO_2} m_{NO_2}). \tag{3}$$

Thus, AOD can be derived as follows:

$$AOD = \frac{1}{m_a} \left(\ln \frac{I_0(\lambda)}{I(\lambda)} - \tau_R m_R - \tau_{O_3} m_{O_3} - \tau_{NO_2} m_{NO_2} \right). \tag{4}$$

Rayleigh scattering

The Rayleigh-scattering contribution to total optical depth would be as follows:

$$\tau_R = \delta_R \frac{m_R}{m_a}, \tag{5}$$

where m$_R$ is written, according to Kasten and Young (1989), as follows:

$$m_R = \frac{1}{\sin \theta + 0.50572(\theta + 6.07995)^{(-1.6364)}}, \tag{6}$$

and m$_a$, according to Kasten (1966), has the following expression:

$$m_a = \frac{1}{\sin \theta + 0.0548(\theta + 2.65)^{(-1.452)}}, \tag{7}$$

where θ is the sun elevation and δ_R can be expressed as follows (Bodhaine et al., 1999):
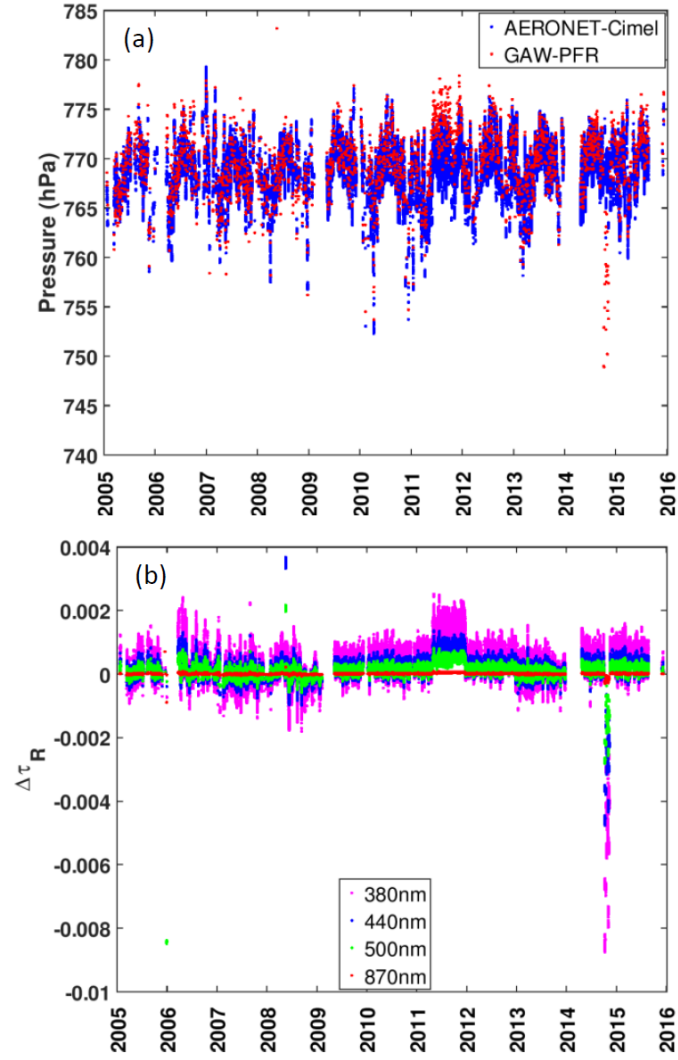
Figure 4: **(a)** The 1 min pressure data (hPa) from GAW-PFR and 6 h pressure data at Izaña Observatory from the National Centers for Environmental Prediction (NCEP) and the National Center for Atmospheric Research (NCAR) reanalysis for the case of AERONET-Cimel and **(b)** corresponding 1 min $\Delta\tau_R$ caused by pressure differences in the period 2005–2015.

$$\delta_R(\lambda) = 0.00864\lambda^{-(3.916+0.074\lambda+\frac{0.050}{\lambda})}\frac{P}{P_0},\tag{8}$$

where $P_0 = 1013.25$ hPa, λ is the wavelength in microns (μ) and P is the pressure in hPa at the measurement site. The depolarization factor recommended by (Young, 1980) is already included in Eq. (8). From Eq. (8), we can derive the differences in

τ_R contribution as follows ($\Delta\tau_R$):

$$\Delta\tau_R = \left(0.00864\lambda^{-\left(3.916+0.074\lambda+\frac{0.050}{\lambda}\right)}\frac{1}{1013.25}\frac{m_R}{m_a}\right)(P_{PFR} - P_{Cimel}). \qquad (9)$$

Accordingly, the main τ_R from GAW-PFR and AERONET-Cimel can arise from the different way the two instruments obtain atmospheric pressure (P_{PFR} and P_{Cimel}, respectively). While AERONET-Cimel obtains the site station pressure from the National Centers for Environmental Prediction (NCEP) and the National Center for Atmospheric Research (NCAR) reanalysis at standard levels, GAW-PFR has a solidstate pressure transducer in the control box to read barometric pressure simultaneously with each PFR measurement. As Giles et al. (2019) have stated, the expected error in the station pressure P_{Cimel} is generally < 2 hPa, provided the elevation of the station is well known and the weather conditions are stable. In order to assess this possible difference, we have compared the 1 min synchronous pressure data of both instruments and the corresponding 1 min $\Delta\tau_R$ from Eq. (9). Note that, in practice, this comparison is performed at 6 h intervals since the NCEP–NCAR reanalysis data are available routinely with this temporal resolution (Kalnay et al., 1996). The results are depicted in Fig. 4.

The results indicate that most of the 1 min pressure differences are within ±5 hPa (Fig. 4a), resulting in 1 min $\Delta\tau_R$ data within ± 0.001. However, when pressure differences are significantly higher, such as those registered at the end of 2014 (> 30 hPa) (Fig. 4a), $\Delta\tau_R$ increases significantly ($\sim$ 0.01) (Fig. 4b). However, it should be noted that only 99 AOD data pairs have been registered for which the pressure difference between PFR and Cimel is greater than 20 hPa at 870 and 440 nm and one AOD data pair at 500 and 380 nm channels. Taking into account that the accuracy of the new barometers built into new radiometers is $\sim$ 3 hPa, only dramatic barometer malfunctioning could cause τ_R > 0.01. As stated by Kazadzis et al. (2018b), the use of erroneous pressure values can lead to wavelength-dependent AOD errors and to large errors in AE. However, these flagrant barometer malfunctions are quickly detected and easily corrected if there are other pressure measurements at the station, as is the case at Izaña.

Differences in O3 absorption

The O_3 optical depth is determined with the following expression:

$$\tau_{O_3}(\lambda) = \sigma_{O_3}(\lambda)\frac{O_3}{1000}\frac{m_{O_3}}{m_a}, \qquad (10)$$

where O_3 is expressed in Dobson units (DU) and the absorption coefficients ($\sigma_{O_3}(\lambda)$) take the following values (Gueymard, 1995): 0.0026 cm^{-1} (440 nm), 0.03150 cm^{-1} (500 nm) and 0.00133 cm^{-1} (870 nm). The ozone absorption is at a maximum in the 500 nm channel and zero in the 380 nm channel. GAW-PFR uses for m_{O_3} the following expression (Komhyr, 1980):

$$m_{O_3} = \frac{R + h}{\sqrt{(R + h)^2 - (R + r)^2 (\cos\theta)^2}},$$ (11)

where R = 6370 km is the mean radius of the Earth, r = 2.370 km is the altitude of the station, h = 22 km is the estimated height of the ozone layer and θ is the solar elevation. However, AERONET-Cimel uses an updated expression (Komhyr et al., 1989) in which h is not fixed and takes a value in function of the latitude and the absorption coefficients are obtained for each particular filter using the spectral response provided by the manufacturer.

For most of the period covered in this study, measured total ozone values from the GAW Izaña station were used to calculate τ_{O_3} (Wehrli, 2008a). If no Brewer data is available, data retrieved from the Total Ozone Mapping Spectrometer (TOMS) satellite sensor was used. Nowadays, GAWPFR uses ozone data from AURA satellite overpass observations with the Ozone Monitoring Instrument (OMI) (McPeters et al., 2015) for daily operations (Kazadzis et al., 2018b). Concerning AERONET-Cimel V2, a NASA TOMS 1°×1.25° resolution O_3 climatology is used. From Eq. (10), the differences in O_3 optical depth $\Delta\tau_{O_3}$ can be derived as follows:

$$\Delta\tau_{O_3} = \sigma_{O_3}(\lambda) \frac{1}{1000} \frac{m_{O_3}(O_{3PFR} - O_{3Cimel})}{m_a}.$$ (12)

The largest influence of total ozone data uncertainty in τ_{O_3} occurs at 500 nm (Fig. 5). According to Wehrli (2008b) and Kazadzis et al. (2018b), total ozone needs to be determined to ±30 DU or 10% of typical values to ensure an uncertainty of ~ 0.001 in τ_{O_3} at 500 nm. In the case of the GAW-PFR– AERONET-Cimel comparison and due to the very different method in which both networks obtained O_3 values for their corresponding corrections, the ozone differences found on some days (1761 out of 71965 d; 2.4%) are very large (> 40 DU), exceeding a difference in the ozone optical depth of 0.001. Even so, the potential contribution to AOD differences outside the U_{95} limits between the two networks is negligible. Total O_3 over IZO shows a relatively small amplitude throughout the year but both surface ozone concentrations and column ozone amounts could sharply increase under the influence of cut-off lows injecting air from the high mid-troposphere into the lower subtropical troposphere, which is not uncommon in spring and the first
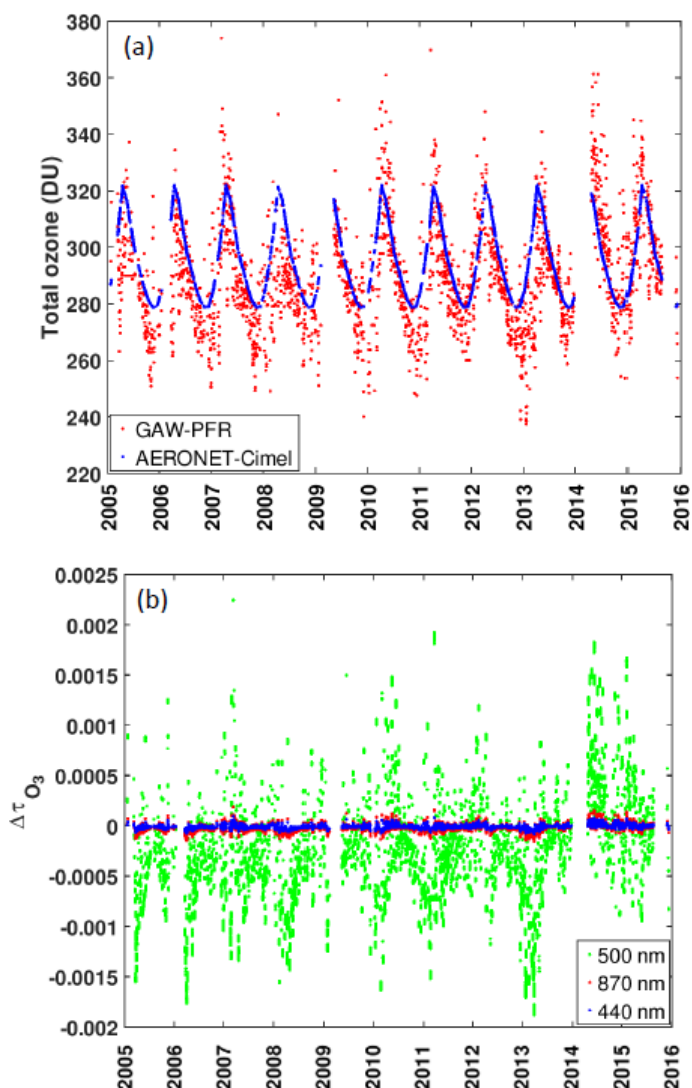
Figure 5: **(a)** Total O_3 used by GAW-PFR (measured Brewer O_3 values from IZO, OMI O_3 overpass or Brewer O3 climatology) and AERONET-Cimel (TOMS O_3 climatology) and **(b)** $\Delta\tau_{O_3}(\lambda)$ caused by differences in daily total O3 between the two instruments in the period 2005–2015.

half of summer (Cuevas et al., 2015; Kentarchos et al., 2000). In addition, the upper and middle troposphere could be enriched in ozone through exchange processes in the upper troposphere–lower stratosphere (UTLS) due to the presence of the subtropical jet (mainly from February to April) (Rodriguez-Franco and Cuevas, 2013). However, if we wanted to repeat this traceability study of 1 min AOD data at middle- or high-latitude stations where sharp O_3 variations (several tens of DU) could be registered in a few hours, the correction of 1 min AOD measurements by

τ_{O_3} might be a challenging issue.

Differences in NO2 absorption

AERONET-Cimel applies a correction by absorption of NO_2, but GAW-PFR does not include this correction. AERONET-Cimel V2 obtains daily total NO_2 data from a $0.25° \times 0.25°$ resolution NO_2 monthly climatology obtained from the ESA Scanning Imaging Absorption SpectroMeter for Atmospheric CHartographY (SCIA-MACHY) (Eskes and Boersma, 2003). AERONET-Cimel V3 uses a geographic and temporally dependent multiyear monthly climatology from the Ozone Monitoring Instrument (OMI) NO_2 concentration (Giles et al., 2019). In order to assess the contribution to AERONET-Cimel 1 min AOD data non-traceability by NO_2 absorption, we have to estimate the NO_2 optical depth ($\tau_{NO_2}(\lambda)$) of AERONET-Cimel since GAW-PFR does not perform this correction. Analogous to $\Delta\tau_{O_3}$, the differences in nitrogen dioxide optical depth 1 $\Delta\tau_{NO_2}$ can be obtained from the following equation:

$$\Delta\tau_{NO_2} = \sigma_{NO_2}(\lambda)\frac{1}{1000}\frac{m_{NO_2}}{m_a}(-NO_{2Cimel}), \qquad (13)$$

where m_a is given by Eq. (7), NO_{2Cimel} (DU) is the daily total NO_2 used by AERONET-Cimel and $\sigma_{NO_2}(\lambda)$ is the NO_2 absorption (Gueymard, 1995) weighted by the specific filter response: 15.6 cm⁻¹ (380 nm), 12.3 cm⁻¹ (440 nm) and 4.62 cm⁻¹ (500 nm). Finally m_{NO_2} has the following expression (Gueymard, 1995):

$$m_{NO_2} = \frac{1}{\sin\theta + 602.30(90 - \theta)^{0.5}(27.96 + \theta)^{-3.4536}}. \qquad (14)$$

In Fig. 6a the total NO_2 used by AERONET-Cimel to evaluate $\sigma_{NO_2}(\lambda)$ is depicted. Figure 6b shows the $\Delta\tau_{NO_2}$ caused by differences in daily total NO_2 between GAW-PFR and AERONET-Cimel. $\Delta\tau_{NO_2}$ is of the order of 10^{-3} for the 380 and 440 nm channels, while for the 500 nm channel it is of the order of 10^{-4}. However, it should be noted that an impact on AOD calculation is expected when replicating similar analysis in highly NO_2 polluted regions. Such cases include large industrial cities from East Asia and Central and Eastern Europe (e.g. Chubarova et al., 2016).

Taking into account the corrections for Rayleigh scattering and for the absorptions by O_3 and NO_2, we have calculated the additional traceable AOD data (Table 9). This percentage is at a maximum at 380 nm with 1.3% (V2) and 1.7% (V3) of the whole dataset. The 870 nm channel is only affected by the Rayleigh correction
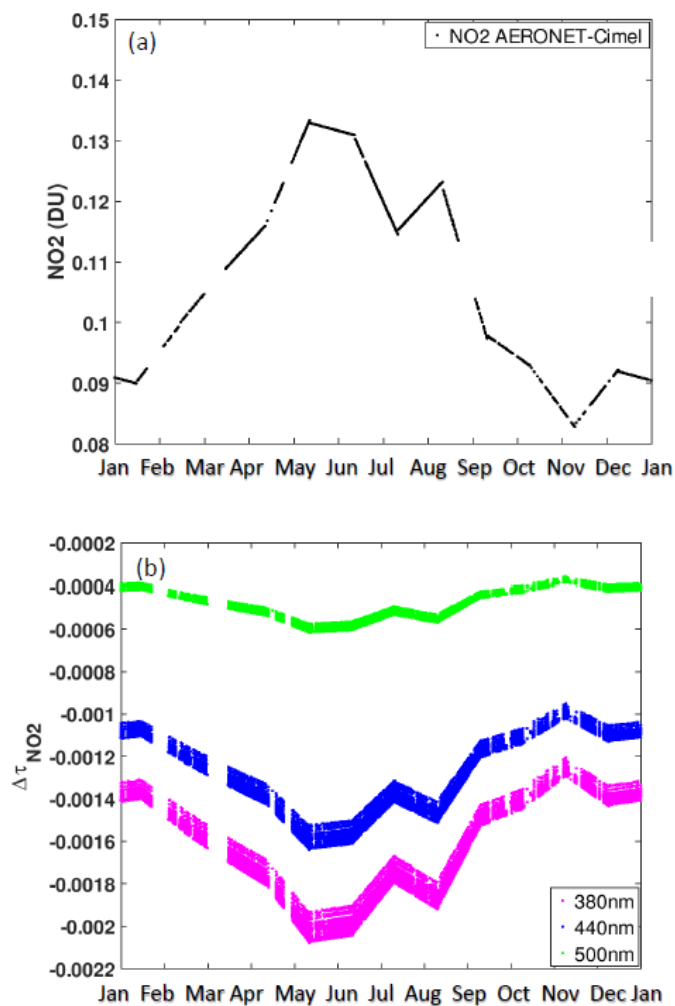
Figure 6: **(a)** NO$_2$ monthly climatology obtained from the ESA SCanning Imaging Absorption SpectroMeter for Atmospheric CHartographY (SCIAMACHY), used by AERONET-Cimel at IZO, and **(b)** $\Delta\tau_{NO_2}$ caused by differences in daily total NO$_2$ between GAW-PFR and AERONET-Cimel in the period 2005–2015. Note that GAW-PFR does not take into account the correction for the NO2 absorption.

component, and therefore the increment of traceable data after the mentioned corrections is minimal.

Table 9: Percentage (%) of additional traceable AERONET-Cimel AOD 1 min data (V2 and V3) after correcting for pressure and total column O_3 and NO_2 for the period 2005–2015.

	Increment (%) of traceable AOD data after P, O_3 and NO_2 corrections	
Channel	V2	V3
380 nm	1.3	1.7
440 nm	0.2	0.3
500 nm	0.3	0.1
870 nm	~ 0.0	~ 0.1

5.4 GAW PFR and AERONET-Cimel comparison under high AOD conditions: the impact of dust forward scattering for different FOVs

When we present the AOD differences between AERONET-Cimel and GAW-PFR versus AOD (GAW-PFR) for AOD > 0.1 (dusty conditions), we note that AERONET-Cimel shows slightly higher AOD values than GAW-PFR (Fig. 7). Similar results for V3 are shown in S12. In fact, the percentage of data outside the U_{95} limits increases as AOD increases (Table 10), thus for dust-related aerosol conditions ($AOD_{500 \, nm} > 0.3$) the percentage of AOD data outside the U_{95} limits is > 50% for 380 and 440 nm (Table 10, percentages in brackets). Similar results are found when using AERONET V3 (see Supplement S13). Taking into account the number of data compared with the total cases, these results show a small but non-negligible percentage of AOD differences outside the U_{95} limits for AOD > 0.1, ranging from $\sim 0.3\%$ at 870 to $\sim 1.9\%$ at 380 nm (Table 10).

Table 10: Percentage of AERONET V2 AOD data outside the U_{95} limits at 380, 440, 500 and 870 nm channels and for three $AOD_{500 \, nm}$ thresholds with respect to all data and with respect to all data for each AOD interval (in brackets).

	Percentage of AOD data outside the U_{95} limits (%)		
	$AOD_{500nm} > 0.1$	$AOD_{500nm} > 0.2$	$AOD_{500 \, nm} > 0.3$
380 nm	1.9 (25.0)	1.2 (47.2)	0.5 (59.8)
440 nm	1.0 (13.5)	0.8 (32.0)	0.5 (57.6)
500 nm	0.6 (8.0)	0.5 (18.7)	0.3 (39.3)
870 nm	0.3 (4.1)	0.2 (6.4)	0.1 (14.0)

Aerosol forward scattering within the FOV of various instruments and calculated AOD was investigated some decades ago by Grassl (1971), who determined that at AOD = 1 and the circumsolar radiation increases the incoming radiation by > 10%. Russell et al. (2004), using dust and marine aerosols data, quantified the effect of

diffuse light for common sun photometer FOV. They reported that the correction to AOD is negligible ($< 1\%$ of AOD) for sun photometers with narrow FOV ($< 2°$), which is greater than the Cimel FOV and slightly smaller than the PFR FOV ($2.5°$). Sinyuk et al. (2012) assessed the impact of the forward-scattering aerosol on the uncertainty of the AERONET AOD, concluding that only dust aerosol with high AOD and low solar elevation could cause a significant bias in AOD (> 0.01).

GAW-PFR has double the FOV ($2.5°$; Wehrli, 2000) compared to the AERONET-Cimel ($1.3°\pm4.8\%$; Torres et al., 2013), so it is reasonable to expect that it is more affected by the circumsolar radiation than the AERONET-Cimel radiometer. Taking advantage of the fact that Saharan dust intrusions regularly affect IZO, we provide a detailed analysis on the impact that dust forward scattering causes on the AOD retrieval of the two radiometers with different FOV, explaining the AOD differences under moderate-to-high dust load (AOD > 0.1) conditions. For this purpose we have used a forward Monte Carlo model (see Sect. 4.4) with which we perform simulations that include accurate dust aerosol near-forward-scattering effects.

Dust aerosol single-scattering properties were computed using Mie theory, assuming a refractive index of $1.47+0.0025i$ at the wavelengths of 380, 440 and 500 nm and $1.46+0.012i$ at 870 nm, based on AERONET measurements at IZO. Seven values of aerosol effective radius (r_e) in the range 0.2 to 3.0 μm were considered and a lognormal size distribution with a geometric standard deviation of 2 was assumed. A middle-latitude summer atmospheric profile starting from the Izaña altitude (2.4 km a.s.l.) was assumed, with the aerosol layer located at 5–6 km a.s.l. (typical of summertime). A spectrally uniform surface albedo of 0.11 was employed. Computations were performed for nine AOD values (AOD = 0, 0.1, 0.2, 0.3, 0.4, 0.5, 0.6, 0.8 and 1.0) and for five solar elevation angles (θ = 80, 60, 45, 30 and 20°). The Monte Carlo model assumes a plane-parallel atmosphere, so the air mass factor is $m = 1/\sin\theta$. A total of 10 million photons were used for each case and wavelength.

Supplement S14 shows the ratio of scattered to direct radiation for cases with AOD up to 0.5. The ratio increases with increasing r_e, as the aerosol forward-scattering peak grows stronger. In the case of Saharan dust intrusions at IZO, the median re determined from both AERONET data inversion and the in situ aerodynamic particle sizer (APS) analyser is ~ 1.5 μm. This value agrees with the dust size distribution found during SAMUM-2 during long-range transport regime (Weinzierl et al., 2011). For this particle size, the ratio of scattered to direct radiation is ~ 3 times larger for FOV of $2.5°$ than FOV of $1.3°$.

The error in the retrieved AOD due to scattered radiation within the instrument
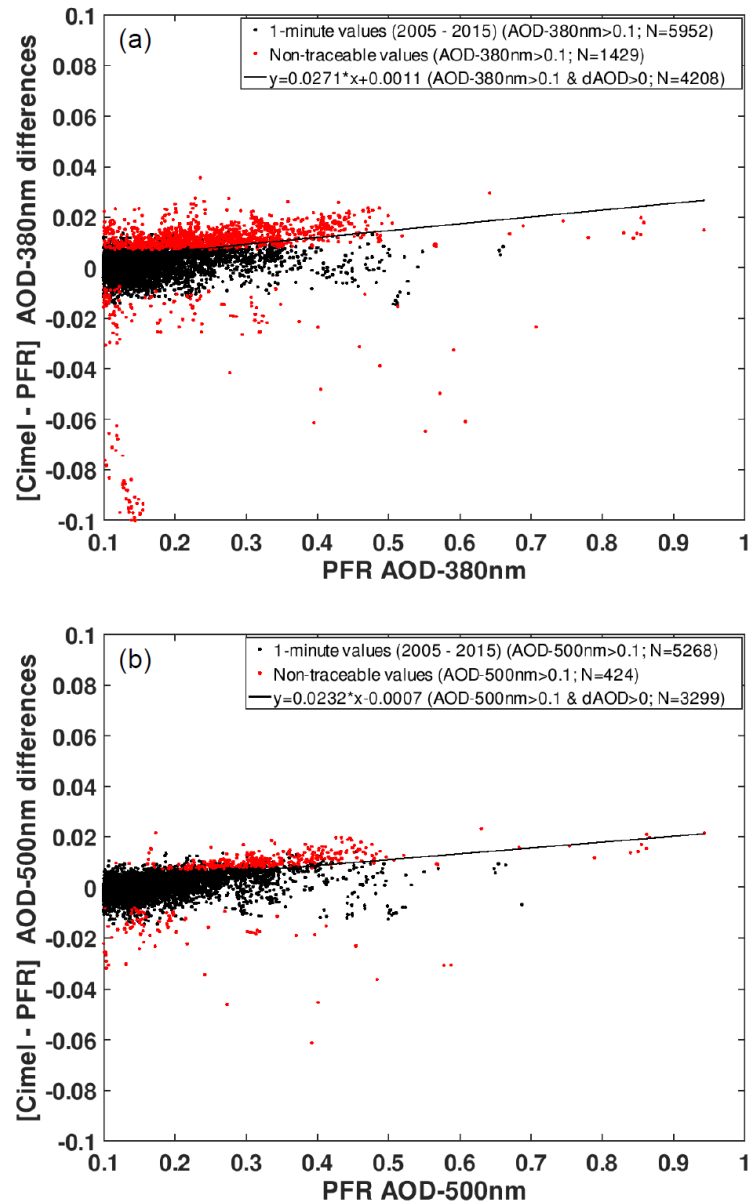
Figure 7: Actual AOD differences between AERONET-Cimel V2 and GAW-PFR versus AOD_{PFR} at **(a)** 380 nm **(b)** and 500 nm for the period 2005–2015. The fitting line has been calculated with those data points with AOD > 0.1 and Cimel–PFR AOD difference > 0. The number of data used in the plots is indicated in the legend. The percentage of non-traceable AOD data with these conditions is ∼ 24% for 380 nm and ∼ 8% for 500 nm. Note that some traceable (black) points show larger AOD differences than non-traceable (red) points because of the air mass dependence of the WMO traceability criterion.

FOV was evaluated by comparing the apparent AODs, defined as follows:

$$AOD_{app,PFR} = -\frac{1}{m} \ln \frac{F_{PFR}}{F_{PFR}(AOD=0)}, \tag{15}$$

$$AOD_{app,Cimel} = -\frac{1}{m} \ln \frac{F_{Cimel}}{F_{Cimel}(AOD=0)}, \tag{16}$$

with the true AOD

$$AOD_{true} = -\frac{1}{m} \ln \frac{F_{dir}}{F_{dir}(AOD=0)}, \tag{17}$$

where F_{dir} is the irradiance due to direct (i.e. non-scattered) radiation and F_{PFR} (F_{Cimel}) is the total irradiance that would be measured by the PFR (Cimel) radiometer, considering the instrument FOV and the FOV angular function. The relative error in AOD depends strongly on the particle size but it is fairly constant for each re value considered (see Supplement S15). For $r_e \sim 1.5$ μm, the relative error in AOD at 380 nm (500 nm) is $\sim 1.6\%$ (1.0%) for Cimel and $\sim 5\%$ ($\sim 3\%$) for PFR. These errors are in good agreement with those estimated by Russell et al. (2004) and slightly higher than the relative AOD error of 0.7% due to coarse dust aerosol forward scattering reported by Eck et al. (1999).

The Monte Carlo simulated relative differences in retrieved AOD (in percentage) that would result from the scattered radiation within the FOV of the PFR and Cimel instruments and the difference in retrieved AOD between PFR and Cimel as a function of the AOD retrieved with PFR, for 380 and 500 nm, are shown in Fig. 8. The main results of these simulations are that (1) the higher FOV of the PFR, compared to that of the Cimel, results in lower AOD values for the PFR and (2) the fractional AOD difference related to the different FOVs of PFR and Cimel is fairly constant for any aerosol effective radius but increases with increasing the effective radius. This fact might explain at least some of the systematic differences seen in Fig. 7. Note that, as lower AOD values derived from the PFR are expected based on its larger FOV, the linear fits in Fig. 7 have been calculated for those data points with the Cimel–PFR AOD differences > 0. In this way, we discard those pairs of AOD data, whose difference is not only due to the different FOV between both instruments, thus obtaining a better approximation to quantify this effect.

The slopes of the fitting lines of the Cimel–PFR AOD differences versus PFR AOD for AOD> 0.1 (dusty conditions) are 2.7% for 380 nm and 2.3% for 500 nm (Fig. 7), which are quite consistent with the percentage differences of AOD between Cimel
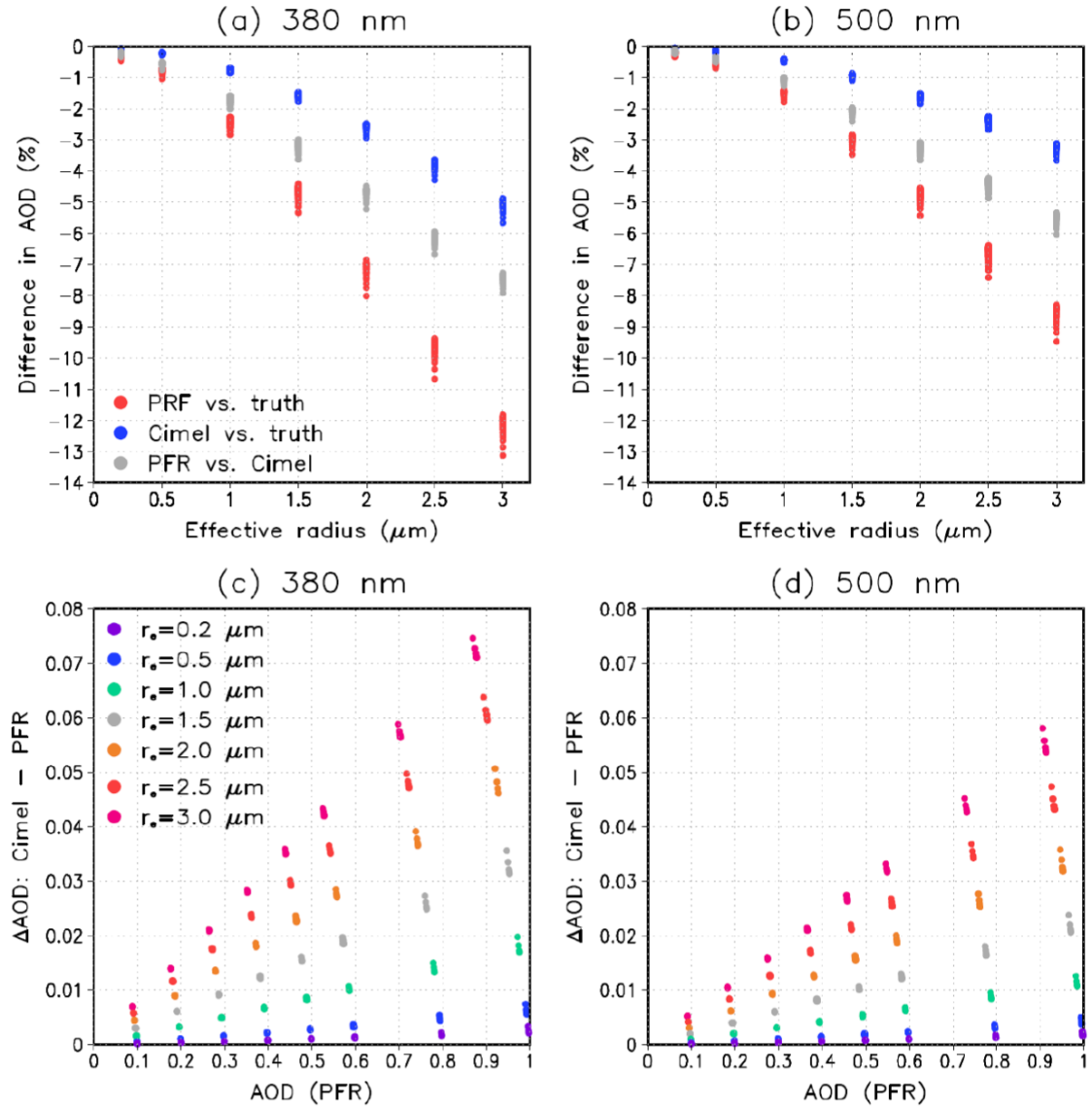
Figure 8: **(a, b)** The simulated relative differences in retrieved AOD (in percentage) that would result from the scattered radiation within the FOV of the PFR and Cimel instruments. The red (blue) dots show the differences between the AOD that would be retrieved using PFR (Cimel) and the actual AOD and the grey dots show the difference between PFR and Cimel at the **(a)** 380 nm and **(b)** 500 nm wavelengths. **(c, d)** The difference in retrieved AOD between PFR and Cimel, plotted as a function of the AOD retrieved with PFR, for seven values of aerosol effective radius between 0.2 and 3.0 μm at **(c)** 380 and **(d)** 500 nm.

and PFR for an effective radius of 1.5 μm (Fig. 8a and 8b). These percentages

correspond to absolute AOD differences of 0.016 at 380 nm and 0.011 at 500 nm for AOD = 0.5 (Fig. 8c and d), which are of sufficient magnitude to cause an appreciable number of 1 min AOD data outside the U_{95} limits, as indicated in Table 10.
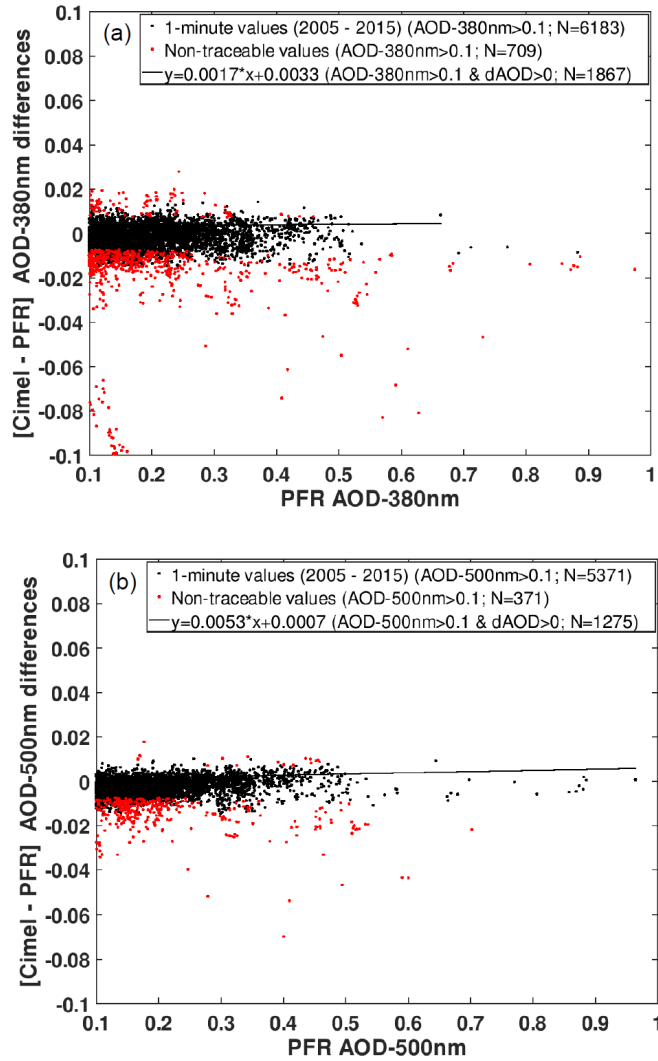
Figure 9: The same as Fig. 7 after correcting the PFR AOD data by adding + 3.3 % at 380 nm and + 2.2 % at 500 nm to the 1 min PFR AOD data > 0.1.

If we apply the corresponding corrections to the 1 min AOD PFR data > 0.1 assuming an effective radius of 1.5 μm, +3.3% at 380 nm and +2.2% at 500 nm, it turns out that the slopes of the fitting lines of the Cimel–PFR AOD differences versus PFR AOD become practically zero (Fig. 9). Moreover, the number of AOD

data outside the U_{95} limits is reduced by approximately 53% for 380 nm and by 13% for 500 nm. It must be taken into account that the percentage of AOD data for AOD > 0.1 outside the U_{95} limits, before the corrections, is only 8% at 500 nm, while at 380 nm it is a significant value (24%).

This AOD "correction" reduces the Cimel–PFR AOD differences substantially but does not eliminate them completely. The main reason is the inherent limitation of data correction using the percentage difference in AOD obtained by model simulation for a fixed effective radius. We have assumed an effective radius of 1.5 μm but, in reality, the radius of dust particles varies. A reasonable range of dust particle radii is between 0.1 and 3 μm (Balkanski et al., 1996; Denjean et al., 2016; Mahowald et al., 2014). So, depending on the distance from the dust source to IZO and the size of the emitted dust, the effective radius could vary slightly between dust episodes. As can be seen in Fig. 8a and b, the percentage differences in AOD between Cimel and PFR for a 1–2 μm effective radius interval, i.e. the Cimel–PFR AOD relative difference at 380 nm (500 nm), might change between $\sim$ -1.8% (-1.1%) to -4.9% (3.3%).

A similar analysis has been carried out for AERONET V3 (see Supplement S16), where we observe that the corrections obtained are not as good as those obtained for V2. The effect of FOV on AOD retrieval should be taken into account for those radiometers with a relatively high FOV ($> 3°$) measuring in regions with relatively high AOD (> 0.2) for most of the year, as is the case in many sites in northern Africa, the Middle East and East Asia (Basart et al., 2009; Cuevas et al., 2015; Eck et al., 1999; Kim et al., 2007). This effect leads to AOD underestimation, and the variable number of high AOD episodes in each season of the year might affect the AOD long-term trends. AOD measurements under these conditions would be especially affected for optical air mass < 3.

5.5 Ångström exponent comparison

We have performed a comparison of the AE provided by GAW-PFR and AERONET-Cimel, using the AOD data obtained from the four common channels (380, 440, 500 and 870 nm) with a total of 70716 data pairs in both cases. The PFR-AOD values have been ordered from lowest to highest by grouping them in intervals of 500 values for which the averages (and corresponding standard deviations) of the Cimel–PFR AE differences have been calculated (Fig. 10a). We proceeded with the PFR-AE values in a similar way (Fig. 10b).

AE differences > 0.2 increase exponentially for AOD < 0.02, reaching AE differences of up to 1.6 under pristine conditions (Fig. 10a). For very low AOD the provided
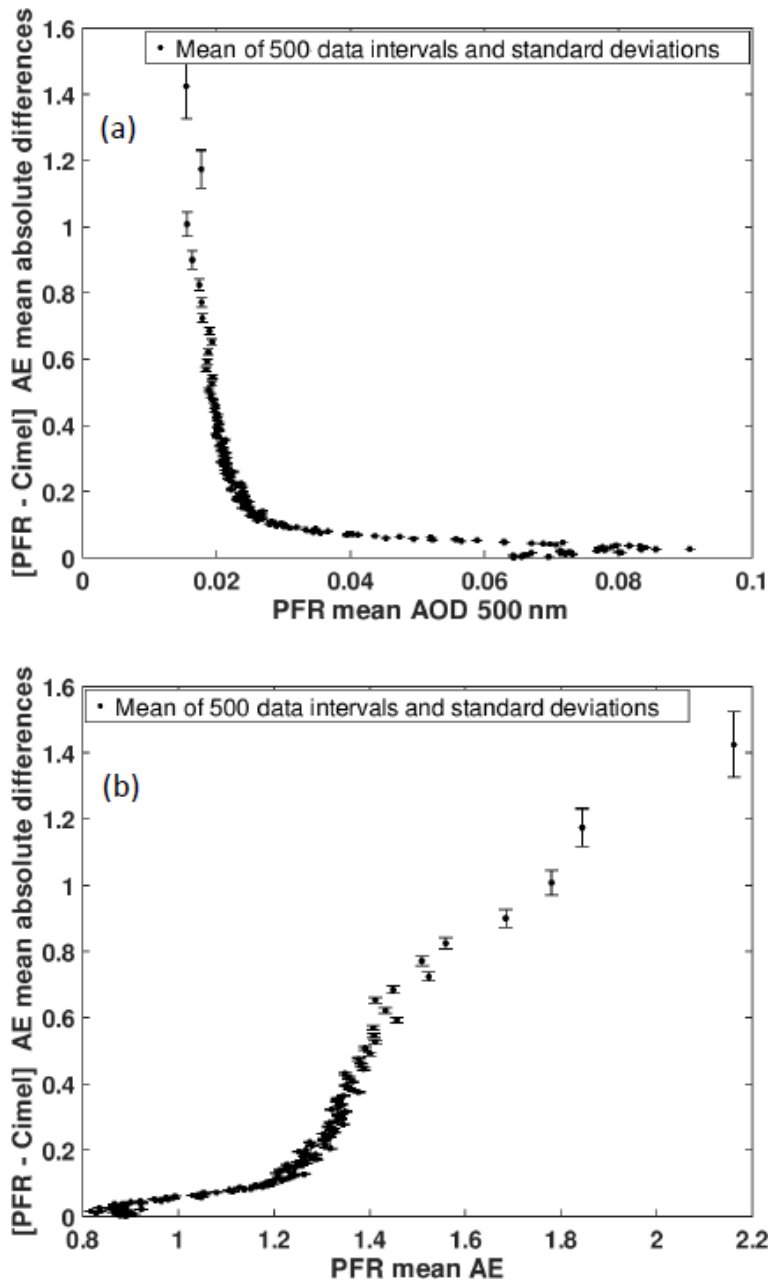
Figure 10: (a) Cimel–PFR AE mean absolute differences (and corresponding standard deviations) versus PFR mean $AOD_{500\ nm}$ in 500 data intervals (b) and versus PFR mean AE in 500 data intervals. AE has been computed for both PFR and Cimel using the four common channels (380, 440, 500 and 870 nm).

instrument's uncertainty is the source of the sharp increase in AE and, at the same time, AE becomes very sensitive to slight AOD changes. However, for AOD < 0.02

the atmospheric aerosol load is practically zero and so its characterization with AE has relatively minor importance in practice.

In addition, the AE differences remain < 0.1 when AE_{PFR} values are < 1 (Fig. 10b), which shows that these differences are small in most of the possible atmospheric scenarios. For $1 < AE_{PFR} < 1.2$ the AE differences increase slightly to values < 0.2 and for $AE_{PFR} > 1.2$ (very fine particles or pristine conditions) the AE differences increase sharply to reach values of ~ 1.2. In our case, the non-pristine conditions, or those with a high content of mineral dust, have associated $AOD > 0.03$ and $AE < 1$, where the AE differences remain < 0.1. In the case of pristine conditions, $AOD \pm 0.03$ and $AE \geq 1$, the AE differences can reach a maximum of 1.6. Wagner and Silva (2008) estimated the usual maximum AE error via error propagation using a pair of spectral channels in which AOD is measured. Their results show that for clean optical conditions ($AOD_{440 \, nm} = 0.06$) the maximum AE error is 1.17 and for hazy conditions ($AOD_{440 \, nm} = 0.17$) the error is 0.17, assuming an underlying AE of 1.5. These values decrease to 0.73 and 0.11, respectively, if $AE = 0$. The AE differences found between GAW-PFR and AERONET-Cimel lie within the estimated errors reported by Wagner and Silva (2008).

In any case, as in our study, the AE has been determined from AOD measured in the four common channels of GAW-PFR and AERONET-Cimel, we estimated the uncertainty in the calculation of the AE for three typical aerosol scenarios at Izaña. Following the methodology shown by Wagner and Silva (2008), the AE uncertainty estimations have been calculated using AOD measurements at four wavelengths and AOD uncertainty error propagation (Table 11). The AE derived from more than two wavelengths is less affected by AOD uncertainties than AE calculated with pairs of wavelengths, since the latter are calculated from the ratio of AOD at two channels (Cachorro et al., 2008).

Table 11: Uncertainty in AE determination for three typical atmospheric situations.

	Uncertainty in AE
Normal pristine conditions	≥ 1
$AOD_{500 \, nm} = 0.03$ and $AE = 1.4$	
Hazy conditions	≥ 0.2
$AOD_{500 \, nm} = 0.14$ and $AE = 1.15$	
Strong dust intrusion	~ 0
$AOD_{500 \, nm} = 0.3$ and $AE = 0.3$	

The AE differences of our study (Fig. 10) are within the AE uncertainty estimated for each type of atmospheric condition (pristine, hazy and heavily dust loaded). However, although AE is a quantitative parameter, it is only used in a qualitative way to estimate the range of sizes (fine, medium, coarse) of the predominant aerosol

in the inevitable mixture of aerosols that we observe. With this parameter, together with the information that is available in the measurement site about the most frequent types of aerosols and their concentration, we can estimate the type of aerosols that are being measured. There are many publications with different thresholds of AE and AOD in order to classify different types of aerosols (e.g. Basart et al., 2009; Cuevas et al., 2015; Dubovik et al., 2002; Guirado et al., 2014; Holben et al., 2001; Kim et al., 2007; Todd et al., 2007; Toledano et al., 2007; Wang et al., 2004). However, there is no consensus on these thresholds since at each site there are different mixtures of aerosols and each type of aerosol shows specific frequencies of appearance and different concentrations. An alternative way of analysing the degree of agreement in AE between GAW-PFR and AERONET-Cimel is to verify to what extent both networks provide the same information regarding the type of aerosol they observe in a certain site.

Considering the AE criteria established by Cuevas et al. (2015) and Berjón et al. (2019), we have identified the following four main categories according to the AE_{PFR} and AE_{Cimel} values:

1. AE_{PFR} and $AE_{Cimel} > 0.6$: pristine conditions.

2. $0.25 < AE_{PFR}$ and $AE_{Cimel} \leq 0.6$: hazy, mineral dust being the main aerosol component.

3. AE_{PFR} and $AE_{Cimel} \leq 0.25$: pure dust.

4. AE_{PFR} and AE_{Cimel}: does not fit any of the previous categories.

In 94.9% of the cases, GAW-PFR and AERONET-Cimel V2 match the AE intervals of each aerosol scenario. Similar results (93.4%) were obtained when comparing with AERONET V3. Most of the agreement ($> 80\%$) occurs in the predominant scenario of pristine conditions despite the AE uncertainty under pristine conditions being ≥ 1. See Supplement S17 for more details. Note that the choice of these categories is not relevant since this is only used to examine the long-term agreement in AE between GAW-PFR and AERONET-Cimel in different atmospheric conditions.

6 Summary and conclusions

While GAW-PFR is the WMO-defined global AOD reference, being directly linked to WMO-CIMO, and was specifically designed to detect long-term AOD trends, AERONET-Cimel is the densest AOD measurement network globally, and the network most frequently used for aerosol characterization and for model and satellite observation evaluation.

An AERONET-Cimel 11-year AOD data series at IZO was obtained using a large number of radiometers. A total of 13 reference instruments were used in the period 2005–2009, which means that approximately every 4.5 months an instrument was replaced by another one to be calibrated. Their calibrations were performed during their respective measurement time periods at IZO. Therefore, these calibrations were not in any way linked with those of the instruments that preceded or replaced them or with GAW-PFR reference. These facts led us to investigate the homogeneity of the AERONET-Cimel AOD data series and their intercomparability with the much more homogeneous AOD data series from GAW-PFR (three instruments in 11 years). The traceability concept for AOD suggested by WMO consists in determining whether the AOD difference of the AERONET CIMELs versus the GAW PFRs lies within the U_{95} limits. We have used uncertainty limits for AOD traceability established by WMO (2005) for these type of instruments with finite FOV. The acceptable traceability is when 95% of the absolute AOD differences lie within these limits, in which case both data populations are considered equivalent. It should be clarified that "traceability" is not used in a strict meteorological sense. This study has addressed the comparison of the GAW-PFR dataset with the two versions of AERONET (V2 and V3) in the period 2005–2015. An excellent agreement between V2 and V3 for the four analysed channels ($R^2 > 0.999$) has been obtained.

More than 70000 synchronous GAW-PFR and AERONET-Cimel 1 min data pairs in each channel in the period 2005–2015 were analysed. An excellent traceability of AOD from the AERONET-Cimel (V2 and V3) is found for 440, 500 and 870 nm as well as fairly good results for 380 nm. The lowest percentage of traceable AOD data is registered at 380 nm, with 92.7% of the 1 min data within the WMO limits, and the highest at 870 nm, with 98.0% of the data within the same limits.

The different possible causes of non-traceability in AOD were investigated as follows:

– *Absolute AOD measurements synchronization.*

Analysing 1 min AOD variability, we concluded that its impact on the AOD differences is quite small, as only $\sim 0.8\%$ of the AOD data have a variability larger than 0.005 in all spectral ranges.

– *Sun tracking misalignments.*

Sun tracking misalignments constitute a serious problem and a major cause of non-traceability of AOD data pairs, as demonstrated by the AOD data outside the U_{95} limits from the period 2005–2009, as a consequence of episodic problems with the sun tracker of the GAW-PFR radiometer. For the 2010–2015 period the percentage of traceable data pairs improves to 93.5% (380 nm),

97.4% (440 nm), 97.2% (500 nm) and 99.1% (870 nm). However, most of these cases could be identified and excluded from the analysis.

– *Cloud screening failure by both network algorithms.*

According to our observations, the simultaneous failure of both cloud screening algorithms might occur only under the presence of large and stable cirrus. In these cases, the radiometers interpret these clouds as aerosol layers and might provide values very different from the real AOD. For the comparison at IZO, however, this effect is negligible since GAW-PFR and AERONET-Cimel cloud screening algorithms provide successful cloud identification of clear direct sun conditions during cloudy skies (FCS < 40%) for 99.75% of the cases.

– *Pressure-measurement-related errors.*

Since the accuracy of the new barometers built into new radiometers is about 3 hPa and only errors in atmospheric pressure > 30 hPa might produce an impact on Rayleigh scattering, the AOD non-traceability due to errors in Rayleigh scattering is negligible.

– *Total column ozone input uncertainty.*

The largest influence of total ozone data uncertainty on ozone absorption occurs mainly at 500 nm. Total ozone needs to be determined to ±30 DU or 10% of typical values to ensure an uncertainty of ±0.001 ozone absorption at 500 nm. In the case of the GAW-PFR– AERONET-Cimel comparison, despite the very different methods in which both networks obtained values for their corresponding corrections, large ozone differences were found (> 40 DU) only on 2.4% of the days, resulting in a difference in the ozone optical depth slightly above ~ 0.001. The potential contribution to non-traceable AOD values between the two networks is negligible. However, at middle- or high-latitude stations where fast O_3 variations of several tens of DU might be registered, the correction of 1 min AOD measurements by ozone absorption might be an issue to be considered.

– *Total column NO_2 input uncertainty.*

The differences in NO_2 absorption caused by differences in daily total NO_2 between GAW-PFR and AERONET-Cimel is of the order of 10^{-3} for 380 and 440 nm channels, while for 500 nm channel it is even lower, of the order of 10^{-4}. Therefore, differences in NO_2 absorption are negligible in the 1 min AOD nontraceability of our study. However, NO_2 absorption might have some impact on AOD in highly polluted regions, such as in large industrial cities,

where column NO_2 values are much larger than the climatological ones.

Taking into account the corrections for Rayleigh scattering and for the absorptions by O_3 and NO_2, we have calculated the combined effect of all of them on the non-traceability of the 1 min AOD values. The highest impact occurs in the 380 nm channel, in which 25% of the AOD data outside the U_{95} limits ($\sim 2\%$ of the total compared data) are due to significant differences in pressure and in O_3 and NO_2 absorption. The 1 min AOD data outside the U_{95} limits by these corrections is negligible in the 870 nm channel.

– *Impact of dust forward scattering in AOD retrieval uncertainty for different instrument FOVs.*

Since GAW-PFR has almost double the FOV ($\sim 2.5°$) compared to the AERONET-Cimel ($\sim 1.3°$) and direct solar irradiance measurements are biased by the amount of aureole radiation that is assumed to be direct solar radiation, it is reasonable to expect that the GAW-PFR is more affected by the circumsolar irradiance than the AERONET-Cimel radiometer when AOD is relatively high. Modelling the dust forward scattering we have shown that a non-negligible percentage of the nontraceable 1 min AOD data for AOD > 0.1, ranging from $\sim 0.3\%$ at 870 nm to $\sim 1.9\%$ at 380 nm is caused by the different FOV. Due to this effect, the GAW-PFR provides AOD values, which are $\sim 3\%$ lower at 380 nm and $\sim 2\%$ lower at 500 nm compared with AERONET-Cimel. However, AOD underestimation could only have some relevance in dusty regions if radiometers with relatively large FOV are used.

A comparison of the AE provided by GAW-PFR and AERONET-Cimel has been performed using AOD data obtained from the four nearby common channels with a total of 70716 data pairs in both cases. This is a very strict AE calculation since it is necessary that AOD be accurately measured by the four channels simultaneously. AE differences > 0.2 increase exponentially under very pristine conditions (AOD ≤ 0.03 and AE ≥ 1), reaching AE differences of up to 1.6. However, for these conditions the atmospheric aerosol load is practically zero and so its characterization with AE does not have any importance in practice. Under non-pristine conditions or those with a high mineral dust content (associated AOD > 0.03 and AE < 1), the AE differences remain < 0.1.

Summarizing, we have presented for the first time a long-term (2005–2015) 1 min AOD comparison among different types of radiometers belonging to different aerosol global networks. This comparison is a very demanding test of both GAW-PFR and AERONET-Cimel validated AOD datasets since aerosol scenarios correspond to extreme conditions: either very low aerosol loading, a "pristine" scenario that reveals small uncertainties in the calibration and in the cloud screening, or large

dust load, which leads to a significant increase in the forward-scattering aerosol with AOD, resulting in a slightly higher AOD underestimation by the GAW-PFR. From this comprehensive comparison, we can conclude that both AOD datasets are representative of the same AOD population, which is a remarkable fact for the global aerosol community. It should be noted that AOD traceability at 380 nm (92.7%) does not reach 95% of the common data, the percentage recommended by WMO U_{95} criterion, so more efforts should be made to improve AOD in the UV range. In this study we have also investigated the data that are outside of the WMO U_{95} limits in order to understand their causes and to be eventually able to correct the small inconsistencies detected in instrumental and methodological aspects in the future.

Our results suggest that WMO-CIMO traceability limits could be redefined as a function of wavelength and the recommended radiometer FOV range should be reconsidered. The widely deployed AERONET-Cimel and GAW-PFR datasets play a crucial role in understanding long-term AOD changes and detecting trends, so it would be desirable for both networks to be linked to the same WMO-GAW-related reference.

the Supplement. RR has coordinated the maintenance and daily checks of the PFR and Cimel radiometers since 2005, resolving technical and logistical problems. CT contributed to the GAW-PFR and AERONET-Cimel calibration aspects addressed in the paper. FA provided detailed information of the Cimel radiometers, taking care of their complex technical problems. JG contributed with concepts of traceability and comparability used in the paper. All authors discussed the results and contributed to the final paper. EC and SK supervised this research activity.

References

Amiridis, V., Marinou, E., Tsekeri, A., Wandinger, U., Schwarz, A., Giannakaki, E., Mamouri, R., Kokkalis, P., Binietoglou, I., Solomos, S., Herekakis, T., Kazadzis, S., Gerasopoulos, E., Proestakis, E., Kottas, M., Balis, D., Papayannis, A., Kontoes, C., Kourtidis, K., Papagiannopoulos, N., Mona, L., Pappalardo, G., Le Rille, O., and Ansmann, A.: LIVAS: a 3-D multi-wavelength aerosol/cloud database based on CALIPSO and EARLINET, Atmos. Chem. Phys., 15, 7127–7153, https://doi.org/10.5194/acp-15-7127-2015, 2015.

Ångström, A.: On the atmospheric transmission of sun radiation and on dust in the air, Geogr. Ann., 11, 156–166, 1929.

Balkanski, Y., Schulz, M., Marticorena, B., Bergametti, G., Guelle, W., Dulac, F., Moulin, C., and Lambert, C.: Importance of the source term and of the size distribution to model the mineral dust cycle, in: The impact of desert dust across the Mediterranean, 69–76, Springer, https://doi.org/10.1007/978-94-017-3354-0_6, 1996.

Barker, H. W.: Solar radiative transfer through clouds possessing isotropic variable extinction coefficient, Q. J. Roy. Meteor. Soc., 118, 1145–1162, https://doi.org/10.1002/qj.49711850807, 1992.

Barker, H. W.: Estimating cloud field albedo using one-dimensional series of optical depth, J. Atmos. Sci., 53, 2826–2837, https://doi.org/10.1175/1520-0469(1996)053⟨2826:ECFAUO⟩2.0.CO;2, 1996.

Barreto, A., Cuevas, E., Pallé, P., Romero, P. M., Guirado, C., Wehrli, C. J., and Almansa, F.: Recovering long-term aerosol optical depth series (1976–2012) from an astronomical potassiumbased resonance scattering spectrometer, Atmos. Meas. Tech., 7, 4103–4116, https://doi.org/10.5194/amt-7-4103-2014, 2014.

Barreto, Á., Cuevas, E., Granados-Muñoz, M.-J., AladosArboledas, L., Romero, P. M., Gröbner, J., Kouremeti, N., Almansa, A. F., Stone, T., Toledano, C., Román, R., Sorokin, M., Holben, B., Canini, M., and Yela, M.: The new sun-skylunar Cimel CE318-T multiband photometer – a comprehensive performance evaluation, Atmos. Meas. Tech., 9, 631–654, https://doi.org/10.5194/amt-9-631-2016, 2016.

Basart, S., Pérez, C., Cuevas, E., Baldasano, J. M., and Gobbi, G. P.: Aerosol characterization in Northern Africa, Northeastern Atlantic, Mediterranean Basin and Middle East from direct-sun AERONET observations, Atmos. Chem. Phys., 9, 8265–8282, https://doi.org/10.5194/acp-9-8265-2009, 2009.

Basart, S., Pérez, C., Nickovic, S., Cuevas, E., and Baldasano, J.: Development and evaluation of the BSCDREAM8b dust regional model over Northern Africa, the Mediterranean and the Middle East, Tellus B, 64, 18539, https://doi.org/10.3402/tellusb.v64i0.18539, 2012.

Benedetti, A., Reid, J. S., Knippertz, P., Marsham, J. H., Di Giuseppe, F., Rémy, S., Basart, S., Boucher, O., Brooks, I. M., Menut, L., Mona, L., Laj, P., Pappalardo, G., Wiedensohler, A., Baklanov, A., Brooks, M., Colarco, P. R., Cuevas, E., da Silva, A., Escribano, J., Flemming, J., Huneeus, N., Jorba, O., Kazadzis, S., Kinne, S., Popp, T., Quinn, P. K., Sekiyama, T. T., Tanaka, T., and Terradellas, E.: Status and future of numerical atmospheric aerosol prediction with a focus on data requirements, Atmos. Chem. Phys., 18, 10615–10643, https://doi.org/10.5194/acp-18-10615-2018, 2018.

Berjón, A., Barreto, A., Hernández, Y., Yela, M., Toledano, C., and Cuevas, E.: A 10-year characterization of the Saharan Air Layer lidar ratio in the subtropical North Atlantic, Atmos. Chem. Phys., 19, 6331–6349, https://doi.org/10.5194/acp-19-6331-2019, 2019.

Bodhaine, B. A., Wood, N. B., Dutton, E. G., and Slusser, J. R.: On Rayleigh optical depth calculations, J. Atmos. Ocean. Tech., 16, 1854–1861, 1999.

Böhm-Vitense, E.: Introduction to stellar astrophysics, Vol. 2. Stellar atmospheres, Cambridge University Press, Cambridge (UK), 12+ 245 p., ISBN 0-521-34403-4, 1989.

Bokoye, A., Royer, A., O'Neil, N., Cliche, P., Fedosejevs, G., Teillet, P., and McArthur, L.: Characterization of atmospheric aerosols across Canada from a ground-based sunphotometer network: AEROCAN, Atmos. Ocean, 39, 429–456, https://doi.org/10.1080/07055900.2001.9649687, 2001.

Cachorro, V., Toledano, C., Sorribas, M., Berjón, A., De Frutos, A., and Laulainen, N.: An "in situ" calibration-correction procedure (KCICLO) based on AOD diurnal cycle: Comparative results between AERONET and reprocessed (KCICLO method) AOD-alpha data series at El Arenosillo, Spain, J. Geophys. Res.- Atmos., 113, D02207, https://doi.org/10.1029/2007JD009001, 2008.

Cachorro, V. E., Romero, P. M., Toledano, C., Cuevas, E., and de Frutos, A. M.: The fictitious diurnal cycle of aerosol optical depth: A new approach for "in situ" calibration and correction of AOD data series, Geophys. Res. Lett., 31, L12106, https://doi.org/10.1029/2004GL019651, 2004.

Campanelli, M., Nakajima, T., and Olivieri, B.: Determination of the solar calibration constant for a sun-sky radiometer: proposal of an in-situ procedure, Appl. Opt., 43, 651–659, 2004.

Carlund, T., Kouremeti, N., Kazadzis, S., and Gröbner, J.: Aerosol optical depth determination in the UV using a four-channel precision filter radiometer, Atmos. Meas. Tech., 10, 905–923, https://doi.org/10.5194/amt-10-905-2017, 2017.

Carrillo, J., Guerra, J. C., and Cuevas, E., and Barrancos, J.: Characterization of the Marine Boundary Layer and the Trade-Wind Inversion over the Sub-tropical North Atlantic, Bound.-Lay. Meteorol., 158, 311–330, https://doi.org/10.1007/s10546-015-0081-1, 2016.

Che, H., Zhang, X.-Y., Xia, X., Goloub, P., Holben, B., Zhao, H., Wang, Y., Zhang, X.-C.,
    Wang, H., Blarel, L., Damiri, B., Zhang, R., Deng, X., Ma, Y., Wang, T., Geng, F.,
    Qi, B., Zhu, J., Yu, J., Chen, Q., and Shi, G.: Ground-based aerosol climatology
    of China: aerosol optical depths from the China Aerosol Remote Sensing Network
    (CARSNET) 2002–2013, Atmos. Chem. Phys., 15, 7619–7652, https://doi.org/10.
    5194/acp-15-7619-2015, 2015.

Chedin, A., Capelle, V., and Scott, N.: Detection of IASI dust AOD trends over Sahara:
    How many years of data required?, Atmos. Res., 212, 120–129, https://doi.org/10.
    1016/j.atmosres.2018.05.004, 2018.

Chubarova, N. Y., Poliukhov, A. A., and Gorlova, I. D.: Long-term variability of aerosol
    optical thickness in Eastern Europe over 2001–2014 according to the measurements
    at the Moscow MSU MO AERONET site with additional cloud and NO2 correction,
    Atmos. Meas. Tech., 9, 313–334, https://doi.org/10.5194/amt-9-313-2016, 2016.

Cuevas, E., González, Y., Rodríguez, S., Guerra, J. C., GómezPeláez, A. J., Alonso-Pérez,
    S., Bustos, J., and Milford, C.: Assessment of atmospheric processes driving ozone
    variations in the subtropical North Atlantic free troposphere, Atmos. Chem. Phys.,
    13, 1973–1998, https://doi.org/10.5194/acp-13-1973-2013, 2013.

Cuevas, E., Camino, C., Benedetti, A., Basart, S., Terradellas, E., Baldasano, J. M.,
    Morcrette, J. J., Marticorena, B., Goloub, P., Mortier, A., Berjón, A., Hernández, Y.,
    Gil-Ojeda, M., and Schulz, M.: The MACC-II 2007–2008 reanalysis: atmospheric dust
    evaluation and characterization over northern Africa and the Middle East, Atmos.
    Chem. Phys., 15, 3991–4024, https://doi.org/10.5194/acp-15-3991-2015, 2015.

Cuevas, E., Gómez-Peláez, A., Rodríguez, S., Terradellas, E., Basart, S., García, R., García,
    O., and Alonso-Pérez, S.: The pulsating nature of large-scale Saharan dust transport
    as a result of interplays between mid-latitude Rossby waves and the North African
    Dipole Intensity, Atmos. Environ., 167, 586–602, https://doi.org/10.1016/j.atmosenv.
    2017.08.059, 2017a.

Cuevas, E., Milford, C., Bustos, J. J., del Campo-Hernández, García, O., D., G. R.,
    Gómez-Peláez, Guirado-Fuentes, C., Marrero, C., Prats, N., Ramos, R., Redondas,
    A., Reyes, E., Rodríguez, S., Romero-Campos, P., Scheneider, M., Belmonte, J., Yela,
    M., Almansa, F., Barreto, A., López-Solano, C., Basart, S., Terradellas, E., Afonso, S.,
    Bayo, C., Berjón, A., Bethencourt, J., Carreño, V., Castro, N. J., Cruz, A. M., Damas,
    M., De Ory-Ajamil, F., García, M. I., Gómez-Trueba, V., González, Y., Hernández, C.,
    Hernández, Y., Hernández-Cruz, B., Jover, M., León, S., López-Fernández, R., López-
    Solano, J., Rodríguez, E., Rodríguez-Franco, J., Rodríguez-Valido, M., Sálamo, C.,
    Sanromá, E., Santana, D., Santo-Tomás, F., Sepúlveda, E., Sierra, M., and Sosa, E.:
    Izaña Atmospheric Research Center Activity Report 2015–2016, State Meteorological
    Agency (AEMET), 2017b.

Denjean, C., Cassola, F., Mazzino, A., Triquet, S., Chevaillier, S., Grand, N., Bourrianne, T., Momboisse, G., Sellegri, K., Schwarzenbock, A., Freney, E., Mallet, M., and Formenti, P.: Size distribution and optical properties of mineral dust aerosols transported in the western Mediterranean, Atmos. Chem. Phys., 16, 1081–1104, https://doi.org/10.5194/acp-16-1081-2016, 2016.

Driemel, A., Augustine, J., Behrens, K., Colle, S., Cox, C., Cuevas-Agulló, E., Denn, F. M., Duprat, T., Fukuda, M., Grobe, H., Haeffelin, M., Hodges, G., Hyett, N., Ijima, O., Kallis, A., Knap, W., Kustov, V., Long, C. N., Longenecker, D., Lupi, A., Maturilli, M., Mimouni, M., Ntsangwane, L., Ogihara, H., Olano, X., Olefs, M., Omori, M., Passamani, L., Pereira, E. B., Schmithüsen, H., Schumacher, S., Sieger, R., Tamlyn, J., Vogt, R., Vuilleumier, L., Xia, X., Ohmura, A., and König-Langlo, G.: Baseline Surface Radiation Network (BSRN): structure and data description (1992–2017), Earth Syst. Sci. Data, 10, 1491–1501, https://doi.org/10.5194/essd-10-1491-2018, 2018.

Dubovik, O., Holben, B., Eck, T. F., Smirnov, A., Kaufman, Y. J., King, M. D., Tanré, D., and Slutsker, I.: Variability of absorption and optical properties of key aerosol types observed in worldwide locations, J. Atmos. Sci., 59, 590–608, https://doi.org/10.1175/1520-0469(2002)059⟨0590:VOAAOP⟩2.0.CO;2, 2002.

Eck, T., Holben, B., Reid, J., Dubovik, O., Smirnov, A., O'neill, N., Slutsker, I., and Kinne, S.: Wavelength dependence of the optical depth of biomass burning, urban, and desert dust aerosols, J. Geophys. Res.-Atmos., 104, 31333–31349, https://doi.org/10.1029/1999JD900923, 1999.

Eskes, H. J. and Boersma, K. F.: Averaging kernels for DOAS totalcolumn satellite retrievals, Atmos. Chem. Phys., 3, 1285–1291, https://doi.org/10.5194/acp-3-1285-2003, 2003.

Freidenreich, S. and Ramaswamy, V.: A new multiple-band solar radiative parameterization for general circulation models, J. Geophys. Res.-Atmos., 104, 31389–31409, https://doi.org/10.1029/1999JD900456, 1999.

García, R. D., Cuevas, E., García, O. E., Cachorro, V. E., Pallé, P., Bustos, J. J., Romero-Campos, P. M., and de Frutos, A. M.: Reconstruction of global solar radiation time series from 1933 to 2013 at the Izaña Atmospheric Observatory, Atmos. Meas. Tech., 7, 3139–3150, https://doi.org/10.5194/amt-7-3139-2014, 2014.

García, R. D., Cuevas, E., Ramos, R., Cachorro, V. E., Redondas, A., and Moreno-Ruiz, J. A.: Description of the Baseline Surface Radiation Network (BSRN) station at the Izaña Observatory (2009–2017): measurements and quality control/assurance procedures, Geosci. Instrum. Method. Data Syst., 8, 77–96, https://doi.org/10.5194/gi-8-77-2019, 2019.

Giles, D. M., Sinyuk, A., Sorokin, M. G., Schafer, J. S., Smirnov, A., Slutsker, I., Eck, T. F., Holben, B. N., Lewis, J. R., Campbell, J. R., Welton, E. J., Korkin, S. V., and

Lyapustin, A. I.: Advancements in the Aerosol Robotic Network (AERONET) Version 3 database – automated near-real-time quality control algorithm with improved cloud screening for Sun photometer aerosol optical depth (AOD) measurements, Atmos. Meas. Tech., 12, 169– 209, https://doi.org/10.5194/amt-12-169-2019, 2019.

Goloub, P., Li, Z., Dubovik, O., Blarel, L., Podvin, T., Jankowiak, I., Lecoq, R., Deroo, C., Chatenet, B., Morel, J., Cuevas, E., and Ramos, R.: PHOTONS/AERONET sunphotometer network overview: description, activities, results, in: Fourteenth International Symposium on Atmospheric and Ocean Optics/Atmospheric Physics, vol. 6936, p. 69360V, International Society for Optics and Photonics, 2007.

Grassl, H.: Calculated circumsolar radiation as a function of aerosol type, field of view, wavelength, and optical depth, Appl. Opt., 10, 2542–2543, https://doi.org/10.1364/AO.10.002542, 1971.

Gueymard, C.: SMARTS2: a simple model of the atmospheric radiative transfer of sunshine: algorithms and performance assessment, Florida Solar Energy Center Cocoa, FL, 1995.

Guirado, C., Cuevas, E., Cachorro, V. E., Toledano, C., AlonsoPérez, S., Bustos, J. J., Basart, S., Romero, P. M., Camino, C., Mimouni, M., Zeudmi, L., Goloub, P., Baldasano, J. M., and de Frutos, A. M.: Aerosol characterization at the Saharan AERONET site Tamanrasset, Atmos. Chem. Phys., 14, 11753– 11773, https://doi.org/10.5194/acp-14-11753-2014, 2014.

Holben, B., Eck, T., Slutsker, I., Tanré, D., Buis, J., Setzer, A., Vermote, E., Reagan, J., and Kaufman, Y.: Multi-band automatic sun and sky scanning radiometer system for measurement of aerosols, CNES, Proceedings of 6th International Symposium on Physical Measurements and Signatures in Remote Sensing, 75– 83, 1994.

Holben, B., Eck, T., Slutsker, I., Tanré, D., Buis, J., Setzer, A., Vermote, E., Reagan, J., Kaufman, Y., Nakajima, T., Lavenu, F., Jankowiak, I., and Smirnov, A.: AERONET – A Federated Instrument Network and Data Archive for Aerosol Characterization, Remote Sens. Environ., 66, 1–16, https://doi.org/10.1016/S0034-4257(98)00031-5, 1998.

Holben, B. N., Tanré, D., Smirnov, A., Eck, T. F., Slutsker, I., Abuhassan, N., Newcomb, W. W., Schafer, J. S., Chatenet, B., Lavenu, F., Kaufman, Y. J., Vande Castle, J., Setzer, A.,Markham, B., Clark, D., Frouin, R., Halthore, R., Karneli, A., O'neill, N. T., Pietras, C., Pinker, C., Voss, K., and Zibordi, G.: An emerging ground-based aerosol climatology: Aerosol optical depth from AERONET, J. Geophys. Res.-Atmos., 106, 12067– 12097, https://doi.org/10.1029/2001JD900014, 2001.

Huijnen, V. and Eskes, H.: Skill scores and evaluation methodology for the MACC II project, MACC-II Deliverable D<_85, 2, availabel at: http://www.gmes-atmosphere.eu/documents/maccii/deliverables/val/MACCII_VAL_DEL_D_85.2_ScoringReport01_20120222.pdf (last access: 5 September 2018), 2012.

Huneeus, N., Basart, S., Fiedler, S., Morcrette, J.-J., Benedetti, A., Mulcahy, J., Terradellas, E., Pérez García-Pando, C., Pejanovic, G., Nickovic, S., Arsenovic, P., Schulz, M., Cuevas, E., Baldasano, J. M., Pey, J., Remy, S., and Cvetkovic, B.: Forecasting the northern African dust outbreak towards Europe in April 2011: a model intercomparison, Atmos. Chem. Phys., 16, 4967–4986, https://doi.org/10.5194/acp-16-4967-2016, 2016.

IPCC: The Physical Science Basis. Intergovernmental Panel on Climate Change, https://doi.org/10.1017/CBO9781107415324, 2013.

Jarosławski, J., Krzyscin, J. W., Puchalski, S., and Sobolewski, P.:´ On the optical thickness in the UV range: Analysis of the groundbased data taken at Belsk, Poland, J. Geophys. Res.-Atmos., 108, 4722, https://doi.org/10.1029/2003JD003571, 2003.

Kahn, R. A. and Gaitley, B. J.: An analysis of global aerosol type as retrieved by MISR, J. Geophys. Res.-Atmos., 120, 4248–4281, https://doi.org/10.1002/2015JD023322, 2015.

Kalnay, E., Kanamitsu, M., Kistler, R., Collins, W., Deaven, D., Gandin, L., Iredell, M., Saha, S., White, G., Woollen, J., Zhu, Y., Chelliah, M., Ebisuzaki, W., Higgins, W., Janowiak, J., Mo, K. C., Ropelewski, C., Wang, J., Leetmaa, A., Reynolds, R., Jenne, R., and Joseph, D.: The NCEP/NCAR 40-year reanalysis project, B. Am. Meteorol. Soc., 77, 437–472, 1996.

Kasten, F.: A new table and approximation formula for the relative optical air mass, Arch. Meteor. Geophy. B, 14, 206–223, https://doi.org/10.1007/BF02248840, 1966.

Kasten, F. and Young, A. T.: Revised optical air mass tables and approximation formula, Appl. Opt., 28, 4735–4738, https://doi.org/10.1364/AO.28.004735, 1989.

Kazadzis, S., Veselovskii, I., Amiridis, V., Gröbner, J., Suvorina, A., Nyeki, S., Gerasopoulos, E., Kouremeti, N., Taylor, M., Tsekeri, A., and Wehrli, C.: Aerosol microphysical retrievals from precision filter radiometer direct solar radiation measurements and comparison with AERONET, Atmos. Meas. Tech., 7, 2013– 2025, https://doi.org/10.5194/amt-7-2013-2014, 2014.

Kazadzis, S., Kouremeti, N., Diémoz, H., Gröbner, J., Forgan, B. W., Campanelli, M., Estellés, V., Lantz, K., Michalsky, J., Carlund, T., Cuevas, E., Toledano, C., Becker, R., Nyeki, S., Kosmopoulos, P. G., Tatsiankou, V., Vuilleumier, L., Denn, F. M., Ohkawara, N., Ijima, O., Goloub, P., Raptis, P. I., Milner, M., Behrens, K., Barreto, A., Martucci, G., Hall, E., Wendell, J., Fabbri, B. E., and Wehrli, C.: Results from the Fourth WMO Filter Radiometer Comparison for aerosol optical depth measurements, Atmos. Chem. Phys., 18, 3185–3201, https://doi.org/10.5194/acp-18-3185-2018, 2018a.

Kazadzis, S., Kouremeti, N., Nyeki, S., Gröbner, J., and Wehrli, C.: The World Optical Depth Research and Calibration Center (WORCC) quality assurance and quality

control of GAW-PFR AOD measurements, Geosci. Instrum. Method. Data Syst., 7, 39– 53, https://doi.org/10.5194/gi-7-39-2018, 2018b.

Kentarchos, A., Roelofs, G., Lelieveld, J., and Cuevas, E.: On the origin of elevated surface ozone concentrations at Izana Observatory, Tenerife during late March 1996, Geophys. Res. Lett., 27, 3699–3702, https://doi.org/10.1029/2000GL011518, 2000.

Kim, S.-W., Jefferson, A., Soon-Chang, Y., Dutton, E., Ogren, J., Valero, F., Kim, J., and Holben, B.: Comparisons of aerosol optical depth and surface shortwave irradiance and their effect on the aerosol surface radiative forcing estimation, J. Geophys. Res.Atmos., 110, D07204, https://doi.org/10.1029/2004JD004989, 2005.

Kim, S.-W., Yoon, S.-C., Kim, J., and Kim, S.-Y.: Seasonal and monthly variations of columnar aerosol optical properties over east Asia determined from multi-year MODIS, LIDAR, and AERONET Sun/sky radiometer measurements, Atmos. Environ., 41, 1634–1651, https://doi.org/10.1016/j.atmosenv.2006.10.044, 2007.

Kim, S.-W., Yoon, S.-C., Dutton, E., Kim, J., and Wehrli, C.and Holben, B.: Global surface-based sun photometer network for long-term observations of column aerosol optical properties: intercomparison of aerosol optical depth, Aerosol Sci. Tech., 42, 1–9, https://doi.org/10.1080/02786820701699743, 2008.

Klingmüller, K., Pozzer, A., Metzger, S., Stenchikov, G. L., and Lelieveld, J.: Aerosol optical depth trend over the Middle East, Atmos. Chem. Phys., 16, 5063–5073, https://doi.org/10.5194/acp-16-5063-2016, 2016.

Komhyr, W.: Dobson spectrophotometer systematic total ozone measurement error, Geophys. Res. Lett., 7, 161–163, 1980.

Komhyr, W. D., Grass, R. D., and Leonard, R. K.: Dobson spectrophotometer 83: A standard for total ozone measurements, 1962–1987, J. Geophys. Res.-Atmos., 94, 9847–9861, https://doi.org/10.1029/JD094iD07p09847, 1989.

Mahowald, N., Albani, S., Kok, J. F., Engelstaeder, S., Scanza, R., Ward, D. S., and Flanner, M. G.: The size distribution of desert dust aerosols and its impact on the Earth system, Aeolian Res., 15, 53–71, https://doi.org/10.1016/j.aeolia.2013.09.002, 2014.

McArthur, L. J. B., Halliwell, D. H., Niebergall, O. J., O'Neill, N. T., Slusser, J. R., and Wehrli, C.: Field comparison of network Sun photometers, J. Geophys. Res.-Atmos., 108, 4596, https://doi.org/10.1029/2002JD002964, 2003.

McPeters, R. D., Frith, S., and Labow, G. J.: OMI total column ozone: extending the long-term data record, Atmos. Meas. Tech., 8, 4845–4850, https://doi.org/10.5194/amt-8-4845-2015, 2015.

Mitchell, R. and Forgan, B.: Aerosol measurement in the Australian outback: Intercomparison of sun photometers, J. Atmos. Ocean. Tech., 20, 54–66, https://doi.org/10.1175/1520-0426(2003)020⟨0054:AMITAO⟩2.0.CO;2, 2003.

Mitchell, R. M., Forgan, B. W., and Campbell, S. K.: The Climatology of Australian Aerosol, Atmos. Chem. Phys., 17, 5131–5154, https://doi.org/10.5194/acp-17-5131-2017, 2017.

Nakajima, T., Yoon, S.-C., Ramanathan, V., Shi, G.-Y., Takemura, T., Higurashi, A., Takamura, T., Aoki, K., Sohn, B.-J., Kim, S.-W., Tsuruta, H., Sugimoto, N., Shimizu, A., Tanimoto, H., Sawa, Y., Lin, N.-H., Lee, C.-T., Goto, D., and Schutgens, N.: Overview of the Atmospheric Brown Cloud East Asian Regional Experiment 2005 and a study of the aerosol direct radiative forcing in east Asia, J. Geophys. Res.-Atmos., 112, D24S91, https://doi.org/10.1029/2007JD009009, 2007.

Nyeki, S., Halios, C., Baum, W., Eleftheriadis, K., Flentje, H., Gröbner, J., Vuilleumier, L., and Wehrli, C.: Ground-based aerosol optical depth trends at three high-altitude sites in Switzerland and southern Germany from 1995 to 2010, J. Geophys. Res.Atmos., 117, D18202, https://doi.org/10.1029/2012JD017493, 2012.

Nyeki, S., Gröbner, J., and Wehrli, C.: Ground-based aerosol optical depth inter-comparison campaigns at European EUSAAR super-sites, in Radiation Processes in the Atmosphere and Ocean (IRS2012), AIP Conf. Proc., 1531, 584–587, https://doi.org/10.1063/1.4804837, 2013.

Nyeki, S., Wehrli, C., Gröbner, J., Kouremeti, N., Wacker, S., Labuschagne, C., Mbatha, N., and Brunke, E.-G.: The GAWPFR aerosol optical depth network: The 2008–2013 time series at Cape Point Station, South Africa, J. Geophys. Res.-Atmos., 120, 5070–5084, 2015.

Räisänen, P. and Lindfors, A. V.: On the computation of apparent direct solar radiation, J. Atmos. Sci., https://doi.org/10.1175/JAS-D-19-0030.1, 2019.

Räisänen, P., Isaac, G. A., Barker, H. W., and Gultepe, I.: Solar radiative transfer for stratiform clouds with horizontal variations in liquid-water path and droplet effective radius, Q. J. Roy. Meteor. Soc., 129, 2135–2149, https://doi.org/10.1256/qj.02.149, 2003.

Rodríguez, S., González, Y., Cuevas, E., Ramos, R., Romero, P. M., Abreu-Afonso, J., and Redondas, A.: Atmospheric nanoparticle observations in the low free troposphere during upward orographic flows at Izaña Mountain Observatory, Atmos. Chem. Phys., 9, 6319–6335, https://doi.org/10.5194/acp-9-6319-2009, 2009.

Rodríguez, S., Alastuey, A., Alonso-Pérez, S., Querol, X., Cuevas, E., Abreu-Afonso, J., Viana, M., Pérez, N., Pandolfi, M., and de la Rosa, J.: Transport of desert dust mixed with North African industrial pollutants in the subtropical Saharan Air Layer, Atmos. Chem. Phys., 11, 6663–6685, https://doi.org/10.5194/acp-11-6663-2011, 2011.

Rodríguez, S., Cuevas, E., Prospero, J. M., Alastuey, A., Querol, X., López-Solano, J., García, M. I., and Alonso-Pérez, S.: Modulation of Saharan dust export by the North African dipole, Atmos. Chem. Phys., 15, 7471–7486, https://doi.org/10.5194/acp-15-7471-2015, 2015.

Rodriguez-Franco, J. J. and Cuevas, E.: Characteristics of the subtropical tropopause region based on long-term highly resolved sonde records over Tenerife, J. Geophys. Res.-Atmos., 118, 10– 754, https://doi.org/10.1002/jgrd.50839, 2013.

Romero, P. M. and Cuevas, E.: Variación diurna del espesor óptico de aerosoles: ¿ficción o realidad?, 3 Asamblea Hispano Portuguesa de Geofísica y Geodesia, Valencia, 2002.

Romero-Campos, P., Cuevas, A., Kazadzis, S., Kouremeti, N., García, R., and Guirado-Fuentes, C.: Análisis de la trazabilidad en los valores del AOD obtenidos a partir de las medidas de las redes AERONET-CIMEL y GAW-PFR durante el período 2005–2015 en el Observatorio Atmosférico de Izaña, 2017.

Russell, P., Livingston, J., Dubovik, O., Ramirez, S., Wang, J., Redemann, J., Schmid, B., Box, M., and Holben, B.: Sunlight transmission through desert dust and marine aerosols: Diffuse light corrections to Sun photometry and pyrheliometry, J. Geophys. Res.-Atmos., 109, D08207, https://doi.org/10.1029/2003JD004292, 2004.

Sakerin, S. M., Kabanov, D., Panchenk, M., Pol'kin, V., Holben, B., Smirnov, A., Beresnev, S., Gorda, S., Kornienko, G., Nikolashkin, S., Poddubnyi, V., and Tashchilin, M.: Monitoring of atmospheric aerosol in the Asian part of Russia in 2004 within the framework of AEROSIBNET program, Atmos. Ocean. Opt., 18, 871–878, 2005.

Sayer, A. M., Hsu, N. C., Bettenhausen, C., Jeong, M.-J., Holben, B. N., and Zhang, J.: Global and regional evaluation of over-land spectral aerosol optical depth retrievals from SeaWiFS, Atmos. Meas. Tech., 5, 1761–1778, https://doi.org/10.5194/amt-5-1761-2012, 2012.

Sayer, A. M., Hsu, N. C., Bettenhausen, C., and Jeong, M.: Validation and uncertainty estimates for MODIS Collection 6 "Deep Blue" aerosol data, J. Geophys. Res.-Atmos., 118, 7864–7872, https://doi.org/10.1002/jgrd.50600, 2013.

Schmid, B. and Wehrli, C.: Comparison of Sun photometer calibration by use of the Langley technique and the standard lamp, Appl. Opt., 34, 4500–4512, https://doi.org/10.1364/AO.34.004500, 1995.

Schmid, B., Michalsky, J., Halthore, R., Beauharnois, M., Harrison, L., Livingston, J., Russell, P., Holben, B., Eck, T., and Smirnov, A.: Comparison of aerosol optical depth from four solar radiometers during the fall 1997 ARM intensive observation period, Geophys. Res. Lett., 26, 2725–2728, https://doi.org/10.1029/1999GL900513, 1999.

107

Sinyuk, A., Holben, B. N., Smirnov, A., Eck, T. F., Slutsker, I., Schafer, J. S., Giles, D. M., and Sorokin, M.: Assessment of error in aerosol optical depth measured by AERONET due to aerosol forward scattering, Geophys. Res. Lett., 39, L25806, https://doi.org/10.1029/2012GL053894, 2012.

Smirnov, A., Holben, B., Eck, T., Dubovik, O., and Slutsker, I.: Cloud-screening and quality control algorithms for the AERONET database, Remote Sens. Environ., 73, 337–349, https://doi.org/10.1016/S0034-4257(00)00109-7, 2000.

Takamura, T. and Nakajima, T.: Overview of SKYNET and its activities, Opt. Pura Apl., 37, 3303–3308, 2004.

Thomason, L., Herman, B. M., Schotland, R. M., and Reagan, J. A.: Extraterrestrial solar flux measurement limitations due to a Beer's law assumption and uncertainty in local time, Appl. Opt., 21, 1191–1195, https://doi.org/10.1364/AO.21.001191, 1982.

Todd, M. C., Washington, R., Martins, J. V., Dubovik, O., Lizcano, G., M'bainayel, S., and Engelstaedter, S.: Mineral dust emission from the Bodélé Depression, northern Chad, during BoDEx 2005, J. Geophys. Res.-Atmos., 112, D06207, https://doi.org/10.1029/2006JD007170, 2007.

Toledano, C., Cachorro, V. E., Berjón, A., de Frutos, A. M., Sorribas, M., de la Morena, B. A., and Goloub, P.: Aerosol optical depth and Ångström exponent climatology at El Arenosillo AERONET site (Huelva, Spain), Q. J. Roy. Meteor. Soc., 133, 795–807, https://doi.org/10.1002/qj.54, 2007.

Toledano, C., Cachorro, V. E., Berjón, A., de Frutos, A. M., Fuertes, D., González, R., Torres, B., Rodrigo, R., Bennouna, Y., Martin, L., and Guirado, C.: RIMA-AERONET network: long term monitoring of aerosol properties, Opt. Pura Apl., 44, 629–633, 2011.

Toledano, C., Cachorro, V., Gausa, M., Stebel, K., Aaltonen, V., Berjón, A., de Galisteo, J. P. O., de Frutos, A. M., Bennouna, . Y., Blindheim, S., Myhre, C. L., Zibordi, G., Wehrli, C., Kratzer, S., Hakansson, B., Carlund, T., de Leeuw, G., Herber, A., and Torres, B.: Overview of Sun Photometer Measurements of Aerosol Properties in Scandinavia and Svalbard, Atmos. Environ., 52, 18–28, https://doi.org/10.1016/j.atmosenv.2011.10.022, 2012.

Toledano, C., González, R., Fuertes, D., Cuevas, E., Eck, T. F., Kazadzis, S., Kouremeti, N., Gröbner, J., Goloub, P., Blarel, L., Román, R., Barreto, Á., Berjón, A., Holben, B. N., and Cachorro, V. E.: Assessment of Sun photometer Langley calibration at the high-elevation sites Mauna Loa and Izaña, Atmos. Chem. Phys., 18, 14555–14567, https://doi.org/10.5194/acp-18-14555-2018, 2018.

Torres, B., Toledano, C., Berjón, A., Fuertes, D., Molina, V., Gonzalez, R., Canini, M., Cachorro, V. E., Goloub, P., Podvin, T., Blarel, L., Dubovik, O., Bennouna, Y., and

de Frutos, A. M.: Measurements on pointing error and field of view of Cimel318 Sun photometers in the scope of AERONET, Atmos. Meas. Tech., 6, 2207–2220, https://doi.org/10.5194/amt-6-2207-2013, 2013.

Wagner, F. and Silva, A. M.: Some considerations about Ångström exponent distributions, Atmos. Chem. Phys., 8, 481–489, https://doi.org/10.5194/acp-8-481-2008, 2008.

Wang, J., Xia, X., Wang, P., and Christopher, S.: Diurnal variability of dust aerosol optical thickness and Ångström exponent over dust source regions in China, Geophys. Res. Lett., 31, L08107, https://doi.org/10.1029/2004GL019580, 2004.

Wehrli, C.: Calibrations of filter radiometers for determination of atmospheric optical depth, Metrologia, 37, 419, https://doi.org/10.1088/0026-1394/37/5/16, 2000.

Wehrli, C.: GAWPFR: A network of aerosol optical depth observations with precision filter radiometers, GLOBAL ATMOSPHERE WATCH, p. 36, 2005.

Wehrli, C.: Precision Filter Radiometer Documentation,Version 4.0, 38 pp., Davos Dorf, 2008a.

Wehrli, C.: Remote sensing of aerosol optical depth in a global surface network, PhD thesis, ETH Zurich, available at: https://www.research-collection.ethz.ch/bitstream/handle/20.500.11850/150574/eth-30693-02.pdf (last access: 1 September 2018), 2008b.

Weinzierl, B., Sauer, D., Esselborn, M., Petzold, A., Veira, A., Rose, M., Mund, S., Wirth, M., Ansmann, A., Tesche, M., Gross, S., and Freudenthaler, V.: Microphysical and optical properties of dust and tropical biomass burning aerosol layers in the Cape Verde region – an overview of the airborne in situ and lidar measurements during SAMUM-2, Tellus B, 63, 589–618, https://doi.org/10.1111/j.1600-0889.2011.00566.x, 2011.

WMO: Recent Progress in Sunphotometry, Determination of theaerosol optical depth, Environmental Pollution Monitoring andResearch Programme, No. 43, 21 pp., November, 1986.

WMO: Recent Progress in Sunphotometry, Determination of the aerosol optical depth, Environmental Pollution Monitoring and Research Programme, No. 43, 21 pp., November, 1986. WMO: Aerosol measurement procedures, guidelines and recommendations, GAW Report No. 153, WMO TD No. 1178, avaible at: https://library.wmo.int/pmb_ged/wmo-td_1178.pdf (last access: 1 September 2018), 2003.

WMO: WMO/GAW Experts Workshop on a Global Surface-Based Network for Long Term Observations of Column Aerosol Optical Properties, GAW Report No. 162, WMO TD No. 1287, available at: https://library.wmo.int/pmb_ged/wmo-td_1287.pdf (last access: 1 September 2018), 2005.

WMO: Abridged final report with resolutions and recommendations, GAW Report WMO TD No. 1019, WMO-CIMO Fourteenth session Geneva 7–14 December 2006, 2007.

WMO: Commission for Instruments and Methods of Observation, Sixteenth session WMO no.1138, Saint Petersburg, Secretariat of the World Meteorological Organization, 2014.

WMO: Aerosol Measurement Procedures, Guidelines and Recommendations, 2nd Edition, WMO No 1177, 2016.

Young, A. T.: Revised depolarization corrections for atmospheric extinction, Appl. Opt., 19, 3427–3428, https://doi.org/10.1364/AO.19.003427, 1980.

7.1.4. Conclusiones

Como conclusión principal, podemos afirmar que el conjunto de datos de AOD proporcionados por AERONET y GAW-PFR, son representativos de la misma población de AOD para las bandas espectrales iguales o próximas a 440, 500 y 870 nm. Para 380 nm, la trazabilidad no llega al 95 % de los datos comunes, por lo que deben realizarse más esfuerzos para mejorar las medidas de AOD en este rango.

Estos resultados sugieren que los límites de trazabilidad de la WMO-CIMO (World Meteorogical Organization - Commission for Instruments and Methods of Observation) podrían redefinirse en función de la longitud de onda y debería reconsiderarse el rango de FOV del radiómetro recomendado. Los conjuntos de datos AERONET y GAW-PFR, ampliamente utilizados, juegan un papel crucial en la comprensión de los cambios de AOD a largo plazo y en la detección de tendencias, por lo que sería deseable que ambas redes estuvieran vinculadas a la misma referencia establecida por WMO-GAW.

7.2. Artículo 2: Un nuevo sistema para la observación del espesor óptico de aerosoles de polvo basado en radiómetros cenitales de banda estrecha (ZEN).
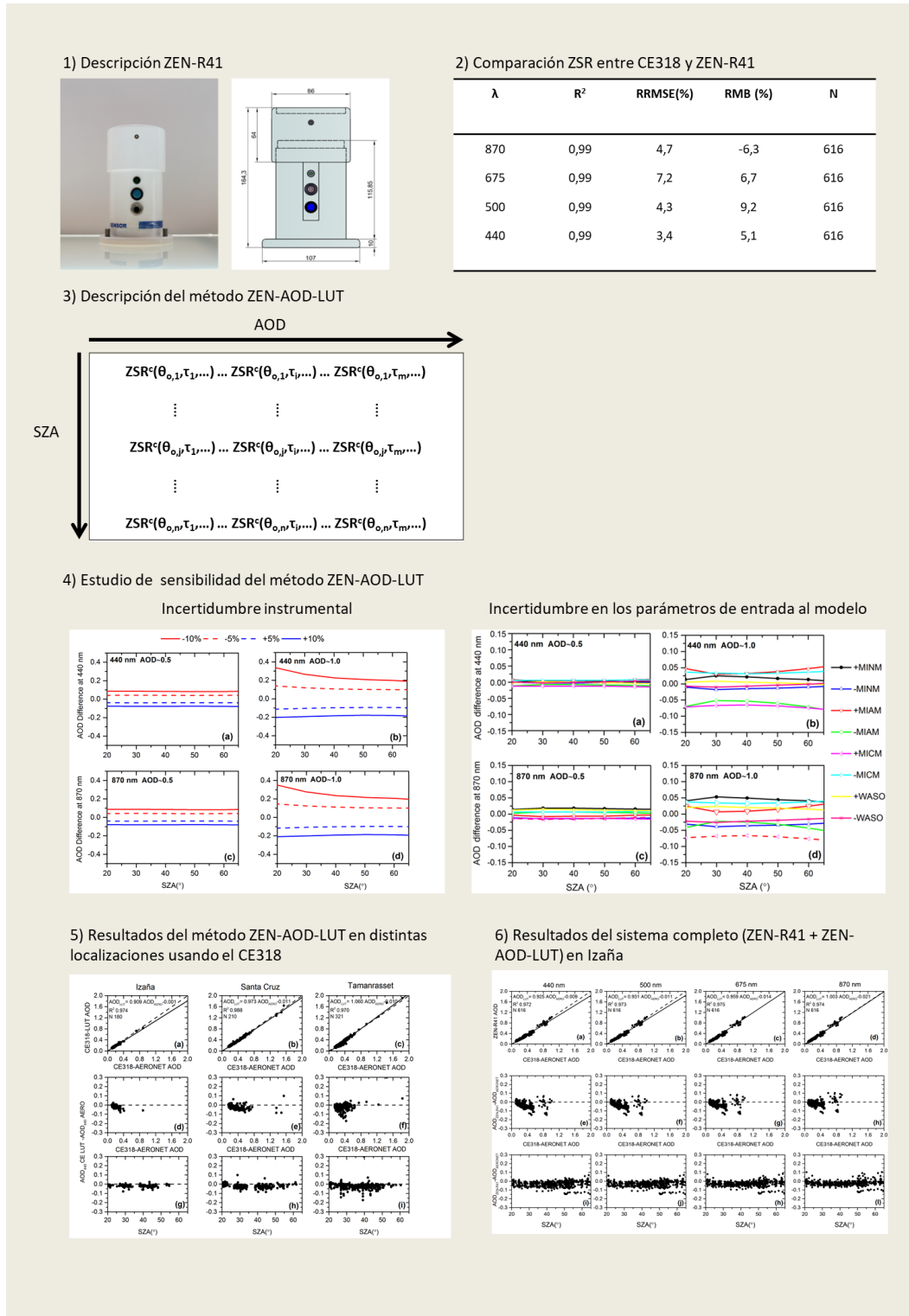
7.2.1. Resumen gráfico

Figura 7.2: Esquema gráfico del artículo 2.

7.2.2. Resumen

En este artículo presentamos los primeros resultados obtenidos con el sistema ZEN, un sistema de teledetección pasiva desde la superficie terrestre concebido para determinar el AOD mediante la medida de la ZSR. Dicho sistema se compone por el radiómetro cenital ZEN-R41 y la metodología tipo LUT ZEN-AOD-LUT. El radiómetro ZEN-R41 tiene un diseño simplificado y sin partes móviles que lo hacen compacto y robusto, ideal para su instalación en lugares remotos donde no es posible llevar a cabo un mantenimiento continuo del dispositivo. El método ZEN-AOD-LUT estima el AOD por comparación de la ZSR medida con una LUT de ZSRs obtenida mediante modelización con un código de transferencia radiativa (véase la sección 6.3).

Para verificar la bondad de las medidas de radiancia obtenidas con el ZEN-R41, se realizó una comparación de ZSR entre el ZEN-R41 y el instrumento de referencia, el fotómetro Cimel CE318, durante el año 2015 en el Observatorio Atmosférico de Izaña. Esta comparativa mostró una alta correlación entre ambas medidas, con un coeficiente de determinación (R^2) para todas las longitudes de onda de 0,99, aunque se observó un sesgo medio relativo (RMB) de entre el $-6,3\%$ a 870 nm y $9,2\%$ a 500 nm.

Se realizó un estudio sensibilidad para estimar la influencia que tienen las principales fuentes de error en el AOD final. Dicho estudio identificó a los errores instrumentales y a los errores cometidos en el establecimiento de los parámetros de los aerosoles, como los contribuyentes más importantes a la incertidumbre final del AOD. Este análisis estimó una incertidumbre estándar combinada del AOD de hasta 0,06 en el caso de $AOD_{500} \approx 0,5$, y 0,15 para $AOD_{500} \approx 1,0$, siempre que los errores instrumentales se minimicen al 5%.

La validación de la técnica ZEN-AOD-LUT fue realizada gracias a la utilización de los datos proporcionados por AERONET. Para dicha validación se comparó el AOD obtenido al aplicar el método ZEN-AOD-LUT en las ZSR del Cimel CE318, (obtenido a partir de las medidas de radiancia de cielo en la secuencia del plano principal; véase la subsección 5.1) y el AOD proporcionado por AERONET (obtenidos a partir de medidas de sol directa), en un periodo de un año, en tres localizaciones distintas afectadas por episodios de intrusión de polvo mineral: Izaña y Santa Cruz de Tenerife en las Islas Canarias y Tamanrasset en Argelia. Los resultados mostraron una alta correlación entre los conjuntos de datos con R^2 de entre 0,97 (Izaña) y 0,99 (Santa Cruz de Tenerife), y raíces de los errores cuadráticos medios (RMSE) de entre 0,010 (Izaña) y 0,032 (Tamanrasset).

Finalmente, se comparó el AOD obtenido con el radiómetro ZEN-R41 con el AOD

proporcionado por AERONET en el Observatorio Atmosférico de Izaña durante el año 2015. Dicha comparación mostró un buen acuerdo entre ambos conjuntos de datos (R^2 de 0,97), con diferencias observadas de hasta 0,15 para el AOD. Además, se comprobó que el ZEN-R41 subestima sistemáticamente el AOD con un sesgo promedio que varía entre $-0,020$ y $-0,030$. Estos resultados están de acuerdo con la incertidumbre esperada para el sistema ZEN.

7.2.3. Artículo 2

A new zenith-looking narrow-band radiometer-based system (ZEN) for dust aerosol optical depth monitoring

A. Fernando Almansa[1,2,4], Emilio Cuevas[1], Benjamín Torres[3], África Barreto[1,2], Rosa D. García[1,5], Victoria E. Cachorro[4], Ángel M. de Frutos[4], César López[6], and Ramón Ramos[1]

[1]Izaña Atmospheric Research Center (IARC), Meteorological State Agency of Spain (AEMET), Santa Cruz de Tenerife, 38001, Spain

[2]Cimel Electronique, Paris, 75011, France

[3]Laboratoire d'Optique Amosphérique, UMR8518, Université des Sciences et Technologies de Lille, Villeneuve d'Ascq, France

[4]Group of Atmospheric Optics, University of Valladolid, Valladolid, 47011, Spain

[5]Air Liquide España, Delegación Canarias, Candelaria, 38509, Spain

[6]Sieltec Canarias S.L., La Laguna, 38230, Spain

Correspondence to: Emilio Cuevas (ecuevasa@aemet.es)

Abstract. A new zenith-looking narrow-band radiometer based system (ZEN), conceived for dust aerosol optical depth (AOD) monitoring, is presented in this paper. The ZEN system comprises a new radiometer (ZEN-R41) and a methodology for AOD retrieval (ZEN-LUT). ZEN-R41 has been designed to be stand alone and without moving parts, making it a low-cost and robust instrument with low maintenance, appropriate for deployment in remote and unpopulated desert areas. The ZEN-LUT method is based on the comparison of the measured zenith sky radiance (ZSR) with a look-up table (LUT) of computed ZSRs. The LUT is generated with the LibRadtran radiative transfer code. The sensitivity study proved that the ZEN-LUT method is appropriate for inferring AOD from ZSR measurements with an AOD standard uncertainty up to 0.06 for $AOD_{500\ nm}$ ~ 0.5 and up to 0.15 for $AOD_{500\ nm} \sim 1.0$, considering instrumental errors of 5%. The validation of the ZEN-LUT technique was performed using data from AErosol RObotic NETwork (AERONET) Cimel Electronique 318 photometers (CE318). A comparison

between AOD obtained by applying the ZEN-LUT method on ZSRs (inferred from CE318 diffuse-sky measurements) and AOD provided by AERONET (derived from CE318 direct-sun measurements) was carried out at three sites characterized by a regular presence of desert mineral dust aerosols: Izaña and Santa Cruz in the Canary Islands and Tamanrasset in Algeria. The results show a coefficient of determination (R^2) ranging from 0.99 to 0.97, and root mean square errors (RMSE) ranging from 0.010 at Izaña to 0.032 at Tamanrasset. The comparison of ZSR values from ZEN-R41 and the CE318 showed absolute relative mean bias (RMB) < 10%. ZEN-R41 AOD values inferred from ZEN-LUT methodology were compared with AOD provided by AERONET, showing a fairly good agreement in all wavelengths, with mean absolute AOD differences < 0.030 and R^2 higher than 0.97.

1 Introduction

Atmospheric aerosols play an important role in the environment, especially affecting air quality and climate. Concerning the Earth's climate, atmospheric aerosols are one of the main drivers of climate change and the most uncertain of them (Stocker et al., 2013). These atmospheric constituents can affect the Earth's radiative balance by scattering and absorbing the incoming solar radiation and the outgoing terrestrial radiation (aerosol–radiation interactions) but also by influencing cloud formation and reflectivity (aerosol– cloud interactions; Klein et al., 2010; Hoose and Möhler, 2012; Stocker et al., 2013). Furthermore, aerosols are not uniformly distributed in the atmosphere, but show a high spatial and temporal variability. For these reasons, a good knowledge of the microphysical and optical properties of atmospheric aerosols is necessary all over the world. In this respect, aerosols remote sensing by means of satellite and ground-based devices is normally used to routinely monitor the aerosols columnar optical and microphysical properties, the latter obtained by inversion techniques (i.e. Dubovik and King, 2000). Regarding the aerosol optical properties, the aerosol optical depth (AOD) and its spectral dependence are the most common and important parameters for aerosol characterization, widely used in models and satellite sensors.

Remote sensing from satellite platforms has proved to be an effective tool for global and long-term monitoring of aerosols in the atmosphere. Early satellite sensors, such as the Advanced Very High Resolution Radiometer (NOAA/AVHRR Stowe et al., 1997) or TOMS (Total Ozone mapping Spectrometer; Herman et al., 1997; Torres et al., 1998), permitted the AOD estimation spanning from 1979 to the present. In recent years, a more advanced generation of active and passive satellite sensors for aerosol detection have been used to estimate aerosol radiative forcing

on a global scale, such as MODIS (Moderate Resolution Imaging Spectrometer), MISR (Multi-angle Imaging Spectro-Radiometer), both in operation since 2000 (Tanré et al., 1997; Zhang and Reid, 2006, 2010), and CALIPSO (Cloud-Aerosol Lidar and Infrared Pathfinder Satellite Observations; Winker et al., 2010). However, as Li et al. (2009) suggested, satellite AOD retrievals are subject to important uncertainties due to radiometric calibration, a priori assumed aerosol properties, cloud contamination and correction of the surface effect. In particular, a reliable determination of the ground reflectance is mandatory, because the signal measured by the on-board sensor is the sum of the top of atmosphere (TOA) reflection and the surface reflection. A reliable determination is especially important over bright land surfaces like deserts, where the main dust sources are located. Moreover, the temporal resolution of satellite-borne sensors over a specific point is quite limited (one observation per day as maximum) and represents a high limitation for dust storm monitoring since they develop very fast in time periods of few hours.

There are currently extensive networks of ground-based sun photometers all over the world dedicated to aerosol monitoring. These networks are integrated by very precise instruments, close to the 0.02 AOD accuracy suggested as a goal by the World Meteorological Organization (WMO; Schmid et al., 1999; WMO, 1993). Among others, the WMO GAW-PFR network (Wehrli, 2005), SKYNET (Takamura and Nakajima , 2004), CARSNET (Che et al., 2015) and AERONET (Holben et al., 1998) are the most important. AERONET (AErosol RObotic NETwork) is the most widespread network using the Cimel Electronique 318 photometer as the standard instrument (hereinafter CE318). At present, this network provides unique long-term open-access data with aerosol optical, microphysical and radiative properties, which constitute an important source of information for climate and environmental sciences, since their results have been widely tested under quite different conditions (Eck et al., 1999, 2001, 2003a, b, 2008, 2009, 2010; Holben et al., 2001). However, in the Northern Hemisphere there is a lack of stations in desert regions, which are the most important source of mineral dust, leading to an unsatisfactory description of dust cycles. Although AERONET sun photometers operate automatically, they need to be checked on a daily basis and frequently maintained by trained staff to assure data quality. These instruments operate using a sun tracker, which is a moving element and the origin of most of the operational problems. In addition, the relatively high cost of sun photometers is a constraint for many developing countries located in desert regions.

For all the above reasons, in this paper we present a new system (ZEN), composed of the radiometer ZEN-R41 and a new methodology especially conceived to estimate AOD from downwelling zenith sky radiance (ZSR) observations for desert dust conditions. This system has been jointly developed by SIELTEC Canarias S.L.

company (SIELTEC) and the Izaña Atmospheric Research Center (IARC) from the State Meteorological Agency of Spain (AEMET). The use of ZSR as the direct measurable magnitude simplifies the design of the radiometer ZEN-R41, avoiding the use of sun tracker, making it more robust, automated and available at a lower cost than classical sun photometers. However, the AOD calculation is not as straightforward and precise as using direct-sun measurements, and some a priori assumptions must be made about aerosol properties, and significant additional efforts must be done in the modelling part. As made in the techniques employed by some on-board satellites sensors (Kaufman et al., 1997; Tanré et al., 1997; Stowe et al., 1997; Torres et al., 1998), and some previous work with ground based instrumentation (Lindfors et al., 2013), we have developed a look-up table (LUT)-based methodology (ZEN-LUT) specifically designed for desert aerosols to estimate AOD. The LUTs are composed of a set of simulated ZSR and AOD values obtained with the radiative transfer code LibRadtran (Mayer and Kylling, 2005). The AOD is then inferred by minimizing a function which depends on the difference between simulated and measured ZSR at all used wavelengths. In this case, the surface albedo does not have as much influence as in the upwelling radiance measured by satellite sensors. These characteristics make the ZEN a suitable system for aerosol monitoring in remote desert areas, filling the current observational gaps and being useful in the validation of satellite sensors and models dust products.

The test sites and ancillary observations used in this study are described in Sect. 2. In Sect. 3 a description of the new ZEN-R41 radiometer and a performance comparison with CE318 are given. The AOD retrieval method, including the results of a sensitivity study performed to examine the impact of key input parameters as well as to assess the influence of the instrumental errors, is examined in Sect. 4. Section 5 describes the AOD comparisons between ZEN-R41 and collocated CE318. Finally, the main conclusions of this work are presented in Sect. 6.

2 Test sites and ancillary information

2.1 Test sites

The ZEN-LUT methodology and the ZEN-R41 instrument have been tested in three different sites impacted by the presence of desert mineral dust (Fig. 1).

The Izaña station (Izaña, Canary Islands, Spain; 28.3° N, 16.5° W, 2373 m a.s.l.) is a high mountain subtropical station which represents atmospheric background conditions most of the time as a consequence of its location over a strong temperature inversion layer as a result of general subsidence processes and the presence

119

Figure 1: Meteosat/TERRA image showing a Saharan dust outbreak over the study area on 12 January 2015. The Izaña, Santa Cruz and Tamanrasset sites are indicated with yellow stars.

of cool trade winds at lower levels. However, the proximity to the Saharan desert introduces an important influence of mineral dust on its aerosol climatology. As Basart et al. (2009) showed, there is an enhancement of dust transport from the Sahara to Izaña altitudes during summer ($AOD_{675\ nm} > 0.15$ and large particles with Angström Exponent, $\alpha_{440\text{-}870\ nm} < 0.25$), with $AOD_{675\ nm}$ values < 0.15 prevailing in the rest of the year, especially in winter, which represent $\sim 85\%$ of the overall conditions. Guirado (2014) also performed a detailed aerosol characterization at Izaña. This author found predominant dust conditions associated to $AOD_{500\ nm} > 0.10$ and large particles with $\alpha < 0.60$. Izaña Observatory is part of the WMO Global Atmosphere Watch programme (GAW) and the Network for the Detection of Atmospheric Composition Change (NDACC). Izaña is an absolute sun calibration site of AERONET and a World Radiation Center (WRC) Global Atmospheric Watch Precision Filter Radiometer (GAW/PFR) station and calibration site. The Izaña station is also a WMO CIMO (Commission for Instruments and Methods of Observation) Testbed for Aerosols and Water Vapour Remote Sensing Instruments (WMO, 2014).

Santa Cruz de Tenerife station (SCO, Canary Islands, Spain; 28.5° N, 16.2° W; 52 m a.s.l.) is an urban station located at sea level. The aerosol climatology at this station is dominated by the well-mixed combination of fine fraction of pollution aerosols and coarse model marine particles (prevailing $AOD_{675\ nm} > 0.15$) with mineral

dust influence from spring to autumn (Basart et al., 2009), increasing AOD and reducing α values. Following the work developed by Guirado et al. (2014), those situations with $AOD_{500 \text{ nm}} > 0.15$ and $\alpha < 0.5$ can be considered prevalent dust conditions at this station.

Tamanrasset station (TAM, Algeria; 22.8° N, 5.5° E, 1377 m a.s.l.) is located in southern Algeria in a key location near the most important dust sources of Mali, Argelia, Lybia and Chad, where there is little impact from industrial activities. Guirado et al. (2014) performed a thorough study to characterize aerosols at this Saharan station. They found that desert mineral dust is the predominant aerosol type in this station, where the dry-cool (winter) season is characterized by prevailing clear-sky conditions ($AOD_{440 \text{ nm}} \sim 0.09$ and $\alpha \sim 0.62$), while high turbidity events with coarse dust particles are frequent during the wet-hot (summer) season, associated to an $AOD_{440 \text{ nm}}$ modal value of 0.15 and $\alpha \sim 0.4$.

2.2 Ancillary information

2.2.1 CE318 sun photometer and AERONET network

In this work we have used AOD data provided by AERONET (Holben et al., 1998) to validate the results obtained with the ZEN-R41 radiometer and the ZEN-LUT technique. AERONET also provides information about microphysical and optical parameters, such as particle size distribution, refractive indices, single scattering albedo (SSA) or phase function using the inversion algorithm developed by Dubovik and King (2000); Dubovik et al. (2002, 2006).

The standard instrument used in AERONET is the CE318 sun photometer, which performs direct-sun and diffuse-sky measurements. Direct-sun measurements performed at 340, 380, 440, 500, 675, 870, 940 and 1020 nm are used to derive accurate AOD and precipitable water vapour with typical AOD uncertainties for field instruments ranging between ±0.01 and ±0.02, with the higher errors in the UV spectral range (Eck et al., 1999). Diffuse-sky measurements with two different routines are performed to infer the aerosol optical and microphysical properties: the almucantar (ALM) and the principal plane (PPL).

In the ALM routine, the azimuth angle is varied while the zenith angle is kept constant (equals to the solar zenith angle). On the other hand, in the PPL routine, the zenith is varied while the azimuth angle is kept constant (equals to the solar azimuth angle). The ALM measurements are performed in two wings: right (azimuth angle displaced towards the right of sun position) and left (azimuth angle displaced towards the left of sun position). In a homogeneous atmosphere, the

signal measured at both wings should be equal, so this fact can be used to detect wrong data, such as cloudcontaminated measurements. Contrary to ALM, PPL is not symmetric but wrong data can also be detected by checking the smoothness of the PPL curve (Holben et al., 1998). In the present study, the CE318 ZSR values are obtained by linear interpolation of the PPL data to the zenith position (it is not possible to do it with ALM measurements). To detect and remove the presence of clouds in data, we have visually checked hemispheric images in those places where an all-sky camera was available. In case an all-sky camera was not available at the station, a smoothness criterion was applied on the PPL curve to detect clouds. This smoothness criterion is based on the analysis of the second derivative of the PPL radiances with respect to the scattering angle. The data are considered cloud contaminated if the second derivative is negative at any scattering angle between 2 and 90°. The threshold value for this smoothness criterion is not 0 but -1×10^{-7}, as determined empirically.

2.2.2 SONA all-sky camera

In the present study we have checked cloud interference by means of independent measurements from all-sky Automatic Cloud Observation System SONA cameras developed by SIELTEC (González et al., 2012). The SONA cameras have been used to detect and remove CE318 and ZEN-R41 cloud-contaminated ZSR data at Izaña and Santa Cruz stations. Cloud cover detection was performed by visual inspection, by analysing each individual hemispheric image from the total sky cameras and identifying the presence of visible clouds around the zenith.

3 The ZEN-R41 narrow-band radiometer

The ZEN-R41 is a prototype radiometer jointly developed by SIELTEC and IARC and designed to obtain AOD from downwelling zenith sky radiation at different wavelengths. This prototype incorporates collimating lenses and internal baffles to achieve a $\sim 3°$ field of view. ZEN-R41 is equipped with four silicon detectors (350–1100 nm) and four optical filters of 10 nm FWHM with nominal wavelengths centred in 440, 500, 675 and 870 nm. These filters are hard coated to prevent ageing of their optical properties. The measurements, made simultaneously in the four channels, are amplified and acquired with 16 bit resolution (65536 counts per each level of amplification). Inside the instrument there are sensors for internal humidity and temperature monitoring, as well as a fan for temperature homogenization and electronic components protection. Using this internal information, ZEN-R41 signal is temperature corrected, allowing the minimization of the temperature dependence

of the silicon detectors. It is equipped with a small aluminum weatherproof (IP67 grade) case (white powder coated), with no moving parts and is protected by a thick borosilicate bk7 window (see Fig. 2), preventing it from damages such as scratches or direct impacts. The device also has a plate base which allows the instrument to be levelled and fixed on flat and rigid surfaces. As a result, the instrument's design is very robust and operates in a wide temperature range, between -40 and 85° C. An external blower attached to the external case is foreseen in order to facilitate the removal of dirt, dust or any other element that may affect measurements. In the case of remote locations, it is possible to use solar panels as a power source.

The on-board electronics comprise an internal 16 bits data logger and a 4 MB internal memory with Ethernet communications for data acquisition, display, download, set-up and diagnosis of the instrument. On-board processing is possible through its microcontroller board, with 16 MIPS of CPU speed and 96 KB of RAM memory, which result in a fast user-oriented data delivery (no additional parts or components are required) and a friendly user interface. The power and communications are performed together through a PoE port.
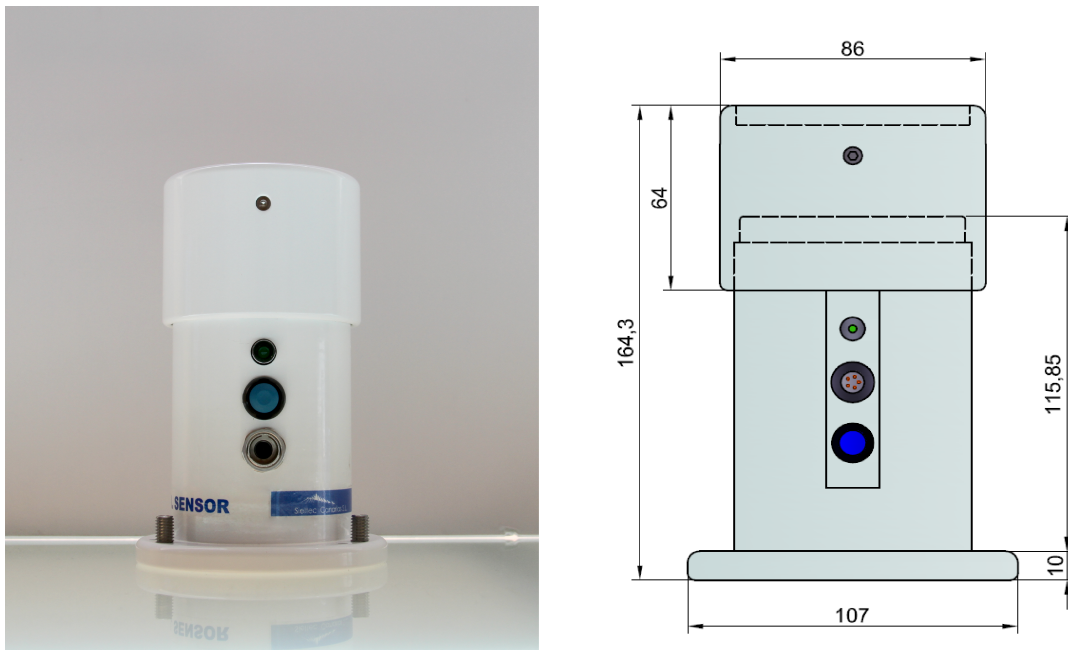

Figure 2: ZEN-R41 scheme and dimensions.

The instrument can work with fixed IP or in DHCP mode. Data can be downloaded manually or automatically and can also be sent via UDP or requested via TCP/IP protocol. It allows ZEN-R41 to form part of a ZEN-1 network for aerosol monitoring. This instrument can be also used independently or as a dependent sensor part of

a weather station or other instrument which requires AOD as input.

The web interface shows alarms when these internal variables are out of the normal ranges. All the settings and calibration factors can be entered via a web graphical user interface. ZEN-R41 was calibrated using an integrating sphere at the IARC facilities in order to convert the output signal into radiance units (W m^{-2} sr^{-1} nm^{-1}). We performed a set of 10 measurements of the sphere's radiance, in which we observed a very low variability in ZEN-R41 digital counts ($\sim$ 2‰). Since the uncertainty involved in this calibration procedure was established in $\sim$ 5% by Walker et al. (1991) and, assuming the sphere has a perfect precision (Holben et al., 1998), we can use this information to estimate the ZEN-R41 radiance uncertainty in a $\sim$ 5%.

3.1 ZEN-R41 and CE318 radiometric comparison at Izaña

In order to check the goodness of the radiometric measurements of the ZEN-R41, we have compared ZSR observations from this device with those provided by CE318 instruments, derived from PPL measurements. The ZSR measurements performed in Izaña station in 2015 were cloud screened using ancillary SONA all-sky images. In this comparison we have not included ZSR data for SZA < 20° and SZA > 65° as we have detected higher discrepancies in ZSR for such SZA ranges. In the case of SZA < 20°, the signal measured by ZEN-R41 device is larger than that obtained with CE318, which might be attributed to the lower stray light rejection and/or larger field of view of the ZEN-R41 radiometer. For SZA > 65°, we attribute the observed discrepancies to lower signals measured, which reduces the signal to noise ratio, increasing the instrument's uncertainty. We present a basic statistics of ZSR intercomparison for the four coincident spectral bands (440, 500, 675 and 870 nm) in Table 1. ZSR measured by both instruments are highly correlated, with coefficients of determination (R^2) $\sim$ 0.99 for the four spectral ranges, discarding possible nonlinearities of ZEN-R41 in the selected measurement range. However, the relative mean bias results (RMB) showed that ZEN-R41 ZSR slightly overestimates at 675, 500 and 440 nm, but underestimates at 870 nm. RMB also showed a moderate variability in the measured ZSR, with values ranging from 6.3% at 870 nm to 9.2% at 500 nm, which is within the combined uncertainty of both instruments ($\sim$ 5%).

Table 1: Coefficient of determination (R^2), relative root mean square error (RRMSE) in %, relative mean bias (RMB) in % and number of coincident data (N) for the ZSR comparisons between CE318 and ZEN-R41 measurements at four different spectral bands (440, 500, 675 and 870 nm) performed at Izaña in 2015.

Wavelength	R^2	RRMSE	RMB	N
870	0.99	4.7	-6.3	616
675	0.99	7.2	6.7	616
500	0.99	4.3	9.2	616
440	0.99	3.4	5.1	616

4 ZEN-LUT method

For estimating the AOD from downwelling ZSR measurements under cloud-free conditions, we used the ZEN-LUT method. This method is based on the comparison of measured ZSRs, corrected from earth–sun distance, with a set of simulated ZSR values at the four wavelengths available in the ZEN-R41 radiometer (440, 500, 675 and 870 nm). The LUT was determined using the LibRadtran radiative transfer model (RTM). This model is available in a complete software package containing a suite of tools for radiative transfer calculations in the Earth's atmosphere (freely available from http://www.libradtran.org; Mayer and Kylling, 2005; Emde et al., 2016). The LibRadtran structures the atmosphere as multi-layers, considering the vertical profiles of temperature, pressure and atmospheric components, such as gases and aerosols. A complete treatment of the absorption scattering processes offers hundreds of options and input parameters to handle all the structure that has a detailed RTM. It also includes several libraries which help to describe the atmosphere and the ground surface contribution on the simulated radiation field. Concerning the aerosol contribution, we have used the OPAC (Optical Properties of Aerosols and Clouds) library (Hess et al., 1998). The aerosols in OPAC can be defined through 10 basic components. These are water insoluble (INSO), water soluble (WASO), soot (SOOT), two sea salt components (sea salt accumulation mode or SSAM and sea salt coarse mode or SSCM), four mineral dust components (mineral nucleus mode, MINM, mineral accumulation mode, MIAM, mineral coarse mode, MICM, and mineral transported, MITR) and the sulfate component (SUSO). Additionally, LibRadtran includes four spheroid components (MINM, MIAM, MITR and MICM spheroids) to define the mineral dust aerosols. The effects of relative humidity are taken into account for those components affected by water. Every component is defined by their microphysical properties, that is, the refractive index, mostly taken from d'Almeida et al. (1991) and a log-normal size distribution (Deepak and Gerber, 1983). Then, through Mie-scattering calculation (Wiscombe, 1980; Bohren

and Huffman, 1983), or the T-matrix method (Mishchenko and Travis, 1998) in the case of spheroids, the optical properties are calculated for every component and normalized to 1 particle cm^{-3}.

The ZSR values were calculated by using the radiative transfer equation (RTE) solver CDISORT (Buras et al., 2011). The extraterrestrial solar flux was selected from Kurucz (1992) with a spectral resolution of 1 nm. The midlatitude summer standard model for the atmosphere profile and the molecular absorption, parameterized with the LOWTRAN band model (Pierluissi and Peng, 1985), as adopted from the SBDART code (Ricchiazzi et al., 1998), were used. We have also used a common normalized Gaussian filter function for the four considered spectral bands centred in the nominal wavelength (440, 500, 675 and 870 nm). To set the surface reflectance contribution, we have considered the albedo definitions given in the IGBP (International Geosphere Biosphere Programme) library, which originates from the NASA CERES/SARB Surface Properties Project (Belward and Loveland, 1996).

Concerning the solar position, only the solar zenith angle (SZA) is given as input to the model, since the computed radiance in the zenith direction for a cloud-free sky is invariable with the solar azimuth angle. The earth–sun distance correction is directly applied in the measured ZSR, so the ZEN-LUT ZSRs are only simulated for the mean earth–sun distance.

The aerosol optical properties were obtained with the OPAC library (Hess et al., 1998) by defining the height profiles of every aerosol component present at every layer. The height of all layers and the mix of aerosol components present at every layer except the boundary layer were set up following the indications given in Hess et al. (1998). In the case of the boundary layer, we decided to set the mix of aerosol components dynamically, adopting the suggestions given in the Global Aerosol Data Set (GADS) report (Koepke et al., 1997) for desert regions. They proposed a mix of four different components, three mineral dust components (MINM, MIAM and MICM), plus a certain fixed quantity of water soluble component (WASO). The ratio of three mineral dust components present in the mixture is variable and depends on the total mineral dust particle density ($N_{mineral}$). The three mineral dust components are related to $N_{mineral}$ through the following expressions (Koepke et al., 1997):

$$\ln\left(N_{MINM}\right) \sim 0.104 + 0.963 \cdot \ln\left(N_{mineral}\right), \tag{1}$$

$$\ln\left(N_{MIAM}\right) \sim -3.94 + 1.29 \cdot \ln\left(N_{mineral}\right), \tag{2}$$

$$\ln\left(N_{MICM}\right) \;\sim\; -13.7 + 2.06 \cdot \ln\left(N_{mineral}\right), \tag{3}$$

In our calculations we have used the spheroid LibRadtran definitions.

It is important to note that the empirical relationships presented on these equations were derived for average conditions in desert areas, therefore they seem to be appropriate to describe the actual aerosols in Tamanrasset station, located in the middle of the Sahara desert, but not for Izaña and Santa Cruz stations, which are located hundreds of kilometres away from the Sahara desert, over the North Atlantic. In the latter, the presence of large mineral dust particles is considerably reduced due to a faster deposition during its transport out of dust source regions and to the predominance of other aerosols in the absence of Saharan intrusions. Because there is not a comprehensive definition of aerosols in terms of OPAC components, we propose a different mixture of components for these sites. This mixture involves the same WASO and MINM contribution as desert-type aerosols, but the MIAM component is replaced by MITR, keeping the same relationship with $N_{mineral}$ as MIAM, and the MICM contribution is discarded.

We have generated the LUT using a set of n values for $N_{mineral}$, ranging from 0 to 4000 particles cm^{-3}, in order to calculate n height profiles, each one composed of all aerosol components present in every layer $(N_i(h))$. Then, with these profiles, we simulate a set of n ZSR values for each SZA, in addition to the corresponding AOD in the ZEN-LUT.

Finally, to find out the right value for $N_{mineral}$ and thus the right AOD from the LUT, we applied an adapted version of the method described in Tanré et al. (1997), originally designed to select the right aerosol model from satellite radiance measurements. In this case, the selection is performed by finding the minimum value of the following expression:

$$\epsilon_l = \sqrt{\frac{1}{N_\lambda}\sum_{\lambda=1}^{N_\lambda}\left(\frac{L_\lambda^m(\theta_v=0,\theta_s)-L_{\lambda,l}^c(\theta_v=0,\theta_s)}{L_\lambda^m(\theta_v=0,\theta_s)}\right)^2}, \tag{4}$$

where L_λ^m and $L_{\lambda,l}^c$ are the measured (earth–sun distance corrected) and the computed radiances in wavelength λ, N_λ is the total number of wavelengths and l is the index indicating a value defined in the array $N_{mineral}$. θ_v is the viewing zenith angle which is equal to zero and θ_s the solar zenith angle. Then the value of the index l, which minimizes the quantity l, indicates the right value for $N_{mineral}$ and AOD.

4.1 ZEN-LUT method sensitivity study

The precision and accuracy of the solution given by the presented ZEN-LUT method are related to random and systematic errors. In the present work we have focused on performing a sensitivity study on the main systematic errors, which can be classified in two categories: instrumental errors, and errors made in the a priori considered RTM inputs, causing underestimation or overestimation in the measured and simulated ZSR, which affects the retrieved AOD. In the first category, radiance calibration error, levelling error, misalignments of the optical parts, the effect of the finite field of view and the stray light contribution are included. The assumed values for surface albedo and the a priori considered mixture of aerosol components are included in the second category.

We have performed this sensitivity study using the inputs previously defined in Sect. 4.

This type of analysis is commonly used to identify the dominant contributors to the output variability. However, if the effect of each source of error is conveniently quantified, it is possible to estimate the contribution of each parameter to the uncertainty in the final AOD retrieval.

4.1.1 Instrumental error sensitivity

Taking into account previous studies in the literature (Eck et al., 1999; Basart et al., 2009; Guirado et al., 2014; Cesnulyte et al., 2014; Cuevas et al., 2015) and AERONET climatology tables (https://aeronet.gsfc.nasa.gov/cgi-bin/climo_menu_v2_new), AOD desert stations such as Tamanrasset (Algeria), Ouarzazate (Morocco), Dakar (Senegal) and Solar Village (Saudi Arabia) show monthly and seasonal values typically ranging between 0.04 (Ouarzazate in January) and 0.67 (Dakar in June), with sporadic AOD maxima > 1 associated with strong desert dust outbreaks or local dust resuspension. Therefore, we have focused our sensitivity study in AOD conditions varying between 0.5, which corresponds to hazy conditions by dust, and 1, indicating strong dust intrusions.

We have assumed the ZEN-R41 calibration uncertainty to be $\sim 5\%$ considering the comparison analysis with an integrating sphere presented in Sect. 3. In order to evaluate the influence of the overall instrumental errors on the inferred AOD we have perturbed the computed ZSR ± 5 and $\pm 10\%$ for two aerosol loads ($AOD_{500\ nm} \sim 0.5$ and 1.0) at all the available wavelengths and SZAs ranging from 20 to 65° in 10° steps. Although this perturbed range should be statistically estimated by comparing several ZEN-R41 instruments, we have selected these values according

to the relative mean bias results obtained in the ZSR comparison between CE318 and ZEN-R41 presented in Sect. 3.1 and Table 1, in which we considered the CE318 as the reference instrument. Differences in AOD obtained from unperturbed and perturbed ZSR values are presented in Fig. 3 for 440 and 870 nm wavelengths. In case of $AOD_{500\ nm} \sim 0.5$, we obtained absolute differences < 0.05 and < 0.1 for perturbed radiances of ± 5 and $\pm 10\%$, which are not dependent on SZA and wavelength. For higher aerosol load conditions ($AOD_{500\ nm} \sim 1.0$), we have found nearly constant AOD differences of approximately -0.1 and -0.2 with SZA for negative radiance perturbations of -5 and -10% respectively. However, in the case of positive ZSR perturbations, we observed a SZA dependence with higher AOD differences as SZA decreases, up to ~ 0.35 for a positive radiance perturbation of 10% and SZA of 20°.

Table 2: Sensitivity study for an albedo perturbation of $\pm 15\%$. AOD differences between perturbed and unperturbed situations (ΔAOD) for 440 and 870 nm spectral bands are shown for two AOD values ($AOD_{500\ nm} \sim 0.5$ and 1.0) and different solar zenith angles (SZA) ranging from 20° to 65°.

AOD	SZA	ΔAOD_{440}	ΔAOD_{870}
0.5	20	-0.006/0.006	-0.006/0.007
	30	-0.010/0.010	-0.011/0.011
	40	-0.013/0.013	-0.013/0.013
	50	-0.015/0.016	-0.015/0.017
	60	-0.017/0.017	-0.017/0.017
	65	-0.016/0.017	-0.016/0.017
1.0	20	-0.016/0.017	-0.016/0.018
	30	-0.023/0.024	-0.025/0.026
	40	-0.028/0.030	-0.031/0.033
	50	-0.032/0.033	-0.035/0.038
	60	-0.033/0.036	-0.037/0.040
	65	-0.033/0.034	-0.037/0.040

4.1.2 RTM input sensitivity

Surface albedo sensitivity

The effect of the albedo uncertainty on the inferred AOD was also assessed for the same AOD and solar zenith angle range. We have performed the study for albedo values $\pm 15\%$ of those values used in the generated look-up table. We have considered this variation range, taking into account the results obtained by Tsvetsinskaya et
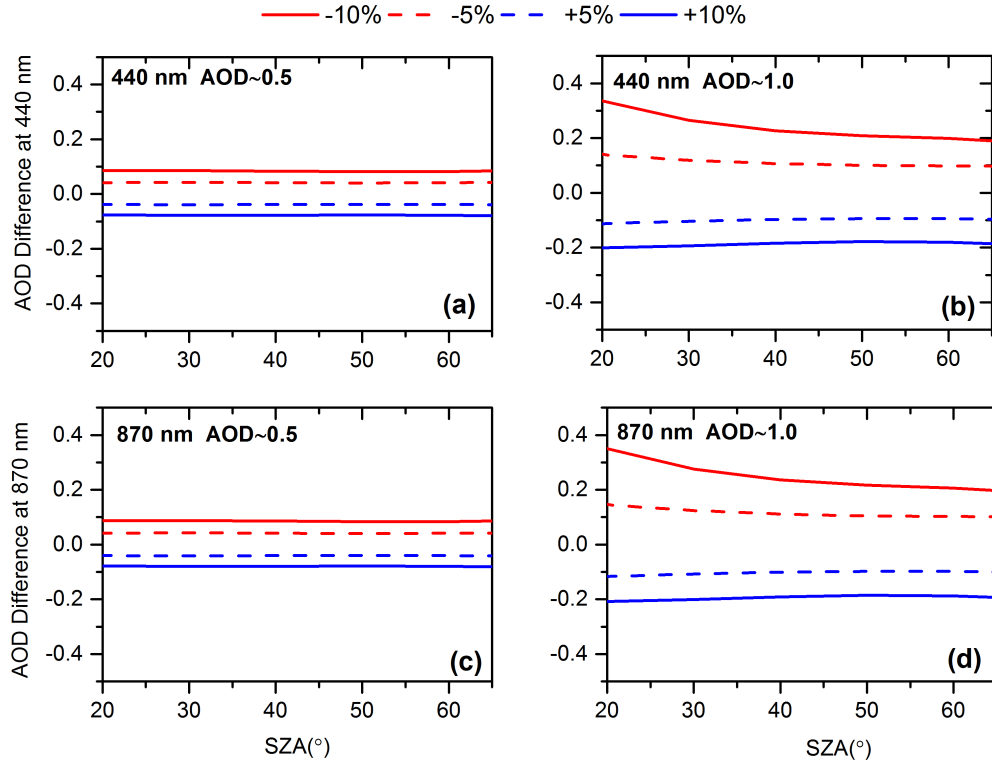
Figure 3: AOD difference versus SZA for different AOD conditions ($AOD_{500\ nm} \sim 0.5$ and 1.0) and ZSR perturbed $\pm 5\%$ and $\pm 10\%$, for 440 nm (a, b) and 870 nm (c, d).

al. (2006), who studied the spatial and temporal variability of surface albedo using MODIS data. They found very stable albedo values with a temporal variability that are essentially negligible in cases of surfaces with high reflectivity, such as deserts, and spatial variations between 14 ($\lambda < 700$ nm) and 9% ($\lambda > 700$ nm). Consequently, a variability in surface albedo of 15% seems reasonable for our sensitivity study. The computed ZSR with the modified albedo values are used as inputs to retrieve the AOD and the result is compared with the actual AOD. The AOD differences for 440 and 870 nm, and several SZA and $AOD_{500\ nm}$ values are shown in Table 2. This table shows that the surface reflectance effect on AOD is relatively low, with AOD differences somewhat higher with SZA, ranging from -0.016 to 0.017 for an $AOD_{500\ nm} \sim 0.5$, and from -0.037 to 0.040 for an $AOD_{500\ nm} \sim 1.0$. The wavelength dependence is also almost negligible.

Mix of aerosol components sensitivity

In order to test the influence of the mixture of aerosol components in the inferred AOD, we have modified the assumed mixing ratio of the reference LUT for mineral dust and WASO components present in the boundary layer. Mineral dust components were perturbed in $\pm 5\%$ of the slope coefficient in Eqs. (1), (2) and (3), and WASO components, assumed as a fixed value, were perturbed assuming a variation in concentration of $\pm 50\%$. AOD differences considering perturbed and unperturbed values for the mix of aerosol components are presented in Fig. 4 for two AOD conditions (AOD$_{500\ nm} \sim 0.5$ and 1.0) and two spectral ranges (440 and 870 nm). We have found negligible influence for AOD$_{500\ nm} \sim 0.5$, with AOD differences ranging from ± 0.02 for all aerosol components, although a slight dependence with SZA and wavelength can be appreciated. For higher aerosol content (AOD$_{500\ nm} \sim 1.0$), we observed little dependence with SZA and wavelength on AOD difference. We found AOD differences ranging from -0.1 to 0.05.
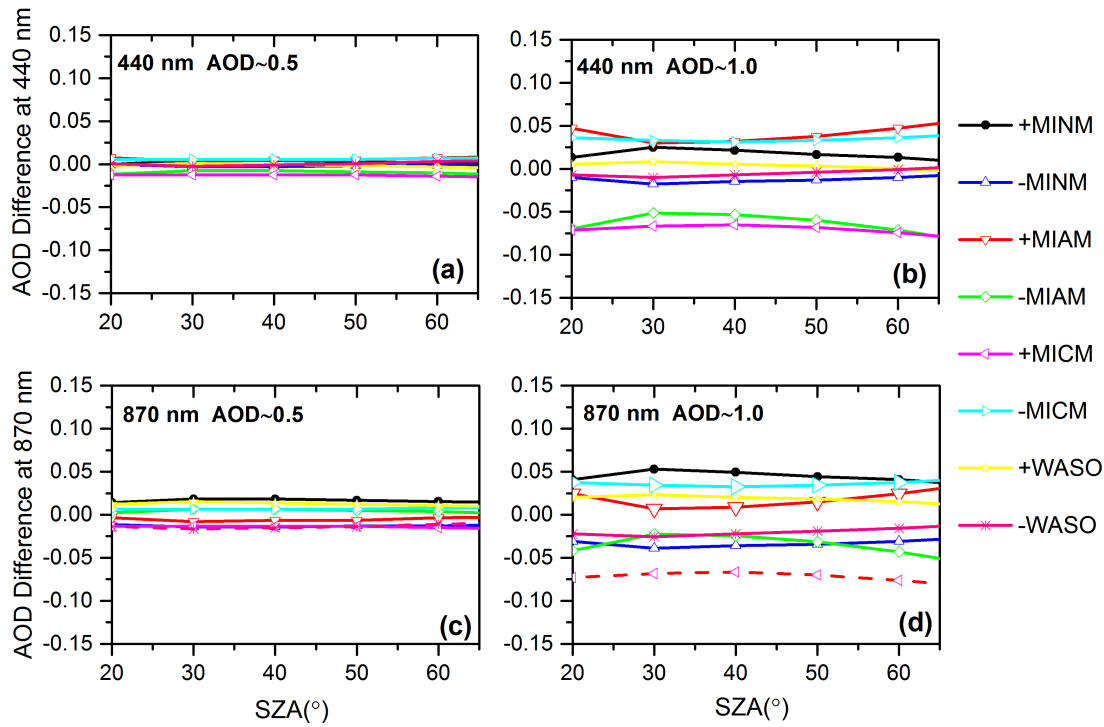
Figure 4: AOD difference versus SZA for different AOD conditions (AOD$_{500\ nm} \sim 0.5$ and 1.0) and 440 nm (a, b) and 870 nm (c, d) wavelengths. We have included different concentrations of four different aerosol components, MINM, MIAM and MICM perturbed in ± 5 WASO concentration perturbed in ± 50 %.

This sensitivity analysis showed that ZEN AOD combined standard uncertainty (determined by means of summation in quadrature of each term analysed in the sensitivity study) is up to 0.06 (for $AOD_{500\ nm} \sim 0.5$) and 0.15 (for $AOD_{500\ nm} \sim 1.0$) when an instrumental error of 5% is considered. Higher AOD uncertainty is expected if instrumental error is > 5%, up to 0.23 in the 10% limit of instrumental error (0.37 in case of very low SZAs).

5 Results

5.1 ZEN-LUT method validation at three different AERONET sites

The performance of the ZEN-LUT methodology was tested in three different sites in which mineral dust plays an important role in their respective aerosol climatologies (Izaña, Santa Cruz and Tamanrasset) using a CE318 instrument as a reference, since it has been already widely tested under quite different conditions (Eck et al., 1999, 2001, 2003a, b, 2010; Holben et al., 2001, 2006; Dubovik et al., 2000). The CE318-LUT AOD was inferred after applying the ZEN-LUT methodology on ZSR data derived from PPL data provided by AERONET.

AOD data from Izaña and Santa Cruz stations were cloud screened using information from the SONA all-sky imager. Since any all-sky camera was available at Tamanrasset station, the cloud screening was performed by applying the PPL smoothness criteria described in Sect. 2.2.1.

We have restricted this analysis to desert dust events. We have identified the desert aerosol conditions following the criteria given in Guirado (2014), and Guirado et al. (2014) (Sect. 2.1). We have used AERONET data for the year 2013, as it was the most recent period of available AERONET 2.0 level AOD data in the three sites. The comparison analysis performed at the three stations at every available wavelength (440, 675 and 870 nm) is shown in Figs. 5, 6 and 7 and Table 3. We present the AOD CE318-LUT/CE318-AERONET scatter plot in Figs. 5a–c, 6a–c and 7a–c, which shows a good agreement for all channels in the three locations, with high correlations ($R^2 > 0.97$). We have also found low RMSE values for Izaña and Santa Cruz (up to 0.011 and 0.021) but higher values for Tamanrasset (up to 0.032). The linear dependence between the two AOD data sets is different in the considered channels, with the lower slope having the shorter wavelength at all sites, and more evidently for Izaña. With regard to the AOD differences plotted in Figs. 5d–i, 6d–i and 7d–i, it can be said that AOD is mostly underestimated by the ZEN-LUT method, with negligible dependence with SZA for the SZA range considered in this study. We have found maximum AOD differences up to -0.07 for Izaña and

between -0.08 and 0.12 for Santa Cruz. These values are in agreement with the expected uncertainty involved in the ZEN-LUT methodology of AOD determination presented in Sect. 4.1. It also confirms the low instrumental errors affecting the CE318 ($\sim 5\%$). The considerably higher differences found for Tamanrasset might be explained by possible dust contamination of the CE318 lenses.

Table 3: Coefficient of determination (R^2), root mean square error (RMSE), mean bias (MB), and number of coincident data (N) for the AOD comparison between CE318-AERONET and CE318-LUT at three different spectral bands (440, 675 and 870 nm) performed at Izaña (IZO), Santa Cruz (SCO) and Tamanrasset (TAM) stations in 2013.

Station	Wavelength (nm)	R^2	$RMSE$	MB	N
IZO	870	0.97	0.011	-0.018	180
	675	0.98	0.010	-0.020	180
	440	0.97	0.011	-0.018	180
SCO	870	0.99	0.021	-0.021	210
	675	0.99	0.021	-0.019	210
	440	0.99	0.021	-0.020	210
TAM	870	0.98	0.030	-0.031	321
	675	0.98	0.030	-0.022	321
	440	0.97	0.032	-0.023	321

5.2 ZEN-R41 and CE318 AERONET AOD comparison at Izaña

We have performed an intercomparison of AOD from ZEN-R41 and CE318 at Izaña station during 2015. ZEN-R41 AOD, retrieved by applying the ZEN-LUT method to cloud-screened ZSR data, was compared with AERONET level 1.5 AOD for the 20-65° SZA range. The results of the intercomparison for the four spectral bands are presented in Fig. 8 and Table 4. In Fig. 8a–d we present a scatter plot between ZEN-R41 and CE318-AERONET AOD. A good correlation can be observed between both AODs, with $R^2 = 0.97$ and RMSEs ~ 0.026-0.027 for all channels, indicating that the ZEN-R41 instrument and ZEN-LUT method together are adequate for AOD estimation. However, as we pointed out in the previous subsection, the linear dependence between the two AOD data sets is different in the four channels. The AOD differences plotted in Fig. 8e–l shows a similar behaviour to those presented in the former subsection for Izaña, showing that AOD is mostly underestimated; although in this case the differences are larger as we have found maximum observed
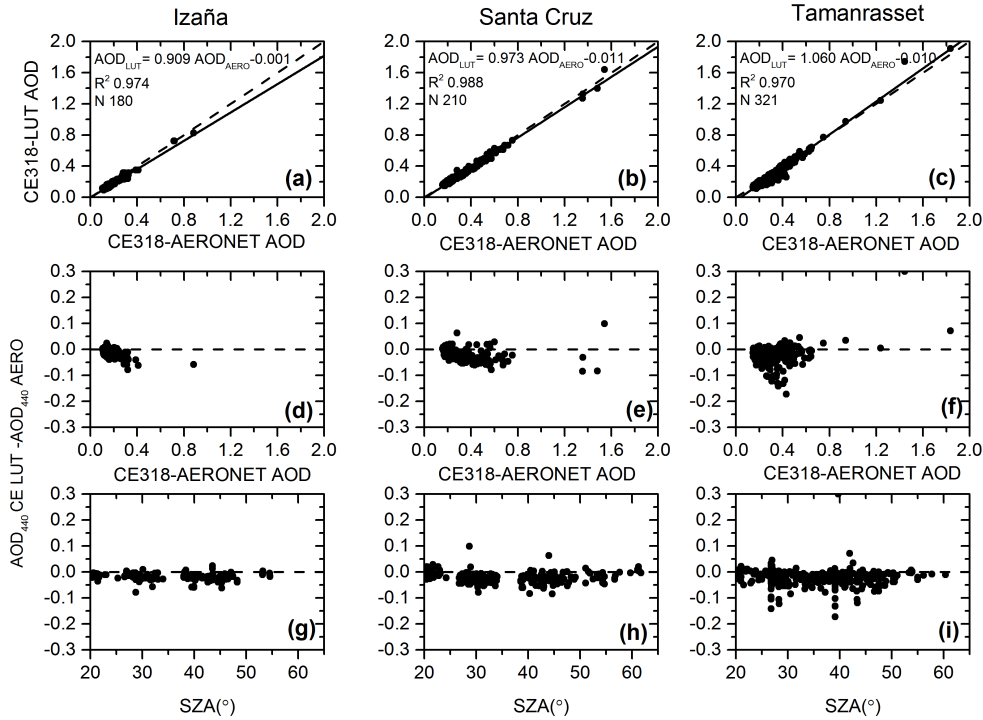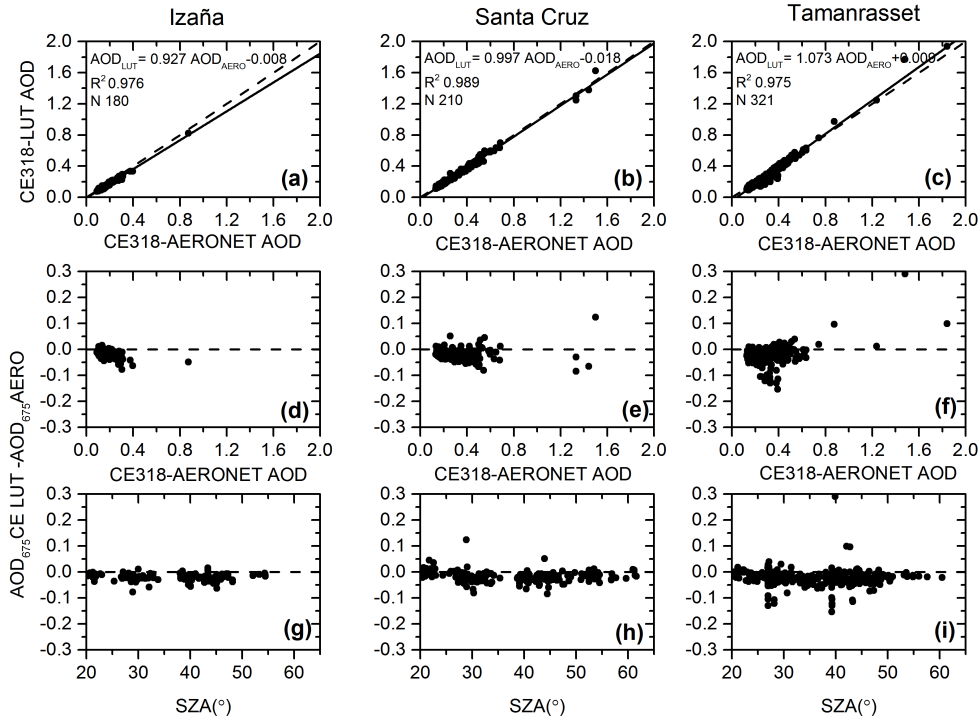
Figure 5: AOD scatter plot at 440 nm between CE318-AERONET and CE318-LUT for Izaña (a), Santa Cruz (b) and Tamanrasset (c) stations in 2013 for $20° < SZA < 65°$ (a, b, c). The black solid lines are the least-square fits, and the dashed lines are the diagonals (y = x). The least-square fit parameters are shown in the legend (slope, intercept, correlation coefficient R and number of data N). AOD differences in 440 nm between CE318-AERONET and CE318-LUT with respect to CE318-AERONET (d, e, f) and SZA (°) (g, h, i).

AOD differences up to 0.15 and RMSE values up to 0.030 (Table 4), but within the uncertainties estimated in Sect. 4.1.

6 Conclusions

In this study we have presented the new ZEN system for dust AOD monitoring from ZSR observations. The ZEN system comprises the development of a new and robust radiometer (ZEN-R41) and a methodology to retrieve AOD from ZSR measurements through a look-up table (LUT) method (ZEN-LUT), especially designed for desert aerosols. This methodology, inspired by previous methodologies commonly applied to on-board satellite sensors, uses the radiative transfer code LibRadtran and its packages to simulate ZSRs and the associated AODs. Then,
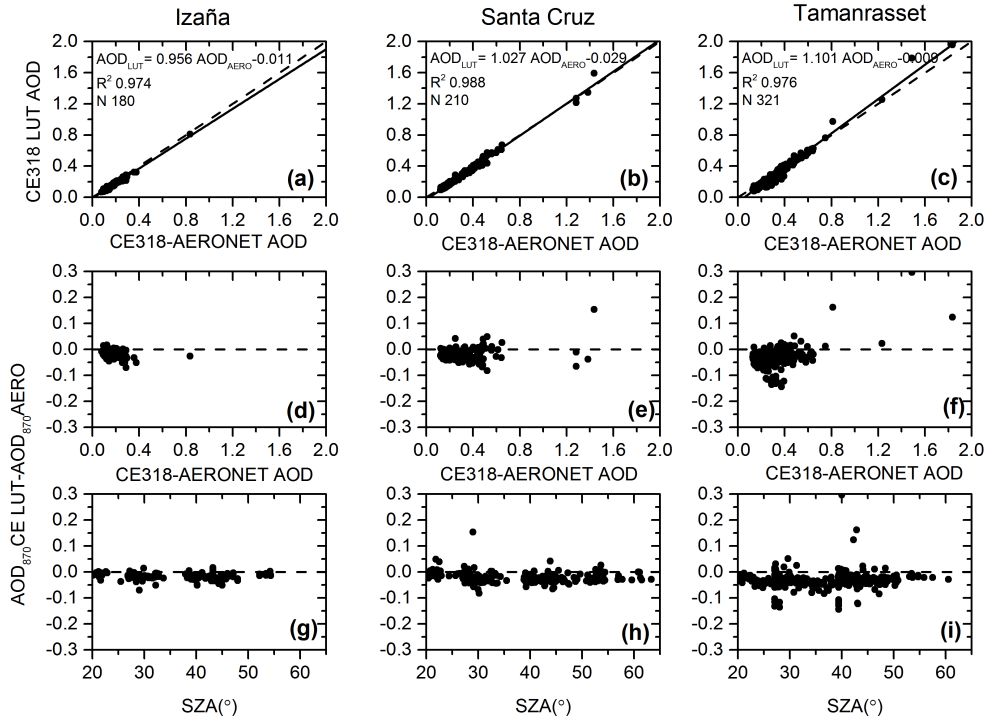
Figure 6: AOD scatter plot at 675 nm between CE318-AERONET and CE318-LUT for Izaña (a), Santa Cruz (b) and Tamanrasset (c) stations in 2013 for $20° < SZA < 65°$ (a, b, c). The black solid lines are the least-square fits, and the dashed lines are the diagonals (y = x). The least-square fit parameters are shown in the legend (slope, intercept, correlation coefficient R and number of data N). AOD differences in 440 nm between CE318-AERONET and CE318-LUT with respect to CE318-AERONET (d, e, f) and SZA (°) (g, h, i).

Table 4: Coefficient of determination (R^2), root mean square error (RMSE), mean bias (MB), and number of coincident data (N) for the AOD comparisons between CE318-AERONET and ZEN-R41 at four different spectral bands (440, 500, 675 and 870 nm) performed at Izaña station in 2015.

Wavelength (nm)	R^2	$RMSE$	MB	N
870	0.97	0.026	- 0.020	616
675	0.97	0.026	-0.025	616
500	0.97	0.026	-0.029	616
440	0.97	0.027	-0.030	616

AOD is inferred by minimizing a function which depends on the differences between simulated and measured ZSR at the corresponding solar zenith angle (SZA) in all

Figure 7: AOD scatter plot at 870 nm between CE318-AERONET and CE318-LUT for Izaña (a), Santa Cruz (b) and Tamanrasset (c) stations in 2013 for $20° < SZA < 65°$ (a, b, c). The black solid lines are the least-square fits, and the dashed lines are the diagonals (y = x). The least-square fit parameters are shown in the legend (slope, intercept, correlation coefficient R and number of data N). AOD differences in 440 nm between CE318-AERONET and CE318-LUT with respect to CE318-AERONET (d, e, f) and SZA (°) (g, h, i).

the available wavelengths.

The main conclusions of this study are as follows.

1. The comparison of ZSR from ZEN-R41 and CE318 showed a high coefficient of determination (R^2) for all wavelengths (0.99), although we observed relative mean bias (RMB) as high as -6.3% at 870 nm and 9.2% at 500 nm.

2. The sensitivity analysis, performed to identify the systematic errors (instrumental and radiative transfer inputs, or RTM) exerting the most influence on the final AOD, showed the instrumental errors and the aerosol model as the most important contributors to the final AOD uncertainty. This analysis estimated an AOD combined standard uncertainty in the ZEN system up to 0.06 in the case of $AOD_{500 \, nm} \sim 0.5$ and 0.15 for $AOD_{500 \, nm} \sim 1.0$, provided
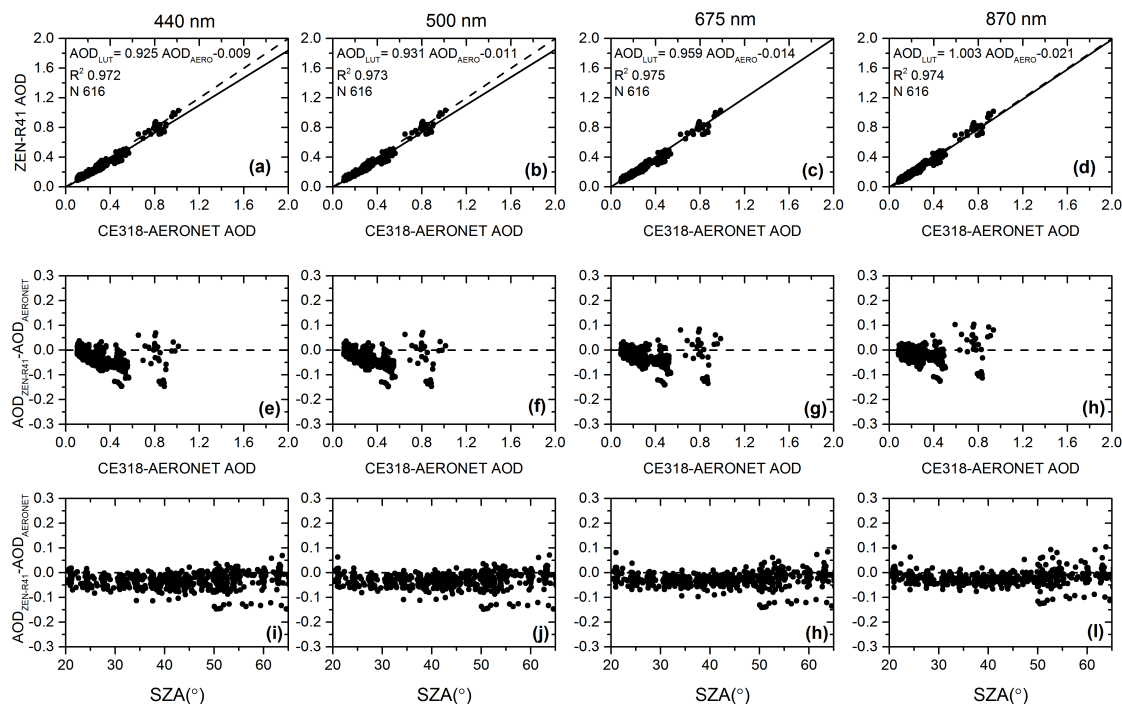
136

Figure 8: AOD comparisons between CE318-AERONET and ZEN-R41 for four different spectral bands (440, 500, 675 and 870 nm) performed at Izaña station in 2015. In the upper panel (a–d) AOD scatter plots AERONET/ZEN41 are presented. The middle panel (e–h) shows the AOD differences versus AERONET AOD. AOD differences versus solar zenith angle (SZA in °) are shown in the lower panel (i–l).

     instrumental errors are minimized ($\sim 5\%$).

3. We have compared AOD from AERONET with AOD retrieved from CE318 ZSR by means of the ZEN-LUT method (CE318-LUT) in a common period in which AERONET level 2.0 is available at three stations (Izana, Santa Cruz and Tamanrasset). A good AOD agreement (R^2 from 0.99 to 0.97) and RMSE values from 0.011 (at Izaña) to 0.032 (at Tamanrasset) have been obtained. The relatively bad results observed at Tamanrasset might be explained by possible contamination of lenses by dust. We observed maximum AOD differences up to -0.07 at Izaña and between 0.08 and 0.12 for Santa Cruz, in agreement with the expected uncertainty involved in the ZEN-LUT methodology.

4. The AOD comparison at Izaña showed a good agreement between ZEN-R41 and AERONET (R^2 of 0.97), with observed AOD differences up to 0.15, and

ZEN-R41 AOD systematically underestimated (mean bias ranging from -0.020 to -0.030). These results are also in agreement with the expected uncertainty for the ZEN system.

The results of this preliminary study indicate that the ZEN-LUT method is appropriate to infer dust AOD from ZSR measurements from the ZEN-R41, with an expected uncertainty between 0.06 and 0.15 in the AOD range between 0.5 and 1.0, which seems reasonable for most Saharan and Middle Eastern sites affected by dust. However, a thorough validation with a higher number of ZEN-R41 radiometers installed in stations located in quite different environments affected by desert dust will be carried out in the near future to confirm and complement the results presented in this paper. The study of the impact caused by other aerosols is an important issue to be addressed in order to adapt this instrument to other environments, far from dust sources. Although clouds are not a major problem in desert regions for much of the year, autonomous cloud-screening system is being implemented into the ZEN-R41 radiometer in order to discriminate cloud-contaminated ZSR data.

With the ZEN system we do not intend at all to replace accurate AOD measurements performed by sun photometer networks (as AERONET) but to complement these observations with the aim of improving mineral dust monitoring in remote locations, where it is difficult to deploy sun photometers for logistical reasons and poor infrastructure. The ZEN system could be used individually with autonomous data processing, to create networks with centralized data processing or ultimately be incorporated into automatic weather stations in desert regions in an inexpensive and simple way. As a consequence, this instrument could play a key role in dust model data assimilation near dust source regions, in satellite validation and in early warning within the WMO Sand and Dust Storm Warning Advisory and Assessment System (SDS-WAS).

7 Data availability

The reference aerosol optical depth and zenith sky radiance data at the three sites (Izaña, Santa Cruz and Tamanrasset) were obtained from Cimel Electronique 318 photometers and they are available from the AERONET website (https:// aeronet.gsfc.nasa.gov/). All the look-up tables as well as the sensitivity study data were generated by means of radiative transfer simulations carried out with LibRadtran version 1.7 code, available at http://www.libradtran.org/. All input files for performing these radiative transfer simulations are available upon request. All ZEN-R41 data are available upon request. The SONA all sky camera images for Izaña and Santa Cruz station are available upon request.

Edited by: Omar Torres Reviewed by: two anonymous referees

References

Basart, S., Pérez, C., Cuevas, E., Baldasano, J. M., and Gobbi, G. P.: Aerosol characterization in Northern Africa, Northeastern Atlantic, Mediterranean Basin and Middle East from direct-sun AERONET observations, Atmos. Chem. Phys., 9, 8265–8282, doi: 10.5194/acp-9-8265-2009, 2009.

Belward, A. and Loveland, T.: The DIS 1km land cover data set, GLOBAL CHANGE, The IGBP Newsletter, 27 pp., 1996.

Bohren, C. F. and Huffman, D. R.: Absorption and Scattering of Light by Small Particles, John Wiley & Sons, New York, doi: 10.1002/9783527618156, 1983.

Buras, R., Dowling, T., and Emde, C.: New secondary-scattering correction in DISORT with increased effiency for forward scattering, J. Quant. Spectrosc. Ra., 112, 2028–2034, doi: 10.1016/j.jqsrt.2011.03.019, 2011.

Cesnulyte, V., Lindfors, A. V., Pitkänen, M. R. A., Lehtinen, K. E. J., Morcrette, J.-J., and Arola, A.: Comparing ECMWF AOD with AERONET observations at visible and UV wavelengths, Atmos. Chem. Phys., 14, 593–608, doi: 10.5194/acp-14-593-2014, 2014.

Che, H., Zhang, X.-Y., Xia, X., Goloub, P., Holben, B., Zhao, H., Wang, Y., Zhang, X.-C., Wang, H., Blarel, L., Damiri, B., Zhang, R., Deng, X., Ma, Y., Wang, T., Geng, F., Qi, B., Zhu, J., Yu, J., Chen, Q., and Shi, G.: Ground-based aerosol climatology of China: aerosol optical depths from the China Aerosol Remote Sensing Network (CARSNET) 2002–2013, Atmos. Chem. Phys., 15, 7619–7652, doi: 10.5194/acp-15-7619-2015, 2015.

Cuevas, E., Camino, C., Benedetti, A., Basart, S., Terradellas, E., Baldasano, J. M., Morcrette, J. J., Marticorena, B., Goloub, P., Mortier, A., Berjón, A., Hernández, Y., Gil-Ojeda, M., and Schulz, M.: The MACC-II 2007–2008 reanalysis: atmospheric dust evaluation and characterization over northern Africa and the Middle East, Atmos. Chem. Phys., 15, 3991–4024, doi: 10.5194/acp-15-3991-2015, 2015.

d'Almeida, G. A., Koepke, P., and Shettle, E. P.: Atmospheric Aerosols: Global Climatology and Radiative Characteristics, A. Deepak Publishing, 561 pp., 1991.

Deepak, A. and Gerber, H. E.: Report of the experts meeting on aerosols and their climatic effects, WCP-55, available from World Meteorological Organization, Case Postale No. 5, CH1211 Geneva, Switzerland, 107 pp., 1983.

Dubovik, O. and King, M. D.: A flexible inversion algorithm for retrieval of aerosol optical properties from sun and sky radiance measurements, J. Geophys. Res., 105, 20673–20696, 2000.

Dubovik, O., Smirnov, A., Holben, B. N., King, M. D., Kaufman, Y. J., Eck, T. F., and Slutsker, I.: Accuracy assessment of aerosol optical properties retrieval from AERONET sun and sky radiance measurements, J. Geophys. Res., 105, 9791–9806, 2000.

Dubovik, O., Holben, B., Lapyonok, T., Sinyuk, A., Mishchenko, M., Yang, P., and Slutsker, I.: Non-spherical aerosol retrieval method employing light scattering by spheroids, Geophys. Res. Lett., 29, 54-1–54-4, doi: 10.1029/2001GL014506, 2002.

Dubovik, O., Sinyuk, A., Lapyonok, T., Holben, B. N., Mishchenko, M., Yang, P., Eck, T., Volten, H., Munoz, O., Veihelmann, B., Van Der Zande, W. J., Leon, J., Sorokin, M., and Slutsker, I.: Application of spheroid models to account for aerosol particle nonsphericity in remote sensing of desert dust, J. Geophys. Res.Atmos., 111, D11208, doi: 10.1029/2005JD006619, 2006.

Eck, T., Holben, B., Reid, J. S., Dubovik, O., Smirnov, A., O'Neill, N. T., Slutsker, I., and Kinne, S.: Wavelength dependence of the optical depth of biomass burning urban and desert dust aerosols, J. Geophys. Res., 104, 31333–31349, doi: 10.1029/1999JD900923, 1999.

Eck, T. F., Holben, B. N., Ward, D. E., Dubovik, O., Reid, J. S., Smirnov, A., Mukelabai, M. M., Hsu, N. C., O'Neill, N. T., and Slutsker, I.: Characterization of the optical properties of biomass burning aerosols in Zambia during the 1997 ZIBBEE field campaign, J. Geophys. Res., 106, 3425–3448, doi: 10.1029/2000JD900555, 2001.

Eck, T. F., Holben, B. N., Reid, J. S., O'Neill, N. T., Schafer, J. S., Dubovik, O., Smirnov, A., Yamasoe, M. A., and Artaxo, P.: High aerosol optical depth biomass burning events: A comparison of optical properties for different source regions, Geophys. Res. Lett., 30, 2035, doi: 10.1029/2003GL017861, 2003a.

Eck, T. F., Holben, B. N., Ward, D. E., Mukelabai, M. M., Dubovik, O., Smirnov, A., Schafer, J. S., Hsu, N. C., Piketh, S. J., Quedace, A., Le Roux, J., Swap, R. J., and Slutsker, I.: Variability of biomass burning aerosol optical characteristics in southern Africa during the SAFARI 2000 dry season campaign and a comparison of single scattering albedo estimates from radiometric measurements, J. Geophys. Res., 108, 8477, doi: 10.1029/2002JD002321, 2003b.

Eck, T. F., Holben, B. N., Reid, J. S., Sinyuk, A. Dubovik, O., Smirnov, A., Giles, D. M., O'Neill, N. T., Tsay, S.-C., Ji, Q., Al Mandoos, A., Ramzan Khan, M., Reid, E. A., Schafer, J. S., Sorokin, M., Newcomb, W., and Slusker, I.: Spatial and temporal variability of column-integrated aerosol optical properties in the southern Arabian Gulf and United Arab Emirates in summer, J. Geophys. Res., 113, D01204, doi: 10. 1029/2007JD008944, 2008.

Eck, T. F., Holben, B. N., Reid, J. S., Sinyuk, A., Hyer, E. J., O'Neill, N. T., Shaw, G. E., Vande Castle, J. R., Chapin, F. S., Dubovik, O., Smirnov, A., Vermote, E., Schafer, J. S., Giles, D., Slutsker, I., Sorokine, M., and Newcomb, W. W.: Optical properties of boreal region biomass burning aerosols in central Alaska and seasonal variation of aerosol optical depth at an Arctic coastal site, J. Geophys. Res., 114, D11201, doi: 10.1029/2008JD010870, 2009.

Eck, T. F., Holben, B. N., Sinyuk, A., Pinker, R. T., Goloub, P., Chen, H., Chatenet, B., Li, Z., Singh, R. P., Tripathi, S. N., Reid, J. S., Giles, D. M., Dubovik, O., O'Neill, N. T., Smirnov, A., Wang, P., and Xia, X.: Climatological aspects of the optical properties of fine/coarse mode aerosol mixtures, J. Geophys. Res., 115, D19205, doi: 10.1029/2010JD014002, 2010.

Emde, C., Buras-Schnell, R., Kylling, A., Mayer, B., Gasteiger, J., Hamann, U., Kylling, J., Richter, B., Pause, C., Dowling, T., and Bugliaro, L.: The libRadtran software package for radiative transfer calculations (version 2.0.1), Geosci. Model Dev., 9, 1647–1672, doi: 10.5194/gmd-9-1647-2016, 2016.

González, Y., López, C., and Cuevas, E.: Automatic observation of cloudiness: Analysis of all-sky images, WMO Technical Conference on Meteorological and Environmental Instruments and Methods of Observation, Session 3, available at: http://www.wmo.int/pages/prog/www/IMOP/publications/IOM-109_TECO-2012/Programme_TECO-2012.html (last access: 15 February 2017), 2012.

Guirado C.: Caracterización de las propiedades de los aerosoles en columna en la región subtropical, PhD thesis, Universidad de Valladolid, Valladolid, Spain, 2014.

Guirado, C., Cuevas, E., Cachorro, V. E., Toledano, C., AlonsoPérez, S., Bustos, J. J., Basart, S., Romero, P. M., Camino, C., Mimouni, M., Zeudmi, L., Goloub, P., Baldasano, J. M., and de Frutos, A. M.: Aerosol characterization at the Saharan AERONET site Tamanrasset, Atmos. Chem. Phys., 14, 11753– 11773, doi: 10.5194/acp-14-11753-2014, 2014.

Herman, J. R., Bhartia, P. K., Torres, O., Hsu, C., Seftor, C. and Celarier, C.: Global distribution of UV-absorbing aerosols from Nimbus7/TOMS data, J. Geophys. Res., 102, 16911–16922, 1997.

Hess, M., Koepke, P., and Schult, I.: Optical Properties of Aerosols and Clouds: The software package OPAC, B. Am. Meteorol. Soc., 79, 831–844, 1998.

Holben, B. N., Eck, T. F., Slutsker, I., Tanré, D., Buis, J. P., Setzer, A., Vermote, E., Reagan, J. A., Kaufman, Y. J., Nakajima, T., Lavenu, F., Jankowiak, I., and Smirnov, A.: AERONET- A federated instrument network and data archive for aerosol characterization, Remote Sens. Environ., 66, 1–16, 1998.

Holben, B.N., Tanré, D., Smirnov, A., Eck, T. F., Slutsker, I., Abuhassan, N., Newcomb, W. W., Schafer, J., Chatenet, B., Lavenue, F., Kaufman, Y. J., Vande Castle, J., Setzer, A., Markham, B., Clark, D., Frouin, R., Halthore, R., Karnieli, A., O'Neill, N. T., Pietras, C., Pinker, R. T., Voss, K., and Zibordi, G.: An emerging ground-based aerosol climatology: Aerosol Optical Depth from AERONET, J. Geophys. Res., 106, 12067–12097, 2001.

Holben, B. N., Slustker, I., Smirnov, A., Sinyuk, A., Shafer, J., Giles, D., and Dubovik, O.: AERONET's version 2.0 quality assurance criteria, in: Proceedings of SPIE, 6408, 6408–27, 2006.

Hoose, C. and Möhler, O.: Heterogeneous ice nucleation on atmospheric aerosols: a review of results from laboratory experiments, Atmos. Chem. Phys., 12, 9817–9854, doi: 10.5194/acp-12-9817-2012, 2012.

Kaufman, Y. J., Tanré, D., Remer, L. A., Vermote, E. F., Chu, A., and Holben, B. N.: Operational remote sensing of tropospheric aerosol over land from EOS moderate resolution imaging spectroradiometer, J. Geophys. Res., 102, 17051–17067, 1997.

Klein, H., Nickovic, S., Haunold, W., Bundke, U., Nillius, B., Ebert, M., Weinbruch, S., Schuetz, L., Levin, Z., Barrie, L. A., and Bingemer, H.: Saharan dust and ice nuclei over Central Europe, Atmos. Chem. Phys., 10, 10211–10221, doi: 10.5194/ acp-10-10211-2010, 2010.

Koepke, P., Hess, M., Schult, I., and Shettle, E. P.: Global Aerosol Data Set, MPI Meteorologie Hamburg Report No. 243, 44 pp., 1997.

Kurucz, R.: Synthetic infrared spectra, in: Proceedings of the 154th Symposium of the International Astronomical Union (IAU), Tucson, Arizona, 2–6 March, 1992, Kluwer, Acad., Norwell, MA, 1992.

Li, Z., Zhao, X., Kahn, R., Mishchenko, M., Remer, L., Lee, K.-H., Wang, M., Laszlo, I., Nakajima, T., and Maring, H.: Uncertainties in satellite remote sensing of aerosols and impact on monitoring its long-term trend: a review and perspective, Ann. Geophys., 27, 2755–2770, 2009.

Lindfors, A. V., Kouremeti, N., Arola, A., Kazadzis, S., Bais, A. F., and Laaksonen, A.: Effective aerosol optical depth from pyranometer measurements of surface solar radiation (global radiation) at Thessaloniki, Greece, Atmos. Chem. Phys., 13, 3733–3741, doi: 10.5194/acp-13-3733-2013, 2013.

Mayer, B. and Kylling, A.: Technical note: The libRadtran software package for radiative transfer calculations – description and examples of use, Atmos. Chem. Phys., 5, 1855–1877, doi: 10.5194/acp-5-1855-2005, 2005.

Mishchenko, M. I. and Travis, L. D.: Capabilities and limitations of a current Fortran implementation of the T-Matrix method for randomly oriented, rotationally symmetric scatterers, J. Quant. Spectrosc. Ra., 60, 309–324, doi: 10.1016/S0022-4073(98)00008-9, 1998.

Pierluissi, J. H. and Peng, G. S.: New Molecular Transmission Band Models For LOW-TRAN, Opt. Eng., 24, 243541, doi: 10.1117/12.7973523, 1985.

Ricchiazzi, P., Yang, S., Gautier, C., and Sowle, D.: SBDART: A Research and Teaching Software Tool for Plane-Parallel Radiative Transfer in the Earth's Atmosphere, B. Am. Meteorol. Soc., 79, 2101–2114, 1998.

Schmid, B., Michalsky, J., Halthore, R., Beauharnois, M., Harrison, L., Livingston, J., Russell, P., Holben, B., Eck, T., and Smirnov, A.: Comparison of aerosol optical depth from four solar radiometers during the Fall 1997 ARM intensive observation period, Geophys. Res. Lett., 26, 2725–2728, 1999.

Stocker, T. F., Qin, D., Plattner, G.-K., Tignor, M., Allen, S. K., Boschung, J., Nauels, A., Xia, Y., Bex, V., and Midgley, P. M.: Climate Change 2013: The Physical Science Basis, Contribution of Working Group I to the Fifth Assessment Report of the Intergovernmental Panel on Climate Change, Cambridge University Press, Cambridge, United Kingdom and New York, NY, USA, 1535 pp., doi: 10.1017/CBO9781107415324, 2013.

Stowe L. L., Ignatov, A. M., and Singh, R. R.: Development, validation, and potential enhancements to the second-generation operational aerosol product at the National Environmental Satellite, Data, and Information Service of the National Oceanic and Atmospheric Administration, J. Geophys. Res., 102, 16923–16934, 1997.

Takamura, T. and T. Nakajima, Overview of SKYNET and its activities, Opt. Pura Apl., 37, 3303–3308, 2004.

Tanré D., Kaufman, N., Herman, M., and Mattoo, M.: Remote sensing of aerosol properties over oceans using the MODIS/EOS spectral radiances, J. Geophys. Res., 102, 16971–16988, 1997.

Torres, O., Bhartia, P. K., Herman, J. R., Ahmad, Z., and Gleason, J.: Derivation of aerosol properties from satellite measurements of backscattered ultraviolet radiation, Theoretical Basis, J. Geophys. Res., 103, 17099–17110, 1998.

Tsvetsinskaya, E. A., Schaaf, C. B., Gao, F., Strahler, A. H., and Dickinson, R. E.: Spatial and temporal variability in M oderate Resolution Imaging Spectroradiometer-derived surface albedo over global arid regions, J. Geophys. Res., 11, D20106, doi: 10.1029/2005JD006772, 2006.

Walker, J. H., Cromer, C. L., and McLean, J. T.: Calibration of passive remote observing optical and microwave instrumentation, in: Proc. SPIE-The International Soc. Of Optical Engineering, 3–5 April, Orlando, FL, 1493, 224–230, 1991.

Wehrli, C.: GAWPFR: A network of Aerosol Optical Depth observations with Precision Filter Radiometers, in: WMO/GAW Experts workshop on a global surface based network for long term observations of column aerosol optical properties, GAW Report No. 162, WMO TD No. 1287, 2005.

Winker, D., Pelon, J., Coakley, J., Ackerman, S., Charlson, R., Colarco, P., Flamant, P., Fu, Q., Hoff, R., Kittaka, C., Kubar, T., Treut, H. L., McCormick, M., Megie, G., Poole, L., Powell, K., Trepte, C., Vaughan, M., and Wielicki, B.: The CALIPSO Mission: a global 3D view of aerosols and clouds, B. Am. Meteor. Soc., 91, 1211–1229, 2010.

Wiscombe, W.: Improved Mie scattering algorithms, Appl. Opt., 19, 1505–1509, doi: 10.1364/AO.19.001505, 1980.

World Meteorological Organization: Report of the WMO workshop on the measurement of atmospheric optical depth and turbidity, Silver Spring, Maryland, 6–10 December 1993, edited by: Hicks, B., obtainable from WMO as Technical Document No. 659 (Geneva, Switzerland), available at: http://www.wmo.int/pages/prog/arep/gaw/gaw-reports.html (last access: 15 February 2017), 28 pp., 1993.

World Meteorological Organization: Commission for Instruments and Methods of Observation, Sixteenth session WMO no. 1138, Saint Petersburg, Secretariat of the World Meteorological Organization, 2014.

Zhang, J. and Reid, J. S.: MODIS Aerosol Product Analysis for Data Assimilation: Assessment of Level 2 Aerosol Optical Thickness Retrievals, J. Geophys. Res, 111, D22207, doi: 10.1029/2005JD006898, 2006.

Zhang, J. and Reid, J. S.: A decadal regional and global trend analysis of the aerosol optical depth using a data-assimilation grade over-water MODIS and Level 2 MISR aerosol products, Atmos. Chem. Phys., 10, 10949–10963, doi: 10.5194/acp-10-10949-2010, 2010.

7.2.4. Conclusiones

Estos resultados indican un buen acuerdo entre los valores de AOD obtenidos por el sistema ZEN y AERONET. Por ello, el sistema ZEN es adecuado para completar los actuales huecos observacionales y complementar las observaciones realizadas por las actuales redes estándares de medida de AOD basadas en fotómetros solares, mejorando las observaciones de polvo mineral en regiones remotas donde es difícil instalar este tipo de instrumentación por razones logísticas y de escasez de infraestructuras y recursos humanos. Por tanto, este instrumento puede jugar un papel importante en la asimilación de datos de modelos de polvo, en la validación de datos de satélite y en las predicciones SDS-WAS.

7.3. Artículo 3: Caracterización del vapor de agua integrado en columna y la carga de aerosoles con el nuevo radiómetro ZEN-R52.

7.3.1. Resumen gráfico
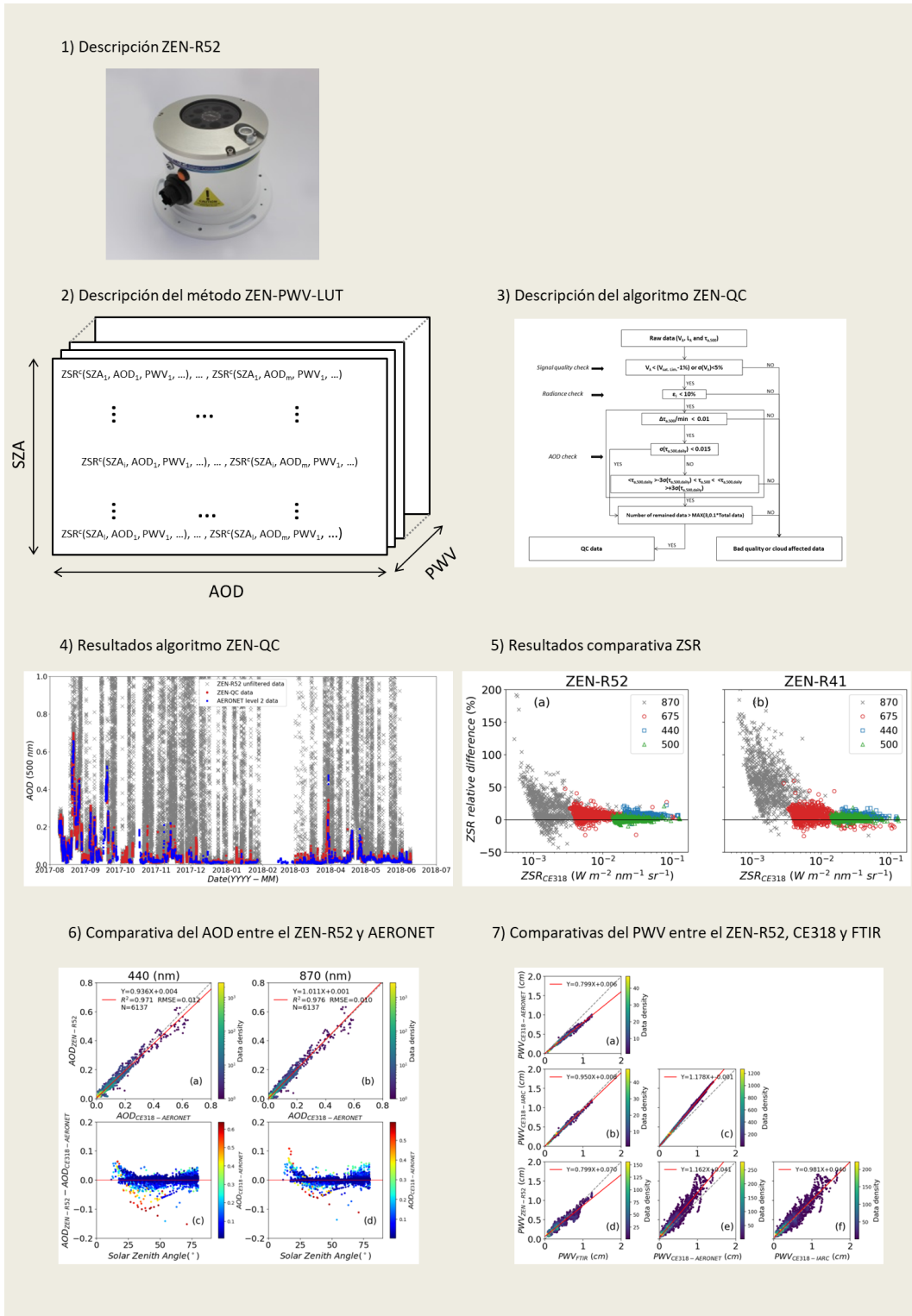
Figura 7.3: Esquema gráfico del artículo 3.

7.3.2. Resumen

En este último trabajo se muestran los primeros resultados del radiómetro ZEN-R52, una versión mejorada y actualizada del prototipo ZEN-R41 descrito en el artículo 2. Además de poder estimar el AOD, el nuevo ZEN-R52 puede inferir el PWV con un alto grado de autonomía y robustez. Las diferencias más notables en comparación con el prototipo anterior son un menor FOV ($< 2°$), una mejor relación señal a ruido, un menor impacto de la luz parásita, y la incorporación de un canal adicional en 940 nm para la determinación del PWV.

El estudio fue realizado en las instalaciones del Observatorio Atmosférico de Izaña, ya que este centro cuenta con la instrumentación adecuada para realizar las comparaciones pertinentes, siendo además banco de pruebas de la CIMO (WMO).

En cuanto a las metodologías aplicadas, en este trabajo se exponen las siguientes: la metodología para la estimación del AOD del ZEN-R52 (ZEN-AOD-LUT) descrita en el artículo 2, la metodología para inferir el PWV con el ZEN-R52 (ZEN-PWV-LUT) y el algoritmo de control de calidad de los datos del ZEN-R52 (ZEN-QC). De manera análoga al método ZEN-AOD-LUT, el método ZEN-PWV-LUT infiere el PWV como resultado de minimizar la raíz cuadrada de las diferencias cuadráticas medias normalizadas entre las ZSR medidas y las ZSR modeladas en 940 nm (véase la sección 6.4). La LUT empleada por este método es una extensión de la LUT utilizada en el método ZEN-AOD-LUT a un conjunto de valores de PWV.

El análisis del algoritmo ZEN-QC mostró un acuerdo del 68,8 % en el número de coincidencias, es decir porcentaje de datos considerados erróneos o no, al comparar los datos de AOD del ZEN-R52 que superaron el control de calidad con los datos de AOD cuasi coincidentes ($\pm 30\ s$) del nivel 2.0 de la red AERONET (versión 3), es decir datos de AOD que superan el control de calidad de AERONET, en un período de 10 meses (de agosto de 2017 a junio de 2018). Además se observó que el número de coincidencias entre los dos conjuntos de datos dependía de la elevación solar, debido a la incidencia de la luz parásita en el ZEN-R52.

Se realizó una comparación de ZSRs, durante el período de tiempo indicado en el párrafo anterior, entre los dos instrumentos ZEN (ZEN-R41 y ZEN-R52) y el Cimel CE318 de AERONET (CE318-AERONET) considerando este último como referencia. Los resultados mostraron la mejora en el rendimiento del ZEN-R52 en comparación con el ZEN-R41, aunque aún se observan los efectos de la luz parásita, principalmente en las longitudes de onda más largas y los SZA más bajos.

Se comparó el AOD del CE318-AERONET con la del ZEN-R52 mostrando una buena correlación entre ambos conjuntos de datos obteniéndose un coeficiente de determinación (R^2) de aproximadamente 0,97 y valores bajos de la raíz del error

cuadrático medio (RMSE) (de 0,010 a 0,012). Sin embargo, la presencia de una dependencia sistemática de las diferencias de AOD con el SZA indica el efecto de las imprecisiones en el modelo de transferencia radiativa y en las medidas instrumentales. Este estudio estimó la incertidumbre del AOD del ZEN-R52 en $\pm 0{,}01 \pm 0{,}13 \times AOD$.

Por último, se realizó una comparación entre el PWV dado por el ZEN-R52 y el FTIR, considerando a este último como referencia. La comparación mostró un buen acuerdo entre ambos, con un RMSE de 0,07 cm, un R^2 de 0,91 y una diferencia promedio del 9,1 %. Además, los datos de estos dos dispositivos se compararon con otros dos conjuntos de datos de PWV diferentes del mismo instrumento Cimel CE318 de referencia de AERONET en el Observatorio Atmosférico de Izaña: el conjunto de datos CE318-AERONET (datos de PWV proporcionados por AERONET) y el conjunto de datos CE318-IARC (datos de PWV obtenidos con una calibración que tiene en cuenta las características específicas del lugar). Al comparar ambos conjuntos de datos con los datos del FTIR, observamos resultados muy similares en cuanto al R^2 (0,99 en ambos casos) y el RMSE (0,025 para CE318-IARC y 0,026 para CE318-AERONET). Sin embargo, al analizar las diferencias promedio con FTIR, se observa un menor sesgo con los datos CE318-IARC ($-0{,}016\ cm$ ($-3{,}4$ %)) que con los datos CE318-AERONET ($-0{,}091\ cm$ ($-19{,}2$ %)). Esta diferencia podría explicarse por el hecho de que el PWV de AERONET es un producto estándar y global que no tiene en cuenta las características particulares de la estación de Izaña. Nuestros resultados muestran que la nueva técnica ZEN-PWV-LUT proporciona estimaciones bastante buenas de PWV, con diferencias relativas de PWV promedio de 9,1 % y 17,1 % con FTIR y CE318-IARC, respectivamente. La incertidumbre esperada de esta técnica se estimó en $\pm 0{,}089$ cm, que es un excelente resultado para un instrumento de bajo coste. Un análisis más detallado, determinó que la incertidumbre en el PWV tiene una dependencia lineal con el PWV para valores de $PWV < 1$ cm, siguiendo la ecuación $\pm 0{,}036 \pm 0{,}061 \times PWV$.

7.3.3. Artículo 3

Column Integrated Water Vapor and Aerosol Load Characterization with the New ZEN-R52 Radiometer

Antonio Fernando Almansa[1,2,3], Emilio Cuevas [2,*] , África Barreto[1,2,3], Benjamín Torres [4], Omaira Elena García[2], Rosa Delia García [2,3], Cristian Velasco-Merino[3], Victoria Eugenia Cachorro[3], Alberto Berjón[2,3], Manuel Mallorquín[5], César López[5], Ramón Ramos[2], Carmen Guirado-Fuentes[2,3], Ramón Negrillo[5] and Ángel Máximo de Frutos[3]

[1]Cimel Electronique, 75011 Paris, France; f-almansa@cimel.fr (A.F.A.); africabv@gmail.com (Á.B.)

[2]Izaña Atmospheric Research Center (IARC), State Meteorological Agency of Spain (AEMET), 38001 Santa Cruz de Tenerife, Spain; ogarciar@aemet.es (O.E.G.); rosa@goa.uva.es (R.D.G.); alberto@goa.uva.es (A.B.); rramosl@aemet.es (R.R.); carmen@goa.uva.es (C.G.-F.)

[3]Grupo de Óptica Atmosférica, Dpto. de Física Teórica Atómica y Óptica, Universidad de Valladolid, 47001 Valladolid, Spain; cristian@goa.uva.es (C.V.-M.); chiqui@goa.uva.es (V.E.C.); angel@goa.uva.es (Á.M.d.F.)

[4]Univ. Lille, CNRS, UMR 8518, LOA—Laboratoire d'Optique Atmosphérique, F-59000 Lille, France; benjamin.torres@grasp-sas.com

[5]Sieltec Canarias S.L., 38230 La Laguna, Spain; manuel.mallorquin@sieltec.es (M.M.); cesar.lopez@sieltec.es (C.L.); ramon.negrillo@sieltec.es (R.N.)

*Correspondence: ecuevasa@aemet.es

Abstract: The study shows the first results of the column-integrated water vapor retrieved by the new ZEN-R52 radiometer. This new radiometer has been specifically designed to monitor aerosols and atmospheric water vapor with a high degree of autonomy and robustness in order to allow the expansion of the observations of these parameters to remote desert areas from ground-based platforms. The ZEN-R52 device shows substantial improvements compared to the previous ZEN-R41 prototype: a smaller field of view, an increased signal-to-noise ratio, better stray light rejection, and an additional channel (940 nm) for precipitable water vapor (PWV) retrieval. PWV is inferred from the ZEN-R52

Zenith Sky Radiance (ZSR) measurements using a lookup table (LUT) methodology. The improvement of the new ZEN-R52 in terms of ZSR was verified by means of a comparison with the ZEN-R41, and with the Aerosol Robotic Network (AERONET) Cimel CE318 (CE318-AERONET) at Izaña Observatory, a Global Atmosphere Watch (GAW) high mountain station (Tenerife, Canary Islands, Spain), over a 10-month period (August 2017 to June 2018). ZEN-R52 aerosol optical depth (AOD) was extracted by means of the ZEN–AOD–LUT method with an uncertainty of $\pm 0.01 \pm 0.13*AOD$. ZEN-R52 PWV extracted using a new LUT technique was compared with quasi-simultaneous (± 30 s) Fourier Transform Infrared (FTIR) spectrometer measurements as reference. A good agreement was found between the two instruments (PWV means a relative difference of 9.1% and an uncertainty of ± 0.089 cm or $\pm 0.036 + 0.061*PWV$ for PWV < 1 cm). This comparison analysis was extended using two PWV datasets from the same CE318 reference instrument at Izaña Observatory: one obtained from AERONET (CE318-AERONET), and another one using a specific calibration of the 940-nm channel performed in this work at Izaña Atmospheric Research Center Observatory (CE318-IARC), which improves the PWV product.

Keywords: precipitable water vapor; aerosol optical depth; zenith sky radiance; remote sensing; lookup table; radiative transfer

1. Introduction

Water vapor induces a strong positive feedback in the climate system [1]. It is the largest contributor to the natural greenhouse effect [2,3], has a key role in tropospheric dynamics and aerosol growth, and has a large temporal and spatial variability. Therefore, water vapor observation still presents a challenge to the scientific community. Precipitable water vapor (hereafter referred to as PWV) is a common variable to quantify atmospheric water vapor content in climatological studies and is defined as the column-integrated water vapor contained in a vertical column of a unit cross section extending between any two specified levels (generally from the Earth's surface to the top of the atmosphere). The estimation of PWV with high temporal and spatial resolution is of great importance not only for climate change research [4–6], but also for the validation of satellite PWV measurements [7,8] and PWV estimates performed by numerical weather prediction (NWP) models, weather forecasting and the assimilation of PWV measurements in NWP models [9,10]. PWV can be monitored with high precision through microwave radiometer profilers (MWPs) [11], the Global Climate Observing System (GCOS) Reference Upper-Air Network (GRUAN) correction algorithm for the Vaisala RS92 radiosondes (GRUAN RS92) [12] or ground-based Fourier

Transform Infrared (FTIR) spectrometers [13]. Less precise devices for PWV monitoring such as Vaisala RS92 [14] and RS41 [15] radiosondes, Global Navigation Satellite System (GNSS) receivers [16–18], sun/moon/star photometers [19–23] or spectroradiometers [24,25] allow us to expand the spatial coverage of the PWV measurements, but with a lower precision, ranging from 7% to 20% and decreasing under dry conditions [13].

As one of the most important radiative forcing agents in the climate system, atmospheric aerosols have been extensively studied in recent decades [26]. They modify the Earth's radiation budget and the hydrological cycle through aerosol-radiation and aerosol-cloud interactions [27]. Aerosol optical depth (AOD) is the single most comprehensive variable to remotely assess the aerosol load of the atmosphere [28] and the most important aerosol-related parameter for radiative forcing studies [29].

The global and long-term AOD and PWV monitoring in the atmosphere can be assessed only by means of satellite measurements. However, their poor temporal resolution, with a single daily quantitative observation in most cases, is a strong limiting factor for AOD and PWV diurnal variation monitoring. Moreover, as [30] suggested, satellite AOD retrievals are subject to important uncertainties due to radiometric calibration, a priori assumed aerosol properties, cloud contamination and surface reflectivity. It is especially important that the latter effect is properly accounted for in the case of bright land surfaces like deserts. In this case, the low aerosol detectability of satellite sensors operating in the visible spectral range further complicate the estimation of the aerosol contribution where the main sources of aerosols are located. As a result, the large uncertainties associated with satellite products prevent their use for model assimilation near source regions.

Despite the fact that satellite remote sensing is the most convenient tool for providing a global perspective of aerosols and PWV, ground-based photometric techniques also play an important role in climate studies. They are especially valuable for validating satellite AOD and PWV products, as well as powerful tools for model assimilation and evaluation. Sun photometers were primarily designed to characterize aerosol loading by measuring atmospheric transmission in the visible and near-infrared spectral range using interference filters. However, sun photometers also appear as one of the most suitable ground-based techniques for estimating near-real PWV time with high spatial coverage [31,32] because of the relatively low cost and easy deployment of this type of instrument. These characteristics have allowed the establishment of several global and international networks of sun photometers in the past decades: the World Meteorological Organization (WMO) Global Atmosphere Watch Precision Filter Radiometer (GAW-PFR) network [33], the China Aerosol Remote Sensing NETwork, (CARSNET) [34], SKYNET [35] and the Aerosol Robotic NETwork (AERONET) [36]. In particular, AERONET is

currently the most widespread ground-based network, providing accurate, standard, and consistent PWV, AOD and inversion products (such as aerosol size distribution and refraction indices) over hundreds of stations around the world. However, photometer networks have some drawbacks, as they cannot provide products under cloudy skies and, more importantly, the observation sites are not evenly distributed around the globe (they are strongly biased toward populated regions). The difficulties in operating these types of photometers limit the number of stations located near the most important aerosol areas, restraining the representativeness of these networks for constraining global and relatively coarse-resolution models [27].

We present, in this paper, the new ZEN-R52 zenith-looking narrow-band radiometer, an improved version of the ZEN-R41 prototype previously presented in [37]. This is a radiometer specifically designed to expand ground-based aerosol load and PWV observations in remote areas, filling the current observational gaps in the current ground-based networks and therefore improving the capability for satellite product validation and aerosol model evaluation and assimilation. The results are focused on the improvement of the new ZEN-R52 in terms of Zenith Sky Radiance (ZSR), in addition to the capabilities of the new ZEN system to provide AOD and PWV by means of measurements performed at the Izaña high-altitude station over a 10-month period (August 2017 to June 2018). As far as we know, apart from the two types of ZEN radiometers, the objects of this study, there are no other filter instruments based on relatively simple but robust ZSR measurements to obtain AOD and PWV.

The experimental facility, the instruments used in this study, the methodologies developed to determine AOD and PWV with the ZEN-R52, the CE318, and the FTIR, as well the quality control procedures applied to ZEN-R52 measurements have been described in Section 2. The main results of the quality control and cloud screening procedures, ZSR, AOD and PWV products of the ZEN-R52 radiometer, together with corresponding comparisons with other collocated reference instruments (CE318 and FTIR) are shown in Section 3. A summary of this study and the main conclusions are provided in the last Section.

2. Materials and Methods

2.1. Test Site

Radiometric measurements have been performed at Izaña Observatory (IZO; http://izana.aemet.es/). IZO is a high-mountain GAW station located in Tenerife (Canary Islands, Spain) at 28.31°N, 16.49°W, at an altitude of 2400 meters above sea level.

IZO is managed by the Izaña Atmospheric Research Center (IARC) from the State Meteorological Agency of Spain (AEMET), and is a WMO Commission for Instruments and Methods of Observations (CIMO) Testbed for Aerosols and Water Vapor Remote Sensing Instruments. Further information on IZO's facilities and its activities can be found in [38].
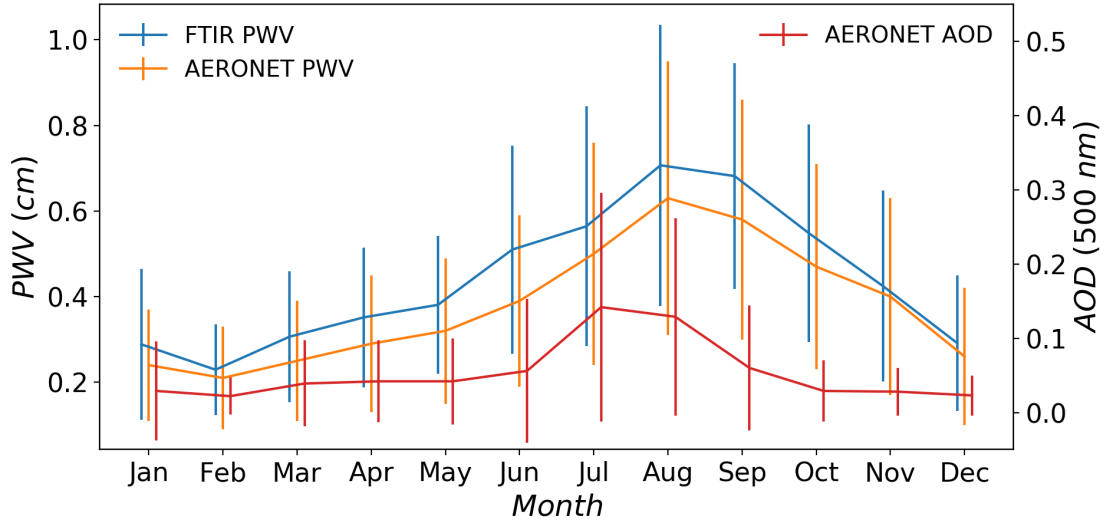

Figure 1: Monthly precipitable water vapor (PWV) and aerosol optical depth (AOD)$_{500}$ averages (solid lines) and corresponding standard deviations (error bars) at Izaña station. PWV annual cycle given by Total Column Carbon Observing Network (TCCON) Fourier Transform Infrared (FTIR) (blue line) has been calculated for 2007–2019. Aerosol Robotic Network (AERONET) PWV (orange line) and AOD$_{500}$ (red line) have been calculated for 2005-2019.

From a meteorological perspective, IZO is characterized by pristine skies, high atmospheric stability and rather low atmospheric humidity, as these conditions are required for radiometer calibration using the Langley technique [39]. These features make IZO a suitable site for background monitoring, representative of free troposphere conditions. As a consequence of the proximity with the Saharan desert, this site is also sporadically affected by dust transport from the Sahara, mainly in summer (see Figure 1), when the predominant conditions are associated to AOD$_{675}$ > 0.15 and large particles with Angstrom Exponent (α_{440_870}) < 0.25 [40,41]. The prevalent conditions during most of the year imply AOD$_{675}$ < 0.15. Regarding PWV, Izaña station is characterized by dry conditions, as a consequence of its altitude and its location in the descending branch of the subtropical Hadley's cell, with the driest conditions occurring during winter, with a minimum PWV in February, while the wettest months occur in summer (maximum in August), coinciding with a higher frequency of dust outbreaks [19]. In Figure 1, the Total Column Carbon

Observing Network (TCCON) FTIR and AERONET PWV averaged annual cycles are shown. It can be seen that both datasets follow a similar seasonal evolution, but with an appreciable bias between them, with a total average PWV of 0.48 cm (standard deviation of 0.28 cm) for TCCON FTIR, and 0.38 (standard deviation of 0.14) for AERONET. Other authors have shown that AERONET products underestimate the PWV compared with other techniques (see [13,23,42,43]), with mean differences ranging between -5% and -25%. An explanation for the observed differences will be given in Section 3.4.

2.2. Instrumentation

2.2.1. ZEN-R41 and ZEN-R52

The ZEN-R41 is a radiometer jointly developed by Sieltec Canarias and the IARC, conceived to monitor AOD from sky radiance measurements at the zenithal direction and at different spectral bands. A complete description of the ZEN-R41 can be found in [37]. The ZEN-R52 (Figure 2) is a newer instrument version whose hardware and software have been significantly improved and optimized. Regarding the main differences of the hardware, both the inclusion of a new channel centered at 940 nm for PWV retrieval and a more powerful Single Board Computer (SBC) inside the instrument are remarkable. These improvements require a larger instrument housing box with cooling fins. Better coated lenses and a special treatment for internal baffles entail a Field of View (FOV) smaller than 2° and a better stray light rejection. Now, the ZEN-R52 uses five hard coated 10 nm Full Width at Half Maximum (FWHM) filters with nominal wavelengths centered at 440, 500, 675, 870 and 940 nm with an estimated precision of ±2 nm in the central wavelength (CWL), in combination with five silicon diodes (350–1050 nm) and a 16-bit resolution, over a high dynamic acquisition range. The choice of the optical filter's spectral range was made based on a compromise between technical requirements, such as the detector's spectral response, low atmospheric gas absorption (except for 940 nm) and commercial availability. A 1020-nm spectral band optical filter would be desirable in future ZEN versions to improve the estimation of AOD at longer wavelengths. The radiance measurements at all the channels are made simultaneously, with a rate of 1 minute (averaged from 30 samples). Moreover, the instrument also contains sensors for internal humidity, temperature and pressure monitoring.

Regarding software improvements, it is worth highlighting the renewed graphical interface, which allows for interactive data preview, database searches, data sending configuration (via FTP or HTTPs), time synchronization through Network Time

Figure 2: ZEN-R52 picture.

Protocol (NTP) servers, and internal manual time configuration. Now, the user has the option to change the precomputed lookup table files or to change the radiometric calibration parameters. Access to the disk configuration and remote software updates are also possible.

The output signal of the instrument, which is provided in analogic-to-digital units (ADU), was transformed into radiance units (W m^{-2} sr^{-1} nm^{-1}) by measuring a calibrated integrating sphere (Labsphere's HELIOS 4-lamps 20″ integrating sphere) at IARC facilities. The uncertainty involved in this calibration procedure was estimated to be 5% by [44]. Thus, we have assumed this estimation as the lower limit value for the radiance uncertainty.

2.2.2. Cimel CE318-AERONET

The CE318-AERONET permanent master at IZO was used in this work to validate the results obtained with the ZEN-R52 radiometer. This is a standard instrument used in AERONET which performs direct sun and diffuse sky measurements. Direct sun measurements are performed at nine different spectral bands to derive accurate AOD and PWV: 340, 380, 440, 500, 675, 870, 1020 and 1640 nm for AOD and 940 for PWV. AERONET version 3 Level 2.0 data were used in this study, which include near-real-time automatic cloud screening, automatic instrument quality controls and pre-field and post-field calibrations [45]. Diffuse sky radiance measurements

are performed by means of two different routines to infer the aerosol optical and microphysical properties: the almucantar (ALM) and the principal plane (PPL) scenarios. With this information, AERONET provides microphysical and optical parameters, such as particle size distribution, refractive indices, single scattering albedo (SSA) or phase function [45,46]. Typical AOD uncertainty for reference instruments ranges between 0.002 and 0.009, with higher errors in the UV spectral range [39,46]. An excellent traceability of AOD from the AERONET-Cimel reference instruments to the world GAW-PFR AOD reference has been shown [40]. According to [45], the AERONET PWV product is accurate to about 10%. However, as [13] showed, PWV uncertainty for sun photometry is dependent on humidity conditions, ranging from 7% for humid conditions to 25% for very dry conditions (PWV $\leq$ 0.2 cm).

In order to simulate the ZEN performance, we have computed CE318-AERONET ZSR measurements (at 440, 500, 675, 870, 1020 and 1640 nm) by means of a linear interpolation of the PPL data to the zenith position. It is worth mentioning that CE318-AERONET does not provide PPL measurements at 940 nm.

2.2.3. Ground-Based FTIR

The FTIR solar measurements started at IZO in 1999 as the result of a collaboration between the IARC and the Institute of Meteorology and Climate Research—Atmospheric Trace Gases and Remote Sensing (IMK—ASF), belonging to the Karlsruhe Institute of Technology (KIT). Since then, two FTIR spectrometers have been operating at the observatory (an IFS 120M between 1999 and 2005 and an IFS 120/5HR from 2005 onwards) in the framework of the international atmospheric composition networks Network for the Detection of Atmospheric Composition Change (NDACC, since 1999) and TCCON (since 2007).

For this work, we use the TCCON FTIR PWV data, which were retrieved with the 2014 version of the GGG processing software [47] by evaluating the measured direct solar absorption spectra in the near-infrared spectral region (4000–9000 cm^{-1}). These solar spectra are acquired at a spectral resolution of 0.02 cm^{-1}. Several scans are co-added in order to increase the signal-to-noise ratio and, thus, the sampling frequency of TCCON FTIR PWV data is about 2 minutes. TCCON data have been calibrated using collocated meteorological radio soundings at globally distributed TCCON sites, from which a correction factor of 1.018 $\pm$ 0.004 (R^2 = 0.993) was determined for the PWV [47]. The TCCON PWV data used here were already divided by this scale factor. Particularly at IZO, when comparing TCCON FTIR PWV values to those obtained from meteorological radiosondes launched on Tenerife island and processed according to the GRUAN scheme for the period

2008-2017, we further confirmed the high precision of the TCCON data used in this work. We document a mean bias (TCCON-GRUAN) of only -0.06 cm (1.33%) and a R^2 of 0.939 (Omaira E. García, personal communication, 2020). Further details of the FTIR program at IZO are given in [13].

2.3. Methodology

2.3.1. AOD Calculation Method Description (ZEN–AOD–LUT)

The ZEN–AOD– lookup table (LUT) method previously described in [37] was used to retrieve AOD from zenith sky measurements. This method compares the ZSR measured at four of the five ZEN-R52 nominal wavelengths (440, 500, 675 and 870 nm) with a LUT of precomputed ZSRs at these wavelengths. This LUT is generated using the radiative transfer model LibRadtran (http://www.libradtran.org) [48,49], whose principal inputs are the solar zenith angle (SZA), the aerosol vertical profile and the surface reflectance. According to [37], a mix of aerosol components as well as their vertical profiles is defined to retrieve the optical properties needed to compute the LUT of ZSR values. Therefore, a set of AOD values is pre-calculated from every aerosol profile. Finally, the LUT estimates AOD by minimizing the normalized root mean squared differences (NRMSD or ϵ_l) of computed and measured ZSRs defined by:

$$\epsilon_l = \sqrt{\frac{1}{N_\lambda} \sum_{\lambda=1}^{N_\lambda} \left(\frac{ZSR_\lambda^m(\theta_v = 0, \theta_s) - ZSR_{\lambda,l}^c(\theta_v = 0, \theta_s)}{ZSR_\lambda^m(\theta_v = 0, \theta_s)} \right)^2}, \tag{1}$$

where N_λ is the number of nominal wavelengths considered and ZSR_λ^m is the measured radiance at the nominal wavelength λ, at zenith direction ($\theta_v = 0$), with the SZA being θ_s. Similarly, $ZSR_{\lambda,l}^c$ is the computed radiance at the nominal wavelength λ in the zenith direction, for the corresponding SZA and the aerosol vertical profile indicated by index l. The dependence of ZSR_λ on surface reflectance, single scattering albedo, AOD, and aerosol phase function have been omitted for the sake of brevity.

In a sensitivity study carried out by [37], the authors showed that the uncertainty of the ZEN–AOD–LUT method increases with AOD, having a standard uncertainty ranging from 0.06 for $AOD_{500} \approx 0.5$ to 0.15 for $AOD_{500} \approx 1.0$, when an instrumental uncertainty of 5% is considered.

2.3.2. PWV Determination Method (ZEN-PWV-LUT)

In a similar manner to the ZEN–AOD–LUT, the ZEN-R52 PWV has been derived by means of the LUT technique (ZEN-PWV-LUT), which is, in fact, an extension of the ZEN–AOD–LUT, considering an ensemble of PWV values as inputs to the radiative model. Therefore, this ZEN-PWV-LUT has a size defined by the length of the ZEN–AOD–LUT (40 aerosol mass concentration values by 80 SZA values) multiplied by the length of the PWV array (20 values ranging from 0 to 2.3 cm). The upper limit of 2.3 cm was chosen as the maximum PWV value observed at Izaňa station with FTIR during the period of this study (1.8 cm, plus 0.5 cm of margin). This method accounts for the absorption of ZSR due to the presence of atmospheric water vapor in the 940-nm spectral band. In addition to the water vapor absorption, other effects on ZSR such as those produced by surface reflectance, Rayleigh scattering and aerosol absorption and scattering, are considered. Surface reflectance and Rayleigh scattering are fixed inputs in the radiative transfer calculations, but the aerosol contribution is estimated from the ZEN–AOD–LUT. Once the aerosol's profile has been estimated, PWV is calculated by minimizing the NRMSD between measured ZSR (ZSR_{940}^{m}) and computed ZSR (ZSR_{940}^{c}) in this spectral range using Equation (1).

It is also important to highlight that the water vapor transmission spectrum in this spectral range has a high number of narrow absorption lines. Considering the wide wavelength range of the optical filters of the instrument (FWHM $\approx$ 10 nm), accurate knowledge of the filter transmission function is an important factor in the accurate determination of PWV. REPTRAN band parametrization [50] included in LibRadtran software package has been adopted in this study with a coarse resolution (15 cm⁻¹) to reduce the high computing time required to simulate ZSR for such a high number of absorption lines in the 940 nm spectral band. The MT_CKD (MlawerTobinCloughKneizysDavies) model for the water vapor continuum absorption [51] is also included. With this band parametrization, only a few representative wavelengths are required to parametrize the desired spectral band. The simulated ZEN-R52's 940-channel ZSRs are obtained by convolving the computed ZSRs at the representative wavelengths with the filter function provided by the manufacturer, which is supplied with a CWL precision of $\pm$ 2 nm.

2.3.3. ZEN Quality Control (ZEN-QC) Process

An algorithm was implemented in order to remove cloud-contaminated and erroneous data from the ZEN-R radiometers dataset. The algorithm includes the following steps (see Figure 3):

1. Signal quality check: the ZEN-R devices perform 30 measurements in one minute, but only 1-minute voltage averages and their corresponding standard deviations (σ_V) are stored. High frequency noise is removed by analysing the signal, considering a threshold of 5% in σ_V, which was determined by empirically analysing aerosol condition data from clean and heavy dust outbreaks. Measurements larger than the saturation value with an error range of 1% were removed;

2. Radiance check: the NRMSD of measured and estimated radiances used in the AOD (τ_a) retrieval process (ZEN–AOD–LUT) were analysed. We have determined a threshold of 10% for the value of ϵ_l, given in Equation (1), and data above this threshold were removed;

3. AOD check: part of the AERONET cloud-screening quality control algorithm [45,52] has been adapted to the ZEN system. It consisted of three different steps:

   - A smoothness check, to verify that cloud-contaminated data were removed by means of the $\tau_{a,500}$ relative change rate. A threshold of 0.01 was considered;

   - An AOD stability check, in which we assumed the criterion presented in [45] based on the standard deviation of the daily $\tau_{a,500}$. Data were accepted if σ was < 0.015;

   - After the two previous checks, a three-sigma check on $\tau_{a,500}$ was performed.

4. Finally, if the remaining data from a certain day were lower than three (or 10% of the total initial number, whatever is higher), data from this day were removed.

2.3.4. PWV Determination Method (CE318-IARC)

In addition to using the PWV AERONET product (see Section 2.2.2) in the comparisons, we also used the PWV obtained with the same CE318 instrument, but calculated using a specific calibration, which we called CE318-IARC PWV. The method followed to calculate the PWV is very similar to that of AERONET, differing only in the water vapor transmittance calculation, where we considered more specific conditions. The method is explained below.

As many authors have already proved ([13,33–37], sun photometric measurements at 940 nm can be used to derive PWV. In this case, the Beer–Lambert–Bouguer law,
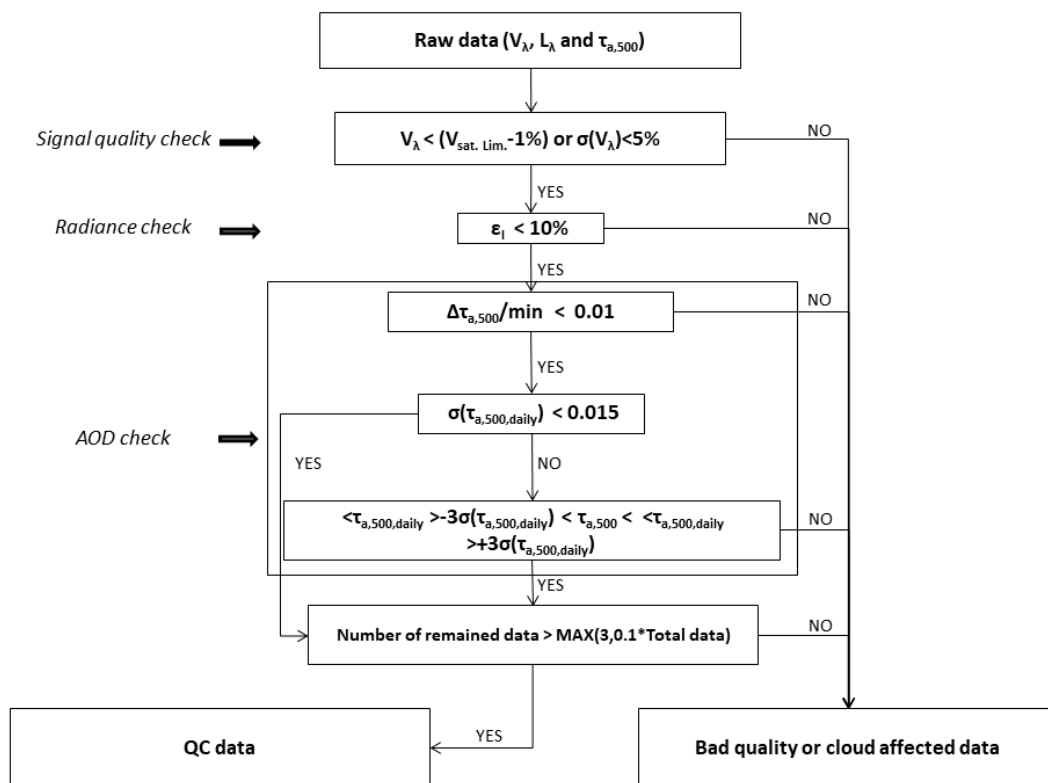
Figure 3: ZEN quality control (ZEN-QC) scheme flowchart.

defined to be applied to regions with a smooth spectral variation in atmospheric transmittance inside the band pass, must be modified to account for the water vapor transmittance ($T_{w,\lambda}$):

$$V_\lambda = V_{0,\lambda} \cdot e^{-(m\tau_\lambda)} \cdot T_{w,\lambda} \tag{2}$$

where V_λ is the photometer voltage, $V_{0,\lambda}$ is the solar extraterrestrial voltage, m is the atmospheric air mass and τ_λ is the spectral optical depth of molecules and aerosols. The following exponential dependence of $T_{w,\lambda}$ on PWV is well accepted ([31,53]):

$$T_{w,\lambda} = e^{-a(m_w \cdot PWV)^b} \tag{3}$$

where m_w is the water vapor optical air mass ([54,55]) and "a" and "b" coefficients are filter-dependent and site-dependent constants, which have to be calculated by

161

considering the central wavelength position, width, and shape of the photometer's filter response and by other parameters such as the vertical distribution of the water vapor ([19]). These two parameters are determined by means of a spectral convolution of the weighted water vapor transmittances simulated using the LibRadTran radiative transfer model with the instrument's response function at 940 nm. REPTRAN band parametrization [50] was adopted in this simulation, as well as the mid-latitude summer atmosphere and the altitude of Izaña (2.4 km height). A variation in m_w between one and six was considered, in addition to a PWV variation between 0 cm and 2.3 cm, in order to cover the interval considered in this study.

Photometry-derived PWV values can be calculated by combining Equations (2) and (3) with the following equation, involving Rayleigh and aerosol optical depths (τ_R and τ_a) and air masses (m_R and m_a):

$$PWV = \frac{1}{m_w} \cdot \left[\frac{1}{a} \cdot \left(\ln\left(\frac{V_{0,940}}{V_{940}}\right) - m_R \cdot \tau_{R,940} - m_a \cdot \tau_{a,940} \right) \right]^{\frac{1}{b}} \qquad (4)$$

A calibration constant at 940 nm ($V_{0,940}$) was determined by means of a modified Langley plot analysis [31] (following Equation (2)) over a 10-month period (August 2017 to June 2018). $\tau_{a,500}$ was restricted to values below 0.015 to ensure clean and stable atmospheric conditions for the Langley analysis. A total of 27 $V_{0,940}$ values were retrieved in this time period, with a coefficient of variation of 2.9%. The values obtained for the coefficients a and b are 0.536 and 0.638, respectively.

3 Results

3.1. ZEN-R52 Quality Control (ZEN-QC) Assessment

The ZEN-R52 quality control (ZEN-QC) method was applied to the ZEN-R52 data over a 10-month period (August 2017 to June 2018). The ratio of removed ZEN-R52 data in each step is shown in Table 1. The first two steps (signal quality and radiance checks) filter 24.0% and 23.4% of total data, respectively, due to both cloud-contaminated data and instrument anomalies. The third ZEN-QC step is an AOD check procedure to refine the cloud screening. This process is able to screen the final 2.2% of total data. Thus, nearly half of ZEN-R52 data were filtered in this three-step algorithm. We studied the number of coincidences with the AERONET (level 2.0 version 3) cloud-screening quality control algorithm (in %) by matching the closest pairs of records (ZEN-R52 and CE318-AERONET) with a time difference within ±30 seconds. According to [40], the natural AOD

variability in this time period is negligible. The 10-month AOD evolutions at 500 nm for the two datasets are shown in Figure 4. The results shown in this figure demonstrate that the ZEN-QC filtering method is a suitable algorithm to screen instrumental errors and clouds, with an agreement of 68.8% with AERONET. The distribution of the coincidences between the two quality control algorithms depends on the solar elevation as shown in Figure 5. The agreement is especially poor for SZA < 15°, where the ZEN-QC rejects most of the ZEN-R52 data as a consequence of the presence of stray light on ZEN-R52 ZSR. However, the agreement is notably improved as SZA increases, especially for SZA > 25°, where the presence of stray light is cosiderably reduced.

Table 1: Ratio (%) of ZEN-R52 filtered data at each step of the ZEN-QC algorithm.

Algorithm stage	Step 1 (Signal Quality Check)	Step 2 (Radiance Check)	Step 3 (AOD Check)
Filtered data (%)	24.0%	23.4%	2.2%
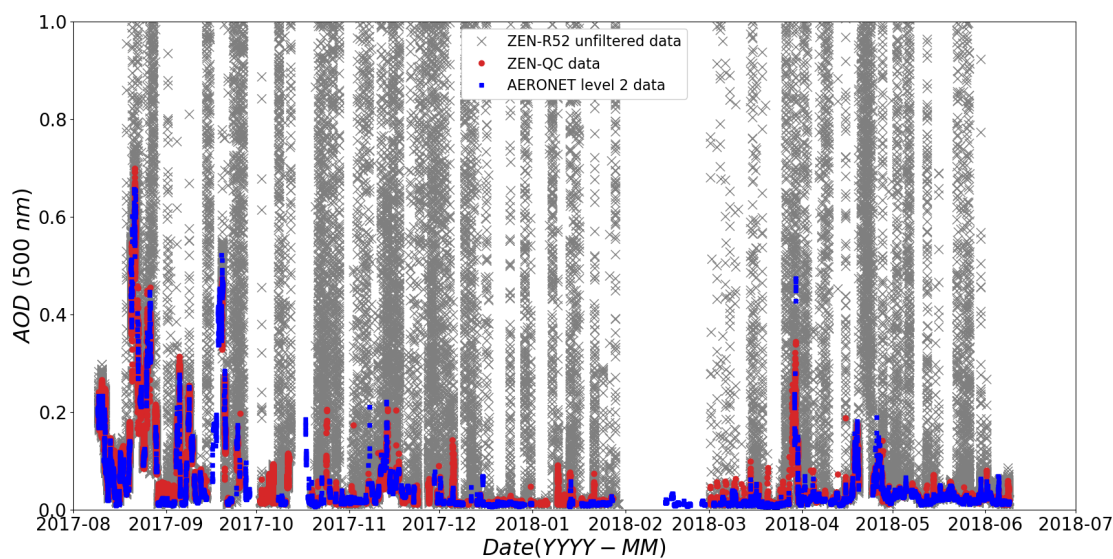
Figure 4: AOD at 500 nm for a 10-month period (August 2017 to June 2018) at Izaña station obtained from ZEN-R52 and CE318-AERONET radiometers. Grey crosses represent ZEN-R52 unfiltered AOD data, red solid circles depict ZEN-R52 AOD after applying the ZEN-QC algorithm, and blue squares show CE318-AERONET level 2.0 AOD data.
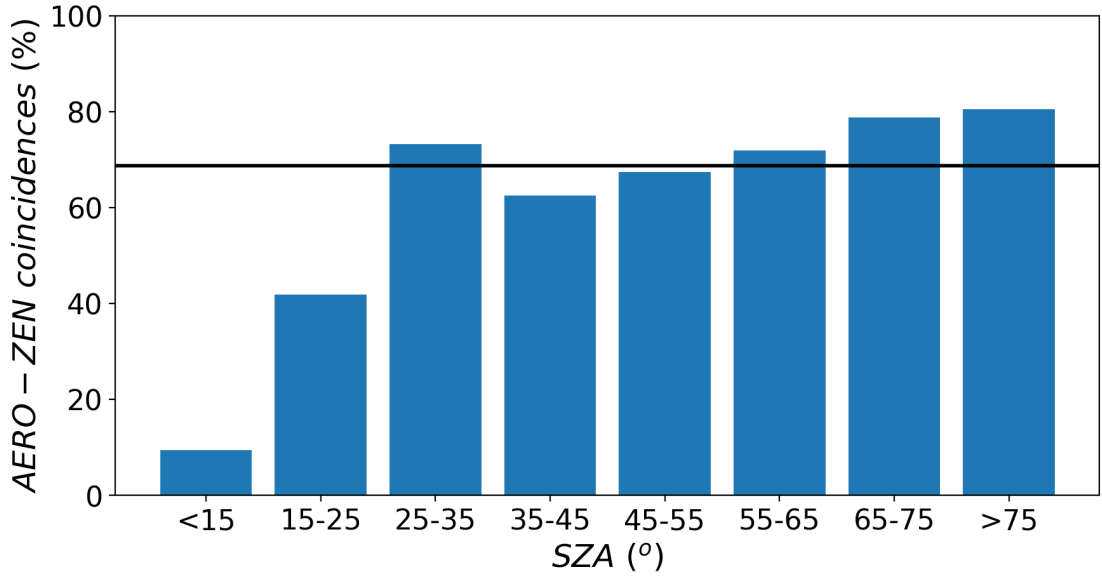
Figure 5: Coincidences (%) between AERONET and ZEN quality control algorithms for eight solar zenith angle (SZA) intervals. The black line represents the average of 68.8% of the coincidences.

3.2. ZSR comparisons

The ZSR measurements performed by ZEN-R41 and ZEN-R52 instruments were compared with the CE318 ZSRs derived from PPL sky radiance measurements. CE318 PPL measurements were done for a set of six nominal wavelengths (440, 500, 675, 870, 1020 and 1640 nm), with a duration of approximately 30 seconds for each spectral band. On the other hand, the ZEN-R's data are 1-minute averaged for all the channels at the same time. All sets of ZEN-R data were screened with the ZEN-QC algorithm previously described in Section 2.3.3. In the case of the CE318 PPL data, we employed the algorithm described in [37], which is based on the smoothness of the PPL curve. The closest data pairs with a time difference within ±30 seconds for the four coincident spectral bands, i.e., 440, 500, 675 and 870 nm, were used for the intercomparison.

The main statistics of the ZSR comparison between CE318-AERONET and ZEN-R41/R52 are presented in Table 2. High coefficients of determination (R^2 of 0.99) and low root mean squared errors (RMSE) for all wavelengths (between 0.0004 and 0.0009 W m^{-2} sr^{-1} nm^{-1}) were observed for both ZEN systems. Relative differences were low for both instruments at 440 and 500 nm, with a mean and standard deviation of relative differences lower than 7%. In particular, in the case of ZEN-R52, the mean bias and standard deviations of relative differences of 6.9%, 2.5%

and 0.9%, 2.3% were found, respectively, at these two wavelengths. However, these values were much higher for the longest wavelength channels, especially for ZEN-R41 at 870 nm, with a mean bias of 53.8% and a standard deviation of 39.8%. These values were reduced to 16.3% and 21.3%, respectively, in the case of the new ZEN-R52.

Table 2: Radiance comparison statistics by instrument and wavelength, taking CE318-AERONET ZSR measurements as references, including the coefficient of determination (R^2) and RMSE (W m^{-2} sr^{-1} nm^{-1}). The Zenith Sky Radiance (ZSR) mean and standard deviation of the relative differences (here represented as $<\Delta ZSR>$ and $\sigma(\Delta ZSR)$), and the number of data (N) are also shown.

Instrument	Channel	R^2	RMSE	$<\Delta$ZSR$>$	$\sigma(\Delta$ZSR$)$	N
	440	0.99	0.0009	6.9%	2.5%	962
ZEN-R52	500	0.99	0.0007	0.9%	2.3%	981
	675	0.99	0.0008	7.7%	6.3%	983
	870	0.99	0.0004	16.3%	21.3%	985
	440	0.99	0.0009	5.1%	2.7%	962
ZEN-R41	500	0.99	0.0007	2.5%	2.6%	981
	675	0.99	0.0008	6.8%	9.0%	983
	870	0.99	0.0007	53.8%	39.8%	985

The relative differences between ZEN-R and CE318 instruments for the four coincident wavelengths are plotted against the CE318 ZSR in Figure 6. It can be observed that the relative differences for ZEN-R versus CE318 increase as ZSRs decrease, which are lower at longer wavelengths. These results indicate that the low radiances measured at 870 nm are close to the detection limit of the ZEN-R, in addition to the presence of an offset signal or stray light, higher for the ZEN-R41, which is more significant for lower ZSR values at longer wavelengths in both systems. These results highlight the importance of increasing the signal-to-noise ratio and decreasing the stray light levels in future ZEN radiometer versions.

3.3. AOD Results

Quality-controlled ZEN-R52 AODs were compared to CE318-AERONET AOD version 3 level 2.0 data at IZO. The matching criterion was the same as the one defined in Section 3.2. CE318-AERONET versus ZEN-R52 AOD scatterplots at 440 and 870 nm are shown in Figure 7a,b. A good correlation between both datasets can be observed, with high coefficients of determination between 0.97 and 0.98 and a low RMSE (0.010 to 0.012).
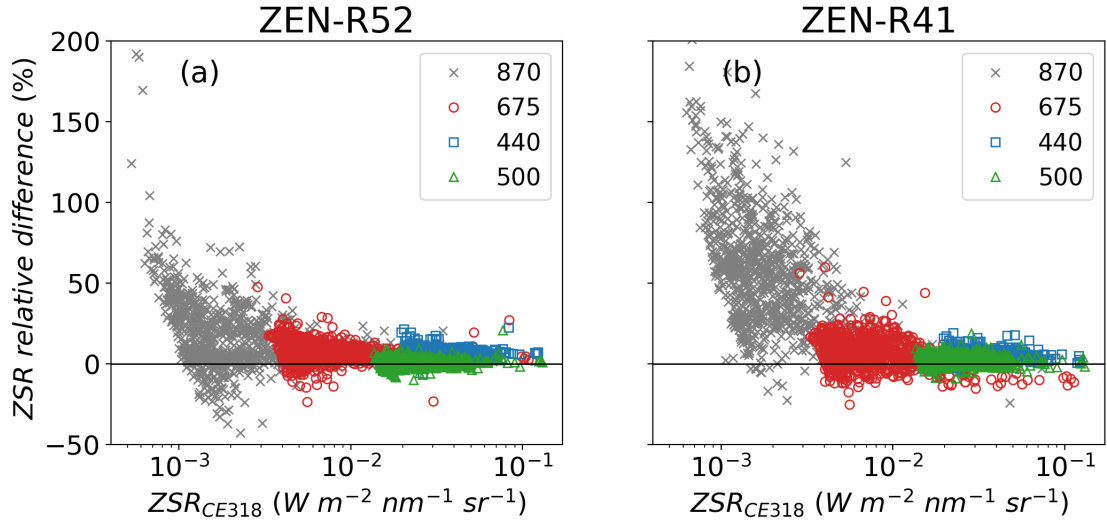
Figure 6: ZSR relative differences between (**a**) ZEN-R52 and (**b**) ZEN-R41 against CE318-AERONET ((ZSR_{ZEN-R}-ZSR_{CE318})/ ZSR_{CE318}) in logarithmic scale at the four coincident channels: 870 nm (grey crosses), 675 nm (red circles), 440 nm (blue squares), and 500 nm (green triangles).

Figure 7c,d show the AOD differences ($AOD_{ZEN-R52}$ - AOD_{CE318}) against SZA, indicating the dependence of $AOD_{ZEN-R52}$ on the solar elevation. For low AOD values (AOD $\leq$ 0.2), the AOD differences show a smooth "smile-shape" curve with the SZA. For SZA > 60°, the higher scatter could be explained because the plane-parallel approach employed by the DIScrete ORdinate Radiative Transfer (DISORT) solver is not a good enough approximation [48,56], while for SZA < 30°, the higher observed differences could be accounted for by ZEN-R52 instrumental issues, like stray light (recall Section 3.1). For higher AOD values (AOD $\geq$ 0.2), this "smile-shape" behaviour is also identified, but the differences are more accentuated, likely because the multiple scattering processes are not fully solved in ZEN–AOD–LUT simulations. This becomes more critical at higher SZAs, when the radiative properties, especially the phase function, estimated from the imposed mixture of aerosol components, could largely deviate from the real properties as the aerosol load increases. This SZA dependence was also shown by [37], highlighting the importance of an accurate aerosol characterization and its impact on the modeling of aerosol scattering in the near-forward direction. Overall, the results presented in this paper are similar to those presented in [37] when the AOD from ZEN-R41 and CE318-AERONET were compared at Izaña. Those authors estimated the uncertainty of the ZEN–AOD–LUT method by means of a sensitivity study of values up to 0.06 (for $AOD_{500} \sim 0.5$) and up to 0.15 (for $AOD_{500} \sim 1.0$) when an instrumental error of 5% was considered. In this work, we empirically
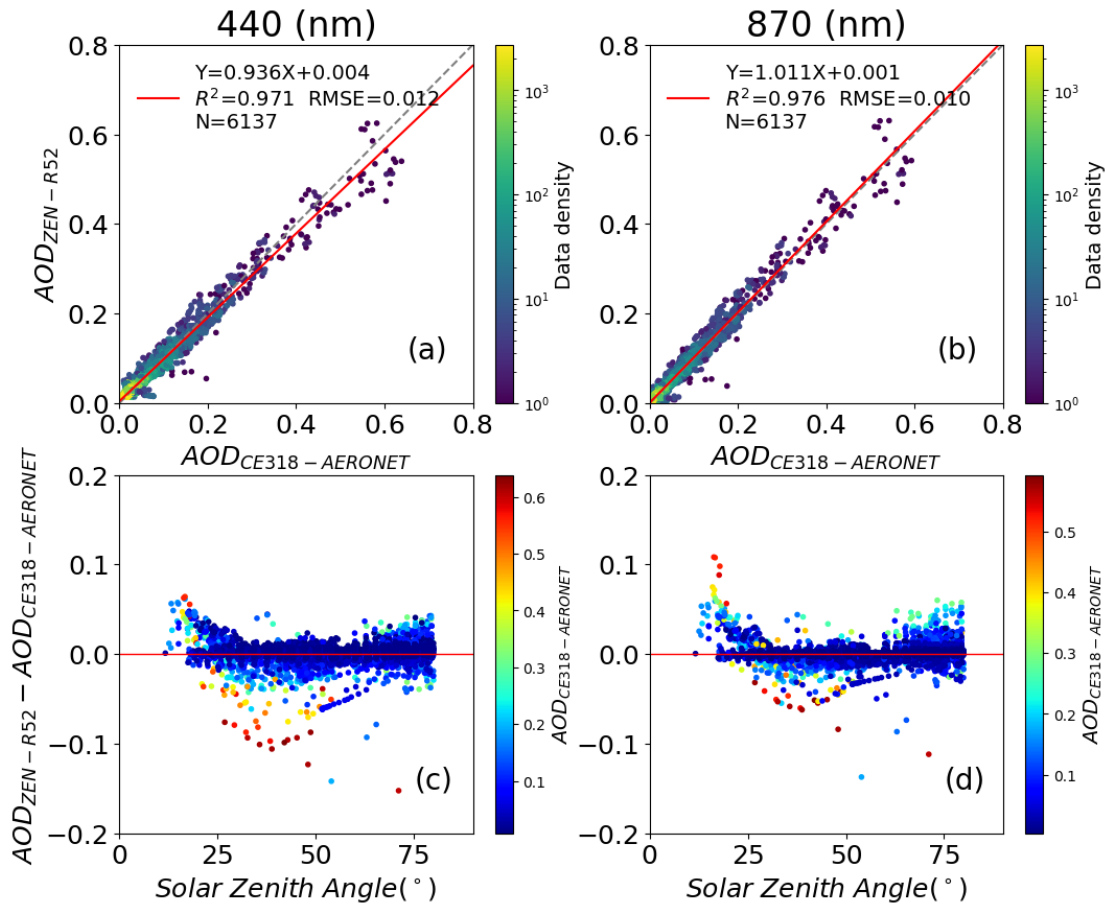
166

Figure 7: AOD scatter plot between AERONET and ZEN-R52 at 440 nm (**a**) and 870 nm (**b**) nominal wavelengths. The red line shows the linear fit equation, the broken grey line shows the diagonal and the colour bar indicates the density of data. ZEN-R52–AERONET AOD differences against the solar zenith angle are shown in (**c**) for 440 nm and in (**d**) for 870 nm, where the colour bar indicates AERONET AOD.

estimated the AOD uncertainty through the comparison of ZEN-R52 with CE318-AERONET, considering the latter as a reference. The standard deviation of the AOD differences for every channel at AOD intervals of 0.05 (between 0 and 0.6) are plotted in Figure 8. The standard deviation of the AOD differences was found to be linearly dependent on the AOD interval considered, with different intercepts (0.003 for the lower interval and -0.015 for the higher) and the same slope (0.13). Considering that CE318 AOD uncertainty is established to be around ±0.01, we estimate the ZEN-R52 AOD 1σ uncertainty to be $\pm 0.01 \pm 0.13 \ast \mathrm{AOD}$.

167
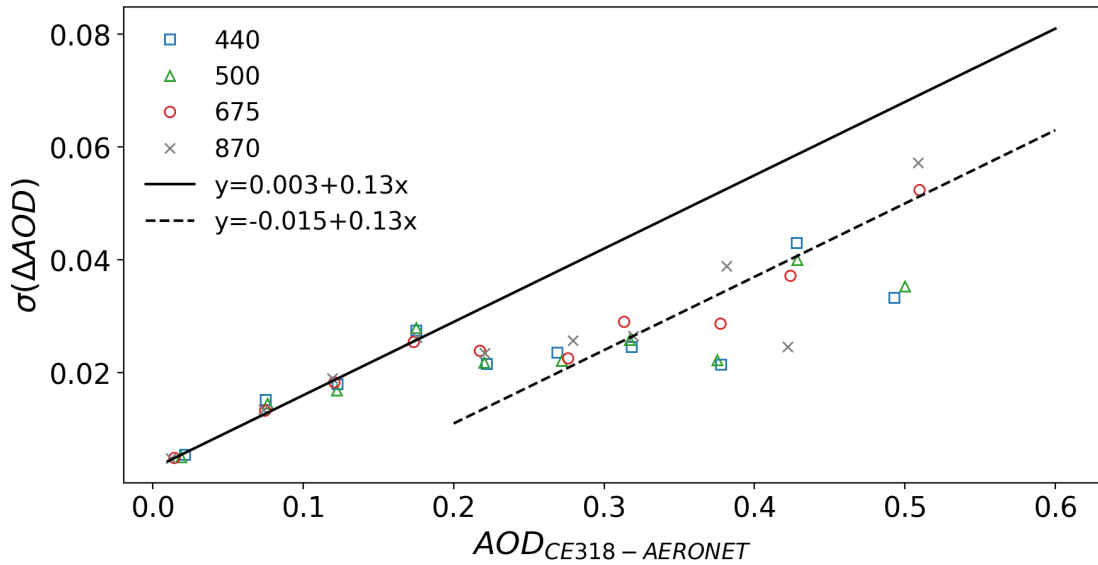
Figure 8: Standard deviation of the AOD differences between CE318-AERONET and ZEN-R52 for different AOD intervals of 0.05 between zero and 0.6. Data at 440, 500, 675, and 870 nm, are represented by blue squares, green triangles, red circles, and grey crosses, respectively. The black solid line represents the fitting equation for the standard deviation of the AOD differences for AOD values between zero and 0.2, while the broken black line depicts the fitting equation for the standard deviation of the AOD differences for higher AOD values (0.25 to 0.55).

3.4. PWV Results

We have compared the ZEN-R52 PWV obtained at IZO with the PWV retrieved by means of a reference FTIR spectrometer. This comparison has been extended, including data from the CE318 master radiometer at IZO.

ZEN-QC and CE318-AERONET level 2.0 (version 3) data were used in this comparison.

With regard to the PWV measurement sequence, the ZEN–R52 performs 1-minute measurements, while CE318-AERONET PWV values were obtained approximately every 15 minutes when the local time was between 9 and 15 hours. Outside this period, the frequency is variable and depends on the air mass. FTIR provides PWV measurements roughly every two minutes. The comparison analysis in the case of PWV is similar to the one described in the previous section for AOD, performed by means of matching the closest pair of records to a time difference within ±30 seconds.

PWV scatterplots including FTIR, CE318 and ZEN-R52 are displayed in Figure 9, and the main statistics between the different datasets are shown in Table 3. In particular, the scatterplot of ZEN-R52 against FTIR PWV is shown in Figure 9d. Relatively high coefficients of determination ($R^2 = 0.91$) and low RMSE (0.070 cm) between these two instruments are observed (Table 3), with a high standard deviation of PWV-relative differences ($\sigma(\Delta PWV/PWV)$ of 30.8%). Regarding the comparison between ZEN-R52 and CE318-AERONET, Figure 9e shows a lower intercept (0.04 cm), a similar R^2 (0.91), but a higher RMSE (0.090 cm) and scatter (39.7%). In this case, important PWV relative differences ($< \Delta PWV > /PWV$) of 40.1% were found.

Table 3: Comparisons statistics between PWV obtained from ZEN-R52, CE318-AERONET, CE318- Izaña Atmospheric Research Center (IARC) and FTIR. Mean and standard deviations of the PWV differences, in cm (here represented as $< \Delta PWV >$ and $\sigma(\Delta PWV)$), are included, in addition to relative PWV differences ($\Delta PWV/PWV$) and the standard deviation of relative PWV differences ($\sigma(\Delta PWV/PWV)$), in %, taking the X dataset as a reference.

Dataset X|Y	No. matches	R^2	RMSE (cm)	$<\Delta PWV>$ $<\Delta PWV/PWV>$	$\sigma(\Delta PWV)$ $\sigma(\Delta PWV/PWV)$
FTIR|CE318-AERO	589	0.99	0.026	-0.091 (-19.2%)	0.064 (6.1%)
FTIR|CE318-IARC	589	0.99	0.025	-0.016 (-3.4%)	0.029 (5.7%)
FTIR|ZEN	2701	0.91	0.070	-0.010 (9.1%)	0.089 (30.8%)
CE318-AERO|CE318-IARC	14253	0.99	0.012	0.071 (17.9%)	0.046 (3.6%)
CE318-AERO|ZEN	4666	0.91	0.090	0.097 (40.1%)	0.099 (39.7%)
CE318-IARC|ZEN	4666	0.90	0.094	0.033 (17.1%)	0.094 (32.0%)

CE318-AERONET and FTIR PWV have also been compared (Figure 9a and Table 3) in order to analyze, in detail, the previous discrepancies. In this comparison, high R^2 values (>0.99) and low RMSE (0.026 cm) indicate the good correlation of the data, and the low scatter between the two datasets is indicated by a low $\sigma(\Delta PWV/PWV$ value of 6.1%. However, a mean PWV difference of -19.2% reveals a remarkable systematic CE318-AERONET PWV underestimation. A similar underestimation was noted previously in the work of [13] using the same instruments at Izaña. Despite the fact that different FTIR products are used in the present study, the high magnitude of this bias could point to the possible calibration inaccuracy of the CE318-AERONET PWV product. As [47] has pointed out, errors due to spectroscopic parameters dominate FTIR systematic uncertainty, but they are expected to cause systematic errors lower than 2%. In fact, as mentioned, the FTIR PWV values used here were re-calibrated following the TCCON protocols
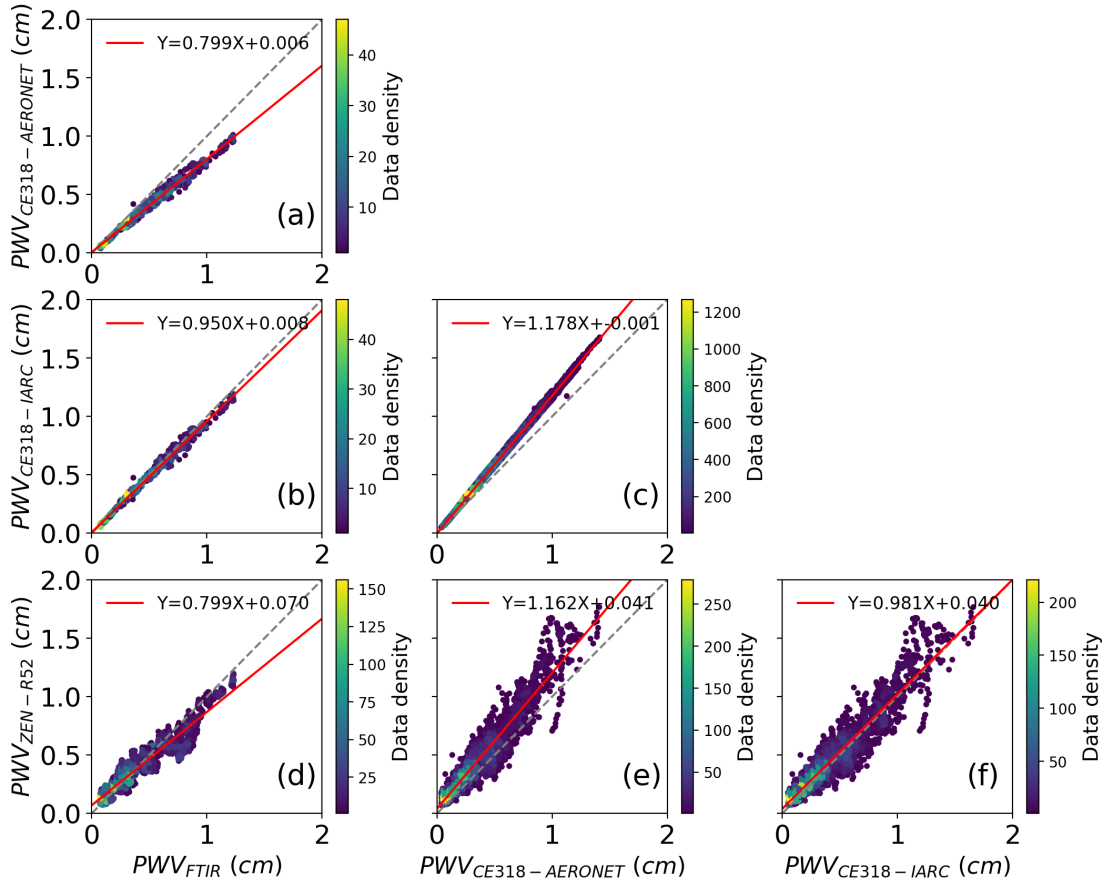
Figure 9: PWV scatterplots between ZEN-R52, CE318-AERONET, CE318-IARC and FTIR at Izaña over a 10-month period (August 2017 to June 2018 **a–f**). The red line shows the linear fit equation, the broken grey line shows the diagonal and the colour bar indicates the density of data.

in order to minimize this wet bias to $\sim 2\%$.

CE318 PWV data retrieved from the same AERONET master at Izaña, but with a self-computed calibration (CE318-IARC), were included in this study in order to understand the cause of this bias in AERONET PWV data in 2017 and 2018. The scatterplot of CE318-AERONET against CE318-IARC PWV (Figure 9c) shows a non-existent intercept and a slope of 1.178 from the regression analysis. A mean PWV difference of 17.9% (Table 3,) in addition to the reduction in $< \Delta PWV >$ between FTIR and CE318-IARC (-3.4%) indicates that the specific calibration of the 940 nm channel significantly improves the PWV estimation compared with the standard AERONET PWV product. The regression analysis in Figure 9b,f shows a close-to-unit slope in the comparison of CE318-IARC versus FTIR and ZEN-

R52 versus CE318-IARC, respectively. A similar scatter (5.7%), but a considerably lower bias (-3.4%) in the CE318-FTIR, when using the self-calibrated dataset, corroborates the better performance of the CE318-IARC calibration at 940 nm. These results are consistent with those reported in [13]. In this regard, using the CE318-IARC calibration, a mean bias of -0.016 cm is retrieved, much lower than that provided by CE318-AERONET in this study (-0.091 cm) and that found in [2] (-0.113 cm) when compared with the same AERONET product.

Regarding the ZEN-R52 PWV product, the intercept of the regression analysis close to 0.07 cm found when compared to FTIR, evidence there is not an important bias affecting PWV, but it is significant for very dry conditions (PWV ≤ 0.2 cm). The value of 0.089 cm for $\sigma(\Delta PWV)$ found for the full dataset between FTIR and ZEN-R52 can be used as a conservative estimator of the ZEN-R52's PWV uncertainty, while $< \Delta PWV >$ values give an estimation of the instrument's accuracy, between 9.1% (FTIR versus ZEN) and 17.1% (CE318-IARC versus ZEN).
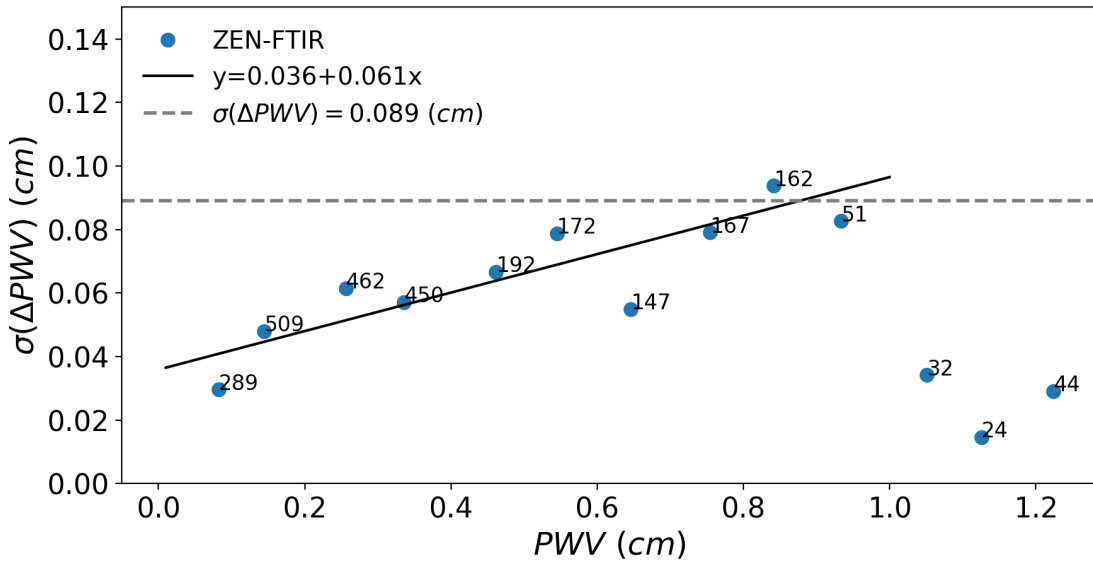
Figure 10: Standard deviation of the PWV differences between FTIR and ZEN-R52 (blue dots) for PWV intervals of 0.1 cm between 0 and 1.3 cm approximately. Numbers near the dots indicate the number of data included in each interval. The black solid line represents the fitting equation for the standard deviation of the PWV differences for PWV values between 0.1 and 1.0 cm. The broken grey line depicts the standard deviation of PWV differences between FTIR and ZEN-R52 for the full dataset.

Analogously to Section 3.3, we can also analyse if the ZEN-R52 PWV uncertainty shows a dependency on the PWV values. For this purpose, in Figure 10, we show the standard deviation of the PWV differences between ZEN-R52 and FTIR for FTIR

PWV intervals of 0.1 cm (between 0 and 1.3 cm). For a better interpretation of the significance of the different PWV intervals, the number of points for each PWV bin is also displayed in the figure. In a similar manner to AOD, two differentiated branches for the $\sigma(\Delta PWV)$ were found. For PWV < 1.0 cm, the standard deviation of the PWV differences show a clear lineal dependence ($R^2 = 0.73$) on the PWV values and, thus, the uncertainty of the ZEN-R52 PWV can be estimated as: $\pm 0.036 \pm 0.061$*PWV. Above the 1 cm limit, PWV observations are scarce, which prevents us from estimating the PWV uncertainty's dependency on this range. Thus, we should assume that the standard deviation of the PWV differences, 0.089 cm, is a conservative value for the ZEN PWV uncertainty above 1 cm.

4. Summary and Conclusions

The new ZEN-R52 has been specifically designed to monitor aerosols and atmospheric water vapor with a high degree of autonomy and robustness. The most remarkable differences in comparison to the previous ZEN-R41 prototype presented in [37] are the reduced field of view (smaller than 2°), the increased signal-to-noise ratio, better stray light rejection and the additional channel at 940 nm for PWV retrieval.

A new LUT methodology was used to estimate PWV (ZEN-PWV-LUT) over a 10-month period (August 2017 to June 2018) at Izaña high-altitude station by minimizing the normalized mean squared differences of computed and measured ZSRs. The new ZEN-PWV-LUT is dependent on the AOD previously retrieved by means of the ZEN-AOD-LUT method. A quality control procedure (ZEN-QC) was specifically designed to remove cloud-contaminated and erroneous data from the ZEN-R52 radiometer dataset. This ZEN-QC was validated against AERONET level 2.0 (version 3) data, showing a good performance.

The validation analysis in terms of quasi-simultaneous (± 30 s) ZSRs was carried out, considering CE318-AERONET ZSRs derived from PPL sky radiance measurements as a reference. Our results showed the improved performance of the ZEN-R52 compared with the ZEN-R41, but some effects of stray light are still discernible at longer wavelengths and lower SZA.

CE318-AERONET versus ZEN-R52 quasi-simultaneous AOD comparison showed a good correlation between both datasets (≈ 0.97) with low RMSE values (0.010 to 0.012). However, the presence of a systematic dependence of the AOD differences on SZA indicates the effect of inaccuracies on the radiative transfer modeling and on the instrumental measurements. This study also estimated the ZEN-R52 AOD uncertainty to be $\pm 0.01 \pm 0.13$*AOD.

A quasi-simultaneous PWV comparison between FTIR and ZEN-R52 indicated the good performance of the ZEN-R52 LUT PWV product, with an RMSE of 0.07 cm, R^2 of 0.91 and a mean PWV difference of 9.1%. Two different CE318 PWV datasets from the AERONET's permanent master at Izaña Observatory have been used: one obtained from AERONET (CE318-AERONET) and another one using a specific calibration performed in this study (CE318-IARC) using on-site actual input atmospheric parameters for the water vapor transmittance modeling. This approach provides better PVW values than those provided by CE318-AERONET when compared with the FTIR results for reference, despite the fact that it is worth admitting that AERONET PWV is a standard and global product. Our results show that the new ZEN-PWV-LUT technique provides fairly good estimations of PWV, with mean PWV relative differences of 9.1% and 17.1% with FTIR and CE318-IARC, respectively. The expected uncertainty of this technique is estimated to be ± 0.089 cm, which is an excellent result for a low-cost instrument. A subsequent uncertainty analysis estimated the PWV uncertainty to be linearly dependent on the PWV for PWV values < 1cm, following the equation $\pm 0.036 \pm 0.061 * PWV$.

The general conclusion is that the ZEN-R52 might be considered a useful tool to expand aerosol and water vapor monitoring from ground-based instrumentation in desert areas, thereby increasing the representativeness of ground measurements for constraining global and relatively coarse-resolution models. The ZEN-R52 might also improve our capabilities for satellite validation and aerosol model evaluation/assimilation in remote areas. The comprehensive validation performed in this paper in terms of ZSR, AOD and PWV against the CE318-AERONET reference instrument at Izaña observatory adds weight to the potential use of a ZEN network to expand aerosol and water vapor observations in remote areas. This study reveals that some improvements in future ZEN systems regarding their optical performance (signal-to-noise ratio and stray light) might be considered. Radiative transfer calculations, employing a higher resolution parametrization for water vapor absorption, which does not entail a greater computing time, would be a noticeable improvement. Finally, a new filter with a sixe of around 1020 nm would improve the AOD estimation at longer wavelengths, and therefore the PWV estimation.

were in charge of ZEN design and hardware/software development, and they contributed to the instrument description. All authors discussed the results and contributed to the final paper. All authors have read and agreed to the published version of the manuscript.

Conflicts of Interest: The authors declare no conflict of interest.

References

1. Myhre, G.; Shindell, D.; Bréon, F.-M.; Collins, W.; Fuglestvedt, J.; Huang, J.; Koch, D.; Lamarque, J.-F.; Lee, D.; Mendoza, B.; et al. Anthropogenic and natural radiative forcing. In Climate Change 2013: The Physical Science Basis. Contribution of Working Group I to the Fifth Assessment Report of the Intergovernmental Panel on Climate Change; Stocker, T.F., Qin, D., Plattner, G.-K., Tignor, M., Allen, S.K., Boschung, J., Nauels, A., Xia, Y., Bex, V., Midgley, P.M., Eds.; Cambridge University Press: Cambridge, UK; New York, NY, USA, 2013; pp. 659–740. ISBN 978-1-107-66182-0.

2. Wagner, T.; Beirle, S.; Grzegorski, M.; Platt, U. Global trends (1996–2003) of total column precipitable water observed by Global Ozone Monitoring Experiment (GOME) on ERS-2 and their relation to near-surface temperature. J. Geophys. Res. Atmos. 2006, 111, D12102. [CrossRef]

3. Chen, B.; Liu, Z. Global water vapor variability and trend from the latest 36 year (1979 to 2014) data of ECMWF and NCEP reanalyses, radiosonde, GPS, and microwave satellite. J. Geophys. Res. Atmos. 2016, 121, 11442–11462. [CrossRef]

4. Intergovernmental Panel on Climate Change. Climate Change 2007: The Physical Science Basis. Contribution of Working Group I to the Fourth Assessment Report of the Intergovernmental Panel on Climate Change; Solomon, S., Qin, D., Manning, M., Chen, Z., Marquis, M., Averyt, K.B., Tignor, M., Miller, H.L., Eds.; Cambridge University Press: Cambridge, UK; New York, NY, USA, 2007.

5. Allan, R.P.; Soden, B.J. Atmospheric warming and the amplification of precipitation extremes. Science 2008, 321, 1481–1484. [CrossRef]

6. Zhang, L.; Wu, L.; Gan, B. Modes and mechanisms of global water vapor variability over the twentieth century. J. Clim. 2013, 26, 5578–5593. [CrossRef]

7. Mieruch, S.; Noël, S.; Bovensmann, H.; Burrows, J.P. Analysis of global water vapour trends from satellite measurements in the visible spectral range. Atmos. Chem. Phys. 2008, 8, 491–504. [CrossRef]

8. Mieruch, S.; Schröder, M.; Noël, S.; Schulz, J. Comparison of decadal global water vapor changes derived from independent satellite time series. J. Geophys. Res. Atmos. 2014, 119, 12489–12499. [CrossRef]

9. Kunz, A.; Spelten, N.; Konopka, P.; Müller, R.; Forbes, R.M.; Wernli, H. Comparison of fast in situ stratospheric hygrometer (FISH) measurements of water vapor in the upper troposphere and lower stratosphere (UTLS) with ECMWF (re)analysis data. Atmos. Chem. Phys. 2014, 14, 10803–10822. [CrossRef]

10. Jiang, J.H.; Su, H.; Zhai, C.; Wu, L.; Minschwaner, K.; Molod, A.M.; Tompkins, A.M. An assessment of upper troposphere and lower stratosphere water vapor in MERRA, MERRA2, and ECMWF reanalyses using Aura MLS observations. J. Geophys. Res. Atmos. 2015, 120, 11468–11485. [CrossRef]

11. Cadeddu, M.P.; Liljegren, J.C.; Turner, D.D. The Atmospheric radiation measurement (ARM) program network of microwave radiometers: Instrumentation, data, and retrievals. Atmos. Meas. Tech. 2013, 6, 2359–2372. [CrossRef]

12. Dirksen, R.J.; Sommer, M.; Immler, F.J.; Hurst, D.F.; Kivi, R.; Vömel, H. Reference quality upper-air measurements: GRUAN data processing for the Vaisala RS92 radiosonde. Atmos. Meas. Tech. 2014, 7, 4463–4490. [CrossRef]

13. Schneider, M.; Romero, P.M.; Hase, F.; Blumenstock, T.; Cuevas, E.; Ramos, R. Continuous quality assessment of atmospheric water vapour measurement techniques: FTIR, Cimel, MFRSR, GPS, and Vaisala RS92. Atmos. Meas. Tech. 2010, 3, 323–338. [CrossRef]

14. Miloshevich, L.M.; Vömel, H.; Whiteman, D.N.; Leblanc, T. Accuracy assessment and correction of Vaisala RS92 radiosonde water vapor measurements. J. Geophys. Res. Atmos. 2009, 114. [CrossRef]

15. Jensen, M.P.; Holdridge, D.J.; Survo, P.; Lehtinen, R.; Baxter, S.; Toto, T.; Johnson, K.L. Comparison of Vaisala radiosondes RS41 and RS92 at the ARM Southern Great Plains site. Atmos. Meas. Tech. 2016, 9, 3115–3129. [CrossRef]

16. Bevis, M.; Businger, S.; Herring, T.A.; Rocken, C.; Anthes, R.A.; Ware, R.H. GPS meteorology: Remote sensing of atmospheric water vapor using the global positioning system. J. Geophys. Res. Atmos. 1992, 97, 15787–15801. [CrossRef]

17. Wang, J.; Zhang, L.; Dai, A.; Hove, T.V.; Baelen, J.V. A near-global, 2-hourly data set of atmospheric precipitable water from ground-based GPS measurements. J. Geophys. Res. Atmos. 2007, 112, D11107. [CrossRef]

18. Alexandrov, M.D.; Schmid, B.; Turner, D.D.; Cairns, B.; Oinas, V.; Lacis, A.A.; Gutman, S.I.; Westwater, E.R.; Smirnov, A.; Eilers, J. Columnar water vapor retrievals from multifilter rotating shadowband radiometer data. J. Geophys. Res. Atmos. 2009, 114, D02306. [CrossRef]

19. Halthore, R.N.; Eck, T.F.; Holben, B.N.; Markham, B.L. Sun photometric measurements of atmospheric water vapor column abundance in the 940-nm band. J. Geophys. Res. Atmos. 1997, 102, 4343–4352. [CrossRef]

20. Schmid, B.; Michalsky, J.J.; Slater, D.W.; Barnard, J.C.; Halthore, R.N.; Liljegren, J.C.; Holben, B.N.; Eck, T.F.; Livingston, J.M.; Russell, P.B.; et al. Comparison of columnar water-vapor measurements from solar transmittance methods. Appl. Opt. 2001, 40, 1886–1896. [CrossRef]

21. Torres, B.; Cachorro, V.E.; Toledano, C.; de Galisteo, J.P.O.; Berjón, A.; de Frutos, A.M.; Bennouna, Y.; Laulainen, N. Precipitable water vapor characterization in the Gulf of Cadiz region (southwestern Spain) based on Sun photometer, GPS, and radiosonde data. J. Geophys. Res. Atmos. 2010, 115, D18103. [CrossRef]

22. Pérez-Ramírez, D.; Navas-Guzmán, F.; Lyamani, H.; Fernández-Gálvez, J.; Olmo, F.J.; Alados-Arboledas, L. Retrievals of precipitable water vapor using star photometry: Assessment with Raman lidar and link to sun photometry. J. Geophys. Res. Atmos. 2012, 117, D05202. [CrossRef]

23. Pérez-Ramírez, D.; Whiteman, D.N.; Smirnov, A.; Lyamani, H.; Holben, B.N.; Pinker, R.; Andrade, M.; Alados-Arboledas, L. Evaluation of AERONET precipitable water vapor versus microwave radiometry, GPS, and radiosondes at ARM sites. J. Geophys. Res. Atmos. 2014, 119, 9596–9613. [CrossRef]

24. Cachorro, V.E.; Utrillas, P.; Vergaz, R.; Durán, P.; de Frutos, A.M.; Martinez-Lozano, J.A. Determination of the atmospheric-water-vapor content in the 940-nm

absorption band by use of moderate spectral-resolution measurements of direct solar irradiance. Appl. Opt. 1998, 37, 4678–4689. [CrossRef] [PubMed]

25. Raptis, P.-I.; Kazadzis, S.; Gröbner, J.; Kouremeti, N.; Doppler, L.; Becker, R.; Helmis, C. Water vapour retrieval using the Precision Solar Spectroradiometer. Atmos. Meas. Tech. 2018, 11, 1143–1157. [CrossRef]

26. Trenberth, K.E.; Jones, P.D.; Ambenje, P.; Bojariu, R.; Easterling, D.; Klein Tank, A.; Parker, D.; Rahimzadeh, F.; Renwick, J.A.; Rusticucci, M.; et al. Observations: Surface and Atmospheric Climate Change. In IPCC, 2007: Climate Change 2007: The Physical Science Basis. Contribution of Working Group I to the Fourth Assessment Report of the Intergovernmental Panel on Climate Change; Solomon, S., Qin, D., Manning, M., Chen, Z., Marquis, M., Averyt, K.B., Tignor, M., Miller, H.L., Eds.; Cambridge University Press: Cambridge, UK; New York, NY, USA, 2007.

27. Boucher, O.; Randall, D.; Artaxo, P.; Bretherton, C.; Feingold, G.; Forster, P.; Kerminen, V.-M.; Kondo, Y.; Liao, H.; Lohmann, U.; et al. Clouds and aerosols. In Climate Change 2013: The Physical Science Basis. Contribution of Working Group I to the Fifth Assessment Report of the Intergovernmental Panel on Climate Change; Stocker, T.F., Qin, D., Plattner, G.-K., Tignor, M., Allen, S.K., Boschung, J., Nauels, A., Xia, Y., Bex, V., Midgley, P.M., Eds.; Cambridge University Press: Cambridge, UK; New York, NY, USA, 2013; pp. 571–658. ISBN 978-1-107-66182-0.

28. Holben, B.N.; Tanré, D.; Smirnov, A.; Eck, T.F.; Slutsker, I.; Abuhassan, N.; Newcomb, W.W.; Schafer, J.S.; Chatenet, B.; Lavenu, F.; et al. An emerging ground-based aerosol climatology: Aerosol optical depth from AERONET. J. Geophys. Res. C Ocean. 2001, 106, 12067–12097. [CrossRef]

29. Kazadzis, S.; Kouremeti, N.; Diémoz, H.; Gröbner, J.; Forgan, B.W.; Campanelli, M.; Estellés, V.; Lantz, K.; Michalsky, J.; Carlund, T.; et al. Results from the Fourth WMO Filter Radiometer Comparison for aerosol optical depth measurements. Atmos. Chem. Phys. 2018, 18, 3185–3201. [CrossRef]

30. Li, Z.; Zhao, X.; Kahn, R.; Mishchenko, M.; Remer, L.; Lee, K.-H.; Wang, M.; Laszlo, I.; Nakajima, T.; Maring, H. Uncertainties in satellite remote sensing of aerosols and impact on monitoring its long-term trend: A review and perspective. Ann. Geophys. 2009, 27, 2755–2770. [CrossRef]

31. Bruegge, C.J.; Conel, J.E.; Green, R.O.; Margolis, J.S.; Holm, R.G.; Toon, G. Water vapor column abundance retrievals during FIFE. J. Geophys. Res. Atmos. 1992, 97, 18759–18768. [CrossRef]

32. Campanelli, M.; Mascitelli, A.; Sanò, P.; Diémoz, H.; Estellés, V.; Federico, S.; Iannarelli, A.M.; Fratarcangeli, F.; Mazzoni, A.; Realini, E.; et al. Precipitable water vapour content from ESR/SKYNET sun–sky radiometers: Validation against

GNSS/GPS and AERONET over three different sites in Europe. Atmos. Meas. Tech. 2018, 11, 81–94. [CrossRef]

33. Wehrli, C. GAWPFR: A network of aerosol optical depth observations with precision filter radiometers. In Proceedings of the WMOGAW Experts Workshop Global Surface Based Network Long Term Observations Column Aerosol Optical Properties, Davos, Switzerland, 8–10 March 2004; pp. 36–39.

34. Che, H.; Zhang, X.-Y.; Xia, X.; Goloub, P.; Holben, B.; Zhao, H.; Wang, Y.; Zhang, X.-C.; Wang, H.; Blarel, L.; et al. Ground-based aerosol climatology of China: Aerosol optical depths from the China Aerosol Remote Sensing Network (CARSNET) 2002–2013. Atmos. Chem. Phys. 2015, 15, 7619–7652. [CrossRef]

35. Takamura, T.; Nakajima, T. Overview of SKYNET and its Activities. Óptica Pura Apl. 2004, 37, 3303–3308.

36. Holben, B.N.; Eck, T.F.; Slutsker, I.; Tanré, D.; Buis, J.P.; Setzer, A.; Vermote, E.; Reagan, J.A.; Kaufman, Y.J.; Nakajima, T.; et al. AERONET—A federated instrument network and data archive for aerosol characterization. Remote Sens. Environ. 1998, 66, 1–16. [CrossRef]

37. Almansa, A.F.; Cuevas, E.; Torres, B.; Barreto, A.; García, R.D.; Cachorro, V.E.; de Frutos, A.M.; López, C.; Ramos, R. A new zenith-looking narrow-band radiometer-based system (ZEN) for dust aerosol optical depth monitoring. Atmos. Meas. Tech. 2017, 10, 565–579. [CrossRef]

38. Cuevas, E.; Milford, C.; Bustos, J.J.R.; García, O.E.; García, R.D.; Gómez-Peláez, A.J.; Guirado-Fuentes, C.; Marrero, C.; Prats, N.; Ramos, L.; et al. Izaña Atmospheric Research Center Activity Report 2017–2018; Cuevas, E., Milford, C., Tarasova, O., Eds.; State Meteorological Agency (AEMET): Madrid, Spain; World Meteorological Organization: Geneva, Switzerland, 2019.

39. Toledano, C.; González, R.; Fuertes, D.; Cuevas, E.; Eck, T.F.; Kazadzis, S.; Kouremeti, N.; Gröbner, J.; Goloub, P.; Blarel, L.; et al. Assessment of Sun photometer Langley calibration at the high-elevation sites Mauna Loa and Izaña. Atmos. Chem. Phys. 2018, 18, 14555–14567. [CrossRef]

40. Cuevas, E.; Romero-Campos, P.M.; Kouremeti, N.; Kazadzis, S.; Räisänen, P.; García, R.D.; Barreto, A.; Guirado-Fuentes, C.; Ramos, R.; Toledano, C.; et al. Aerosol optical depth comparison between GAW-PFR and AERONET-Cimel radiometers from long-term (2005–2015) 1 min synchronous measurements. Atmos. Meas. Tech. 2019, 12, 4309–4337. [CrossRef]

41. Basart, S.; Perez, C.; Cuevas, E.; Baldasano, J.M.; Gobbi, G.P. Aerosol characterization in Northern Africa, Northeastern Atlantic, Mediterranean Basin and Middle East from direct-sun AERONET observations. Atmos. Chem. Phys. 2009, 9, 8265–8282. [CrossRef]

42. Andrey, J.; Cuevas, E.; Parrondo, M.C.; Alonso-Pérez, S.; Redondas, A.; Gil-Ojeda, M. Quantification of ozone reductions within the Saharan air layer through a 13-year climatologic analysis of ozone profiles. Atmos. Environ. 2014, 84, 28–34. [CrossRef]

43. Gui, K.; Che, H.; Chen, Q.; Zeng, Z.; Liu, H.; Wang, Y.; Zheng, Y.; Sun, T.; Liao, T.; Wang, H.; et al. Evaluation of radiosonde, MODIS-NIR-Clear, and AERONET precipitable water vapor using IGS ground-based GPS measurements over China. Atmos. Res. 2017, 197, 461–473. [CrossRef]

44. Walker, J.; Cromer, C.L.; McLean, J.T. Technique for improving the calibration of large-area sphere sources. In Calibration of Passive Remote Observing Optical and Microwave Instrumentation, Proceedings of the International Society for Optics and Photonics, Orlando, FL, USA, 4–5 April 1991; Guenther, B.W., Ed.; Society of Photo-Optical Instrumentation Engineers (SPIE): Bellingham, WA, USA, 1991; Volume 1493, pp. 224–230.

45. Giles, D.M.; Sinyuk, A.; Sorokin, M.G.; Schafer, J.S.; Smirnov, A.; Slutsker, I.; Eck, T.F.; Holben, B.N.; Lewis, J.R.; Campbell, J.R.; et al. Advancements in the Aerosol Robotic Network (AERONET) Version 3 database–automated near-real-time quality control algorithm with improved cloud screening for Sun photometer aerosol optical depth (AOD) measurements. Atmos. Meas. Tech. 2019, 12, 169–209. [CrossRef]

46. Eck, T.F.; Holben, B.N.; Reid, J.S.; Dubovik, O.; Smirnov, A.; O'Neill, N.T.; Slutsker, I.; Kinne, S. Wavelength dependence of the optical depth of biomass burning, urban, and desert dust aerosols. J. Geophys. Res. Atmos. 1999, 104, 31333–31349. [CrossRef]

47. Wunch, D.; Toon, G.C.; Sherlock, V.; Deutscher, N.M.; Liu, C.; Feist, D.G.; Wennberg, P.O. Documentation for the 2014 TCCON Data Release (Version GGG2014.R0). CaltechDATA 2015. [CrossRef]

48. Mayer, B.; Kylling, A. Technical note: The libRadtran software package for radiative transfer calculations–description and examples of use. Atmos. Chem. Phys. 2005, 5, 1855–1877. [CrossRef]

49. Emde, C.; Buras-Schnell, R.; Kylling, A.; Mayer, B.; Gasteiger, J.; Hamann, U.; Kylling, J.; Richter, B.; Pause, C.; Dowling, T.; et al. The libRadtran software package for radiative transfer calculations (version 2.0.1). Geosci. Model Dev. 2016, 9, 1647–1672. [CrossRef]

50. Gasteiger, J.; Emde, C.; Mayer, B.; Buras, R.; Buehler, S.A.; Lemke, O. Representative wavelengths absorption parameterization applied to satellite channels and spectral bands. J. Quant. Spectrosc. Radiat. Transf. 2014, 148, 99–115. [CrossRef]

51. Clough, S.A.; Shephard, M.W.; Mlawer, E.J.; Delamere, J.S.; Iacono, M.J.; Cady-Pereira, K.; Boukabara, S.; Brown, P.D. Atmospheric radiative transfer modeling: A summary of the AER codes. J. Quant. Spectrosc. Radiat. Transf. 2005, 91, 233–244. [CrossRef]

52. Smirnov, A.; Holben, B.N.; Eck, T.F.; Dubovik, O.; Slutsker, I. Cloud-Screening and quality control algorithms for the AERONET database. Remote Sens. Environ. 2000, 73, 337–349. [CrossRef]

53. Halthore, R.N.; Markham, B.L.; Deering, D.W. Atmospheric correction and calibration during kurex-91. In Proceedings of the IGARSS '92 International Geoscience and Remote Sensing Symposium, Houston, TX, USA, 26–29 May 1992; Volume 2, pp. 1278–1280.

54. Schmid, B.; Thorne, K.J.; Demoulin, P.; Peter, R.; Mätzler, C.; Sekler, J. Comparison of modeled and empirical approaches for retrieving columnar water vapor from solar transmittance measurements in the 0.94-µm region. J. Geophys. Res. Atmos. 1996, 101, 9345–9358. [CrossRef]

55. Kasten, F. A new table and approximation formula for the relative optial air mass. Arch. Für Meteorol. Geophys. Bioklimatol. Ser. B 1965, 14, 206–223. [CrossRef]

56. Dahlback, A.; Stamnes, K. A new spherical model for computing the radiation field available for photolysis and heating at twilight. Planet. Space Sci. 1991, 39, 671–683. [CrossRef]

7.3.4. Conclusiones

La validación completa de medidas de ZSR, AOD y PWV del ZEN-R52 frente a instrumentos de referencia (CE318-AERONET y FTIR) en el Observatorio Atmosférico de Izaña indican que el ZEN-R52 es un instrumento que proporciona datos de la suficiente calidad como para ser utilizado en nuevas redes de observación que complementen a las clásicas, sobre todo, en áreas desérticas, incrementando así la capacidad observacional y aumentando así la representatividad de las medidas desde la superficie terrestre. El ZEN-R52 también podría mejorar nuestras capacidades para la validación de datos de satélite y la evaluación / asimilación de los modelos de aerosoles en áreas remotas. Este estudio también revela que podrían considerarse algunas mejoras en los futuros sistemas ZEN con respecto a su rendimiento óptico (relación señal a ruido y luz parásita).

8. Conclusiones generales

A continuación se presentan las principales conclusiones obtenidas a partir de los resultados obtenidos en esta tesis doctoral.

1. La comparación a largo plazo del AOD entre las redes GAW-PFR y AERONET a partir de medidas síncronas realizada en el Observatorio Atmosférico de Izaña que involucró más de 70000 datos minutales en longitudes de onda comunes (380, 440, 500 y 870 nm) mostró los siguientes resultados parciales:

   - Una excelente trazabilidad (95-98 %) para las tres longitudes de onda más largas (440-870 nm).

   - La trazabilidad en el canal centrado a 380 nm resultó inferior al 95 %.

   - La influencia en las discrepancias de AOD observadas de la variabilidad del AOD en 1 minuto, de los distintos algoritmos de detección de nubes o de las diferencias en los parámetros atmosféricos cómo la presión o la concentración de O_3 o NO_2, es muy baja salvo en 380 nm.

   - Las diferencias en el AOD observadas entre los dos conjuntos de datos se atribuyen, principalmente, al desalineamiento del seguidor solar del radiómetro PFR y al impacto del mayor FOV del mismo (2,5°) en relación al FOV más reducido del radiómetro Cimel CE318 (1,3°), diferencia que toma especial relevancia en condiciones de alta turbiedad.

   - Las diferencias de AE entre los dos conjuntos de datos, son superiores a 0,2 aumentando exponencialmente hasta alcanzar un valor de 1,6 en condiciones muy limpias ($AOD \leq 0,03$ y $AE \geq 1$). No obstante, en la práctica, la caracterización del AE para una carga de aerosoles tan baja carece de utilidad. Por otro lado, en condiciones con un alto contenido de polvo mineral (AOD asociado> 0,03 y $AE < 1$), las diferencias de AE permanecen < 0,1.

   - Esta comparación muestra que los conjuntos de datos de AOD, AE-

RONET y GAW-PFR, son representativos de la misma población de AOD para las citadas bandas. Este resultado justifica que se utilice, por razones prácticas, Cimel AERONET como referencia de AOD en los dos artículos que abordan los sistemas ZEN-R41 y ZEN-R52.

- Se propone la redefinición de los límites de trazabilidad de la WMO-CIMO en función de la longitud de onda.

- Se debe tener en cuenta las dimensiones del FOV del radiómetro que proporcione las medidas de AOD para realizar una posible corrección de las mismas si se han obtenido en condiciones de alta turbiedad.

2. En relación al desarrollo del sistema ZEN-R41:

- Se ha demostrado que el sistema ZEN, compuesto por el radiómetro cenital ZEN-R41 y la metodología tipo LUT desarrollada a partir del código de transferencia radiativa libRadtran, es capaz de estimar el AOD con una incertidumbre estándar combinada de hasta 0,06 en el caso de $AOD_{500} \approx 0,5$ y 0,15 para $AOD_{500} \approx 1,0$.

- La validación de la técnica LUT para el cálculo del AOD se realizó utilizando medidas de radiancia de cielo en la secuencia del plano principal obtenidas con el radiómetro Cimel CE318 de la red AERONET y comparándolas con el AOD obtenido de esa misma red en un periodo de un año, en tres localizaciones distintas afectadas por eventos episódicos de polvo mineral: Izaña y Santa Cruz de Tenerife en las Islas Canarias y Tamanrasset en Argelia. Los resultados mostraron una alta correlación entre los conjuntos de datos con R^2 de entre 0,97 (Izaña y Tamanrasset) y 0,99 (Santa Cruz de Tenerife), y valores de RMSE relativamente bajos, entre 0,010 en Izaña y 0,032 en Tamanrasset.

- La comparación en términos de AOD entre el radiómetro ZEN-R41 con los datos proporcionado por AERONET fue realizada en Izaña durante el año 2015, mostrando un buen acuerdo entre ambos conjuntos de datos (R^2 de 0,97), con diferencias observadas de hasta 0,15 para el AOD. Además, se comprobó que el ZEN-R41 subestima sistemáticamente el AOD con un sesgo promedio que varía entre $-0,020$ y $-0,030$.

- Esta comparativa demuestra que el sistema ZEN-R41 es un sistema adecuado para completar los actuales huecos observacionales, complementando las observaciones realizadas por las actuales redes de fotómetros solares, y mejorando así las observaciones de polvo mineral en regiones remotas, donde es difícil instalar este tipo de instrumentación por razones logísticas y escasez de infraestructuras y recursos humanos.

3. En relación al desarrollo del sistema ZEN-R52:

- El nuevo radiómetro ZEN-R52, una versión mejorada y actualizada del prototipo ZEN-R41 capaz de determinar no sólo el AOD sino también el PWV con un alto grado de autonomía y robustez.

- Sus principales mejoras incluyen un menor FOV (menor de 2°), una mejor relación señal a ruido, un menor impacto de la luz parásita y un canal adicional en 940 nm para la determinación del PWV.

- El sistema ZEN incluye el radiómetro ZEN-R52, así como una metodología LUT para la estimación del AOD y del PWV y un nuevo algoritmo de control de calidad (ZEN-QC).

- La comparación en términos de radiancia cenital de los radiómetros ZEN-R41 y ZEN-R52 entre sí y con datos del Cimel CE318 mostraron la mejora en el rendimiento del ZEN-R52 en comparación con el ZEN-R41, aunque aún se observan los efectos de la luz parásita, principalmente en las longitudes de onda más largas y los ángulos cenitales del sol (SZA) más bajos.

- La validación del producto de AOD del radiómetro ZEN-R52 con datos de AERONET mostró una buena correlación entre ambos conjuntos de datos, obteniéndose un R^2 de aproximadamente 0,97 y valores bajos RMSE (de 0,010 a 0,012). Sin embargo, la presencia de una dependencia sistemática de las diferencias de AOD con el SZA indica el efecto de las imprecisiones en los parámetros de entrada del modelo de transferencia radiativa y en las medidas instrumentales. La incertidumbre del AOD del ZEN-R52 se estableció en $\pm 0,01 \pm 0,13 \times AOD$.

- La validación del producto de PWV del ZEN-R52 con respecto al FTIR, tomado como referencia, mostró un buen acuerdo entre ambos, con un RMSE de 0,07 cm, un R^2 de 0,91 y una diferencia promedio del 9,1 %.

- Una posterior validación del PWV incluyó datos del radiómetro Cimel CE318. Por un lado, se usaron datos extraídos de AERONET (CE318-AERONET) y por otro lado datos del mismo Cimel CE318 utilizando una calibración específica realizada en este estudio (CE318-IARC), en la que se incluían parámetros de entrada más acordes con el lugar de medida para el modelado de transmitancia del vapor de agua. Se encontraron diferencias promedio en el PWV de 40,1 % y 17,1 %, respectivamente.

- La incertidumbre en el PWV para el ZEN-R52 se estimó en $\pm 0,089$ cm, que es un excelente resultado para un instrumento de bajo coste.

Un análisis de incertidumbre posterior estimó que la incertidumbre del PWV es linealmente dependiente con el PWV para valores de PWV < 1 cm, siguiendo la ecuación $\pm 0{,}036 \pm 0{,}061 \times PWV$.

Debido a la alta precisión en la determinación del AOD alcanzada por los fotómetros solares, las observaciones desde tierra de este parámetro son indispensables para la validación de las medidas desde satélites, así como la validación y asimilación tanto de modelos climáticos como de predicción de aerosoles. Los resultados de la intercomparación entre GAW-PFR y AERONET llevada a cabo en este trabajo avalan el uso de ambas redes fotométricas como referentes en la medida del AOD gracias al excelente acuerdo encontrado entre ambas. Por otro lado, la cobertura ofrecida por estas redes dista mucho de ser completa y sufre de muchos vacíos observacionales, especialmente en zonas desérticas remotas debido a su coste y su necesidad de mantenimiento por parte de personal cualificado. Por ello, a la luz de los resultados obtenidos con el sistema ZEN y gracias a su simplicidad, robustez y bajo coste económico, pensamos que este sistema sería una herramienta muy útil para su despliegue en regiones remotas donde no es posible instalar un fotómetro de manera continua. Esto ayudaría a mejorar el conocimiento de la distribución espacio-temporal de los aerosoles y el vapor de agua.

9. Líneas futuras

El trabajo desarrollado en la presente tesis doctoral podría ser completado y mejorado si se abordaran algunas de las siguientes líneas futuras de investigación:

1. Optimización del sistema ZEN mediante la disminución de la luz parásita y la extensión del rango espectral, añadiendo un filtro pasabanda centrado en 1020 nm que mejoraría la estimación del AOD en longitudes de onda más largas y, por lo tanto, la estimación del PWV.

2. Extensión de la metodología ZEN-LUT, actualmente desarrollada específicamente para aerosoles tipo desértico, a otros diferentes tipos de aerosol así como a sus posibles grados de mezcla.

3. Mejora de las LUT del método ZEN-PWV-LUT empleando una parametrización de mayor resolución para la transmisividad de vapor de agua.

4. Realización de un estudio de sensibilidad del PWV con el fin de identificar las fuentes de error más influyentes en el cálculo del PWV.

5. Implementación operativa del sistema ZEN como complemento a las redes actuales de observación, en especial, y gracias a su alto grado de autonomía y robustez, en regiones remotas desérticas que no estén cubiertas por otros radiómetros para la observación del AOD y el PWV. Este nuevo sistema puede jugar un papel importante en el sistema de detección SDS-WAS de la WMO, proporcionando información para mejorar nuestro conocimiento actual sobre los procesos de emisión, propiedades ópticas y radiativas en zonas fuente de polvo mineral, así como en la validación/asimilación de modelos de aerosoles.

6. Uso del sistema ZEN en campañas de observación del AOD. Al ser económico y robusto se podría cubrir un área mayor que con otros instrumentos, aunque siempre se debería contar con un instrumento de referencia para su verificación.

7. Vinculación de las actividades de las futuras redes basadas en sistemas ZEN con los productos proporcionados por plataformas satelitales. La validación de muchas propiedades y productos de aerosoles por teledetección basados en satélites sigue siendo inadecuada, en muchos casos. Las mediciones terrestres son esenciales para estas validaciones. Cabe destacar que representan una pequeña fracción del costo de una misión satelital y añaden una gran cantidad de valor a las observaciones de satélite.

8. Extensión de los productos de aerosoles del sistema ZEN proporcionando propiedades ópticas y radiativas gracias al uso del código de inversión GRASP (General Retrieval of Atmosphere and Surface Properties).

Bibliografía

Abouchami, W., Näthe, K., Kumar, A., Galer, S. J. G., Jochum, K. P., Williams, E., Horbe, A. M. C., Rosa, J. W. C., Balsam, W., Adams, D., Mezger, K., and Andreae, M. O.: Geochemical and isotopic characterization of the Bodélé Depression dust source and implications for transatlantic dust transport to the Amazon Basin, Earth and Planetary Science Letters, 380, 112 – 123, doi: 10.1016/j.epsl.2013.08. 028, 2013.

Al-Hemoud, A., Al-Sudairawi, M., Neelamanai, S., Naseeb, A., and Behbehani, W.: Socioeconomic effect of dust storms in Kuwait, Arabian Journal of Geosciences, 10, 18, doi: 10.1007/s12517-016-2816-9, 2017.

Albrecht, B. A.: Aerosols, Cloud Microphysics, and Fractional Cloudiness, Science, 245, 1227–1230, doi: 10.1126/science.245.4923.1227, 1989.

Alexandrov, M. D., Schmid, B., Turner, D. D., Cairns, B., Oinas, V., Lacis, A. A., Gutman, S. I., Westwater, E. R., Smirnov, A., and Eilers, J.: Columnar water vapor retrievals from multifilter rotating shadowband radiometer data, Journal of Geophysical Research: Atmospheres, 114, doi: 10.1029/2008JD010543, 2009.

Allan, R. P. and Soden, B. J.: Atmospheric Warming and the Amplification of Precipitation Extremes, Science, 321, 1481–1484, doi: 10.1126/science.1160787, 2008.

Almansa, A. F., Cuevas, E., Torres, B., Barreto, Á., García, R. D., Cachorro, V. E., de Frutos, Á. M., López, C., and Ramos, R.: A new zenith-looking narrow-band radiometer-based system (ZEN) for dust aerosol optical depth monitoring, Atmospheric Measurement Techniques, 10, 565–579, doi: 10.5194/amt-10-565-2017, 2017.

Alonso-Pérez, S., Cuevas, E., Querol, X., Viana, M., and Guerra, J.: Impact of the Saharan dust outbreaks on the ambient levels of total suspended particles (TSP) in the marine boundary layer (MBL) of the Subtropical Eastern North Atlantic

Ocean, Atmospheric Environment, 41, 9468 – 9480, doi: 10.1016/j.atmosenv.2007.08.049, 2007.

Anderson, G., Clough, S., Kneizys, F., Chetwynd, J., and Shettle, E.: AFGL Atmospheric Constituent Profiles (0 - 120 km), Environmental research papers, Air Force Cambridge Research Laboratories, Office of Aerospace Research, URL https://books.google.es/books?id=rUTfvgEACAAJ, 1986.

Ångström, A.: On the Atmospheric Transmission of Sun Radiation and on Dust in the Air, Geografiska Annaler, 11, 156–166, URL http://www.jstor.org/stable/519399, 1929.

Ångström, A.: Techniques of Determinig the Turbidity of the Atmosphere1, Tellus, 13, 214–223, doi: 10.1111/j.2153-3490.1961.tb00078.x, 1961.

Ångström, A.: The parameters of atmospheric turbidity, Tellus, 16, 64–75, doi: 10.1111/j.2153-3490.1964.tb00144.x, 1964.

Ångström, A.: Apparent solar constant variations and their relation to the variability of atmospheric transmission, Tellus, 22, 205–218, doi: 10.3402/tellusa.v22i2.10215, 1970.

Ansmann, A., Bösenberg, J., Chaikovsky, A., Comerón, A., Eckhardt, S., Eixmann, R., Freudenthaler, V., Ginoux, P., Komguem, L., Linné, H., Márquez, M. Á., Matthias, V., Mattis, I., Mitev, V., Müller, D., Music, S., Nickovic, S., Pelon, J., Sauvage, L., Sobolewsky, P., Srivastava, M. K., Stohl, A., Torres, O., Vaughan, G., Wandinger, U., and Wiegner, M.: Long-range transport of Saharan dust to northern Europe: The 11–16 October 2001 outbreak observed with EARLINET, Journal of Geophysical Research: Atmospheres, 108, doi: 10.1029/2003JD003757, 2003.

Atkinson, J. D., Murray, B. J., Woodhouse, M. T., Whale, T. F., Baustian, K. J., Carslaw, K. S., Dobbie, S., O'Sullivan, D., and Malkin, T. L.: The importance of feldspar for ice nucleation by mineral dust in mixed-phase clouds, Nature, 498, 355–358, doi: 10.1038/nature12278, 2013.

Baez-Ferrer, N., Dominguez Rodriguez, A., Hernandez-Vaquero, D., Rodriguez, S., Avanzas, P., Abreu-Gonzalez, P., and Cuevas, E.: P3420Is there an association between Saharan dust events and acute coronary syndrome incidence?, European Heart Journal, 40, doi: 10.1093/eurheartj/ehz745.0294, 2019.

Bakker, N. L., Drake, N. A., and Bristow, C. S.: Evaluating the relative importance of northern African mineral dust sources using remote sensing, Atmospheric Chemistry and Physics, 19, 10 525–10 535, doi: 10.5194/acp-19-10525-2019, 2019.

Baldasano, J. M. and Massagué, J.: Trends and patterns of air quality in Santa Cruz de Tenerife (Canary Islands) in the period 2011–2015, Air Quality, Atmosphere & Health, 10, 939–954, doi: 10.1007/s11869-017-0484-x, 2017.

Barkan, J. and Alpert, P.: Synoptic analysis of a rare event of Saharan dust reaching the Arctic region, Weather, 65, 208–211, doi: 10.1002/wea.503, 2010.

Barker, H. W.: Solar Radiative Transfer Through Clouds Possessing Isotropic Variable Extinction Coefficient, Quarterly Journal of the Royal Meteorological Society, 118, 1145–1162, doi: 10.1002/qj.49711850807, 1992.

Barker, H. W.: Estimating Cloud Field Albedo Using One-Dimensional Series Of Optical Depth, Journal of the Atmospheric Sciences, 53, 2826–2837, doi: 10.1175/1520-0469(1996)053⟨2826:ECFAUO⟩2.0.CO;2, 1996.

Barreto, Á., Cuevas, E., Granados-Muñoz, M.-J., Alados-Arboledas, L., Romero, P. M., Gröbner, J., Kouremeti, N., Almansa, A. F., Stone, T., Toledano, C., Román, R., Sorokin, M., Holben, B., Canini, M., and Yela, M.: The new sun-sky-lunar Cimel CE318-T multiband photometer – a comprehensive performance evaluation, Atmospheric Measurement Techniques, 9, 631–654, doi: 10.5194/amt-9-631-2016, 2016.

Barreto, Á., García, O. E., Schneider, M., García, R. D., Hase, F., Sepúlveda, E., Almansa, A. F., Cuevas, E., and Blumenstock, T.: Spectral Aerosol Optical Depth Retrievals by Ground-Based Fourier Transform Infrared Spectrometry, Remote Sensing, 12, doi: 10.3390/rs12193148, 2020.

Basart, S., Pérez, C., Cuevas, E., Baldasano, J. M., and Gobbi, G. P.: Aerosol characterization in Northern Africa, Northeastern Atlantic, Mediterranean Basin and Middle East from direct-sun AERONET observations, Atmospheric Chemistry and Physics, 9, 8265–8282, doi: 10.5194/acp-9-8265-2009, 2009.

Ben-Ami, Y., Koren, I., Rudich, Y., Artaxo, P., Martin, S. T., and Andreae, M. O.: Transport of North African dust from the Bodélé depression to the Amazon Basin: a case study, Atmospheric Chemistry and Physics, 10, 7533–7544, doi: 10.5194/acp-10-7533-2010, 2010.

Bevis, M., Businger, S., Herring, T. A., Rocken, C., Anthes, R. A., and Ware, R. H.: GPS meteorology: Remote sensing of atmospheric water vapor using the global positioning system, Journal of Geophysical Research: Atmospheres, 97, 15 787–15 801, doi: 10.1029/92JD01517, 1992.

Bohren, C. and Huffman, D.: Absorption and Scattering of Light by Small Particles, Wiley Science Series, Wiley, URL https://books.google.es/books?id=ib3EMXXIRXUC, 2008.

Bou Karam, D., Flamant, C., Knippertz, P., Reitebuch, O., Pelon, J., Chong, M., and Dabas, A.: Dust emissions over the Sahel associated with the West African monsoon intertropical discontinuity region: A representative case-study, Quarterly Journal of the Royal Meteorological Society, 134, 621–634, doi: 10.1002/qj.244, 2008.

Boucher, O.: Atmospheric Aerosols: Properties and Climate Impacts, Springer Netherlands, doi: 10.1007/978-94-017-9649-1, 2015.

Buras, R., Dowling, T., and Emde, C.: New secondary-scattering correction in DISORT with increased efficiency for forward scattering, Journal of Quantitative Spectroscopy and Radiative Transfer, 112, 2028 – 2034, doi: 10.1016/j.jqsrt.2011.03.019, 2011.

Cachorro, V. E., Utrillas, P., Vergaz, R., Durán, P., Frutos, A. M. d., and Martinez-Lozano, J. A.: Determination of the atmospheric-water-vapor content in the 940-nm absorption band by use of moderate spectral-resolution measurements of direct solar irradiance, Appl. Opt., 37, 4678–4689, doi: 10.1364/AO.37.004678, 1998.

Cadeddu, M. P., Liljegren, J. C., and Turner, D. D.: The Atmospheric radiation measurement (ARM) program network of microwave radiometers: instrumentation, data, and retrievals, Atmospheric Measurement Techniques, 6, 2359–2372, doi: 10.5194/amt-6-2359-2013, 2013.

Calpini, B., Ruffieux, D., Bettems, J.-M., Hug, C., Huguenin, P., Isaak, H.-P., Kaufmann, P., Maier, O., and Steiner, P.: Ground-based remote sensing profiling and numerical weather prediction model to manage nuclear power plants meteorological surveillance in Switzerland, Atmospheric Measurement Techniques, 4, 1617–1625, doi: 10.5194/amt-4-1617-2011, 2011.

Carrillo, J., Guerra, J. C., Cuevas, E., and Barrancos, J.: Characterization of the Marine Boundary Layer and the Trade-Wind Inversion over the Subtropical North Atlantic, Boundary-Layer Meteorology, 158, 311–330, doi: 10.1007/s10546-015-0081-1, 2016.

Chandrasekhar, S.: Radiative Transfer, Dover books on advanced mathematics, Dover Publications, URL https://books.google.es/books?id=zPVQAAAAMAAJ, 1960.

Chen, B. and Liu, Z.: Global water vapor variability and trend from the latest 36 year (1979 to 2014) data of ECMWF and NCEP reanalyses, radiosonde, GPS, and microwave satellite, Journal of Geophysical Research: Atmospheres, 121, 11,442–11,462, doi: 10.1002/2016JD024917, 2016.

Clarisse, L., Coheur, P.-F., Prata, F., Hadji-Lazaro, J., Hurtmans, D., and Clerbaux, C.: A unified approach to infrared aerosol remote sensing and type specification, Atmospheric Chemistry and Physics, 13, 2195–2221, doi: 10.5194/acp-13-2195-2013, 2013.

Clough, S. A., Shephard, M. W., Mlawer, E. J., Delamere, J. S., Iacono, M. J., Cady-Pereira, K., Boukabara, S., and Brown, P. D.: Atmospheric radiative transfer modeling: a summary of the AER codes, Journal of Quantitative Spectroscopy and Radiative Transfer, 91, 233 – 244, doi: 10.1016/j.jqsrt.2004.05.058, 2005.

Cuesta, J., Edouart, D., Mimouni, M., Flamant, P. H., Loth, C., Gibert, F., Marnas, F., Bouklila, A., Kharef, M., Ouchène, B., Kadi, M., and Flamant, C.: Multiplatform observations of the seasonal evolution of the Saharan atmospheric boundary layer in Tamanrasset, Algeria, in the framework of the African Monsoon Multidisciplinary Analysis field campaign conducted in 2006, Journal of Geophysical Research: Atmospheres, 113, doi: 10.1029/2007JD009417, 2008.

Cuesta, J., Marsham, J. H., Parker, D. J., and Flamant, C.: Dynamical mechanisms controlling the vertical redistribution of dust and the thermodynamic structure of the West Saharan atmospheric boundary layer during summer, Atmospheric Science Letters, 10, 34–42, doi: 10.1002/asl.207, 2009.

Cuesta, J., Lavaysse, C., Flamant, C., Mimouni, M., and Knippertz, P.: Northward bursts of the West African monsoon leading to rainfall over the Hoggar Massif, Algeria, Quarterly Journal of the Royal Meteorological Society, 136, 174–189, doi: 10.1002/qj.439, 2010.

Cuevas, E.: Establishing a WMO Sand and Dust Storm Warning Advisory and Assessment System Regional Node for West Asia: Current Capabilities and Needs, WMO–No. 1121, Geneva, Switzerland, URL https://library.wmo.int/index.php?lvl=notice_display&id=15839#.X-IZpBYWVPZ, 2013.

Cuevas, E., Camino, C., Benedetti, A., Basart, S., Terradellas, E., Baldasano, J. M., Morcrette, J. J., Marticorena, B., Goloub, P., Mortier, A., Berjón, A., Hernández, Y., Gil-Ojeda, M., and Schulz, M.: The MACC-II 2007–2008 reanalysis: atmospheric dust evaluation and characterization over northern Africa and the Middle East, Atmospheric Chemistry and Physics, 15, 3991–4024, doi: 10.5194/acp-15-3991-2015, 2015.

Cuevas, E., Gómez-Peláez, A., Rodríguez, S., Terradellas, E., Basart, S., García, R., García, O., and Alonso-Pérez, S.: The pulsating nature of large-scale Saharan dust transport as a result of interplays between mid-latitude Rossby waves and the North African Dipole Intensity, Atmospheric Environment, 167, 586 – 602, doi: 10.1016/j.atmosenv.2017.08.059, 2017.

Cuevas, E., Romero-Campos, P. M., Kouremeti, N., Kazadzis, S., Räisänen, P., García, R. D., Barreto, A., Guirado-Fuentes, C., Ramos, R., Toledano, C., Almansa, F., and Gröbner, J.: Aerosol optical depth comparison between GAW-PFR and AERONET-Cimel radiometers from long-term (2005–2015) 1 min synchronous measurements, Atmospheric Measurement Techniques, 12, 4309–4337, doi: 10.5194/amt-12-4309-2019, 2019.

D'Almeida, G., Koepke, P., and Shettle, E.: Atmospheric Aerosols: Global Climatology and Radiative Characteristics, Studies in geophysical optics and remote sensing, A. Deepak Pub., URL https://books.google.es/books?id= C1wRAQAAIAAJ, 1991.

Davidson, C. I., Phalen, R. F., and Solomon, P. A.: Airborne Particulate Matter and Human Health: A Review, Aerosol Science and Technology, 39, 737–749, doi: 10.1080/02786820500191348, 2005.

De Mazière, M., Thompson, A. M., Kurylo, M. J., Wild, J. D., Bernhard, G., Blumenstock, T., Braathen, G. O., Hannigan, J. W., Lambert, J.-C., Leblanc, T., McGee, T. J., Nedoluha, G., Petropavlovskikh, I., Seckmeyer, G., Simon, P. C., Steinbrecht, W., and Strahan, S. E.: The Network for the Detection of Atmospheric Composition Change (NDACC): history, status and perspectives, Atmospheric Chemistry and Physics, 18, 4935–4964, doi: 10.5194/acp-18-4935-2018, 2018.

Deepak, A. and Gerber, H. E.: Report of the experts meeting on aerosols and their climatic effects., no. 55 in WCP, WMO, Geneva, 1983.

Dirksen, R. J., Sommer, M., Immler, F. J., Hurst, D. F., Kivi, R., and Vömel, H.: Reference quality upper-air measurements: GRUAN data processing for the Vaisala RS92 radiosonde, Atmospheric Measurement Techniques, 7, 4463–4490, doi: 10.5194/amt-7-4463-2014, 2014.

Dominguez-Rodriguez, A., Abreu-Gonzalez, P., Rodríguez, S., Avanzas, P., and Juarez-Prera, R. A.: Short-term effects of air pollution, markers of endothelial activation, and coagulation to predict major adverse cardiovascular events in patients with acute coronary syndrome: insights from AIRACOS study, Biomarkers, 22, 389–393, doi: 10.3109/1354750X.2016.1160430, 2017.

Dominguez-Rodriguez, A., Baez-Ferrer, N., Rodríguez, S., Avanzas, P., Abreu-Gonzalez, P., Terradellas, E., Cuevas, E., Basart, S., and Werner, E.: Saharan Dust Events in the Dust Belt -Canary Islands- and the Observed Association with in-Hospital Mortality of Patients with Heart Failure, Journal of Clinical Medicine, 9, doi: 10.3390/jcm9020376, 2020.

Dubovik, O. and King, M. D.: A flexible inversion algorithm for retrieval of aerosol optical properties from Sun and sky radiance measurements, Journal of Geophysical Research: Atmospheres, 105, 20 673–20 696, doi: 10.1029/2000JD900282, 2000.

Dubovik, O., Holben, B. N., Lapyonok, T., Sinyuk, A., Mishchenko, M. I., Yang, P., and Slutsker, I.: Non-spherical aerosol retrieval method employing light scattering by spheroids, Geophysical Research Letters, 29, 54–1–54–4, doi: 10.1029/2001GL014506, 2002.

Dubovik, O., Sinyuk, A., Lapyonok, T., Holben, B. N., Mishchenko, M., Yang, P., Eck, T. F., Volten, H., Muñoz, O., Veihelmann, B., van der Zande, W. J., Leon, J.-F., Sorokin, M., and Slutsker, I.: Application of spheroid models to account for aerosol particle nonsphericity in remote sensing of desert dust, Journal of Geophysical Research: Atmospheres, 111, doi: 10.1029/2005JD006619, 2006.

Eck, T., Holben, b., Reid, J., Dubovik, O., Smirnov, A., Neill, Slutsker, I., and Kinne, S.: Wavelength dependence of the optical depth of biomass burning, urban, and desert dust aerosols, Journal of Geophysical Research: Atmospheres, 104, 31 333–31 349, doi: 10.1029/1999JD900923, 1999.

Emde, C., Buras-Schnell, R., Kylling, A., Mayer, B., Gasteiger, J., Hamann, U., Kylling, J., Richter, B., Pause, C., Dowling, T., and Bugliaro, L.: The libRadtran software package for radiative transfer calculations (version 2.0.1), Geoscientific Model Development, 9, 1647–1672, doi: 10.5194/gmd-9-1647-2016, 2016.

Engelstaedter, S., Tegen, I., and Washington, R.: North African dust emissions and transport, Earth-Science Reviews, 79, 73 – 100, doi: 10.1016/j.earscirev.2006.06.004, 2006.

Erel, Y., Pehkonen, S. O., and Hoffmann, M. R.: Redox chemistry of iron in fog and stratus clouds, Journal of Geophysical Research: Atmospheres, 98, 18 423–18 434, doi: 10.1029/93JD01575, 1993.

Escudero, M., Castillo, S., Querol, X., Avila, A., Alarcón, M., Viana, M. M., Alastuey, A., Cuevas, E., and Rodríguez, S.: Wet and dry African dust episodes over eastern Spain, Journal of Geophysical Research: Atmospheres, 110, doi: 10.1029/2004JD004731, 2005.

Flamant, C., Chaboureau, J.-P., Parker, D. J., Taylor, C. M., Cammas, J.-P., Bock, O., Timouk, F., and Pelon, J.: Airborne observations of the impact of a convective system on the planetary boundary layer thermodynamics and aerosol distribution in the inter-tropical discontinuity region of the West African Monsoon, Quarterly Journal of the Royal Meteorological Society, 133, 1175–1189, doi: 10.1002/qj.97, 2007.

Forgan, B. W.: Bias in a solar constant determination by the Langley method due to structured atmospheric aerosol: comment, Appl. Opt., 27, 2546–2548, doi: 10.1364/AO.27.002546, 1988.

Forgan, B. W.: General method for calibrating Sun photometers, Appl. Opt., 33, 4841–4850, doi: 10.1364/AO.33.004841, 1994.

Galle, S., Grippa, M., Peugeot, C., Moussa, I. B., Cappelaere, B., Demarty, J., Mougin, E., Panthou, G., Adjomayi, P., Agbossou, E., Ba, A., Boucher, M., Cohard, J.-M., Descloitres, M., Descroix, L., Diawara, M., Dossou, M., Favreau, G., Gangneron, F., Gosset, M., Hector, B., Hiernaux, P., Issoufou, B.-A., Kergoat, L., Lawin, E., Lebel, T., Legchenko, A., Abdou, M. M., Malam-Issa, O., Mamadou, O., Nazoumou, Y., Pellarin, T., Quantin, G., Sambou, B., Seghieri, J., Séguis, L., Vandervaere, J.-P., Vischel, T., Vouillamoz, J.-M., Zannou, A., Afouda, S., Alhassane, A., Arjounin, M., Barral, H., Biron, R., Cazenave, F., Chaffard, V., Chazarin, J.-P., Guyard, H., Koné, A., Mainassara, I., Mamane, A., Oi, M., Ouani, T., Soumaguel, N., Wubda, M., Ago, E., Alle, I., Allies, A., Arpin-Pont, F., Awessou, B., Cassé, C., Charvet, G., Dardel, C., Depeyre, A., Diallo, F., Do, T., Fatras, C., Frappart, F., Gal, L., Gascon, T., Gibon, F., Guiro, I., Ingatan, A., Kempf, J., Kotchoni, D., Lawson, F., Leauthaud, C., Louvet, S., Mason, E., Nguyen, C., Perrimond, B., Pierre, C., Richard, A., Robert, E., Román-Cascón, C., Velluet, C., and Wilcox, C.: AMMA-CATCH, a Critical Zone Observatory in West Africa Monitoring a Region in Transition, Vadose Zone Journal, 17, 180 062, doi: 10.2136/vzj2018.03.0062, 2018.

Gasteiger, J., Emde, C., Mayer, B., Buras, R., Buehler, S. A., and Lemke, O.: Representative wavelengths absorption parameterization applied to satellite channels and spectral bands, Journal of Quantitative Spectroscopy and Radiative Transfer, 148, 99 – 115, doi: 10.1016/j.jqsrt.2014.06.024, 2014.

Giles, D. M., Sinyuk, A., Sorokin, M. G., Schafer, J. S., Smirnov, A., Slutsker, I., Eck, T. F., Holben, B. N., Lewis, J. R., Campbell, J. R., Welton, E. J., Korkin, S. V., and Lyapustin, A. I.: Advancements in the Aerosol Robotic Network (AERONET) Version 3 database – automated near-real-time quality control algorithm with improved cloud screening for Sun photometer aerosol optical

depth (AOD) measurements, Atmospheric Measurement Techniques, 12, 169–209, doi: 10.5194/amt-12-169-2019, 2019.

Gisi, M., Hase, F., Dohe, S., and Blumenstock, T.: Camtracker: a new camera controlled high precision solar tracker system for FTIR-spectrometers, Atmospheric Measurement Techniques, 4, 47–54, doi: 10.5194/amt-4-47-2011, 2011.

González, R., Toledano, C., Román, R., Fuertes, D., Berjón, A., Mateos, D., Guirado-Fuentes, C., Velasco-Merino, C., Antuña Sánchez, J. C., Calle, A., Cachorro, V. E., and de Frutos, A. M.: Daytime and nighttime aerosol optical depth implementation in CÆLIS, Geoscientific Instrumentation, Methods and Data Systems, 9, 417–433, doi: 10.5194/gi-9-417-2020, 2020.

González, Y. and Rodríguez, S.: A comparative study on the ultrafine particle episodes induced by vehicle exhaust: A crude oil refinery and ship emissions, Atmospheric Research, 120-121, 43 – 54, doi: 10.1016/j.atmosres.2012.08.001, 2013.

González, Y., Rodríguez, S., Guerra García, J. C., Trujillo, J. L., and García, R.: Ultrafine particles pollution in urban coastal air due to ship emissions, Atmospheric Environment, 45, 4907 – 4914, doi: 10.1016/j.atmosenv.2011.06.002, 2011.

Goudie, A. and Middleton, N.: Saharan dust storms: nature and consequences, Earth-Science Reviews, 56, 179 – 204, doi: 10.1016/S0012-8252(01)00067-8, 2001.

Guirado-Fuentes, C.: Caracterización de las propiedades de los aerosoles en columna en la región subtropical, Ph.D. Thesis, Universidad de Valladolid, doi: 10.35376/10324/13220, 2015.

Guirado-Fuentes, C., Cuevas Agulló, E., Cachorro, V. E., Mimouni, M., Zeudmi, L., Toledano, C., Alonso-Pérez, S., Basart, S., Blarel, L., Goloub, P., and Baldasano, J. M.: Preliminary characterization of columnar aerosol properties (AOD-AE) at the Saharan Tamanrasset (Algeria) station, Óptica Pura y Aplicada, 44, 635–639, 2011.

Guirado-Fuentes, C., Cuevas, E., Cachorro, V. E., Toledano, C., Alonso-Pérez, S., Bustos, J. J., Basart, S., Romero, P. M., Camino, C., Mimouni, M., Zeudmi, L., Goloub, P., Baldasano, J. M., and de Frutos, A. M.: Aerosol characterization at the Saharan AERONET site Tamanrasset, Atmospheric Chemistry and Physics, 14, 11 753–11 773, doi: 10.5194/acp-14-11753-2014, 2014.

Halthore, R. N., Eck, T. F., Holben, B. N., and Markham, B. L.: Sun photometric measurements of atmospheric water vapor column abundance in the 940-nm

band, Journal of Geophysical Research: Atmospheres, 102, 4343–4352, doi: 10. 1029/96JD03247, 1997.

Hess, M., Koepke, P., and Schult, I.: Optical Properties of Aerosols and Clouds: The Software Package OPAC, Bulletin of the American Meteorological Society, 79, 831–844, doi: 10.1175/1520-0477(1998)079⟨0831:OPOAAC⟩2.0.CO;2, 1998.

Holben, B., Eck, T., Slutsker, I., Tanre, D., Buis, J.-P., Setzer, A., Vermote, E., Reagan, J., and Kaufman, Y.: Multi-band automatic sun and sky scanning radio-meter system for measurement of aerosols, in: Sixième Symposium International: Mesures Physiques et Sygnatures en Teledetection, Val d'Isère, France, 17-21 Janvier 1994, 1994.

Holben, B. N., Eck, T. F., Slutsker, I., Tanré, D., Buis, J. P., Setzer, A., Vermote, E., Reagan, J. A., Kaufman, Y. J., Nakajima, T., Lavenu, F., Jankowiak, I., and Smirnov, A.: AERONET—A Federated Instrument Network and Data Archive for Aerosol Characterization, Remote Sensing of Environment, 66, 1 – 16, doi: 10. 1016/S0034-4257(98)00031-5, 1998.

Hussain, A., Batra, A., and Pachauri, R.: An experimental study on effect of dust on power loss in solar photovoltaic module, Renewables: Wind, Water, and Solar, 4, 9, doi: 10.1186/s40807-017-0043-y, 2017.

ICAO: European Guidance Material On All Weather Aero-drome Operations, EUR Doc 013, fifth edn., URL https:// www.icao.int/EURNAT/EURandNATDocuments/EURDocuments/ EURDocuments/013-EURGuidanceMaterialonAWOatAerodromes/ EURDoc013-GuidMatonAWOEdition5.pdf, 2016.

IPCC: Climate Change 2007 : The Physical Science Basis. Contribution of Working Group I to the Fourth Assessment Report of the Intergovernmental Panel on Climate Change, Cambridge University Press, Cambridge, United Kingdom and New York, NY, USA, URL https://www.ipcc.ch/report/ar4/wg1/, 2007.

IPCC: Climate Change 2013: The Physical Science Basis. Contribution of Working Group I to the Fifth Assessment Report of the Intergovernmental Panel on Climate Change, Cambridge University Press, Cambridge, United Kingdom and New York, NY, USA, doi: 10.1017/CBO9781107415324, 2013.

Israelevich, P., Ganor, E., Alpert, P., Kishcha, P., and Stupp, A.: Predominant transport paths of Saharan dust over the Mediterranean Sea to Europe, Journal of Geophysical Research: Atmospheres, 117, doi: 10.1029/2011JD016482, 2012.

Israelevich, P. L., Ganor, E., Levin, Z., and Joseph, J. H.: Annual variations of physical properties of desert dust over Israel, Journal of Geophysical Research: Atmospheres, 108, doi: 10.1029/2002JD003163, 2003.

Jiang, J. H., Su, H., Zhai, C., Wu, L., Minschwaner, K., Molod, A. M., and Tompkins, A. M.: An assessment of upper troposphere and lower stratosphere water vapor in MERRA, MERRA2, and ECMWF reanalyses using Aura MLS observations, Journal of Geophysical Research: Atmospheres, 120, 11,468–11,485, doi: 10.1002/2015JD023752, 2015.

Jickells, T. D., An, Z. S., Andersen, K. K., Baker, A. R., Bergametti, G., Brooks, N., Cao, J. J., Boyd, P. W., Duce, R. A., Hunter, K. A., Kawahata, H., Kubilay, N., laRoche, J., Liss, P. S., Mahowald, N., Prospero, J. M., Ridgwell, A. J., Tegen, I., and Torres, R.: Global Iron Connections Between Desert Dust, Ocean Biogeochemistry, and Climate, Science, 308, doi: 10.1126/science.1105959, 2005.

Karyampudi, V. M., Palm, S. P., Reagen, J. A., Fang, H., Grant, W. B., Hoff, R. M., Moulin, C., Pierce, H. F., Torres, O., Browell, E. V., and Melfi, S. H.: Validation of the Saharan Dust Plume Conceptual Model Using Lidar, Meteosat, and ECMWF Data, Bulletin of the American Meteorological Society, 80, 1045–1076, doi: 10.1175/1520-0477(1999)080⟨1045:VOTSDP⟩2.0.CO;2, 1999.

Kazadzis, S., Kouremeti, N., Diémoz, H., Gröbner, J., Forgan, B. W., Campanelli, M., Estellés, V., Lantz, K., Michalsky, J., Carlund, T., Cuevas, E., Toledano, C., Becker, R., Nyeki, S., Kosmopoulos, P. G., Tatsiankou, V., Vuilleumier, L., Denn, F. M., Ohkawara, N., Ijima, O., Goloub, P., Raptis, P. I., Milner, M., Behrens, K., Barreto, A., Martucci, G., Hall, E., Wendell, J., Fabbri, B. E., and Wehrli, C.: Results from the Fourth WMO Filter Radiometer Comparison for aerosol optical depth measurements, Atmospheric Chemistry and Physics, 18, 3185–3201, doi: 10.5194/acp-18-3185-2018, 2018a.

Kazadzis, S., Kouremeti, N., Nyeki, S., Gröbner, J., and Wehrli, C.: The World Optical Depth Research and Calibration Center (WORCC) quality assurance and quality control of GAW-PFR AOD measurements, Geoscientific Instrumentation, Methods and Data Systems, 7, 39–53, doi: 10.5194/gi-7-39-2018, 2018b.

Kim, J., Yoon, J.-M., Ahn, M. H., Sohn, B. J., and Lim, H. S.: Retrieving aerosol optical depth using visible and mid-IR channels from geostationary satellite MTSAT-1R, International Journal of Remote Sensing, 29, 6181–6192, doi: 10.1080/01431160802175553, 2008.

Kinne, S., Schulz, M., Textor, C., Guibert, S., Balkanski, Y., Bauer, S. E., Berntsen, T., Berglen, T. F., Boucher, O., Chin, M., Collins, W., Dentener, F., Diehl, T.,

Easter, R., Feichter, J., Fillmore, D., Ghan, S., Ginoux, P., Gong, S., Grini, A., Hendricks, J., Herzog, M., Horowitz, L., Isaksen, I., Iversen, T., Kirkevåg, A., Kloster, S., Koch, D., Kristjansson, J. E., Krol, M., Lauer, A., Lamarque, J. F., Lesins, G., Liu, X., Lohmann, U., Montanaro, V., Myhre, G., Penner, J., Pitari, G., Reddy, S., Seland, O., Stier, P., Takemura, T., and Tie, X.: An AeroCom initial assessment – optical properties in aerosol component modules of global models, Atmospheric Chemistry and Physics, 6, 1815–1834, doi: 10.5194/acp-6-1815-2006, 2006.

Knippertz, P. and Stuut, J.: Mineral Dust: A Key Player in the Earth System, Springer Netherlands, URL https://books.google.es/books?id=_5pBvgAACAAJ, 2016.

Koepke, P., Hess, M., Schult, I., and Shettle, E. P.: Global aerosol data set, Report 243, Max-Planck-Institut für Meteorologie, Hamburg, URL https://core.ac.uk/display/40581675, 1997.

Koren, I., Kaufman, Y. J., Washington, R., Todd, M. C., Rudich, Y., Martins, J. V., and Rosenfeld, D.: The Bodélé depression: a single spot in the Sahara that provides most of the mineral dust to the Amazon forest, Environmental Research Letters, 1, 014 005, doi: 10.1088/1748-9326/1/1/014005, 2006.

Kunz, A., Spelten, N., Konopka, P., Müller, R., Forbes, R. M., and Wernli, H.: Comparison of Fast In situ Stratospheric Hygrometer (FISH) measurements of water vapor in the upper troposphere and lower stratosphere (UTLS) with ECMWF (re)analysis data, Atmospheric Chemistry and Physics, 14, 10 803–10 822, doi: 10.5194/acp-14-10803-2014, 2014.

Kurucz, R. L.: Synthetic infrared spectra, Kluwer, Acad., Norwell, MA, 1992, Tucson, Arizona, U.S.A, 1992.

Lebel, T., Parker, D. J., Flamant, C., Bourlès, B., Marticorena, B., Mougin, E., Peugeot, C., Diedhiou, A., Haywood, J. M., Ngamini, J. B., Polcher, J., Redelsperger, J.-L., and Thorncroft, C. D.: The AMMA field campaigns: multiscale and multidisciplinary observations in the West African region, Quarterly Journal of the Royal Meteorological Society, 136, 8–33, doi: 10.1002/qj.486, 2010.

Lebel, T., Parker, D. J., Flamant, C., Höller, H., Polcher, J., Redelsperger, J.-L., Thorncroft, C., Bock, O., Bourles, B., Galle, S., Marticorena, B., Mougin, E., Peugeot, C., Cappelaere, B., Descroix, L., Diedhiou, A., Gaye, A., and Lafore, J.-P.: The AMMA field campaigns: accomplishments and lessons learned, Atmospheric Science Letters, 12, 123–128, doi: 10.1002/asl.323, 2011.

Lenoble, J., Remer, L., and Tanre, D., eds.: Aerosol Remote Sensing, Springer-Verlag, Berlin Heidelberg, doi: 10.1007/978-3-642-17725-5, 2013.

Li, Z., Blarel, L., Podvin, T., Goloub, P., Buis, J.-P., and Morel, J.-P.: Transferring the calibration of direct solar irradiance to diffuse-sky radiance measurements for CIMEL Sun-sky radiometers, Appl. Opt., 47, 1368–1377, doi: 10.1364/AO.47.001368, 2008.

Li, Z., Zhao, X., Kahn, R., Mishchenko, M., Remer, L., Lee, K.-H., Wang, M., Laszlo, I., Nakajima, T., and Maring, H.: Uncertainties in satellite remote sensing of aerosols and impact on monitoring its long-term trend: a review and perspective, Annales Geophysicae, 27, 2755–2770, doi: 10.5194/angeo-27-2755-2009, 2009.

López-Solano, J., Redondas, A., Carlund, T., Rodriguez-Franco, J. J., Diémoz, H., León-Luis, S. F., Hernández-Cruz, B., Guirado-Fuentes, C., Kouremeti, N., Gröbner, J., Kazadzis, S., Carreño, V., Berjón, A., Santana-Díaz, D., Rodríguez-Valido, M., De Bock, V., Moreta, J. R., Rimmer, J., Smedley, A. R. D., Boulkelia, L., Jepsen, N., Eriksen, P., Bais, A. F., Shirotov, V., Vilaplana, J. M., Wilson, K. M., and Karppinen, T.: Aerosol optical depth in the European Brewer Network, Atmospheric Chemistry and Physics, 18, 3885–3902, doi: 10.5194/acp-18-3885-2018, 2018.

Loveland, T. R. and Belward, A. S.: The IGBP-DIS global 1km land cover data set, DISCover: First results, International Journal of Remote Sensing, 18, 3289–3295, doi: 10.1080/014311697217099, 1997.

Loÿe-Pilot, M. D., Martin, J. M., and Morelli, J.: Influence of Saharan dust on the rain acidity and atmospheric input to the Mediterranean, Nature, 321, 427–428, doi: 10.1038/321427a0, 1986.

Lu, X., Chen, M., Liu, Y., Miralles, D. G., and Wang, F.: Enhanced water use efficiency in global terrestrial ecosystems under increasing aerosol loadings, Agricultural and Forest Meteorology, 237-238, 39 – 49, doi: 10.1016/j.agrformet.2017.02.002, 2017.

Madonna, F., Amodeo, A., Boselli, A., Cornacchia, C., Cuomo, V., D'Amico, G., Giunta, A., Mona, L., and Pappalardo, G.: CIAO: the CNR-IMAA advanced observatory for atmospheric research, Atmospheric Measurement Techniques, 4, 1191–1208, doi: 10.5194/amt-4-1191-2011, 2011.

Marticorena, B. and Bergametti, G.: Modeling the atmospheric dust cycle: 1. Design of a soil-derived dust emission scheme, Journal of Geophysical Research: Atmospheres, 100, 16 415–16 430, doi: 10.1029/95JD00690, 1995.

Mattis, I., Ansmann, A., Althausen, D., Jaenisch, V., Wandinger, U., Müller, D., Arshinov, Y. F., Bobrovnikov, S. M., and Serikov, I. B.: Relative-humidity profiling in the troposphere with a Raman lidar, Appl. Opt., 41, 6451–6462, doi: 10.1364/AO.41.006451, 2002.

Mayer, B. and Kylling, A.: Technical note: The libRadtran software package for radiative transfer calculations - description and examples of use, Atmospheric Chemistry and Physics, 5, 1855–1877, doi: 10.5194/acp-5-1855-2005, 2005.

Mayer, B., Seckmeyer, G., and Kylling, A.: Systematic long-term comparison of spectral UV measurements and UVSPEC modeling results, Journal of Geophysical Research: Atmospheres, 102, 8755–8767, doi: 10.1029/97JD00240, 1997.

Mie, G.: Beiträge zur Optik trüber Medien, speziell kolloidaler Metallösungen, Annalen der Physik, 330, 377–445, doi: 10.1002/andp.19083300302, 1908.

Mieruch, S., Noël, S., Bovensmann, H., and Burrows, J. P.: Analysis of global water vapour trends from satellite measurements in the visible spectral range, Atmospheric Chemistry and Physics, 8, 491–504, doi: 10.5194/acp-8-491-2008, 2008.

Mieruch, S., Schröder, M., Noël, S., and Schulz, J.: Comparison of decadal global water vapor changes derived from independent satellite time series, Journal of Geophysical Research: Atmospheres, 119, 12,489–12,499, doi: 10.1002/2014JD021588, 2014.

Miloshevich, L. M., Vömel, H., Whiteman, D. N., and Leblanc, T.: Accuracy assessment and correction of Vaisala RS92 radiosonde water vapor measurements, Journal of Geophysical Research: Atmospheres, 114, doi: 10.1029/2008JD011565, 2009.

Mishchenko, M. I. and Travis, L. D.: Capabilities and limitations of a current FORTRAN implementation of the T-matrix method for randomly oriented, rotationally symmetric scatterers, Journal of Quantitative Spectroscopy and Radiative Transfer, 60, 309–324, doi: 10.1016/S0022-4073(98)00008-9, 1998.

Mona, L., Liu, Z., Müller, D., Omar, A., Papayannis, A., Pappalardo, G., Sugimoto, N., and Vaughan, M.: Lidar Measurements for Desert Dust Characterization: An Overview, Advances in Meteorology, 2012, 36, doi: 10.1155/2012/356265, 2012.

Myhre, C. L. and Baltensperger, U.: Recommendations for a Composite Surface-Based Aerosol Network, no. 207 in GAW Report, WMO, European Network of Networks (ENAN) Workshop, Emmetten, Switzerland, 28-29 April 2009, 2012.

Myhre, G., Shindell, D., Bréon, F.-M., Collins, W., Fuglestvedt, J., Huang, J., Koch, D., Lamarque, J.-F., Lee, D., Mendoza, B., Nakajima, T., Robock, A., Stephens, G., Takemura, T., and Zhang, H.: Anthropogenic and natural radiative forcing, in: Climate Change 2013: The Physical Science Basis. Contribution of Working Group I to the Fifth Assessment Report of the Intergovernmental Panel on Climate Change, edited by Stocker, T. F., Qin, D., Plattner, G.-K., Tignor, M., Allen, S. K., Doschung, J., Nauels, A., Xia, Y., Bex, V., and Midgley, P. M., pp. 659–740, Cambridge University Press, Cambridge, UK, doi: 10.1017/CBO9781107415324.018, 2013.

N'Datchoh, E. T., Diallo, I., Konaré, A., Silué, S., Ogunjobi, K. O., Diedhiou, A., and Doumbia, M.: Dust induced changes on the West African summer monsoon features, International Journal of Climatology, 38, 452–466, doi: 10.1002/joc.5187, 2018.

Neher, I., Buchmann, T., Crewell, S., Evers-Dietze, B., Pfeilsticker, K., Pospichal, B., Schirrmeister, C., and Meilinger, S.: Impact of atmospheric aerosols on photovoltaic energy production Scenario for the Sahel zone, Energy Procedia, 125, 170 – 179, doi: 10.1016/j.egypro.2017.08.168, 2017.

Nickovic, S., Cuevas, E., Baldasano, J., Terradellas, E., Nakazawa, T., and Baklanov, A.: Sand and Dust Storm Warning Advisory and Assessment System (SDS-WAS) : Science and Implementation Plan 2015-2020, WMO, WWRP 2015 – 5, Geneva, URL https://library.wmo.int/index.php?lvl=notice_display&id=19816#.X2uBS4uCFPY, 2015.

O'Neill, N. T., Dubovik, O., and Eck, T. F.: Modified Ångström exponent for the characterization of submicrometer aerosols, Applied Optics, 40, 2368–2375, doi: 10.1364/AO.40.002368, 2001a.

O'Neill, N. T., Eck, T. F., Holben, B. N., Smirnov, A., Dubovik, O., and Royer, A.: Bimodal size distribution influences on the variation of Angstrom derivatives in spectral and optical depth space, Journal of Geophysical Research: Atmospheres, 106, 9787–9806, doi: 10.1029/2000JD900245, 2001b.

O'Neill, N. T., Eck, T. F., Smirnov, A., Holben, B. N., and Thulasiraman, S.: Spectral discrimination of coarse and fine mode optical depth, Journal of Geophysical Research: Atmospheres, 108, doi: 10.1029/2002JD002975, 2003.

Ortiz de Galisteo Marín, J. P.: Análisis del contenido total en columna de vapor de agua atmosférico sobre la Península Ibérica medido con distintas técnicas: radiosondas, fotómetros solares y sistema GPS, Ph.D. thesis, Universidad de Valladolid, doi: 10.35376/10324/888, 2011.

Pacyna, J. and Ottar, B.: Origin of natural constituents in the Arctic aerosol, Atmospheric Environment (1967), 23, 809 – 815, doi: 10.1016/0004-6981(89) 90485-X, 1989.

Pehkonen, S. O., Siefert, R., Erel, Y., Webb, S., and Hoffmann, M. R.: Photoreduction of iron oxyhydroxides in the presence of important atmospheric organic compounds, Environmental Science & Technology, 27, 2056–2062, doi: 10.1021/es00047a010, 1993.

Pierluissi, J. H. and Peng, G.-S.: New Molecular Transmission Band Models For LOWTRAN, Optical Engineering, 24, 243 541, doi: 10.1117/12.7973523, 1985.

Prospero, J. M.: Saharan Dust Transport Over the North Atlantic Ocean and Mediterranean: An Overview, in: The Impact of Desert Dust Across the Mediterranean, edited by Guerzoni, S. and Chester, R., Environmental Science and Technology Library, pp. 133–151, Springer Netherlands, Dordrecht, doi: 10.1007/ 978-94-017-3354-0_13, 1996.

Prospero, J. M. and Carlson, T. N.: Vertical and areal distribution of Saharan dust over the western equatorial north Atlantic Ocean, Journal of Geophysical Research (1896-1977), 77, 5255–5265, doi: 10.1029/JC077i027p05255, 1972.

Prospero, J. M. and Mayol-Bracero, O. L.: Understanding the Transport and Impact of African Dust on the Caribbean Basin, Bulletin of the American Meteorological Society, 94, 1329–1337, doi: 10.1175/BAMS-D-12-00142.1, 2013.

Pérez-Ramírez, D., Navas-Guzmán, F., Lyamani, H., Fernández-Gálvez, J., Olmo, F. J., and Alados-Arboledas, L.: Retrievals of precipitable water vapor using star photometry: Assessment with Raman lidar and link to sun photometry, Journal of Geophysical Research: Atmospheres, 117, doi: 10.1029/2011JD016450, 2012.

Pérez-Ramírez, D., Whiteman, D. N., Smirnov, A., Lyamani, H., Holben, B. N., Pinker, R., Andrade, M., and Alados-Arboledas, L.: Evaluation of AERONET precipitable water vapor versus microwave radiometry, GPS, and radiosondes at ARM sites, Journal of Geophysical Research: Atmospheres, 119, 9596–9613, doi: 10.1002/2014JD021730, 2014.

Querol, X., Alastuey, A., Rodríguez, S., Viana, M. M., Artíñano, B., Salvador, P., Mantilla, E., García do Santos, S., Fernandez Patier, R., de La Rosa, J., Sanchez de la Campa, A., Menéndez, M., and Gil, J. J.: Levels of particulate matter in rural, urban and industrial sites in Spain, The Science of the Total Environment, 334-335, 359–376, doi: 10.1016/j.scitotenv.2004.04.036, 2004.

Raptis, P.-I., Kazadzis, S., Gröbner, J., Kouremeti, N., Doppler, L., Becker, R., and Helmis, C.: Water vapour retrieval using the Precision Solar Spectroradiometer, Atmospheric Measurement Techniques, 11, 1143–1157, doi: 10.5194/amt-11-1143-2018, 2018.

Ravelo-Pérez, L. M., Rodríguez, S., Galindo, L., García, M. I., Alastuey, A., and López-Solano, J.: Soluble iron dust export in the high altitude Saharan Air Layer, Atmospheric Environment, 133, 49–59, doi: 10.1016/j.atmosenv.2016.03.030, 2016.

Redelsperger, J.-L., Thorncroft, C. D., Diedhiou, A., Lebel, T., Parker, D. J., and Polcher, J.: African Monsoon Multidisciplinary Analysis: An International Research Project and Field Campaign, Bulletin of the American Meteorological Society, 87, 1739–1746, doi: 10.1175/BAMS-87-12-1739, 2006.

Redemann, J., Zhang, Q., Schmid, B., Russell, P. B., Livingston, J. M., Jonsson, H., and Remer, L. A.: Assessment of MODIS-derived visible and near-IR aerosol optical properties and their spatial variability in the presence of mineral dust, Geophysical Research Letters, 33, doi: 10.1029/2006GL026626, 2006.

Reid, J. S., Kinney, J. E., Westphal, D. L., Holben, B. N., Welton, E. J., Tsay, S.-C., Eleuterio, D. P., Campbell, J. R., Christopher, S. A., Colarco, P. R., Jonsson, H. H., Livingston, J. M., Maring, H. B., Meier, M. L., Pilewskie, P., Prospero, J. M., Reid, E. A., Remer, L. A., Russell, P. B., Savoie, D. L., Smirnov, A., and Tanré, D.: Analysis of measurements of Saharan dust by airborne and ground-based remote sensing methods during the Puerto Rico Dust Experiment (PRIDE), Journal of Geophysical Research: Atmospheres, 108, doi: 10.1029/2002JD002493, 2003.

Rodríguez, S., Cuevas, E., Prospero, J. M., Alastuey, A., Querol, X., López-Solano, J., García, M. I., and Alonso-Pérez, S.: Modulation of Saharan dust export by the North African dipole, Atmospheric Chemistry and Physics, 15, 7471–7486, doi: 10.5194/acp-15-7471-2015, 2015.

Rodríguez, S., Cuevas, E., González, Y., Ramos, R., Romero, P. M., Pérez, N., Querol, X., and Alastuey, A.: Influence of sea breeze circulation and road traffic emissions on the relationship between particle number, black carbon, PM1, PM2.5 and PM2.5–10 concentrations in a coastal city, Atmospheric Environment, 42, 6523 – 6534, doi: 10.1016/j.atmosenv.2008.04.022, 2008.

Rodríguez, S., Alastuey, A., Alonso-Pérez, S., Querol, X., Cuevas, E., Abreu-Afonso, J., Viana, M., Pérez, N., Pandolfi, M., and de la Rosa, J.: Transport of desert dust mixed with North African industrial pollutants in the subtropical Saharan

Air Layer, Atmospheric Chemistry and Physics, 11, 6663–6685, doi: 10.5194/acp-11-6663-2011, 2011.

Räisänen, P. and Lindfors, A. V.: On the Computation of Apparent Direct Solar Radiation, Journal of the Atmospheric Sciences, 76, 2761–2780, doi: 10.1175/JAS-D-19-0030.1, 2019.

Räisänen, P., Isaac, G. A., Barker, H. W., and Gultepe, I.: Solar radiative transfer for stratiform clouds with horizontal variations in liquid-water path and droplet effective radius, Quarterly Journal of the Royal Meteorological Society, 129, 2135–2149, doi: 10.1256/qj.02.149, 2003.

Schepanski, K., Tegen, I., Todd, M. C., Heinold, B., Bönisch, G., Laurent, B., and Macke, A.: Meteorological processes forcing Saharan dust emission inferred from MSG-SEVIRI observations of subdaily dust source activation and numerical models, Journal of Geophysical Research: Atmospheres, 114, doi: 10.1029/2008JD010325, 2009.

Schmid, B. and Wehrli, C.: Comparison of Sun photometer calibration by use of the Langley technique and the standard lamp, Appl. Opt., 34, 4500–4512, doi: 10.1364/AO.34.004500, 1995.

Schmid, B., Spyak, P. R., Biggar, S. F., Wehrli, C., Sekler, J., Ingold, T., Mätzler, C., and Kämpfer, N.: Evaluation of the applicability of solar and lamp radiometric calibrations of aprecision sun photometer operating between 300 and 1025 nm, Appl. Opt., 37, 3923–3941, doi: 10.1364/AO.37.003923, 1998.

Schmid, B., Michalsky, J. J., Slater, D. W., Barnard, J. C., Halthore, R. N., Liljegren, J. C., Holben, B. N., Eck, T. F., Livingston, J. M., Russell, P. B., Ingold, T., and Slutsker, I.: Comparison of columnar water-vapor measurements from solar transmittance methods, Applied Optics, 40, 1886–1896, doi: 10.1364/AO.40.001886, 2001.

Schneider, M., Romero, P. M., Hase, F., Blumenstock, T., Cuevas, E., and Ramos, R.: Continuous quality assessment of atmospheric water vapour measurement techniques: FTIR, Cimel, MFRSR, GPS, and Vaisala RS92, Atmospheric Measurement Techniques, 3, 323–338, doi: 10.5194/amt-3-323-2010, 2010a.

Schneider, M., Sepúlveda, E., García, O., Hase, F., and Blumenstock, T.: Remote sensing of water vapour profiles in the framework of the Total Carbon Column Observing Network (TCCON), Atmospheric Measurement Techniques, 3, 1785–1795, doi: 10.5194/amt-3-1785-2010, 2010b.

Schuster, G. L., Dubovik, O., and Holben, B. N.: Angstrom exponent and bimodal aerosol size distributions, Journal of Geophysical Research: Atmospheres, 111, doi: 10.1029/2005JD006328, 2006.

Schwartz, J., Dockery, D. W., and Neas, L. M.: Is daily mortality associated specifically with fine particles?, Journal of the Air & Waste Management Association (1995), 46, 927–939, 1996.

Seinfeld, J. H. and Pandis, S. N.: Atmospheric Chemistry and Physics: From Air Pollution to Climate Change, John Wiley & Sons, New York, 2nd edition edn., 2016.

Shaw, G. E., Reagan, J. A., and Herman, B. M.: Investigations of Atmospheric Extinction Using Direct Solar Radiation Measurements Made with a Multiple Wavelength Radiometer, Journal of Applied Meteorology, 12, 374–380, doi: 10.1175/1520-0450(1973)012⟨0374:IOAEUD⟩2.0.CO;2, 1973.

Siefert, R. L., Pehkonen, S. O., Erel, Y., and Hoffmann, M. R.: Iron photochemistry of aqueous suspensions of ambient aerosol with added organic acids, Geochimica et Cosmochimica Acta, 58, 3271 – 3279, doi: 10.1016/0016-7037(94)90055-8, 1994.

Sinyuk, A., Holben, B. N., Eck, T. F., Giles, D. M., Slutsker, I., Korkin, S., Schafer, J. S., Smirnov, A., Sorokin, M., and Lyapustin, A.: The AERONET Version 3 aerosol retrieval algorithm, associated uncertainties and comparisons to Version 2, Atmospheric Measurement Techniques, 13, 3375–3411, doi: 10.5194/amt-13-3375-2020, 2020.

Smirnov, A., Holben, B., Eck, T., Dubovik, O., and Slutsker, I.: Cloud-Screening and Quality Control Algorithms for the AERONET Database, Remote Sensing of Environment, 73, 337 – 349, doi: 10.1016/S0034-4257(00)00109-7, 2000.

Sokolik, I. N. and Toon, O. B.: Direct radiative forcing by anthropogenic airborne mineral aerosols, Nature, 381, 681–683, doi: 10.1038/381681a0, 1996.

Stamnes, K., Tsay, S.-C., Wiscombe, W., and Jayaweera, K.: Numerically stable algorithm for discrete-ordinate-method radiative transfer in multiple scattering and emitting layered media, Applied Optics, 27, 2502–2509, doi: 10.1364/AO.27.002502, 1988.

Stevens, B. and Feingold, G.: Untangling aerosol effects on clouds and precipitation in a buffered system, Nature, 461, 607–613, doi: 10.1038/nature08281, 2009.

Stokes, G. G.: On the Effect of Internal Friction of Fluids on the Motion of Pendulums, Transaction of the Cambridge Philosophical Society, 9, 8–106, 1851.

Takamura, T., Sasano, Y., and Hayasaka, T.: Tropospheric aerosol optical properties derived from lidar, sun photometer, and optical particle counter measurements, Applied Optics, 33, 7132–7140, doi: 10.1364/AO.33.007132, 1994.

Tanaka, T. Y., Kurosaki, Y., Chiba, M., Matsumura, T., Nagai, T., Yamazaki, A., Uchiyama, A., Tsunematsu, N., and Kai, K.: Possible transcontinental dust transport from North Africa and the Middle East to East Asia, Atmospheric Environment, 39, 3901 – 3909, doi: 10.1016/j.atmosenv.2005.03.034, 2005.

Tao, R., Che, H., Chen, Q., Wang, Y., Sun, J., Zhang, X., Lu, S., Guo, J., Wang, H., and Zhang, X.: Development of an integrating sphere calibration method for Cimel sunphotometers in China aerosol remote sensing network, Particuology, 13, 88 – 99, doi: 10.1016/j.partic.2013.04.009, 2014.

Taylor, J. W., Haslett, S. L., Bower, K., Flynn, M., Crawford, I., Dorsey, J., Choularton, T., Connolly, P. J., Hahn, V., Voigt, C., Sauer, D., Dupuy, R., Brito, J., Schwarzenboeck, A., Bourriane, T., Denjean, C., Rosenberg, P., Flamant, C., Lee, J. D., Vaughan, A. R., Hill, P. G., Brooks, B., Catoire, V., Knippertz, P., and Coe, H.: Aerosol influences on low-level clouds in the West African monsoon, Atmospheric Chemistry and Physics, 19, 8503–8522, doi: 10.5194/acp-19-8503-2019, 2019.

Terradellas, E., Baldasano, J., and Cuevas, E.: Regional Center for Northern Africa, Middle East and Europe of the WMO Sand and Dust Storm Warning Advisory and Assessment System: Activity Report 2010-2012, Geneva, Switzerland, URL https://library.wmo.int/index.php?lvl=notice_display&id=19818# .X742U7MWVPY, 2014.

Toledano, C., Wiegner, M., Garhammer, M., Seefeldner, M., Gasteiger, J., Müller, D., and Koepke, P.: Spectral aerosol optical depth characterization of desert dust during SAMUM 2006, Tellus B: Chemical and Physical Meteorology, 61, 216–228, doi: 10.1111/j.1600-0889.2008.00382.x, 2009.

Toledano, C., González, R., Fuertes, D., Cuevas, E., Eck, T. F., Kazadzis, S., Kouremeti, N., Gröbner, J., Goloub, P., Blarel, L., Román, R., Barreto, Á., Berjón, A., Holben, B. N., and Cachorro, V. E.: Assessment of Sun photometer Langley calibration at the high-elevation sites Mauna Loa and Izaña, Atmospheric Chemistry and Physics, 18, 14 555–14 567, doi: 10.5194/acp-18-14555-2018, 2018.

Torres, B., Cachorro, V. E., Toledano, C., Galisteo, J. P. O. d., Berjón, A., Frutos, A. M. d., Bennouna, Y., and Laulainen, N.: Precipitable water vapor characterization in the Gulf of Cadiz region (southwestern Spain) based on Sun photometer,

GPS, and radiosonde data, Journal of Geophysical Research: Atmospheres, 115, doi: 10.1029/2009JD012724, 2010.

Torres, B., Toledano, C., Berjón, A., Fuertes, D., Molina, V., Gonzalez, R., Canini, M., Cachorro, V. E., Goloub, P., Podvin, T., Blarel, L., Dubovik, O., Bennouna, Y., and de Frutos, A. M.: Measurements on pointing error and field of view of Cimel-318 Sun photometers in the scope of AERONET, Atmospheric Measurement Techniques, 6, 2207–2220, doi: 10.5194/amt-6-2207-2013, 2013.

Torres, B., Dubovik, O., Toledano, C., Berjon, A., Cachorro, V. E., Lapyonok, T., Litvinov, P., and Goloub, P.: Sensitivity of aerosol retrieval to geometrical configuration of ground-based sun/sky radiometer observations, Atmospheric Chemistry and Physics, 14, 847–875, doi: 10.5194/acp-14-847-2014, 2014.

Tsamalis, C., Chédin, A., Pelon, J., and Capelle, V.: The seasonal vertical distribution of the Saharan Air Layer and its modulation by the wind, Atmospheric Chemistry and Physics, 13, 11 235–11 257, doi: 10.5194/acp-13-11235-2013, 2013.

Twomey, S.: The Influence of Pollution on the Shortwave Albedo of Clouds, Journal of the Atmospheric Sciences, 34, 1149–1152, doi: 10.1175/1520-0469(1977) 034⟨1149:TIOPOT⟩2.0.CO;2, 1977.

Valsan, A. E., Ravikrishna, R., Biju, C. V., Pöhlker, C., Després, V. R., Huffman, J. A., Pöschl, U., and Gunthe, S. S.: Fluorescent biological aerosol particle measurements at a tropical high-altitude site in southern India during the southwest monsoon season, Atmospheric Chemistry and Physics, 16, 9805–9830, doi: 10.5194/acp-16-9805-2016, 2016.

Wagner, T., Beirle, S., Grzegorski, M., and Platt, U.: Global trends (1996–2003) of total column precipitable water observed by Global Ozone Monitoring Experiment (GOME) on ERS-2 and their relation to near-surface temperature, Journal of Geophysical Research: Atmospheres, 111, doi: 10.1029/2005JD006523, 2006.

Walker, J., Cromer, C. L., and McLean, J. T.: Technique for improving the calibration of large-area sphere sources, in: Proc. SPIE 1493, Calibration of Passive Remote Observing Optical and Microwave Instrumentation, edited by Guenther, B. W., pp. 224–230, Orlando, FL, United States, doi: 10.1117/12.46707, 1991.

Wang, J., Zhang, L., Dai, A., Hove, T. V., and Baelen, J. V.: A near-global, 2-hourly data set of atmospheric precipitable water from ground-based GPS measurements, Journal of Geophysical Research: Atmospheres, 112, doi: 10.1029/2006JD007529, 2007.

Wehrli, C.: Calibrations of filter radiometers for determination of atmospheric optical depth, Metrologia, 37, 419–422, doi: 10.1088/0026-1394/37/5/16, 2000.

Wehrli, C.: GAW-PFR: A Network of Aerosol Optical Depth Observations with Precision Filter Radiometers, in: WMO/GAW Experts Workshop on a Global Surface-Based Network for Long Term Observations of Column Aerosol Optical Properties (8-10 March 2004; Davos, Switzerland), edited by Baltensperger, U., Barrie, L., and Wehrli, C., WMO/GAW Report No. 162, Geneva, 2005.

Wehrli, C.: Precision Filter Radiometer Documentation, URL ftp://ftp.pmodwrc.ch/pub/projects/worcc/PFRManual.pdf, 2008a.

Wehrli, C. J.: Remote Sensing of Aerosol Optical Depth in a global surface network, Doctoral Thesis, ETH Zurich, Zurich, doi: 10.3929/ethz-a-005659798, 2008b.

Weinzierl, B., Sauer, D., Minikin, A., Reitebuch, O., Dahlkötter, F., Mayer, B., Emde, C., Tegen, I., Gasteiger, J., Petzold, A., Veira, A., Kueppers, U., and Schumann, U.: On the visibility of airborne volcanic ash and mineral dust from the pilot's perspective in flight, Physics and Chemistry of the Earth, Parts A/B/C, 45-46, 87 – 102, doi: 10.1016/j.pce.2012.04.003, 2012.

Whitby, K. T.: The physical characteristics of sulfur aerosols, Atmospheric Environment (1967), 12, 135–159, doi: 10.1016/0004-6981(78)90196-8, 1978.

White, W. H. and Roberts, P. T.: On the nature and origins of visibility-reducing aerosols in the los angeles air basin, Atmospheric Environment (1967), 11, 803–812, doi: 10.1016/0004-6981(77)90042-7, 1977.

Whiteman, D. N., Rush, K., Rabenhorst, S., Welch, W., Cadirola, M., McIntire, G., Russo, F., Adam, M., Venable, D., Connell, R., Veselovskii, I., Forno, R., Mielke, B., Stein, B., Leblanc, T., McDermid, S., and Vömel, H.: Airborne and Ground-Based Measurements Using a High-Performance Raman Lidar, Journal of Atmospheric and Oceanic Technology, 27, 1781–1801, doi: 10.1175/2010JTECHA1391.1, 2010.

Whiteman, D. N., Cadirola, M., Venable, D., Calhoun, M., Miloshevich, L., Vermeesch, K., Twigg, L., Dirisu, A., Hurst, D., Hall, E., Jordan, A., and Vömel, H.: Correction technique for Raman water vapor lidar signal-dependent bias and suitability for water vapor trend monitoring in the upper troposphere, Atmospheric Measurement Techniques, 5, 2893–2916, doi: 10.5194/amt-5-2893-2012, 2012.

WHO: Air quality guidelines global update 2005 : particulate matter, ozone, nitrogen dioxide and sulfur dioxide, WHO Regional Office for Europe, Copenhagen, 2006.

Wiscombe, W. J.: Improved Mie scattering algorithms, Applied Optics, 19, 1505–1509, doi: 10.1364/AO.19.001505, 1980.

WMO: Recent progress in sunphotometry: determination of the aerosol optical depth, GAW Report No. 43, WMO/TD No. 143, 1986.

WMO: Report on the measurements of atmospheric turbidity in BAPMoN, GAW Report No. 94, WMO/TD No. 603, 1994.

WMO: WMO/GAW Experts Workshop on a Global Surface-Based Network for Long Term Observations of Column Aerosol Optical Properties (8-10 March 2004; Davos, Switzerland), GAW Report No. 162, 2005.

WMO: Commission for Instruments and Methods of Observation (CIMO) - Fourteenth session : Abridged final report with resolutions and recommendations, WMO No. 1019, 2007.

WMO: WMO/GAW Aerosol Measurement Procedures, Guidelines and Recommendations, GAW Report No. 227, Geneva, 2nd edn., 2016.

WMO: WMO Global Atmosphere Watch (GAW) Implementation Plan: 2016-2023, GAW Report No. 228, Geneva, 2017.

WMO: Sand and Dust Storm Warning Advisory and Assessment System: Science Progress Report, GAW Report- No. 254/WWRP 2020-4, 2020.

Wunch, D., Toon, G. C., Blavier, J.-F. L., Washenfelder, R. A., Notholt, J., Connor, B. J., Griffith, D. W. T., Sherlock, V., and Wennberg, P. O.: The Total Carbon Column Observing Network, Philosophical Transactions of the Royal Society A: Mathematical, Physical and Engineering Sciences, 369, 2087–2112, doi: 10.1098/rsta.2010.0240, 2011.

Xiao, S., Wang, Q. Y., Cao, J. J., Huang, R. J., Chen, W. D., Han, Y. M., Xu, H. M., Liu, S. X., Zhou, Y. Q., Wang, P., Zhang, J. Q., and Zhan, C. L.: Long-term trends in visibility and impacts of aerosol composition on visibility impairment in Baoji, China, Atmospheric Research, 149, 88–95, doi: 10.1016/j.atmosres.2014.06.006, 2014.

Zhang, L., Wu, L., and Gan, B.: Modes and Mechanisms of Global Water Vapor Variability over the Twentieth Century, Journal of Climate, 26, 5578–5593, doi: 10.1175/JCLI-D-12-00585.1, 2013.

A. Anexo 1: Suplemento del artículo 1
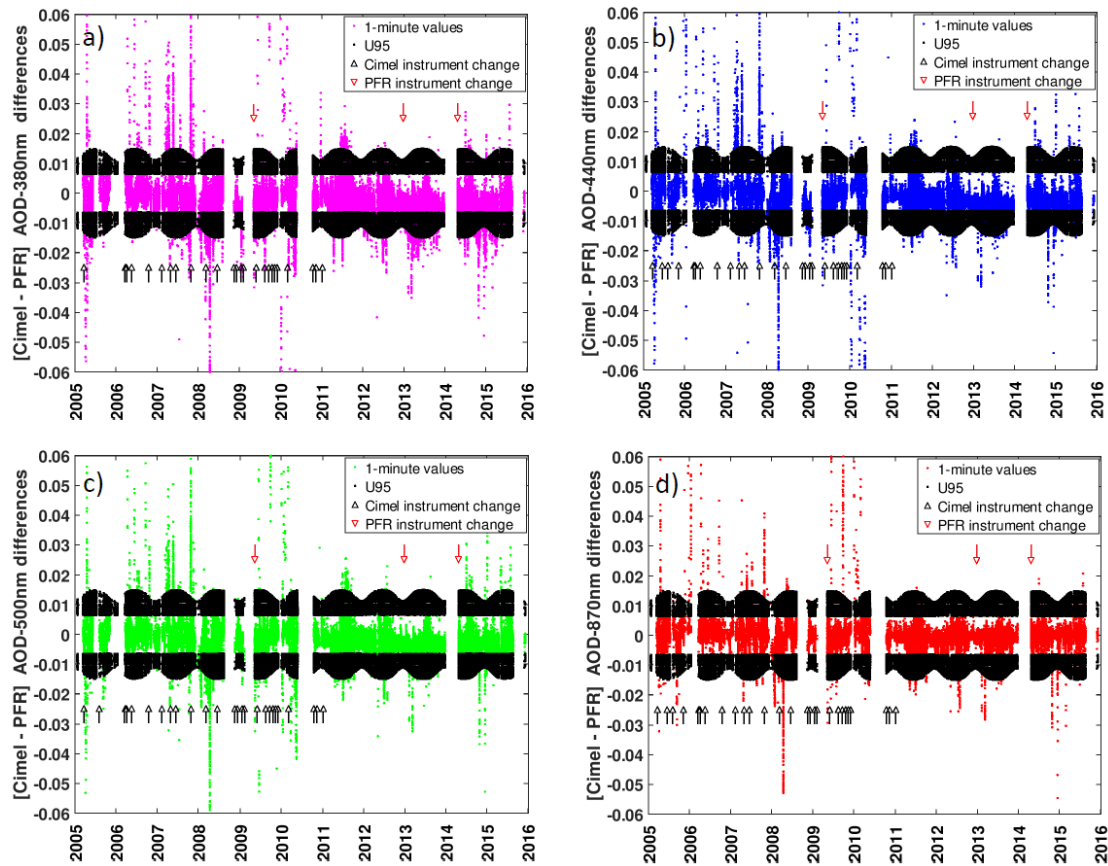
Supplement of

Aerosol optical depth comparison between GAW-PFR and AERONET-Cimel radiometers from long-term (2005–2015) 1 min synchronous measurements

Emilio Cuevas et al.

Correspondence to: Emilio Cuevas (ecuevasa@aemet.es)

Supplement S1. One-minute AOD data differences between AERONET-Cimel (V3) and GAW-PFR.

S1: One-minute AOD data differences between AERONET-Cimel (V3) and GAW-PFR for (a) 380 nm (75303 datapairs), (b) 440 nm (76290 data-pairs), (c) 500 nm (75335 data-pairs) and (d) 870 nm (76307 data-pairs) for the period 2005-2015. Black dots correspond to the U_{95} limits. A small number of outliers are out of the ±0.06 AOD differences range. Black arrows indicate a change of Reference AERONET-Cimel radiometer and red arrows indicate a change of the GAW-PFR instrument.

Supplement S2. Percentage of [Cimel (V3)-PFR] 1-minute AOD differences meeting the WMO criteria for the four compared channels.

S2.1: Percentage of AERONET-Cimel 1-minute AOD data (V3) meeting the WMO criteria for the four compared channels, and different AOD and AE scenarios for the period 2005-2015, number of data pairs are shown in brackets. The last row corresponds to the total percentages for the sub-period 2010-2015. AOD and AE traceability > 95% are marked in bold. This Table is equivalent to Table 4 of the manuscript for AERONET V2.

% of data within WMO limits	380 nm	440 nm	500 nm	870 nm
AOD ≤ 0.05	93.6 (60264)	**96.3 (62836)**	**97.1 (62545)**	**98.4 (64213)**
0.5 < AOD ≤ 0.10	91.0 (5138)	92.0 (5217)	92.6 (5222)	94.7 (5372)
AOD > 0.10	77.1 (4085)	84.1 (4537)	81.6 (4326)	93.3 (5034)
AE ≤ 0.25	78.7 (2472)	82.3 (2588)	79.0 (2483)	92.9 (6530)
0.25 < AE ≤ 0.6	90.2 (5941)	94.3 (6321)	94.9 (6255)	**97.4 (6530)**
AE > 0.6	94.1 (56952)	**96.5 (59181)**	**97.1 (58793)**	**98.7 (60514)**
Total 2005-2015	92.3 (69487)	**95.2 (72590)**	**95.7 (72093)**	**97.8 (74619)**
Total 2010-2015	92.8 (42463)	**96.8 (44328)**	**96.8 (44329)**	**98.8 (44329)**

S2.2: Percentage of AERONET-Cimel 1-minute AOD data (V3) meeting the WMO criteria for optical air mass > 5.0 for the period 2005-2015. The number of data pairs are shown in brackets.

% of data within WMO limits	380 nm	440 nm	500 nm	870 nm
m > 5.0	90.9 (9328)	93.4 (9474)	94.7 (9412)	96.7 (9475

Supplement S3. AOD variability 1-minute interval.
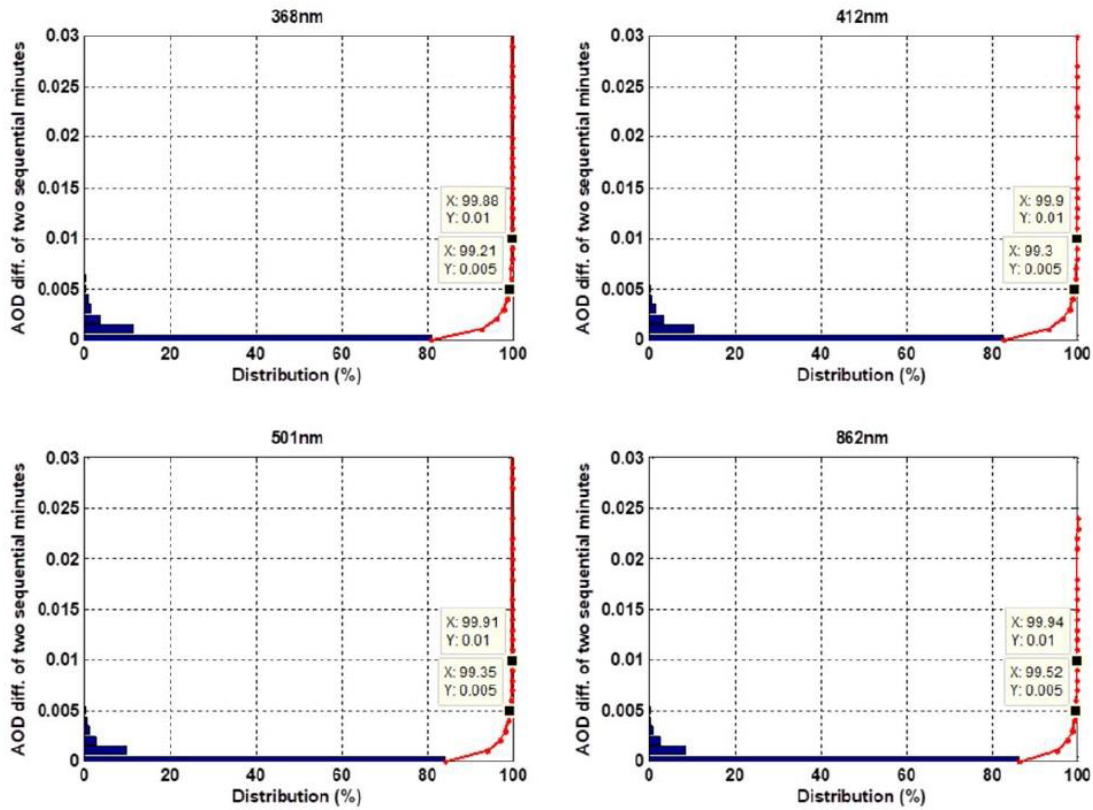
S3.1: Percentage of data with 1-minute AOD variability for the four GAW-PFR channels (368 nm, 412 nm, 501 nm, and 862 nm).

S3.2: Percentage of 1-minute AOD data from the Cimel triplets (year 2013) whose range of variation AOD_{max}-AOD_{min} > 0.015, for several AOD intervals, and for 380 nm and 500 nm. This value is half of the WMO traceability interval when m = 1 (maximum possible interval) (see Eq. 2 of the manuscript).

380 nm: 114 points outside WMO limits

AOD range	# cases outside WMO limit	Total # cases	% in AOD range	% in total # cases
≤ 0.03	13	11800	0.11	6.5×10^{-4}
(0.03-0.05]	14	3712	0.38	7.0×10^{-4}
(0.05-0.1]	18	1932	0.93	9.0×10^{-4}
(0.1-1.0]	61	2637	2.31	0.30
Total [0.0-1.0]	106	20081	0.52	0.52

500nm: 64 points outside WMO limits

AOD range	# cases outside WMO limit	Total # cases	% in AOD range	% in total # cases
≤ 0.03	2	13629	0.01	9.9×10^{-5}
(0.03-0.05]	11	2401	0.46	5.4×10^{-4}
(0.05-0.1]	9	1600	0.56	4.5×10^{-4}
(0.1-1.0]	42	2484	1.69	0.20
Total [0.0-1.0]	64	20114	0.32	0.32

Supplement S4. One-minute AOD differences between AERONET-Cimel (V2 and V3) and GAW-PFR versus optical air mass (m).
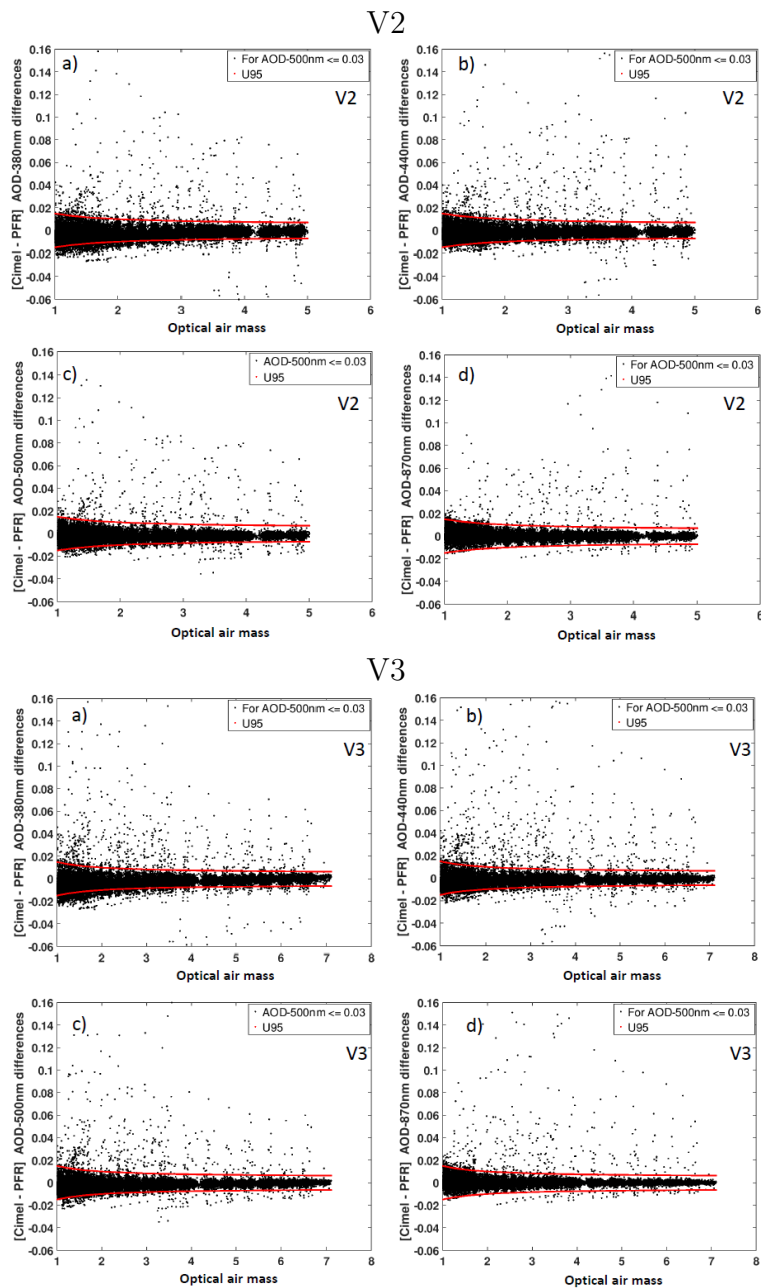
S4: One-minute AOD differences between AERONET-Cimel (V2 and V3) and GAW-PFR versus optical air mass (m) under pristine conditions ($AOD_{500nm} \leq 0.03$) in the period 2005-2015 for (a) 380 nm, (b) 440 nm, (c) 500 nm and (d) and 870 nm.

Supplement S5. Percentage of [Cimel (V3)-PFR] 1-minute AOD differences meeting the WMO criteria for each wavelength and for different optical air mass.

S5: Percentage of 1-minute AOD data (V3) meeting the WMO criteria for each wavelength for different optical air mass intervals under pristine conditions ($AOD_{500nm} \leq 0.03$) in the period 2005-2015. This Table is equivalent to Table 7 in the manuscript for AERONET V2.

Percentage of AOD differences within the U_{95} limits $AOD_{500\,nm} \leq 0.03$	Total (%)	$1 \leq m < 2$ (%)	$2 \leq m < 3$ (%)	$3 \leq m < 4$ (%)	$4 \leq m < 5$ (%)	$5 \leq m < 6$ (%)
380 nm	94.9	92.9	95.5	96.7	96.6	96.6
440 nm	97.5	97.2	97.3	98.0	97.6	97.7
500 nm	98.3	98.2	98.2	98.5	98.2	98.3
870 nm	99.0	99.1	99.1	99.1	98.6	98.7

Supplement S6. AOD diurnal range corresponding to AOD outliers under pristine conditions.
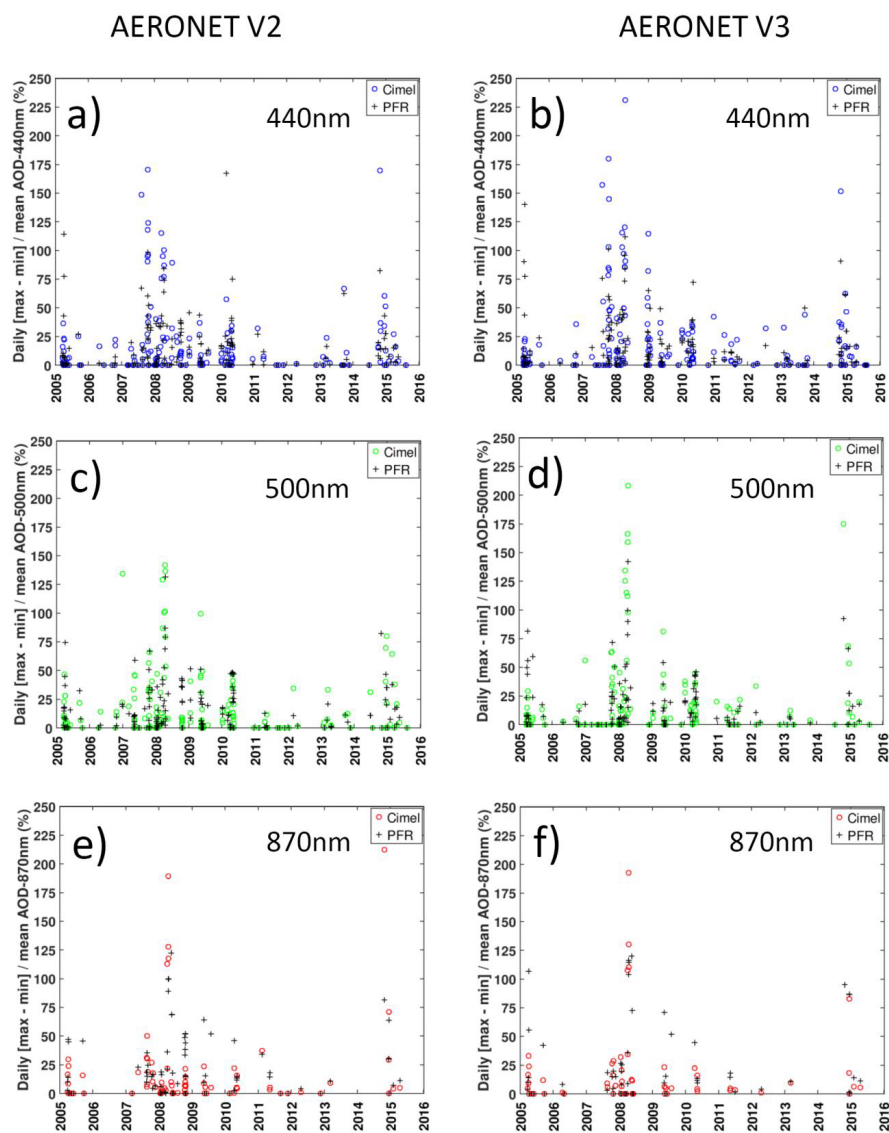
S6: AOD diurnal range variation (maximum value minus minimum value of AOD in one day) corresponding to AOD outliers (non-traceable AOD) under pristine conditions ($AOD_{Cimel-500 nm} \leq 0.03$) in the period 2005-2015 for AERONET V2 and V3 and for 440 nm, 500 nm and 870 nm: a) 440 nm V2; b) 440 nm V3; c) 500 nm V2; d) 500 nm V3; e) 870 nm V2; and f) 870 nm V3. This Figure is equivalent to Figure 3 of the manuscript for 380 nm.

Supplement S7. Percentage of AOD$_{380\,nm}$ outliers of GAW-PFR and AERONET Cimel (V3).

S7: Percentage of cases with AOD$_{380\,nm}$ outliers of both GAW-PFR and AERONET Cimel (V3) under pristine conditions (Cimel AOD$_{500\,nm} \leq 0.03$). In these cases the diurnal AOD range was higher than 25% of the daily mean AOD value for which a certain cause has been determined: calibration inaccuracies, cloud screening algorithm failures, mixture of the two previous causes, poor sun pointing, or unknown causes.

	PFR 51 cases	Cimel 81 cases
Calibration inaccuracies	7.8%	44.4%
Cloud screening failures	29.4%	21.0%
Calibration+ cloud screening errors	9.8%	11.1%
Sun misalignments	17.6%	0%
Unknown	35.3%	33.5%

Supplement S8. Examples of fictitious AOD diurnal variation in both GAW-PFR and AERONET-Cimel.
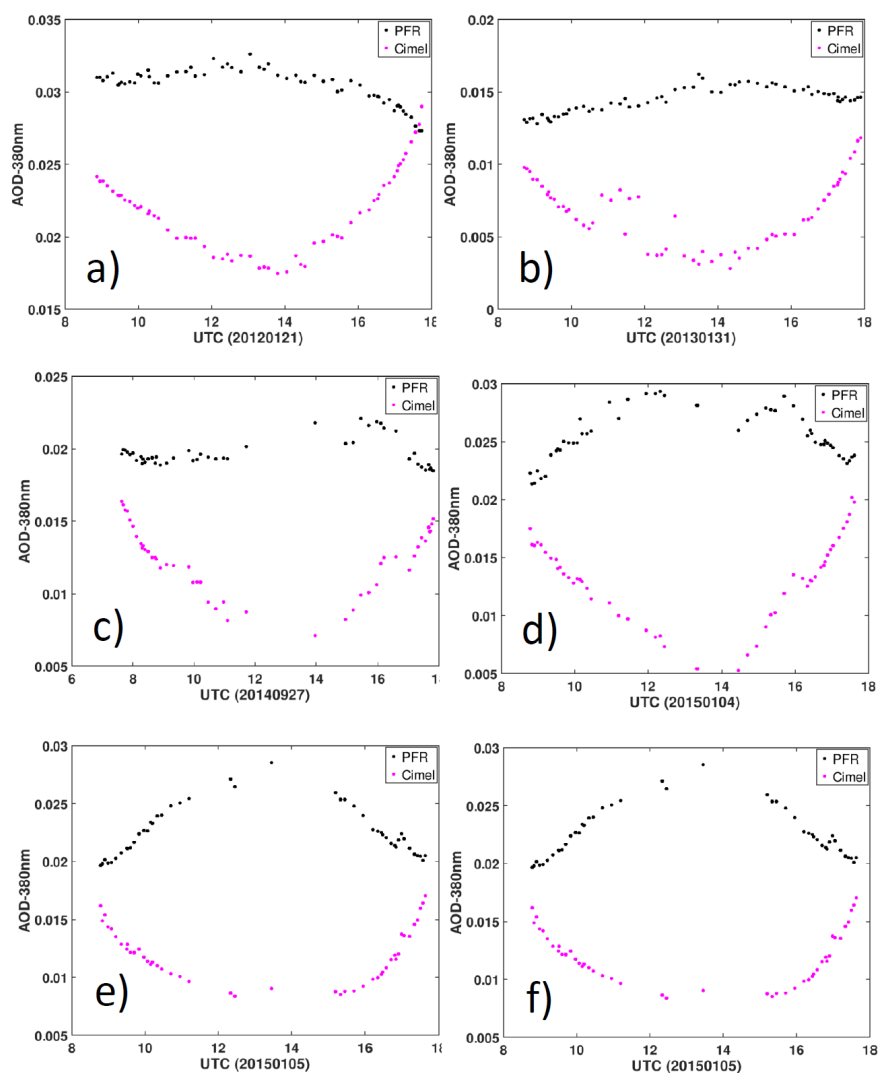
S8: Six examples of fictitious AOD diurnal variation in both GAW-PFR and AERONET-Cimel V3 due to small calibration inaccuracies in the UV channel (368 nm for GAW-PFR and 380 nm for AERONET-Cimel). The date is indicated in the x-axis. In all these cases a clear fictitious AOD diurnal cycle is observed in AERONET-Cimel V3, normally less than 0.01. In cases d), e), and f) an anomalous diurnal cycle is also observed, but in the opposite direction (convex curve), in the case of the GAW-PFR.

These cases reflect a non-perfect calibration in the UV channel and are a cause of non-traceability.

Supplement S9. Examples of AOD diurnal variation of all chanels from AERONET-Cimel Level 2 V3.

The screenshots of AERONET V3 level 2 show that the fictitious diurnal cycle is accentuated, or only clearly observed, in the 340 and 380 nm channels.

Screenshots from http://aeronet.gsfc.nasa.gov (last access: 1 february 2019). Izana AERONET station Level 2 Version 3.
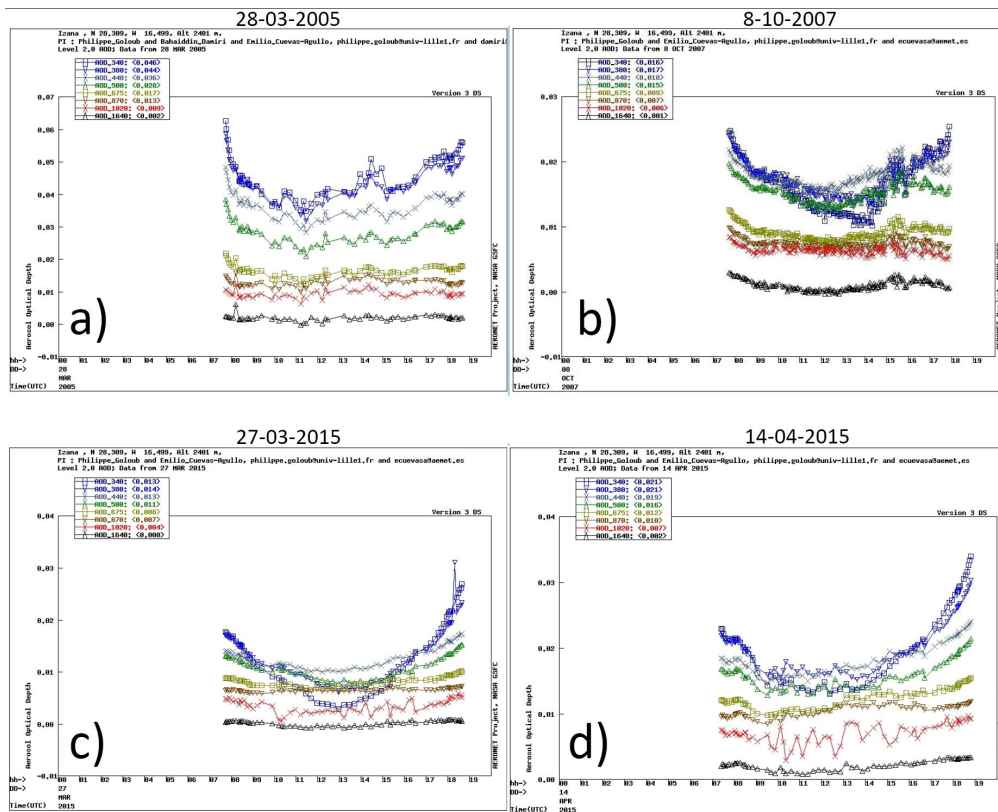
S9: AERONET V3 level 2 AOD Screenshots for all the wavelenghts: a) March 28th, 2005; b) October 8th; 2007; c) March 27th, 2015; and d) April 14th, 2015.

S10. Case analysis of cirrus clouds.

A type of clouds that cause problems in AOD retrieval are the cirrus clouds, usually being present at Izaña between January and April, associated with the presence of the subtropical jet that is normally found in the vicinity of the Canary Islands at this time of year (Rodríguez-Franco and Cuevas, 2013). A constant cloud optical thickness (COT) corresponding to a cloud of a certain horizontal extension would cause the successive measurements within a minute to correspond to the same cloud stage, and therefore it would not be discernible from the extinction caused by aerosols. In the case of very thin cirrus clouds, AOD could increase up to 0.03 (Chew et al., 2011; Giannakaki et al., 2007) with small fluctuations, that cloud-screening algorithms could interpret as the presence of an aerosol layer. Huang et al. (2012) evaluated the impact on AERONET level 2.0 AOD retrievals from cirrus contamination highlighting the difficulties to remove completely their signature, mainly from those subvisual thin cirrus. According to Kinne et al. (1997), optical depth estimates from cirrus derived with sunphotometers have to include forward-scattering effects. Their results show that for cirrus, and instruments with 2.0° and 2.4° FOV, the correction factors vary between 1.6 and 2.5 depending on the crystal size. Taking into account that the FOV of the GAW-PFR is 2.5°, while that of the AERONET-Cimel is 1.3°, such cases will affect the comparison results.

Three case analyses on cirrus clouds are shown below.
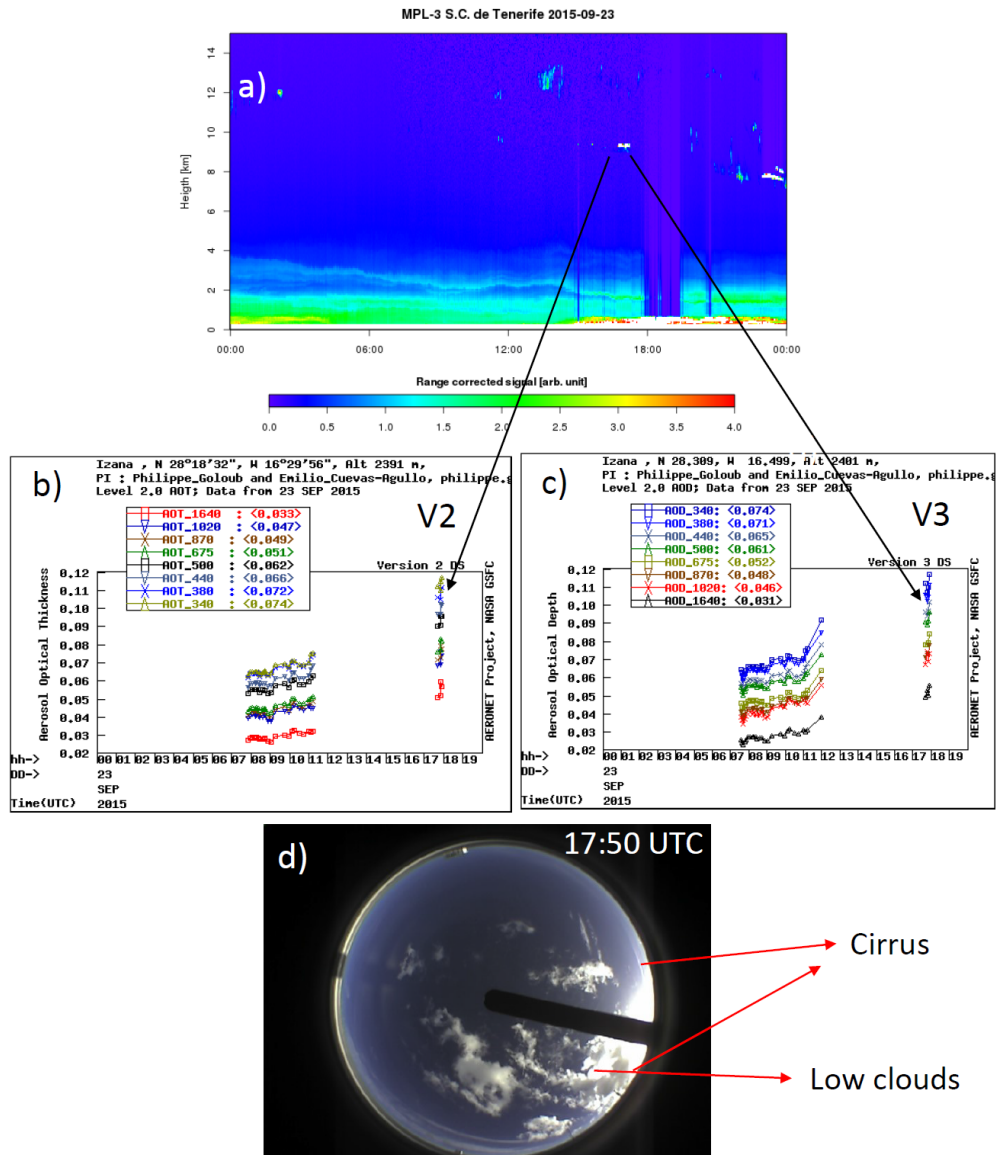
S10.1: Case analysis September 23, 2015: The range corrected backscattering signal vertical cross section of the Micropulse lidar (MPL) (a) shows scattered cirrus clouds throughout the day (a), and one in particular around 17:45 UTC that affects the Cimel AOD measurements. Unfortunately, we do not have measurements for the PFR at this time. The all-sky camera confirms the presence of cirrus clouds at that time (d). The AERONET V2 snapshot registers the impact of the cirrus (b), punctually increasing the AOD values by two. AERONET V3 (c) does not filter these values.
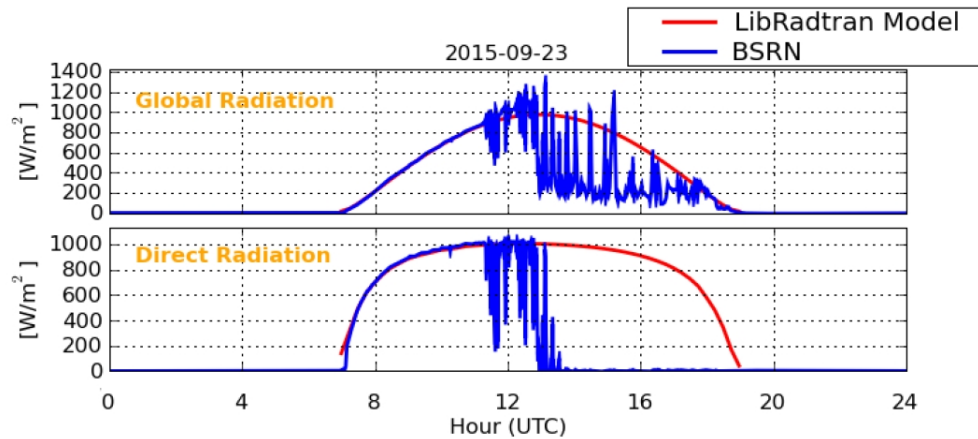
S10.2: Case analysis September 23, 2015: Global Horizontal (GHI) (top) and Direct Normal Irradiance (DNI) (bottom) from the Surface baseline radiation Network (BSRN) program at Izaña.

Global Horizontal (GHI) and Direct Normal Irradiance (DNI) from the Surface Baseline Radiation Network (BSRN) program at Izaña Observatory clearly indicates the presence of clouds in the second half of the day. A high attenuation in DNI from just before 14UTC and during the rest of the day is observed what is not compatible with relatively high AOD measurements at around 17:45UTC (S10.1)

17:45 UTC: Cirrus clouds
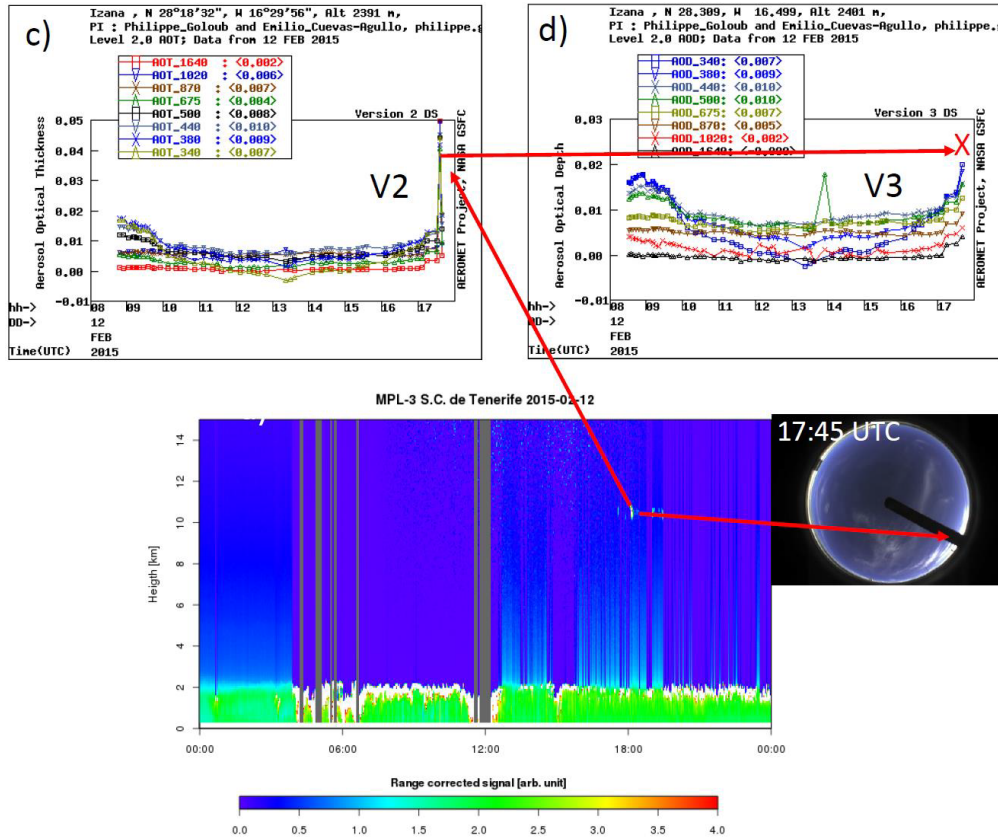
S10.3: Case analysis February 12, 2015: The range corrected backscattering signal vertical cross section of the Micropulse lidar (MPL) (a) shows the presence of cirrus clouds at around 11 km height between 17:30 and 19:00UTC (a), this is confirmed by the all-sky camera image (b). These cirrus clouds affected the AERONET V2 AOD, increasing the AOD values between 2 and 5 times, depending on the channel (c). AERONET V3 cloud screening correctly filtered these anomalous AOD values (d).
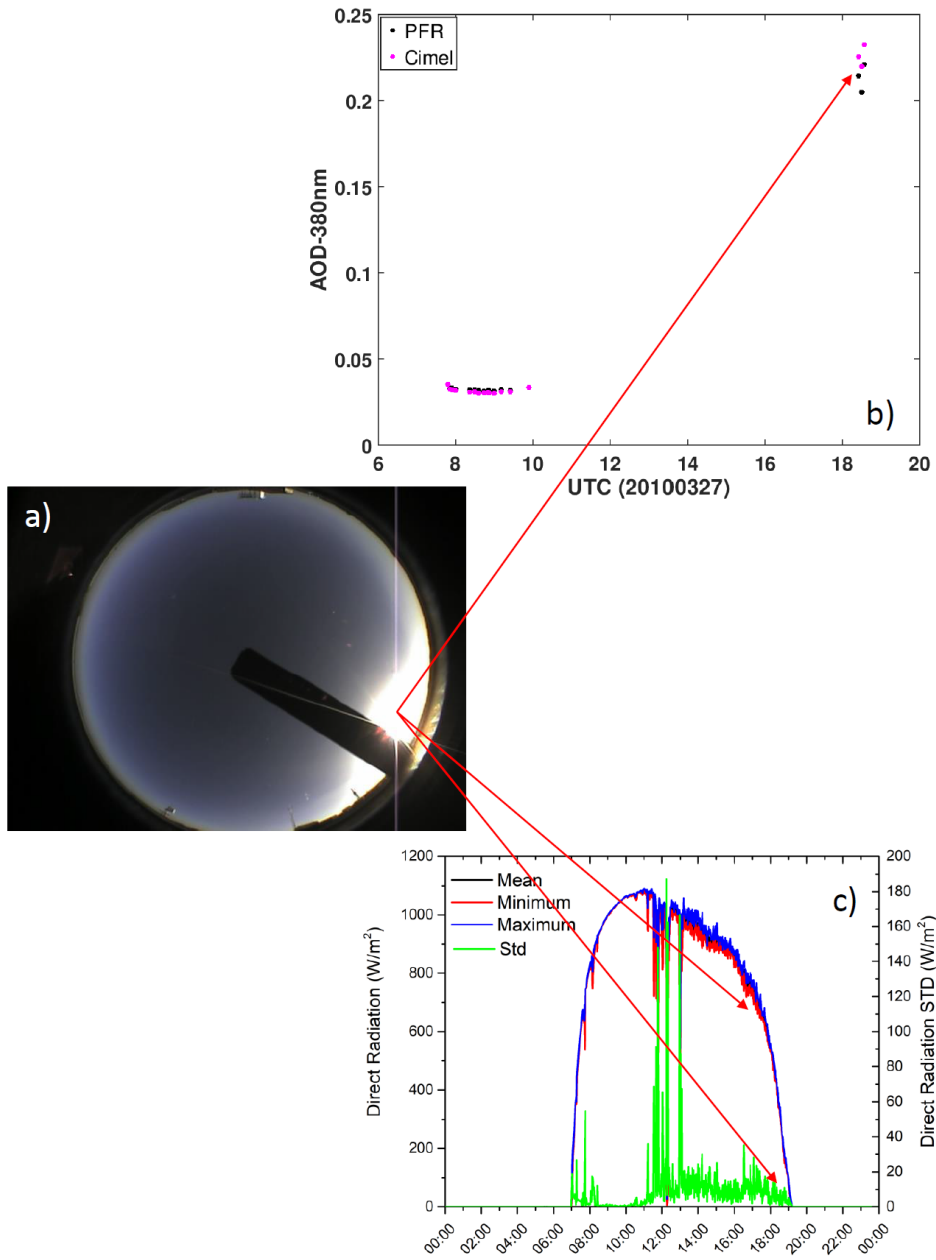
S10.4: Case analysis March 27, 2010: The cirrus cloud observed by the all-sky camera around 18:30UTC (a) affected both GAW-PFR and AERONET V3, giving AOD values about 8 times higher than those observed early in the morning (b). The erroneous AOD values of the GAW-PFR are slightly lower than those of AERONET V3. The cause could be a greater forward-scattering effect of the cirrus cloud on the GAW-PFR due to its higher FOV (compared with that of the Cimel). The presence of cirrus has been confirmed with the direct normal irradiance records (c) that shows a typical noisy signal (relatively high standard deviation) until 19 UTC.

Supplement S11. Impact of low stratocumulus on AOD retrieval.

Another cloud scenario that can affect AOD traceability is the presence of low clouds (stratocumulus) that sometimes exceed the observatory height level because the temperature inversion is around 2400 m height.

The selected case analysis is really interesting. Moreover, it is representative of a relatively frequent situation in winter, when the temperature inversion is very close to the altitude of the Izaña Observatory.

The Modis image of that day (S11.1a) shows a large part of the island of Tenerife covered with stratocumulus except in its central part corresponding to the summits of the island (2400 m a.s.l. plateau) in whose NE limit the Izaña Observatory is located. This is confirmed by the range corrected backscattering signal vertical cross section of the Micropulse lidar (MPL) (S11.1b) indicating a quasi-permanent stratocumulus layer above 2000 m a.s.l. throughout the day. In these cases, the appearance of intermittent fog banks in the Observatory or on the horizon (S11.1c), in its vicinity, is very common.

The AOD outliers measured by the PFR around 08:00 UTC (S11.1d) are due precisely to these intermittent fog blanks on the horizon and/or above Izaña Observatory. In S11.2 we can see a sequence of all-sky images from 07:30 UTC. Although the all-sky camera records some frozen ice on its dome, it does not appear in the sunlit part. The PFR external lens were free of frozen ice all the time. From the all-sky camera imagery, the presence of fog from around 08:00 UTC to 09:00 UTC is observed. This is confirmed with DNI and other radiation-components measurements (S11.3). Early morning fog veils caused erroneous AOD values from PFR but not from Cimel. The explanation is in the measurement mode. As the sky conditions changes are very fast under intermittent fog blanks, the 1-second measurements (at 1-minute intervals) of the PFR may not capture this AOD variation, while the triplets of the Cimel (3 consecutive 1-second measurements) might do so, correctly functioning the cloud screening in this case.
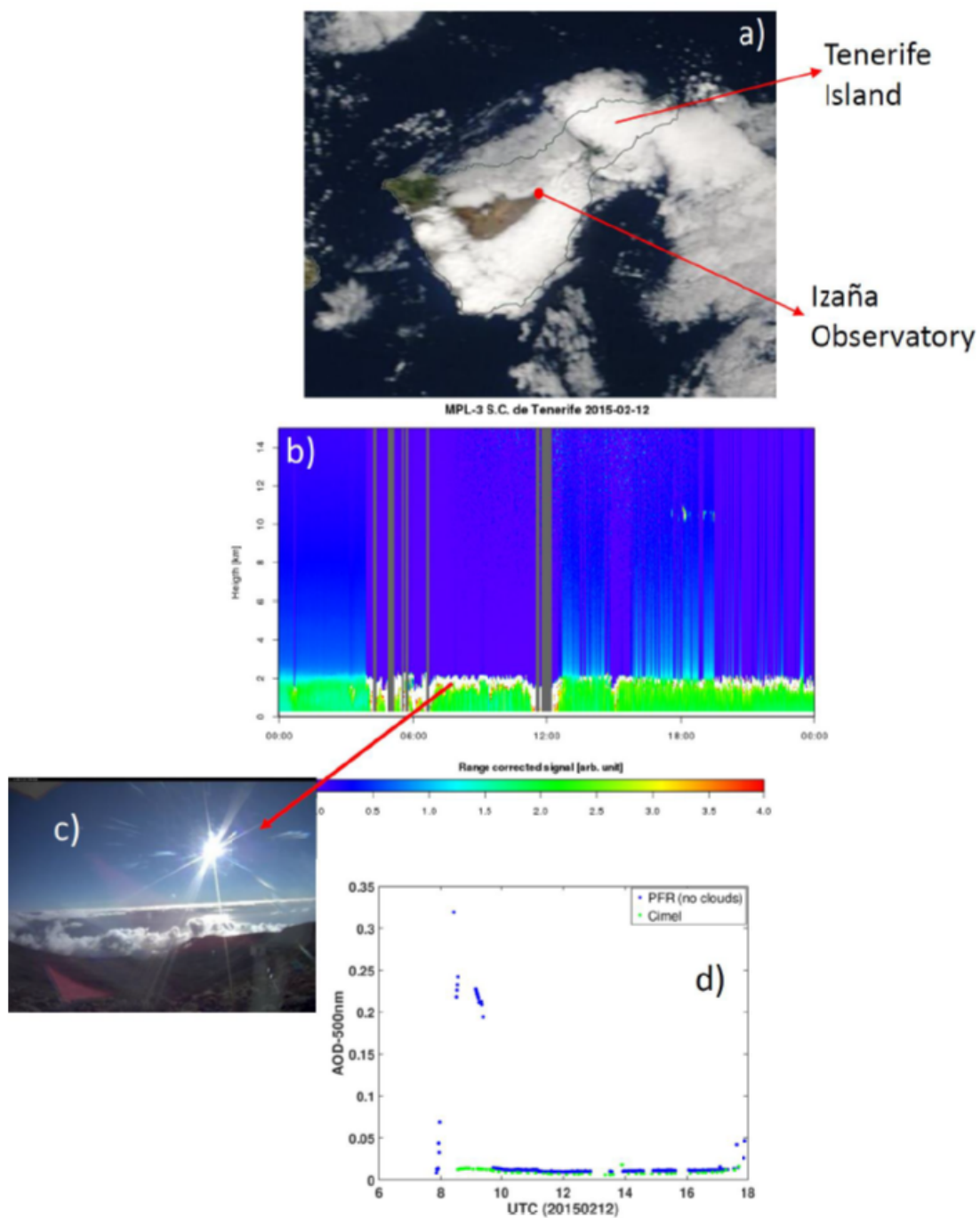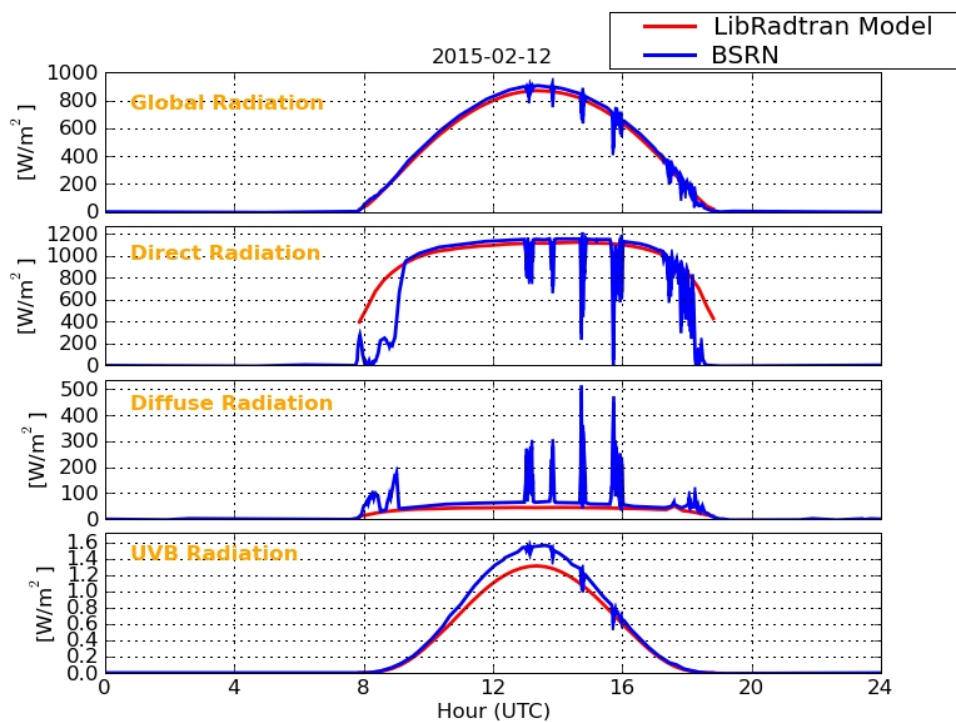
S11.1: February 12, 2015: Modis visible image; the range corrected backscattering signal vertical cross section of the Micropulse lidar (MPL) (b);East facing webcam picture around 09:00 UTC; PFR and Cimel AOD (d).
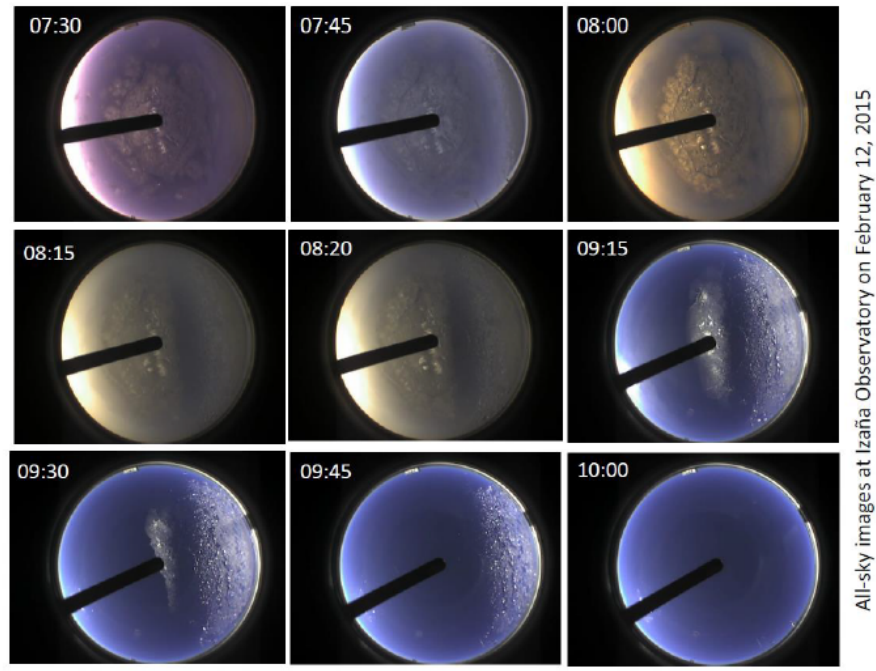
S11.2: All-sky images sequence on February 12, 2015.
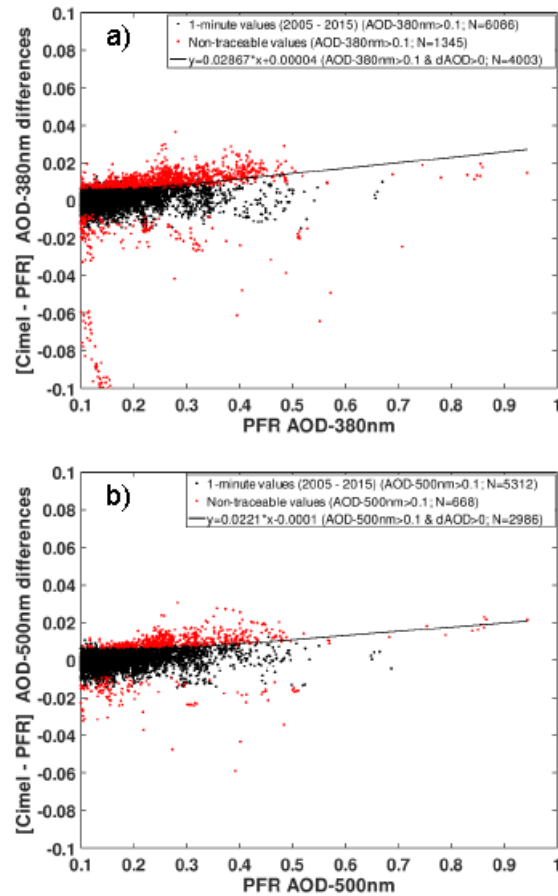
S11.3: Global Horizontal (GHI), Direct Normal Irradiance (DNI), Difuse Horizontal Irradiance (DHI) and UVB radiation from the Surface Baseline Radiation Network (BSRN) program at Izaña Observatory on February 12, 2015.

**Supplement S12. Actual AOD differences between AERONET-Cimel
V3 and GAW-PFR vs PFR AOD**

S12: Actual AOD differences between AERONET-Cimel V3 and GAW-PFR vs PFR
AOD at (a) 380 nm (b) and 500 nm for the period 2005-2015. The fitting line has been
calculated with AOD data > 0.1 and Cimel-PFR AOD difference > 0. Number of data
used in the plots are indicated in the legend. The percentage of non-traceable AOD data
with these conditions is $\sim 22\%$ for 380 nm, and $\sim 13\%$ for 500 nm. Note that some
traceable (black) points show larger AOD differences than non-traceable (red) points
because of air mass dependence of the WMO traceability criterion.

Supplement S13. Percentage of AERONET V3 AOD data outside the U_{95} limits for high AOD conditions

S13: Percentage of AERONET V3 AOD data outside the U_{95} limits at 380 nm, 440 nm, 500 nm and 870 nm channels and for three $AOD_{500\ nm}$ thresholds with respect to all data and with respect to all data for each AOD interval (in brackets).

	Percentage of AOD data outside the U_{95} limits (%)		
	$AOD_{500\ nm} > 0.1$	$AOD_{500\ nm} > 0.2$	$AOD_{500\ nm} > 0.3$
380 nm	1.6 (22.9)	1.1 (42.0)	0.4 (54.4)
440 nm	1.1 (15.9)	0.9 (32.5)	0.4 (49.0)
500 nm	1.3 (18.4)	1.0 (37.6)	0.5 (55.7)
870 nm	0.5 (6.7)	0.4 (13.4)	0.2 (19.0)

Comparing versions V2 and V3, we can see that, except for the 380 nm channel, in V3 the non-AOD traceability increases with respect to that found in V2.

Supplement S14. Simulations of scattered to direct radiation simulations.
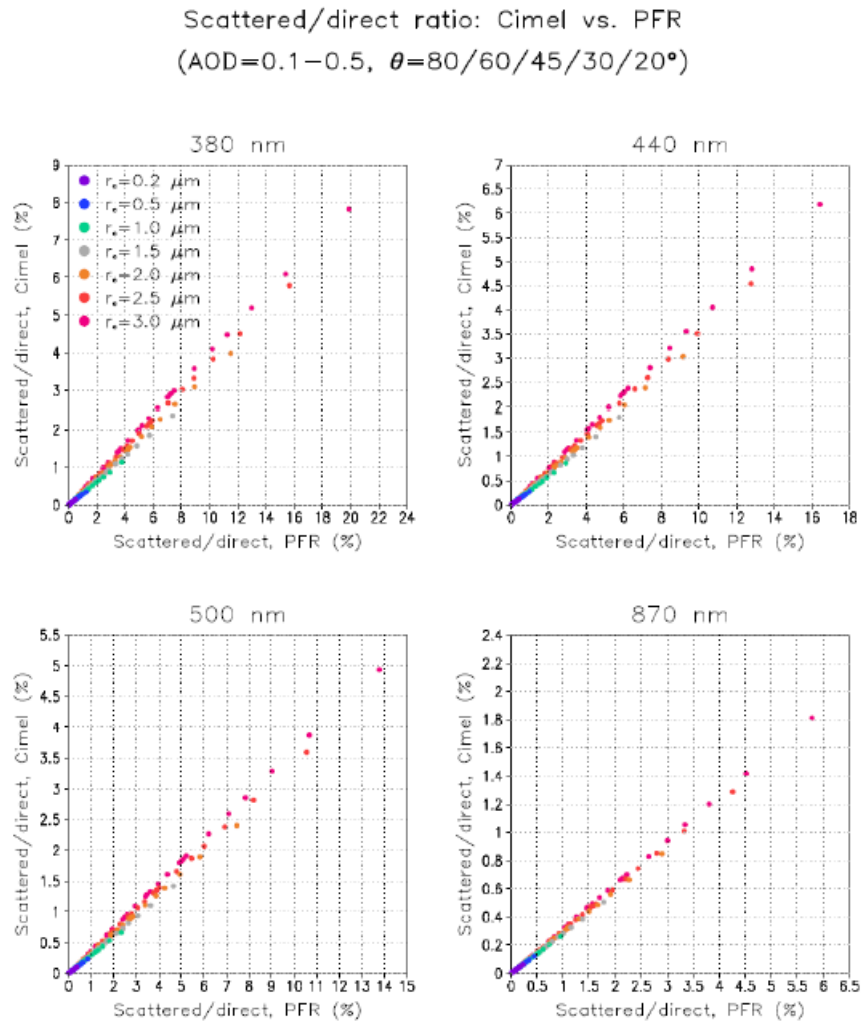
S14: Scattered to direct radiation simulations made with a forward Monte Carlo model (Barker 1992, Barker 1996, Räisänen et al. 2003) for FOVs of 2.5° and 1.2° for seven values of effective radius (r_e = 0.2, 0.5, 1.0, 1.5, 2.0, 2.5, and 3.0 μm), for five AOD values (AOD = 0.1, 0.2, 0.3, 0.4, and 0.5), and for five solar zenith angles (θ = 20°, 30°, 45°, 60° and 80°).

Supplement S15. Relative error in AOD for PFR and Cimel.
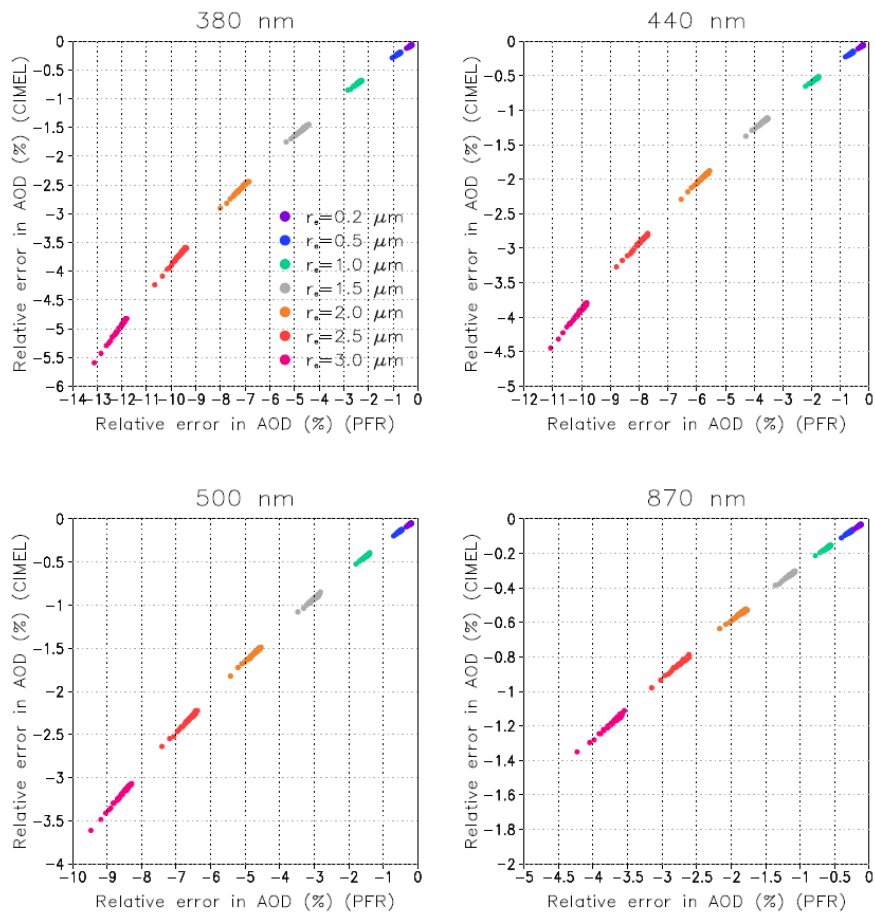
S15: Relative error in AOD for PFR (x-axis) and Cimel (y-axis) for seven values of effective radius (r_e =0.2, 0.5, 1.0, 1.5, 2.0, 2.5 and 3.0 μm), for five AOD values (AOD = 0.1, 0.2, 0.3, 0.4, and 0.5), and for five solar zenith angles ($\theta = 20°$, $30°$, $45°$, $60°$ and $80°$).

Supplement S16. Actual AOD differences between AERONET-Cimel V3 and GAW-PFR vs PFR AOD after AOD$_{PFR}$ correction.
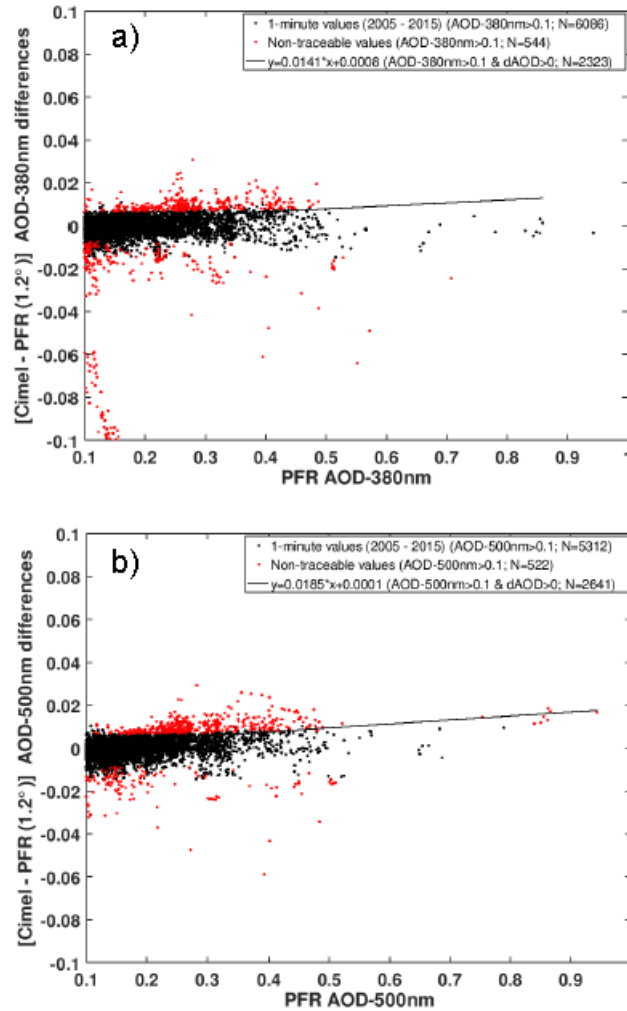
S16: The same as the Figure of Supplement S13 (AERONET V3) after the PFR AOD data were "corrected" by adding + 3.3% at 380 nm and + 2.2% at 500 nm to the 1-minute AOD PFR data > 0.1.

Supplement S17. Ångström exponent comparison

This basic statistic indicates the degree of agreement between GAW-PFR and AERONET-Cimel in the aerosol "characterization" in the long term using only AE. Therefore, we did not include AOD as it would have been strictly necessary to carry out a proper characterization of the aerosol types present in a specific site. The four chosen categories are very close to the real ones at Izaña but without including AOD. What is relevant here in is not the chosen categories, but the degree of agreement that both radiometers have to provide the same aerosol category according to the AE. This requires a very high simultaneous agreement in AOD in the four channels.
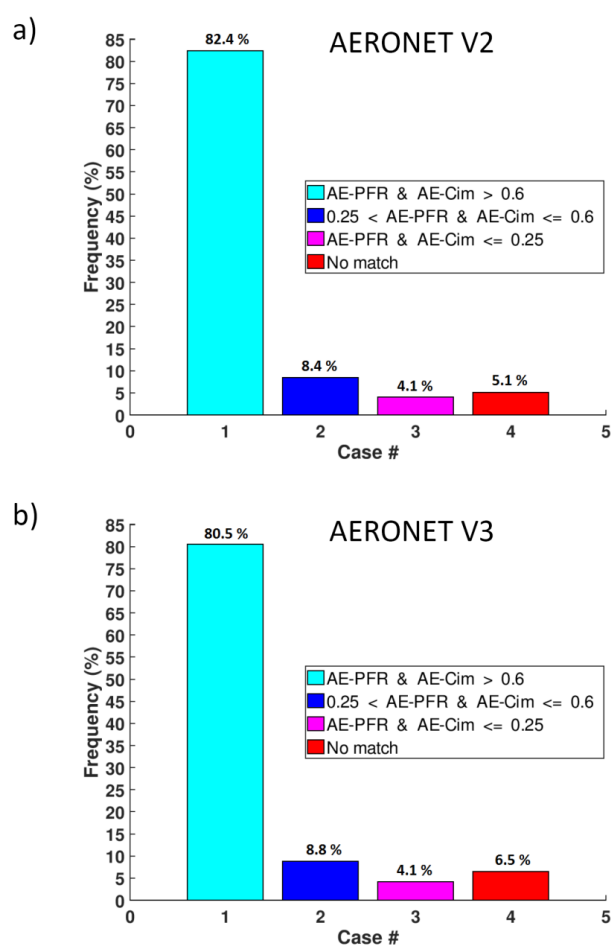
S17: Percentage of cases in which GAW PFR and AERONET V2 (a) and V3 (b) coincide in each AE scenario (period 2005-2015).

References

Chew, B. N., Campbell, J.R., Reid, J.S., Giles, D.M., Welton, E.J., Salinas, S.V., and Liew, S.C.: Tropical cirrus cloud contamination in sun photometer data, Atmos. Environ., 45, 6724-6731. 10.1016/j.atmosenv.2011.08.017, 2011.

Giannakaki, E., Balis, D. S., Amiridis, V., and Kazadzis, S.: Optical and geometrical characteristics of cirrus clouds over a Southern European lidar station, Atmos. Chem. Phys., 7, 5519-5530, https://doi.org/10.5194/acp-7-5519-2007, 2007.

Huang, J., Hsu, N.C., Tsay, S.-C., Holben, B.N., Welton, E.J., Smirnov, A., Jeong, M.-J., Hansell, R.A., Berkoff, T.A., Liu, Z., Liu, G.-R., Campbell, J.R., Liew, S.C., and Barnes, J.E.: Evaluations of cirrus contamination and screening in ground aerosol observations using collocated lidar systems, J. Geophys. Res., 117, D15204, doi:10.1029/2012JD017757, 2012.

Kinne, S., Akerman, T. P., Shiobara, M., Uchiyama, A., Heymsfield, A. J., Miloshevich, L., Wendell, J., Eloranta, E., Purgold, C., and Bergstrom, R. W.: Cirrus cloud radiative and microphysical properties from ground observations and in situ measurements during FIRE 1991 and their application to exhibit problems in cirrus solar radiative transfer modeling, J. Atmos. Sci., 54, 2320–2344, https://doi.org/10.1175/1520-0469(1997)054¡2320:CCRAMP¿2.0.CO;2, 1997.

Rodriguez-Franco, J. J., and Cuevas, E.: Characteristics of the subtropical tropopause region based on long-term highly-resolved sonde records over Tenerife, J. Geophys. Res. Atmos., 118, doi:10.1002/jgrd.50839, 2013.

B. Anexo 2: Publicaciones

A continuación se citan la relación trabajos científicos en los que he participado durante el periodo de realización de la tesis, incluyendo las contribuciones a congresos, informes y artículos científicos.

Participaciones en congresos:

- Almansa, A. F., Cuevas, E., Torres, B., Barreto, A., García, R., Cachorro, V., Guirado, C., de Frutos, Á. M., López, C. and Ramos, R.: Desert dust remote sensing with the new zenith looking narrow-band radiometer based system (ZEN), in Technical Conference on Meteorological and Environmental Instruments and Methods of Observation (2016), p. 12., 2016.

- Almansa, A. F., Cuevas, E., Barreto, A., Torres, B. and López, C.: Dust aerosol optical depth (DOD) monitoring with a ZEN-R52 radiometer: An upgraded version of the ZEN-R41 prototype, in The 9th International Workshop on Sand / Dust storm and Associated Dustfall, 2018.

Informes científicos:

- Cuevas, E., Milford, C., Bustos, J. J., del Campo-Hernández, R., García, O. E., García, R. D., Gómez-Peláez, A. J., Ramos, R., Redondas, A., Reyes, E., Rodríguez, S., Romero-Campos, P. M., Schneider, M., Belmonte, J., Gil-Ojeda, M., Almansa, F., Alonso-Pérez, S., Barreto, A., González-Morales, Y., Guirado-Fuentes, C., López-Solano, C., Afonso, S., Bayo, C., Berjón, A., Bethencourt, J., Camino, C., Carreño, V., Castro, N. J., Cruz, A.M., Damas, M., De Ory-Ajamil, F., García, M. I., Fernández-de Mesa, C. M., González, Y., Hernández, C., Hernández, Y., Hernández, M. A., Hernández-Cruz, B., Jover, M., Kühl, S. O., López-Fernández, R., López-Solano, J., Peris, A., Rodríguez-Franco, J. J., Sálamo, C., Sepúlveda, E. and Sierra, M.: Izaña Atmospheric Research Center Activity Report2012-2014. (Eds. Cuevas, E., Milford, C. and Tarasova, O.), State Meteorological Agency (AEMET), Madrid, Spain, and World Meteorological Organization, Geneva, Switzerland, NIPO: 281-15-004-2, WMO/GAW Report No. 219, 2015.

- Cuevas, E., Milford, C., Bustos, J. J., del Campo-Hernández, R., García, O. E., García, R. D., Gómez-Peláez, A. J., Guirado-Fuentes, C., Marrero, C., Prats, N., Ramos, R., Redondas, A., Reyes, E., Rodríguez, S., Romero-Campos, P. M., Schneider, M., Belmonte, J., Yela, M., Almansa, F., Barreto, A., López-Solano, C., Basart, S., Terradellas, E., Afonso, S., Bayo, C., Berjón, A., Bethencourt, J., Carreño, V., Castro, N. J., Cruz, A.M., Damas, M., De Ory-Ajamil, F., García, M.I., Gómez-Trueba, V., González, Y., Hernández, C., Hernández, Y., Hernández-Cruz, B., Jover, M., León-Luís, S. F., López-Fernández, R., López-Solano, J., Rodríguez, E., Rodríguez-Franco, J. J., Rodríguez-Valido,

M., Sálamo, C., Sanromá, E., Santana, D., Santo Tomás, F., Sepúlveda, E., Sierra, M., and Sosa, E.: Izaña Atmospheric Research Center Activity Report 2015-2016. (Eds. Cuevas, E., Milford, C., and Tarasova, O.), State Meteorological Agency (AEMET), Madrid, Spain and World Meteorological Organization, Geneva, Switzerland, NIPO: 014-17-012-9, WMO/GAW Report No. 236, 2017.

- Cuevas, E., Milford, C., Bustos, J. J., R., García, O. E., García, R. D., Gómez-Peláez, A. J., Guirado-Fuentes, C., Marrero, C., Prats, N., Ramos, R., Redondas, A., Reyes, E., Rivas-Soriano, P. P., Rodríguez, S., Romero-Campos, P. M., Torres, C. J., Schneider, M., Yela , M., Belmonte, J., del Campo-Hernández, R., Almansa, F., Barreto, A., López-Solano, C., Basart, S., Terradellas, E., Werner, E., Afonso, S., Bayo, C., Berjón, A., Carreño, V., Castro, N. J., Chinea, N., Cruz, A. M., Damas, M., De Ory-Ajamil, F., García, M.I., Gómez-Trueba, V., Hernández, C., Hernández, Y., Hernández-Cruz , B., León -Luís , S. F., López-Fernández, R., López-Solano, J., Parra, F., Rodríguez, E., Rodríguez-Valido, M., Sálamo, C., Sanromá, E., Santana, D., Santo Tomás, F., Sepúlveda, E., and Sosa, E.: Izaña Atmospheric Research Center Activity Report 2017-2018. (Eds. Cuevas, E., Milford, C. and Tarasova, O.), State Meteorological Agency (AEMET), Madrid, Spain and World Meteorological Organization, Geneva, Switzerland, WMO/GAW Report No. 247, 2019.

Artículos científicos

- Almansa, A. F., Cuevas, E., Torres, B., Barreto, Á., García, R. D., Cachorro, V. E., de Frutos, Á. M., López, C., and Ramos, R.: A new zenith-looking narrow-band radiometer-based system (ZEN) for dust aerosol optical depth monitoring, Atmos. Meas. Tech., 10, 565–579, https://doi.org/10.5194/amt-10-565-2017, 2017.

- Almansa, A. F., Cuevas, E., Barreto, Á., Torres, B., García, O. E., Delia García, R., Velasco-Merino, C., Cachorro, V. E., Berjón, A., Mallorquín, M., López, C., Ramos, R., Guirado-Fuentes, C., Negrillo, R. and de Frutos, Á. M.: Column Integrated Water Vapor and Aerosol Load Characterization with the New ZEN-R52 Radiometer, Remote Sensing, 12(9), 1424, https://doi.org/10.3390/rs12091424, 2020.

- Barreto, Á., Cuevas, E., Pallé, P., Romero, P. M., Guirado, C., Wehrli, C. J., and Almansa, F.: Recovering long-term aerosol optical depth series (1976–2012) from an astronomical potassium-based resonance scattering spectrometer, Atmos. Meas. Tech., 7, 4103–4116, https://doi.org/10.5194/amt-7-4103-2014, 2014.

- Barreto, Á., Cuevas, E., Granados-Muñoz, M.-J., Alados-Arboledas, L., Romero, P. M., Gröbner, J., Kouremeti, N., Almansa, A. F., Stone, T., Toledano, C., Román, R., Sorokin, M., Holben, B., Canini, M., and Yela, M.: The new sun-sky-lunar Cimel CE318-T multiband photometer – a comprehensive performance evaluation, Atmos. Meas. Tech., 9, 631–654, https://doi.org/10.5194/amt-9-631-2016, 2016.

- Barreto, Á., Román, R., Cuevas, E., Berjón, A. J., Almansa, A. F., Toledano, C., González, R., Hernández, Y., Blarel, L., Goloub, P., Guirado, C., and Yela, M.: Assessment of nocturnal aerosol optical depth from lunar photometry at the Izaña high mountain observatory, Atmos. Meas. Tech., 10, 3007–3019, https://doi.org/10.5194/amt-10-3007-2017, 2017.

- Barreto, A., Román, R., Cuevas, E., Pérez-Ramírez, D., Berjón, A. J., Kouremeti, N., Kazadzis, S., Gröbner, J., Mazzola, M., Toledano, C., Benavent-Oltra, J.A., Doppler, L., Juryšek, J., Almansa, A. F., Victori, S., Maupin, F., Guirado-Fuentes, C., González, R., Vitale, V., Goloub, P., Blarel, L., Alados-Arboledas, L., Woolliams, E., Taylor, S., Antuña, J.C.,and Yela, M.: Evaluation of nighttime aerosols measurements and lunar irradiance models in the frame of the first multi-instrument nocturnal intercomparison campaign, Atmospheric Environment, 202, 190–211, https://doi.org/10.1016/j.atmosenv.2019.01.006, 2019.

- Barreto, Á., García, O. E., Schneider, M., García, R. D., Hase, F., Sepúlveda, E., Almansa, A. F., Cuevas, E., and Blumenstock, T.: Spectral Aerosol Optical Depth Retrievals by Ground-Based Fourier Transform Infrared Spectrometry, Remote Sensing, 12(19), 3148, https://doi.org/10.3390/rs12193148, 2020.

- Cuevas, E., Romero-Campos, P. M., Kouremeti, N., Kazadzis, S., Räisänen, P., García, R. D., Barreto, A., Guirado-Fuentes, C., Ramos, R., Toledano, C., Almansa, F., and Gröbner, J.: Aerosol optical depth comparison between GAW-PFR and AERONET-Cimel radiometers from long-term (2005–2015) 1 min synchronous measurements, Atmos. Meas. Tech., 12, 4309–4337, https://doi.org/10.5194/amt-12-4309-2019, 2019.

- Lakkala, K., Redondas, A., Meinander, O., Thölix, L., Hamari, B., Almansa, A. F., Carreno, V., García, R. D., Torres, C., Deferrari, G., Ochoa, H., Bernhard, G., Sanchez, R., and de Leeuw, G.: UV measurements at Marambio and Ushuaia during 2000–2010, Atmos. Chem. Phys., 18, 16019–16031, https://doi.org/10.5194/acp-18-16019-2018, 2018.